SMOOTH AND ROUGHENED HORIZONTAL CYLINDERS IN PERIODIC WAVES AND CURRENT

Report for

The National Science Foundation

and

The Oregon State University Sea Grant College Program

by

Chung-Chu Teng

and

John H. Nath

Department of Civil Engineering
Ocean Engineering Program
Oregon State University
Corvallis, OR 97331

ACKNOWEDGEMENTS

This report is essentially the thesis for the partial fulfillment of the Ph.D. program in Civil Engineering with emphasis in Ocean Engineering for the first author. Major support was received from the National Science Foundation, grant number CEE-8310732-01, and the OSU Sea Grant College Program, project number R/CE-20-PD. Partial support also was provided by the American Petroleum Institute, the Chevron Oil Field Research Company, and the OSU Milne Computer Center. The authors are grateful to all these agencies.

ABSTRACT

The support structures for offshore platforms that are used to recover raw petroleum consist of veritcal, horizontal, and inclined cylindrical members. Since the design for these platforms is increasingly refined for large, expensive structures, the knowledge of forces on individal cylindrical members becomes increasingly important. This thesis emphasizes information about the horizontal cylindrical members in periodic waves and in periodic waves with towing (waves plus current approximation).

This thesis presents the results of a series of laboratory experiments on four horizontal cylinders with different surfaces: smooth, sand-roughened, barnacle-roughened, and one with rigid artificial sea anemones. Both amplitudes and phases of harmonic components of horizontal and vertical forces are analyzed by using Fourier analysis. It is shown that the fundamental harmonic force coefficients and phases, which come mainly from the inertia and drag force, correlate well with the Keulegan-Carpenter number, K. Some degree of correlation with the shape parameter of the fluid particle motions, Ω, is also shown. The higher harmonic force components, which contain the vortex-induced forces and the nonlinear Morison forces, become more important as K increases or Ω decreases. The force coefficients, C_d and C_m, based on the vector form of the Morison equation are utilized as well as the root-mean-square and the maximum force coefficients to illustrate differences brought on by K, Ω, and roughness (e/D).

In this thesis, new information on horizontal cylinders that were towed toward waves, which simulates the superposition principle of waves and current, is shown. When the tow velocity becomes larger than the maximum wave-induced velocity, the drag and the rms force coefficients decrease rapidly, and the drag and the steady horizontal force coefficients approach the drag coefficients for steady flow.

Flow visualization techniques are used to observe flow patterns around stationary horizontal cylinders in waves, which are strongly affected by K and Ω.

From measurements, the wave-to-wave variations of forces are clearly observed. It is found that the vortex motions contribute strongly to the variations of force coefficients. The variations are smaller in the horizontal direction and for the rougher cylinders.

TABLE OF CONTENTS

TABLE OF CONTENTS
(Continued)

LIST OF FIGURES

LIST OF FIGURES
(Continued)

LIST OF FIGURES
(Continued)

LIST OF FIGURES
(Continued)

LIST OF FIGURES
(Continued)

LIST OF FIGURES
(Continued)

LIST OF FIGURES
(Continued)

LIST OF FIGURES
(Continued)

LIST OF TABLES

LIST OF SYMBOLS

C	Wave celerity [$=\omega/k$]
C_a	Added mass coefficient ($=C_m-1$)
C_d	Drag coefficient
C_{ds}	Drag coefficient for steady flow
C_{d0}	Coefficient for steady component of drag force
C_{d1}	Coefficient for oscillatory component of drag force
$C_{\ell r}$	rms transverse force coefficient
$C_{\ell \mu}$	Maximum transverse force coefficient
$C_\ell(n)$	nth harmonic transverse force coefficient
C_m	Inertia coefficient
C_{tr}	Total rms force coefficient [Eq.(5.3-3)]
C_{xr}	Horizontal rms force coefficient [Eq.(5.3-1)]
C_x	Maximum in-line force coefficient [Eq.(5.5-1)]
$C_x(n)$	nth harmonic horizontal coefficient [Eq.(5.4-1)]
$C_x'(n)$	Relative nth harmonic horizontal coefficient [$=C_x(n)/C_x(1)$]
C_{zr}	Vertical rms force coefficient [Eq.(5.3-2)]
$C_z(n)$	nth harmonic vertical force coefficient [Eq.(5.4-2)]
$C_z'(n)$	Relative nth harmonic vertical coefficient [$=C_z(n)/C_z(1)$]
C_μ	Maximum total force coefficient [Eq.(5.3-4)]
D	Diameter of circular cylinder
E_{rms}	Root-mean-square error [Eq.(5.2-1)]
F	Wave force per unit of cylinder length
F_x, F_z	Wave force in horizontal and vertical direction
F_D	Drag force
F_I	Inertia force

F_n	Fourier transform of f(t) or f_j
F_{xm}, F_{zm}	Measured force in horizontal and vertical direction
F_{xp}, F_{zp}	Predicted force in horizontal and vertical direction
H	Wave height
K	Keulegan-Carpenter number [$=u_\mu T/D$]
L	Length of test cylinder
R	Reynolds number [$=u_\mu D/\nu$]
T	Wave period
T_{ap}	Apparent wave period [Eq.(4-1)]
U	Current velocity or towing velocity
U_r	Relative current (tow) velocity
VM	Verley and Moe number [=UT/D]
X	Horizontal force due to vortex motion [Eq.(2-27)]
Z	Vertical force due to vortex motion [Eq.(2-28)]
a_n	Fourier coefficient [Eq.(2-16)]
b_n	Fourier coefficient [Eq.(2-17)]
e	Surface roughness
f_j	Discrete time series
f(t)	Periodic function with fundamental period T
h	Water depth
k	Wave number [$=2\pi/\lambda$]
m	mean value
n	The order of harmonics
$\vec{q}$	Total velocity
$\vec{q}'$	Total acceleration
u	Horizontal component of water particle velocity

u_μ	Maximum horizontal velocity
u_w	Horizontal wave induced velocity
$u_{w\mu}$	Maximum horizontal wave-induced velocity
u'	Horizontal component of water particle acceleration
u^*	Horizontal velocity of vortex
w	Vertical component of water particle velocity
w_μ	Maximum vertical velocity
w_w	Vertical wave-induced velocity
w'	Vertical component of water particle acceleration
w^*	Vertical velocity of vortex
x	Horizontal coordinate
x_o	Amplitude of cylinder oscillation
$\dot{x}$	Velocity of a oscillating cylinder
$\ddot{x}$	Acceleration of a oscillating cylinder
z	Vertical coordinate, direction measured positive upwards from still water level
β	Frequency parameter [=D2/Tν]
ϵ	Relative surface roughness [=e/D]
θ	Angular coordinate around a cylinder [Fig. 3-4]
ν	Kinematic viscosity
ρ	Density of water
σ	Standard deviation
ω	Angular wave frequency [=2π/T]
Ω	Shape parameter [=w_μ/u_μ]
$\phi_x(n)$	Phase angle of nth harmonic horizontal force
$\phi_z(n)$	Phase angle of nth harmonic vertical force

Γ	Strength of vortex
δ	Effective diameter factor [ratio of effective diameter to smooth diameter, see Table 4-1]
λ	Wave length

Subscripts

r	rms value
μ	Maximum value
w	Wave-induced value
x	Value in horizontal direction
z	Value in vertical direction

SMOOTH AND ROUGHENED HORIZONTAL CYLINDERS IN PERIODIC WAVES AND CURRENT

1. INTRODUCTION

1.1 Background

The interest in wave forces on cylinders continues to be strong because the subject knowledge is important, yet incomplete, for the design of ocean structures. The main focus for this thesis is on new information regarding the forces from periodic waves, current and waves, and surface roughness effects, for horizontal cylinders.

1.1.1 Horizontal Cylinders in Periodic Waves

Since Morison et al. (1951) proposed the well-known Morison equation, most studies on this subject emphasized wave forces on vertical cylinders or similar conditions (either oscillating a cylinder in still water or generating a planar oscillatory flow past a stationary cylinder). Vertical cylinders are of most importance because they are usually support members and they constitute the main portion of the projected elevation area of a platform. Horizontal cylinders have been of less importance, so wave force information on them is scarce. However, as designs are increasingly refined for large, expensive structures, the forces on horizontal cylindrical members are becoming more important.

The flow and resulting force characteristics around a horizontal cylinder are different from those for a vertical cylinder, or the similar cases mentioned above. The axis of a vertical cylinder lies on the same plane as that of the undisturbed velocity vector and the

vortex wake formed on one half wave cycle will sweep past the body during a subsequent half cycle. To evaluate the force that is in-line with the direction of wave propagation, only the horizontal component of the time-dependent velocity and acceleration are usually considered. The vertical forces from the vertical wave motion are parallel to the cylinder axis and consitute mostly skin friction drag which is negligible compared to the form drag of the in-line and vortex-induced transverse forces. The in-line force, which consists of the drag and the inertia force, can be predicted by the Morison equation. The vortex-induced transverse force with uncertain magnitude, phase and sign is normal to the plane of the velocity vector and the in-line force.

For a horizontal cylinder with its axis parallel to the wave crests, the velocity vectors rotate around the cylinder in an elliptic motion. In this case, the drag force (which is in-line with the velocity vector) is not always in line with the inertia force (which is in-line with the acceleration vector). The vortex wake formed over a horizontal cylinder rotates, depending on Ω (the orbital shape parameter, which is the ratio of the maximum vertical velocity to the maximum horizontal velocity), around the cylinder which is different from that for a vertical cylinder. Under this circumstance, the vortex-induced force, which is customarily defined to be perpendicular to the velocity vector, is not always normal to the inertia force and is in the same plane of the velocity vector, i.e., in the same

plane of the drag and the inertia forces. This makes the already complicated hydrodynamic force problem more complicated.

This thesis concentrates on the forces on horizontal cylinders.

1.1.2 Current Effect on Wave Forces

It is well known that there are currents generated by wind, earth gravity, tides and waves in the open sea. The interaction between waves and currents are often considered in oceanography and engineering, e.g. Longuet-Higgins (1961) and Ismail (1983). The existence of a current for a cylinder in waves will cause a bias to the wake structure around the cylinder. Thus, the forces will differ from those on a cylinder in purely wavy flow or in steady flow. However, the forces on cylinders in waves and current are nearly impossible to determine experimentally because laboratories cannot generate waves superimposed on currents at a Reynolds number sufficiently large. In the field, it is not possible to control the waves and current independently and it is difficult to separate the current effects from the wave measurements.

Engineering designers and some researchers use the simple superposition principle for waves and current because it is expedient. Some studies (Chandler and Hinwood, 1982; Ismail, 1983; Knoll and Herbich, 1980) have shown this approximation to be sufficiently valid for most design purposes. This principle is used in this study.

1.1.3 Marine Roughness Effect on Forces

Marine structures act as artificial substrata for marine plants and animals. Marine growth can be found, more or less, on most of the offshore structures in the world. Heideman et al. (1979) reported there were 1 inch barnacles attached to the Ocean Test Structure just 8 months after the installation of the structure. Ralph and Troake (1980) described marine growth on North Sea oil and gas platforms with respect to water depth. Sharma (1983) reported on the marine growth on the Hondo platform in the Santa Barbara Channel and suggested the marine growth thickness and height for future structures near the Hondo platform after comparing the data reported by Nath (1981b) from two other platforms near Santa Barbara. Nath (1983c and 1985b) also reported the 1-, 2-, and 3-year accumulations of marine growth from the CHEVRON SOUTH PASS 77"B" platform in the Gulf of Mexico.

Heaf (1979) discussed the effects of marine growth on the loading of a structure in five ways: (i) increased effective diameter, (ii) increased drag coefficient due to the roughness, (iii) increased mass and hydrodynamic added mass leading to a low natural frequency and an increased dynamic amplification factor, (iv) increased structural weight, and (v) a change in the hydrodynamic instability from the mass change and the vortex shedding frequency changes.

In this thesis, the influence on some aspects of marine biofouling on hydrodynamic forces on horizontal cylinders either in waves or under waves plus current will be studied.

1.2 Literature Review

There are a number of excellent reviews and summaries on the studies of the wave-induced forces on marine structures, e.g. Sarpkaya and Isaacson (1981), Hogben et al. (1977), Lin and Nath (1980), Fallon (1984), etc. In this section, it is intended to give necessary information for later discussion and a short review of some important literature that will be cited in later chapters.

1.2.1 Planar Oscillatory Flow and Vertical Cylinders in Waves

The planar oscillatory flow around a cylinder is a fundamental and important condition to study and understand for the complex problem of hydrodynamic forces. A cylinder in such flow can be considered to be an extreme case for a horizontal cylinder in shallow water periodic waves where the vertical ambient velocity is zero (Ω=0).

There are two orthogonal forces on a cylinder in planar oscillatory flow: the in-line force and the transverse force. "In-line" means co-linear with the flow direction and "transverse" means normal to it and the cylinder axis.

The in-line force on slender cylinders is usually determined by the Morison equation, which is a linear combination of a velocity-dependent drag term and an acceleration-dependent inertia term.

$$F = \frac{\rho D L}{2} C_d u|u| + \frac{\rho \pi D^2 L}{4} C_m \dot{u} \qquad (1.2.1\text{-}1)$$

in which F = the in-line force acting on the cylinder, which is uniform over the length considered,

L = the length of the cylinder on which the uniform force acts,

ρ = the fluid density,

D = the diameter of the cylinder,

$u, \dot{u}$ = the velocity and acceleration of the water particle, respectively, and

C_d, C_m = the drag and inertia force coefficients.

The force coefficients may be determined from the Fourier-averaged method, least squares method, and maximum kinematics and dynamics method, and force-phase method. A lot of research work has been done for planar oscillatory flow using the Morison equation, including those done by Sarpkaya (1976), Garrison (1980), Yamamoto and Nath (1976) and Bearman et al. (1981). They showed that C_d and C_m correlate well with Keulegan-Carpenter number, K ($=u_\mu T/D$), and frequency parameter β ($=D^2/\nu T$). In the above parameters, T is the wave period, ν is kinematic viscosity, and μ represents the maximum value.

The differences between vertical cylinders in periodic waves and cylinders in planar oscillatory flow are the velocity gradient along the vertical cylinder axis and the orbital water particle motion around vertical cylinders. The horizontal velocities encountered by a vertical cylinder in periodic waves vary with depth except for shallow water waves. Besides, due to the orbital motion of the fluid particles, the wake and vortices generated during one half wave cycle might not be swept back to the same elevation of the cylinder during the next half cycle, i.e., the vortices could move downward (after crests pass) or upward (after troughs pass). In addition, the small

axial skin drag force, which is induced by the vertical velocity, acts on the surface of the cylinder and generates local disturbances, which are greater if the surface is rougher. The disturbances will modify the flow and wake characteristics in some presently unknown way as discussed by Nath (1983a).

Chakrabarti (1980) showed that C_d and C_m obtained from local forces on vertical cylinders in waves may be nearly equal to those from planar oscillatory flow (at least in some regions of K) as seen in Fig. 1.2.1-1. From this figure, for $K > 36$, the C_d values from Chakrabarti are lower than Sarpkaya's planar oscillatory flow data, but C_m values are higher. For small K, data from these two different flows match well.

The maximum in-line force coefficients ($C_{x\mu}$) and the rms in-line force coefficients (C_{xr}), defined in Eqs. (1.2.1-2) and (1.2.1-3), were studied by Sarpkaya (1976, 1986), Bearman et al. (1978, 1985a,b), and Nath et al. (1984b, 1986). These coefficients are

$$C_{x\mu} = \frac{F_{x\mu}}{\frac{1}{2}\rho D L u_\mu^2} \tag{1.2.1-2}$$

and

$$C_{xr} = \frac{F_{xr}}{\frac{1}{2}\rho D L u_\mu^2} \tag{1.2.1-3}$$

in which μ represents the maximum value and r represents the root-mean-square value.

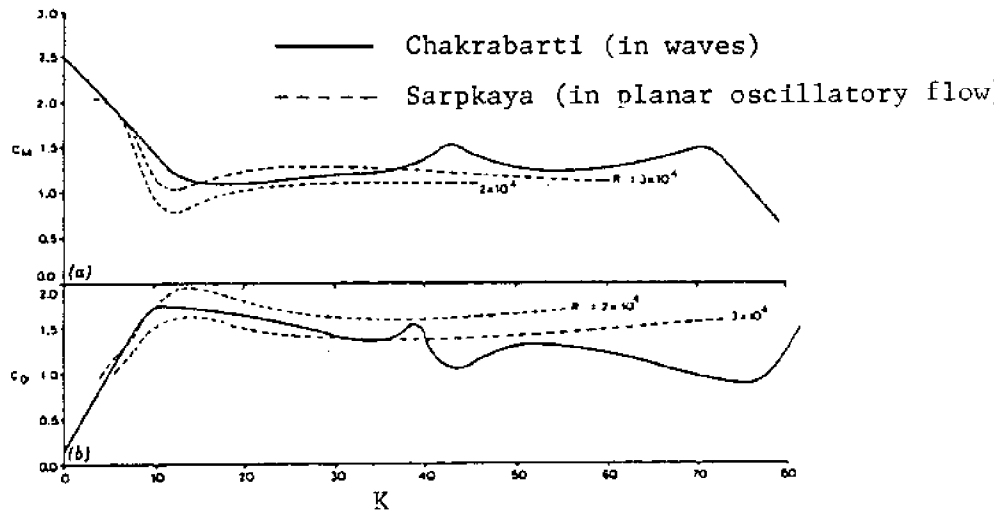

Fig. 1.2.1-1 Comparison of C_d and C_m between cylinders around planar oscillatory flow and vertical cylinders in waves (from Chakrabarti, 1980).

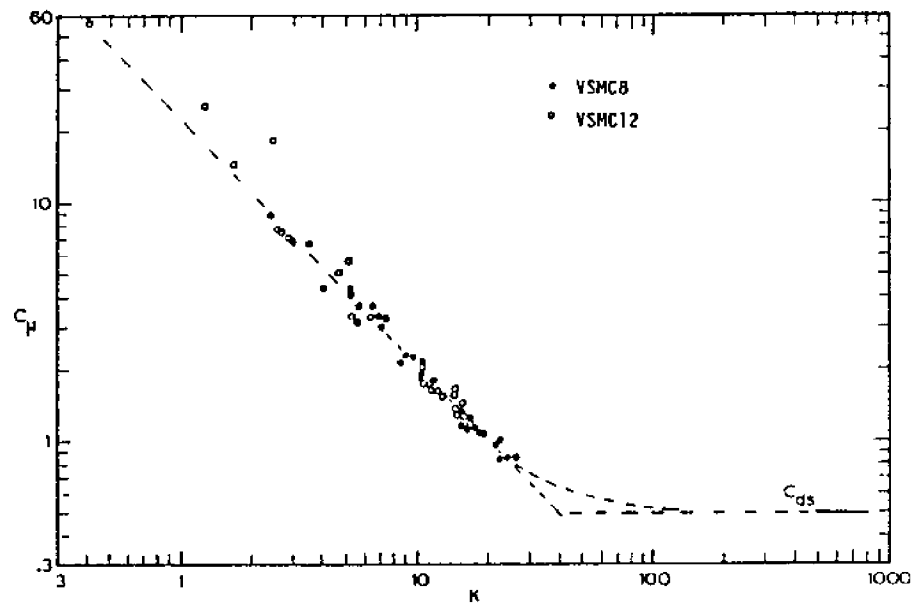

Fig. 1.2.1-2 Maximum force coefficient for vertical smooth cylinders in waves (from Nath, et al. 1984).

Figure 1.2.1-2 shows the maximum in-line force coefficients from Nath, et al. (1984b), which correlate quite well with K. In this figure, C_{ds} is the drag coefficient for steady flow. They also proposed a new technique to obtain C_d and C_m by using maximum force coefficients and the phase shift.

As to forces on roughened cylinders, only a few studies in the open literature have been devoted to this topic. Sarpkaya (1976) and Garrison (1980) reported that C_d increases and C_m decreases as the relative roughness, ϵ (=e/D) increases for planar oscillatory flow. Figure 1.2.1-3 shows the results from Sarpkaya (1976). Most studies of forces on roughened vertical cylinders in the open literature were conducted by Nath (1983a, 1983b, 1984a, and 1985b). The C_d, C_m, and $C_{x\mu}$ for the smooth (VSMC), the sand-roughened (VSRC, ϵ =.02), and the artificially marine-roughened (VAMRC, ϵ =0.09) vertical cylinders are plotted in Fig. 1.2.1-4 after Nath (1983a). The C_d and the $C_{x\mu}$ increase significantly as the relative roughness increases. The difference of C_m between the smooth and the sand roughened cylinder is not clear, but the C_m increases rapidly for the artificially marine-roughened cylinder.

The transverse force is mainly generated by the asymmetric vortex shedding and is strongly affected by the resulting pattern and frequencies. Due to the complexity and irregular nature of this phenomenon, there is not a widely accepted model that predicts the transverse force trace (magnitude, phase, and direction).

Most of the studies (e.g. Sarpkaya 1976 and 1986, Yamamoto and Nath 1976, Isaacson and Maull 1976) used the maximum transverse coef-

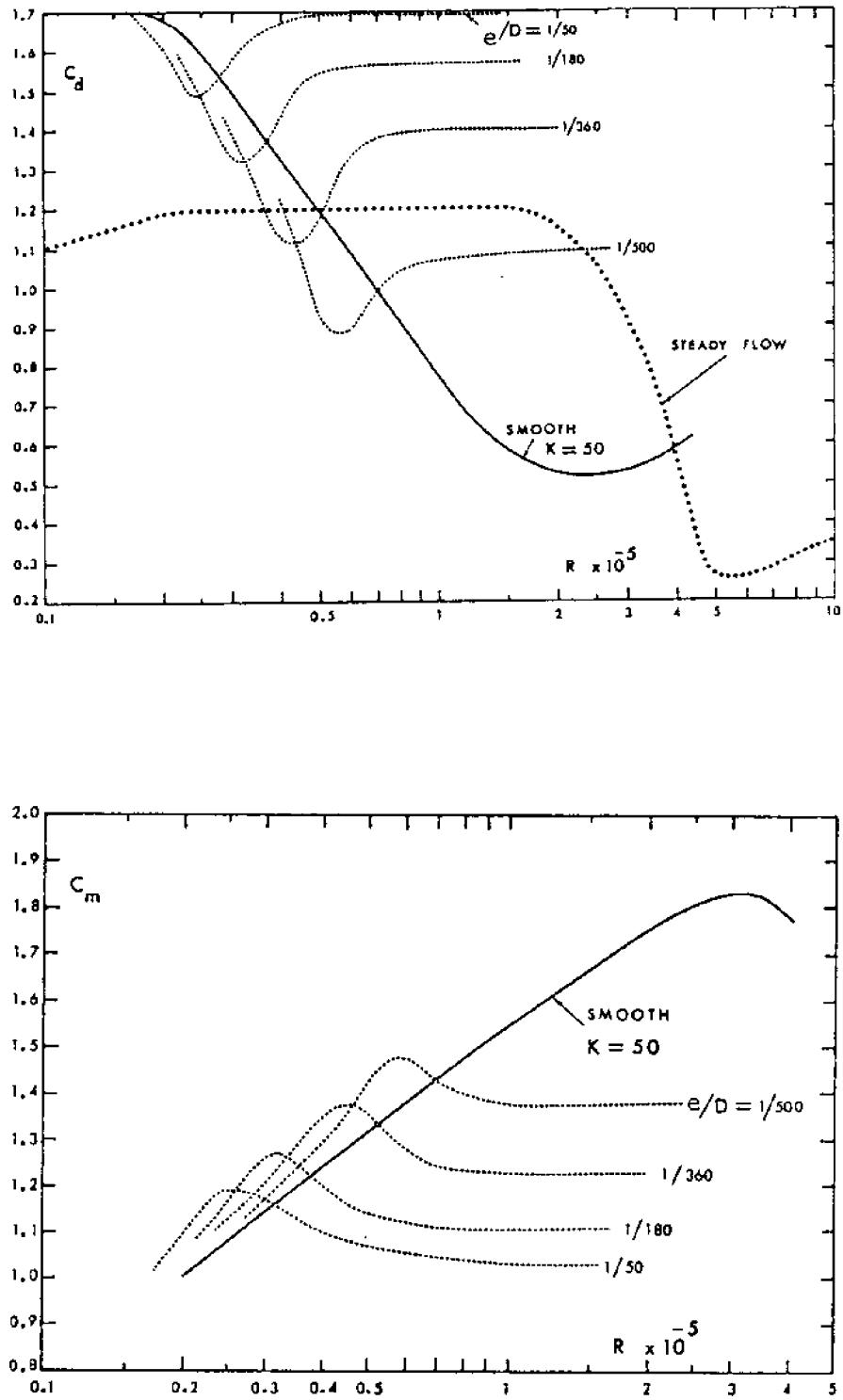

Fig. 1.2.1-3 C_d and C_m of planar oscillatory flow versus R for various roughnesses for K=50 (from Sarpkaya, 1976).

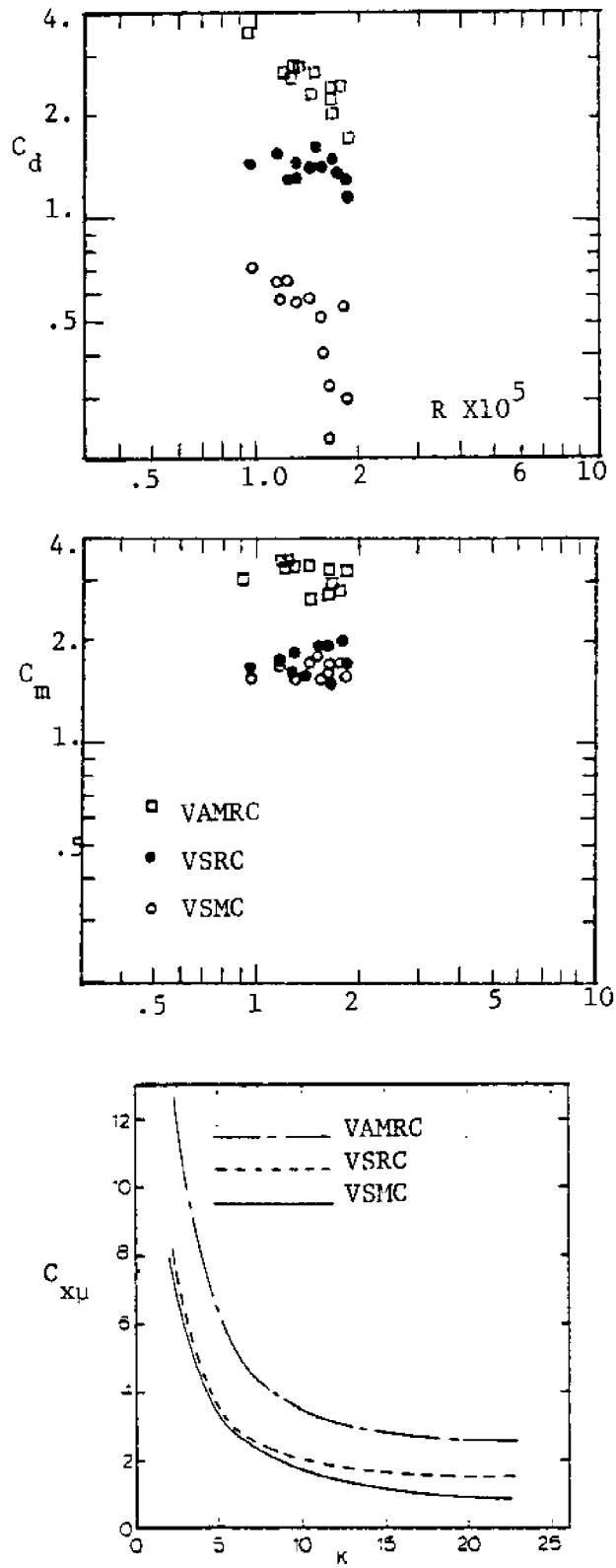

Fig. 1.2.1-4 Force coefficients for the smooth and roughened vertical cylinders in waves (from Nath, 1983).

ficient ($C_{\ell\mu}$) and the rms transverse coefficient ($C_{\ell r}$), that have similar definitions as in Eqs. (1.2.1-2) and (1.2.1-3), to characterize the lift force. Figure 1.2.1-5 shows values of $C_{\ell\mu}$ and $C_{\ell r}$ obtained by Sarpkaya (1976 and 1986) were highly correlated with K and β. Several researchers (Chakrabarti, et al. 1976; Isaacson and Maull 1976; Maull and Milliner 1978) studied the harmonic transverse force coefficients, as defined by using Fourier analysis, as follows:

$$C_\ell(n) = \frac{F_\ell(n)}{\frac{1}{2}\rho D L u_\mu^2} \qquad (1.2.1\text{-}4)$$

Recently, Sarpkaya (1986) presented the first five harmonics of transverse force coefficients as a function of K as shown in Fig.1.2.1-6 for β=2300. It is clear that $C_\ell(1)$ is much smaller than $C_\ell(2)$. Similar to $C_{\ell\mu}$, $C_\ell(2)$ has a maximum value at K=12.

Sarpkaya (1976) found that the maximum transverse force sometimes has the same order as, or is higher than, the maximum in-line force. Chakrabarti, et al. (1976) also concluded that the resultant force (vector sum of the in-line force and the transverse force) may be as much as 60% higher than the in-line force. Sawaragi, et al. (1976) also reported that the ratio of the maximum resultant force to the maximum in-line force has a maximum value of 1.4. Thus, the transverse force is important and should not be neglected in calculation of the total force on a cylinder.

Sarpkaya (1976) claimed that the maximum transverse force coefficient does not clearly vary with β or ε (Fig. 1.2.1-7). But, his new report in 1986 showed that the rms transverse coefficient

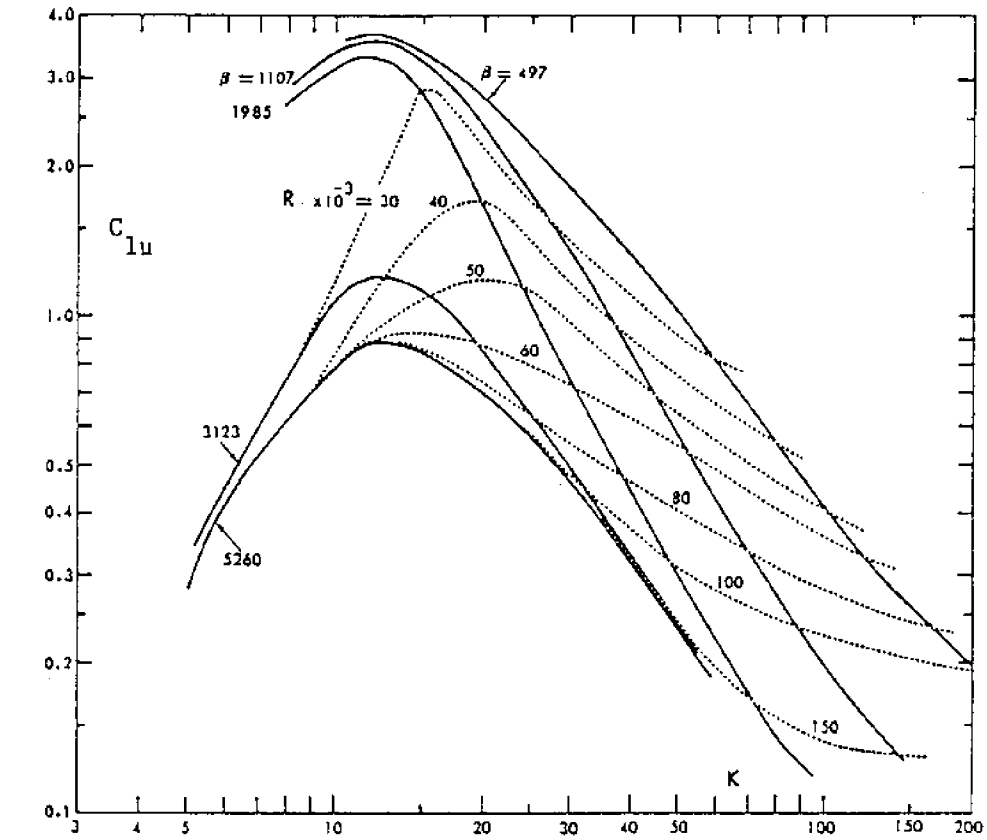

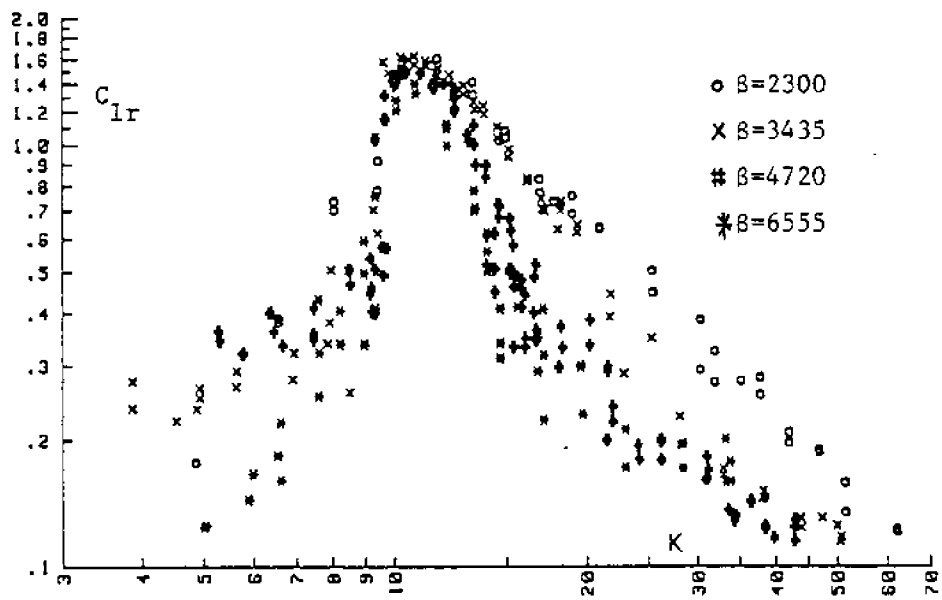

Fig. 1.2.1-5 Maximum and rms transverse coefficients versus K for various β (from Sarpkaya, 1976 and 1986).

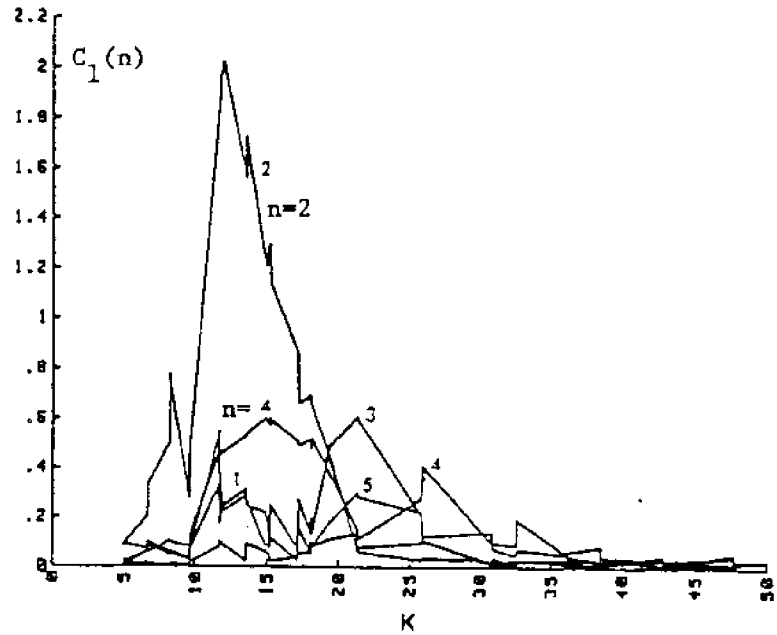

Fig. 1.2.1-6 Amplitude of the harmonics of transverse froce for a smooth cylinder in planar oscillatory flow (from Sarpkaya, 1986).

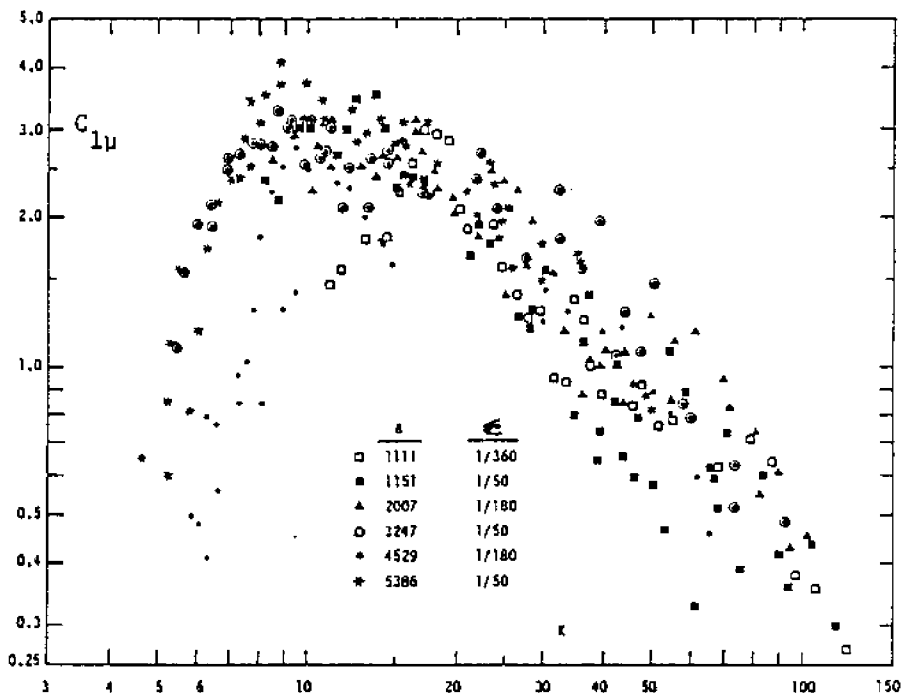

Fig. 1.2.1-7 $C_{\ell\mu}$ versus K for various values of e/D and β for cylinders in planar oscillatory flow (from Sarpkaya, 1976).

increased significantly from the smooth cylinder to the roughened cylinder as shown in Fig. 1.2.1-8.

Flow visualization is probably one of the most useful tools to study the role of vortices around cylinders in oscillatory flow. Several flow visualization experiments under planar oscillatory flow have been conducted by Bearman, et al. (1981), Sarpkaya and Wilson (1984), and Williamson (1985). They all concluded that the vortex shedding patterns are highly correlated with K, which are summarized herein and sketched in Fig. 1.2.1-9. The capital letters in the parentheses in the following discussion represent the vortices shown in Fig. 1.2.1-9.

(i) For $K < 3$, no vortices could be observed.

(ii) For $K=4$, there is symmetric pairing of attached vortices and no resultant transverse force.

(iii) For $4 < K < 8$, there is asymmetric pairing of attached vortices with unequal strength, yielding resultant transverse forces.

(iv) For $8 < K < 15$, a pair of vortices forms in each half cycle and the larger one (B) sheds. When flow reverses, (B) is swept back over the cylinder and makes the new formed vortex (E) on the same side stronger than (D) on the other side. Thus, the shedding and backwash of vortices always occurs on the same half of the cylinder. The smaller vortices (C) and (D) are always swept on to the cylinder and disappear.

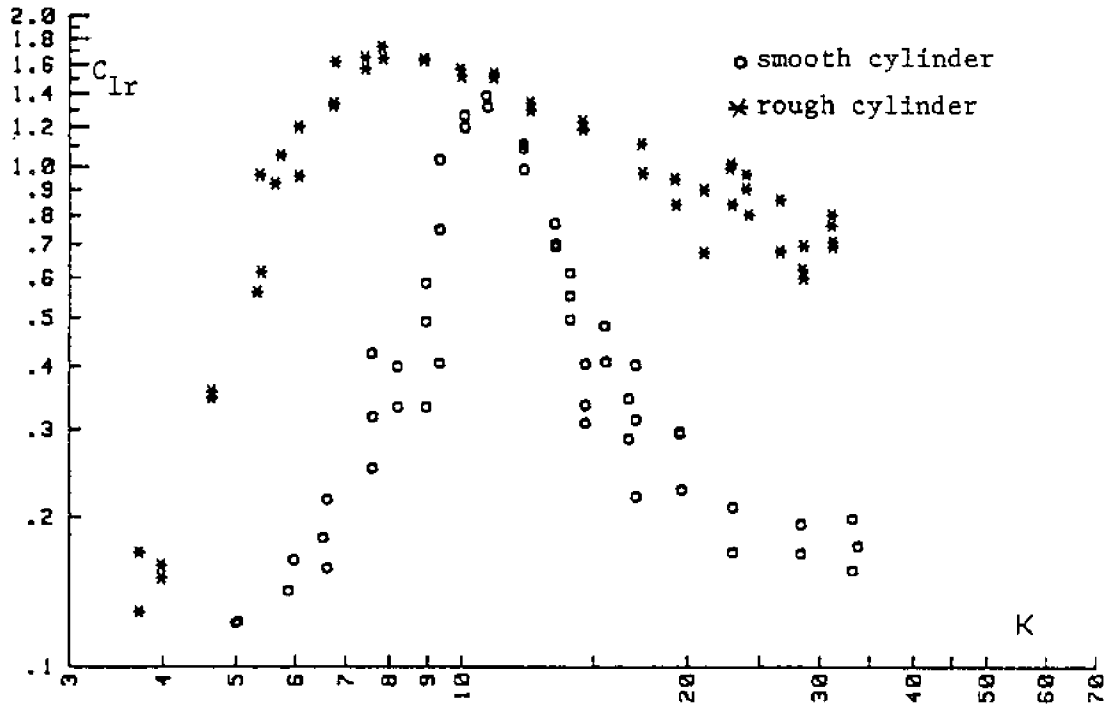

Fig. 1.2.1-8 $C_{\ell r}$ for a smooth and sand roughened cylinder in planar oscillatory flow (from Sarpkaya, 1986).

(i) K < 3:

(ii) K 4:

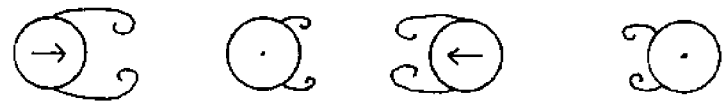

(iii) 8 > K > 4:

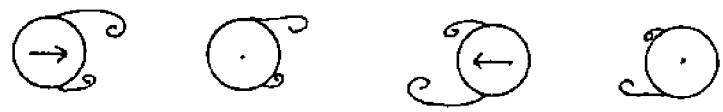

(iv) 15 > K > 8:

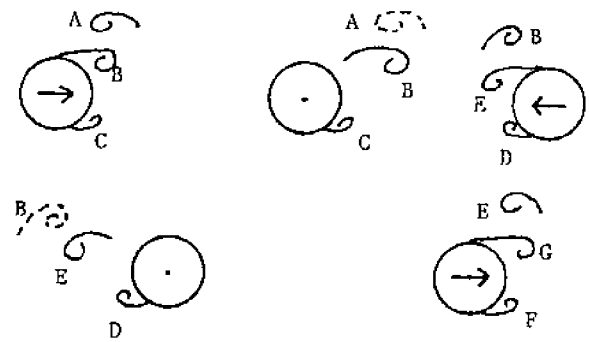

(v) 24 > K > 15:

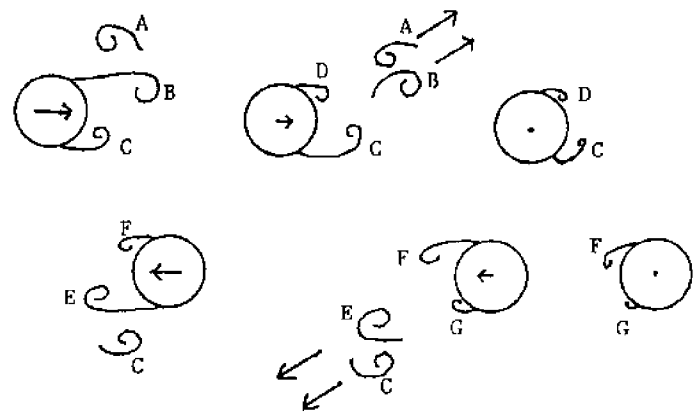

Fig. 1.2.1-9 Vortex shedding patterns for cylinders in planar oscillatory flow. (The arrows at cylinder centers indicate the flow direction and the relative magnitude.)

(v) For $15 < K < 24$, two asymmetric vortices form at first and the larger one (B) sheds and flows away with (A), which was formed during the previous half cycle. The smaller one (C) continues to grow. A new vortex (D) forms at the same side as (B). Then, (C) is swept over the shoulder and (D) hits on the cylinder.

(vi) For $K > 24$, more vortices are formed and detached in each half cycle. More pairs of vortices will move together. As the flow reverses, these vortices, or pairs, will convect, dissipate, or be canceled by mixing with the others or the boundaries.

Sawaragi and Nakamura (1979) and Zdravkovich and Namork (1977) also conducted flow visualization experiments to observe the flow patterns for a vertical cylinder in periodic waves at the water surface. The vortex shedding patterns they observed were similar to those for planar oscillatory flow sketched in Fig. 1.2.1-9.

Grass et al. (1981) indicated that quantitative measurements of the positions of the centers of the dominant vortices show up certain differences between a vertical cylinder in real oscillatory waves and a cylinder in planar oscillatory flow through the flow visualization experiments of both conditions. These differences may cause differences of induced forces.

1.2.2 Horizontal Cylinders in Periodic Waves

The significant features of a horizontal cylinder with its axis parallel to the wave crests are that (i) the velocity vector, the wake and vortices tend to rotate around the cylinder and are not always swept back onto the cylinder, and (ii) the plane of the velocity vector is normal to the axis of the cylinder with no axial component of velocity. Thus, the induced forces, i.e., the drag, the inertia, and the vortex-induced force, are in the same plane of the velocity vector and there is no axial force.

It is customary to assume that the drag and inertia components are in the direction of the velocity and acceleration vectors respectively and the vortex-induced component is perpendicular to the velocity vector with unknown sign. Because the acceleration vector is not necessarily in line with the velocity vector in waves, there is an angle between the drag force (velocity) and the inertia force (acceleration) depending on the wave condition and phase angles. Thus, the vortex-induced force is not normal to the inertia force and these two forces mix with each other. Because the vortex-induced force acts, at least until now, with unpredictable magnitude, frequency and sign, this phenomenon makes this problem more complicated.

Neglecting the vortex-induced component, a lot of researchers used the following vector form of the Morison equation to study the forces on a horizontal cylinder in waves, e.g. Nath (1982), Teng and Nath (1983), Ramberg and Niedzwecki (1979,1985), Holmes and Chaplin (1978), Chaplin (1985a,b), and Bearman et al. (1985a).

$$\vec{F} = \frac{\rho DL}{2} C_d \vec{q}|\vec{q}| + \frac{\rho \pi D^2 L}{4} C_m \vec{q}' \qquad (1.2.2\text{-}1)$$

in which $\vec{q}$ is the velocity vector and $\vec{q}'$ is the total acceleration vector.

The force coefficients obtained from a large wave flume by Bearman et al. (1985a) were relatively scattered as shown in Fig. 1.2.2-1. One can see that no clear dependence of force coefficients, C_d and C_m, on the shape parameter, Ω, can be found. Because the Morison equation does not include a term to take the vortex-induced force into account, the force therefore will appear as noise and will contaminate the C_d and C_m values. This is thought to be the main reason for the scatter of the force coefficients.

Ramberg and Niedzwecki (1983) used a vector form of the Morison equation with one pair of C_d and C_m in the horizontal direction and another in the vertical direction. Their experiments, from a small wave flume, showed no clear trend of C_d and C_m on Ω, although the scatter of their data is less than those from Bearman, et al. (1985a).

In order to achieve high R and K, a complete range of Ω, precise water particle kinematics, and to avoid nonlinearities, some researchers used alternative experimental techniques to simulate the condition of a horizontal cylinder in periodic waves. By driving a cylinder in an elliptical path, in otherwise still water, to simulate a horizontal cylinder in wave-type orbital flow where $0 < \Omega < 1$, Chaplin (1985b) obtained estimates of C_d and C_m, as shown in Fig. 1.2.2-2 for K=14. His results showed the inertia coefficient reduced

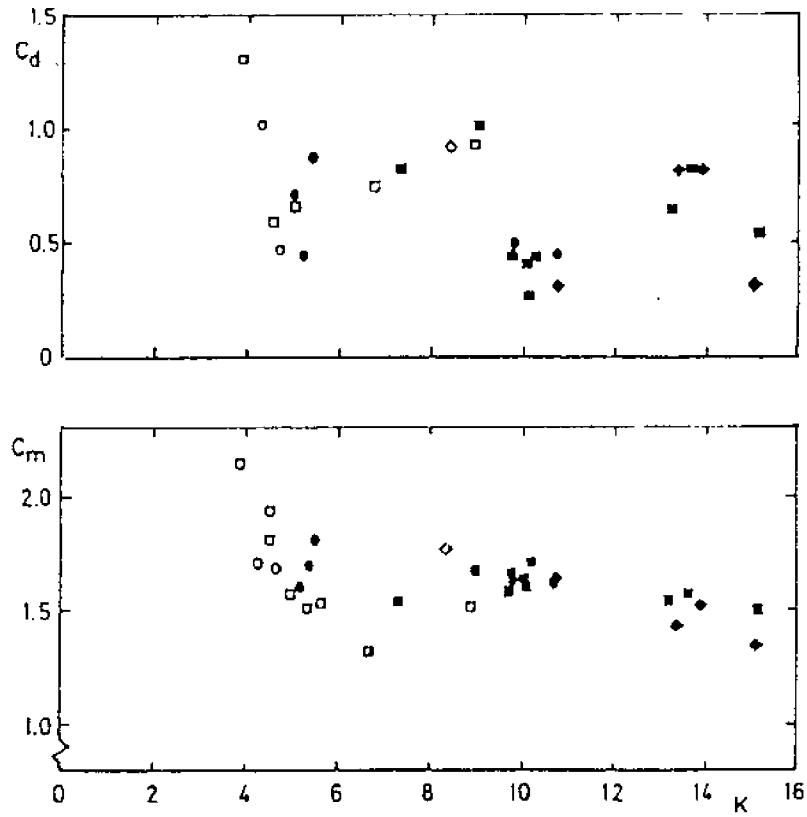

Fig. 1.2.2-1 C_d and C_m of a smooth horizontal cylinder in waves versus K for various Ω (from Bearman, et al., 1985a).

Empty symbols: $10^5 < R < 3x10^5$

Solid symbols: $3x10^5 < R < 5x10^5$

o: $0.50<\Omega<0.75$; □ : $0.25<\Omega<0.50$; ◇ : $0.15<\Omega<0.25$

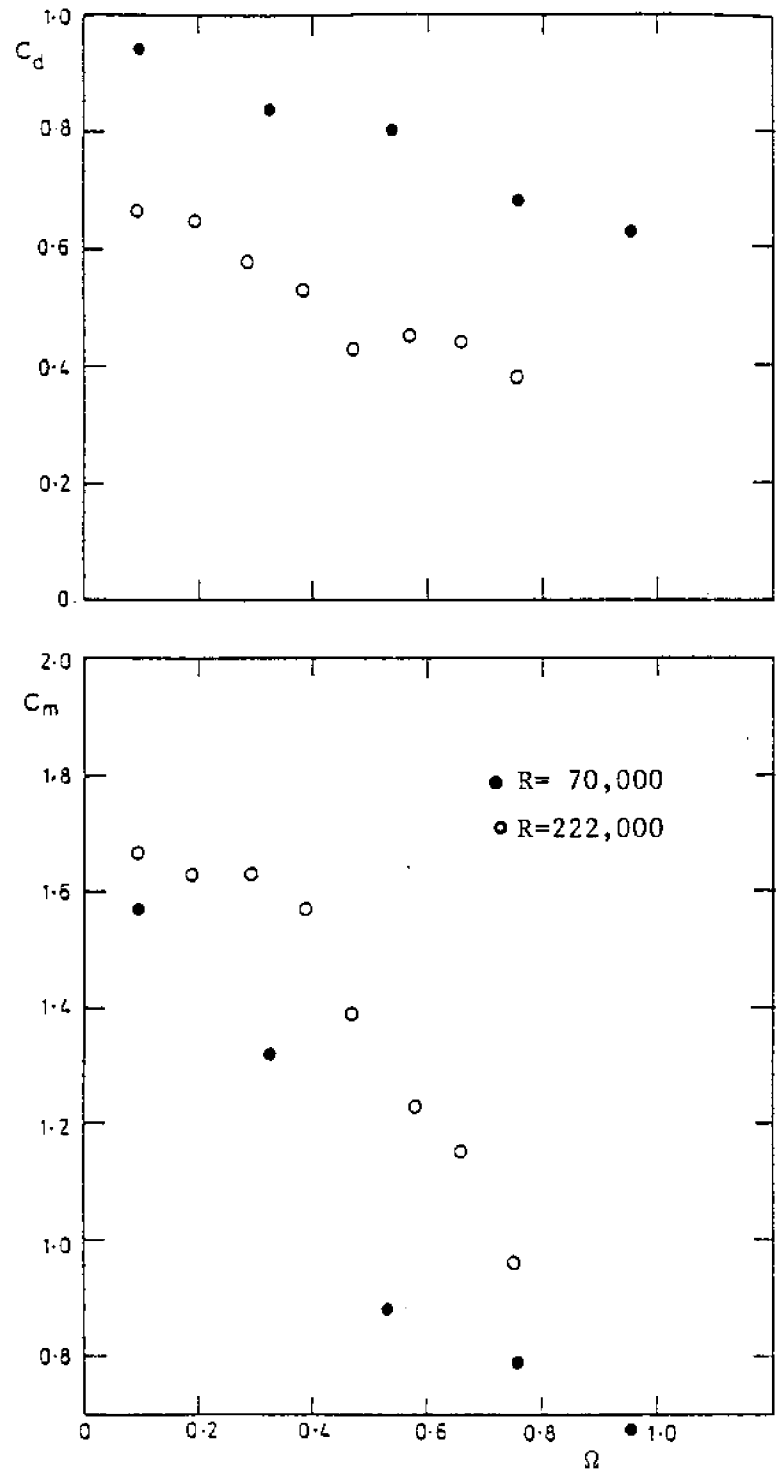

Fig. 1.2.2-2 C_d and C_m versus Ω for a smooth cylinder in orbital flow for K=14 (from Chaplin, 1985b).

rapidly as Ω increased, but C_d decreased with larger Ω, for large K. Using the same experimental technique with the particle velocity measurements under the wave-induced orbital flow around a cylinder, Chaplin (1981) concluded the direction of the drag force lags, in time, that of the velocity vector. This time lag will make the drag force have a component opposing the inertia force, which always leads the velocity vector by 90° for deep water waves.

Rodenbusch and Gutierrez (1983) conducted experiments in a large basin (88m x 39m x 3.5m) and their data and results became public in 1985. They towed a large vertical cylinder (D=1m) in still water. This cylinder was suspended from a bridge, which moved along the long axis of the basin, and a subcarriage on the bridge, which moved along the short axis of the basin. They made elliptical oscillations of the cylinder and used a velocity tracking analysis, which takes the projection of forces and accelerations on the direction of the velocity vector into account, to obtain C_d and C_a ($=C_m-1$). Figure 1.2.2-3 shows their results. In this figure, the A_x and A_y are the amplitudes of the motion in the x and y direction, respectively. The C_d values they reported decreased with increasing Ω, but, the C_a values did not seem to follow any simple pattern. They explained two reasons for this irregularity. One is the interference of the vortex-induced forces with the inertia force (as discussed at the beginning of this section). The other reason is that the conditioning for determining C_a is worse due to the relatively small inertia force (note that C_a was obtained from the part of the inertia force which is in the direction of the velocity vector).

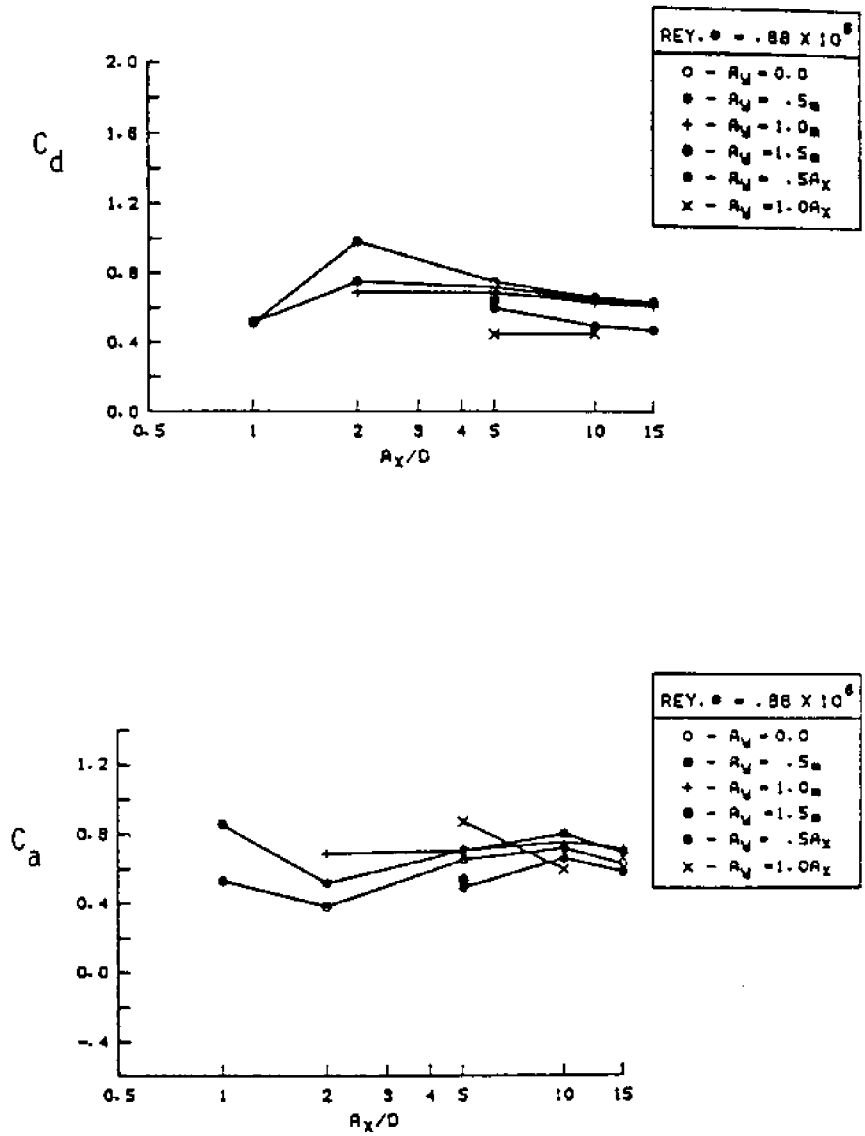

Fig. 1.2.2-3 C_d and C_a for a smooth cylinder during elliptical oscillations as a function of amplitude to diameter ratio (from Rodenbusch and Gutierrez, 1983).

Sarpkaya (1984) oscillated a horizontal cylinder sinusoidally in the vertical direction under horizontally planar sinusoidal flow (both with the same period) in his U tube to simulate a horizontal cylinder in periodic waves. He determined C_d and C_m from the in-line force and showed that C_d decreases and C_m increases as Ω increases for $K < 35$. Grass, et al. (1984) conducted experiments similar to Chaplin's (1985b) but with smaller equipment and estimated C_d and C_m for the in-line force only. But, they showed both C_d and C_m decreased as Ω increased. Note that both Sarpkaya's and Grass's force coefficients can not be directly compared to those from Bearman, et al. (1985a), Teng and Nath (1985), Chaplin (1985b), and Rodenbusch and Gutierrez (1983), because the latter are for total forces with the vector form of the Morison equation.

Without using the Morison equation, Maull and Norman (1978) obtained, from a small wave flume, the rms force coefficients in both the horizontal and vertical directions for each harmonic (the wave frequency is the fundamental frequency). These coefficients in the horizontal direction were defined as follows

$$C_{xr}(n) = \frac{F_{xr}(n)}{\frac{1}{2}\rho D L u_r^2} \qquad (1.2.2\text{-}2)$$

in which n is the order of harmonics, u_r is the rms horizontal velocity, and $F_{xr}(n)$ is the nth harmonic horizontal force. Their results showed the rms coefficients of the first harmonic horizontal force are functions of Ω and decrease with increasing Ω. Bearman, et al. (1985a) calculated the first harmonic rms coefficient and no trend on

Ω was observed, but their data fell in the range of Maull and Norman's as shown in Fig. 1.2.2-4.

Maull and Norman also conducted flow visualization experiments by using hydrogen bubbles to observe the vortex shedding pattern around a horizontal cylinder in waves. They concluded that the presence of the vertical velocity reduces the horizontal force by altering the trajectory of the vortices developed and reduces the vertical force by constraining the movement of the vortices in the horizontal direction.

The total rms force coefficient, which is defined in Eq. (1.2.2-3), was estimated by Bearman et al. (1985a) and Chaplin (1985b) to be

$$C_{tr} = \frac{(F_{xr}^2 + F_{zr}^2)^{1/2}}{\frac{1}{2}\rho DL(u_r^2 + w_r^2)} \qquad (1.2.2\text{-}3)$$

in which F_{zr} is the vertical rms force and w_r is the rms vertical velocity. Figure 1.2.2-5 shows the C_{tr} values for K=14 for both studies. Chaplin showed the C_{tr} decreased as Ω increased for the simulated orbital flow. The trend for Bearman's data (which were obtained from periodic waves) is not clear. This shows the difference between horizontal cylinders in these two flows. Chaplin also said it would be unreasonable to assume the results from one case should be directly applicable to the other.

In Fig. 1.2.2-5, Chaplin also presented the rms horizontal force ceofficient, C_{xr}. This coefficient clearly decreases as Ω increases.

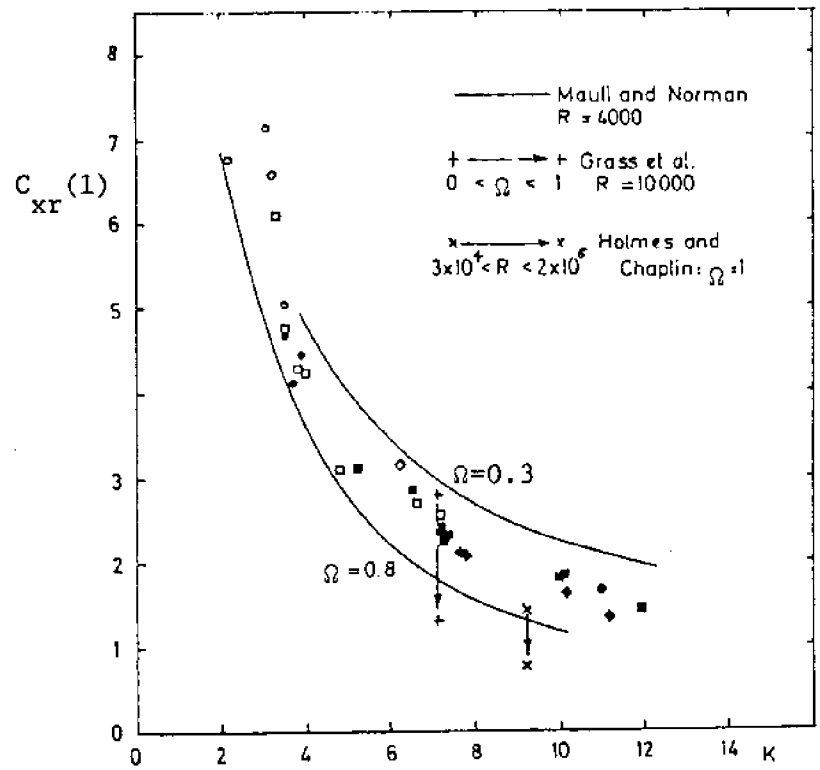

Fig. 1.2.2-4 $C_{xr}(1)$ of a smooth horizontal cylinder in regular waves versus K for various Ω (from Bearman, et al., 1985a). Symbols: see Fig. 1.2.2-1.

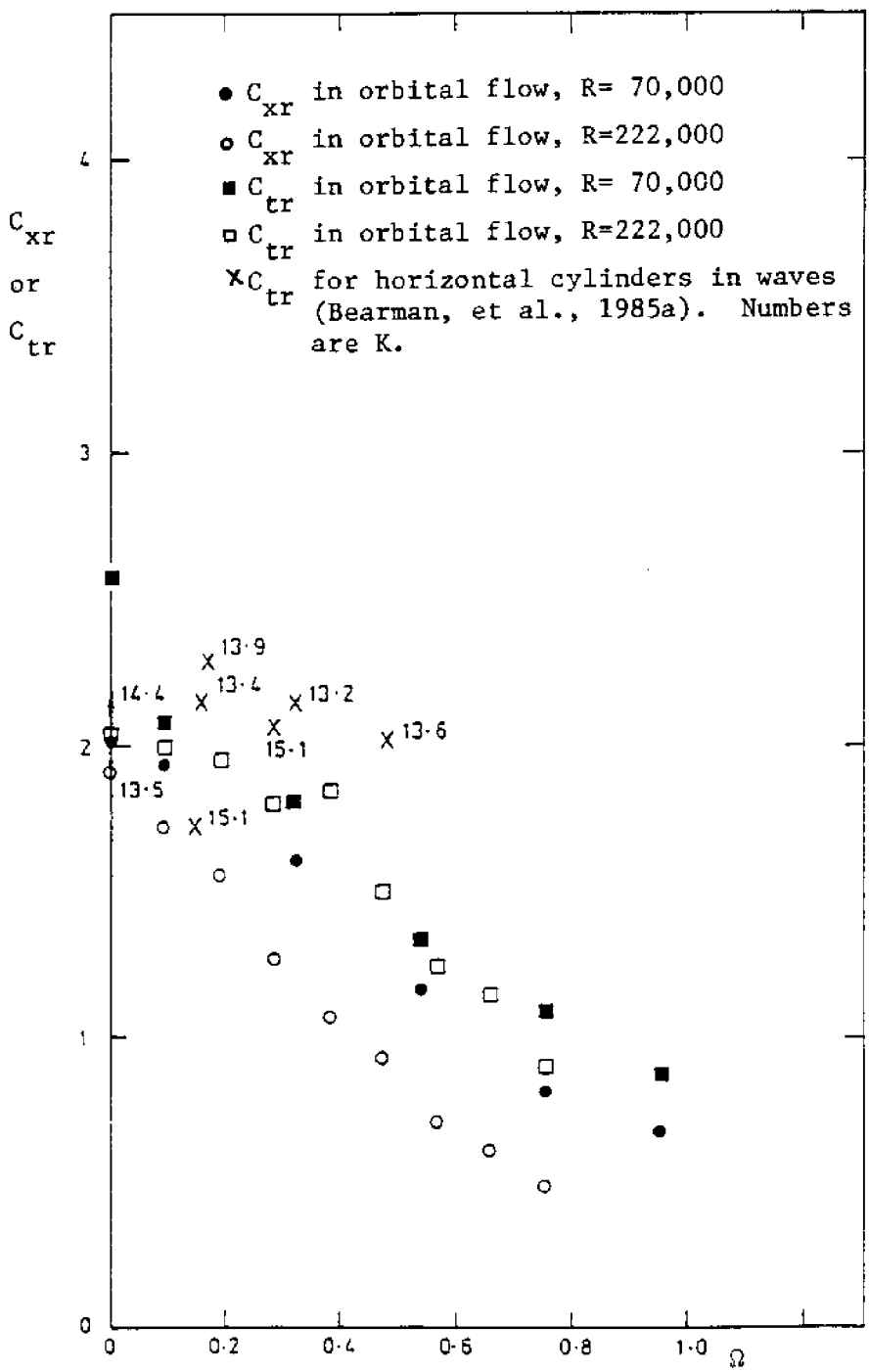

Fig. 1.2.2-5 RMS force coefficients of horizontal cylinders in elliptical orbital flow and in real waves for K≡14 (from Chaplin, 1985b).

Grass, et al. (1984) obtained the same result. This coefficient and the rms vertical force coefficient are defined as

$$C_{xr} = \frac{F_{xr}}{\frac{1}{2}\rho DLu_r^2} \qquad (1.2.2\text{-}4)$$

and

$$C_{zr} = \frac{F_{zr}}{\frac{1}{2}\rho DLu_r^2} \qquad (1.2.2\text{-}5)$$

Figure 1.2.2-6 shows that the C_{xr} and C_{zr} values obtained from waves experiments by Ramberg and Niedzwecki (1985) correlates well with K. But, no clear trend on Ω can be observed, which is not similar to Chaplin's and Grass's simulated orbital flow.

Teng and Nath (1984) calculated the maximum force coefficient for horizontal cylinders, which is defined as

$$C_\mu = \frac{F_\mu}{\frac{1}{2}\rho DLu_\mu^2} \qquad (1.2.2\text{-}6)$$

In Fig. 1.2.2-7, the C_μ values for the smooth cylinder are presented. It can be seen that the C_μ values correlate well with K.

Figure 1.2.2-8 shows the C_d and C_m data for the roughened horizontal cylinders from Teng and Nath (1984). It is clear that C_d increases as ε increases. The C_m values obviously increase for the barnacle cylinder and no difference between the smooth and sand-roughened cylinder is observed. This result is similar to that obtained by Nath (1983a,b) for vertical roughened cylinders as dis-

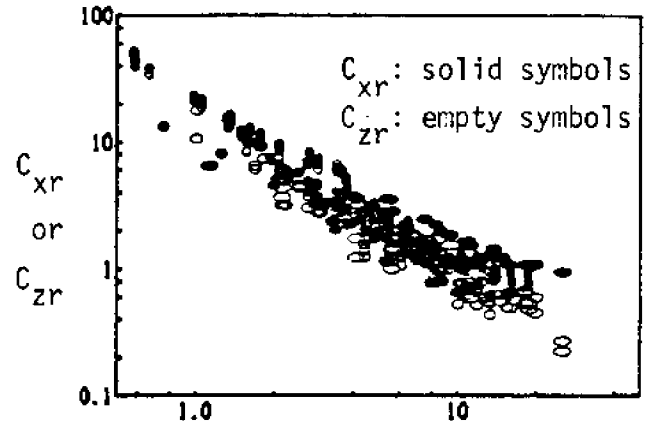

Fig. 1.2.2-6 C_{xr} and C_{zr} of a horizontal cylinder in waves for various Ω. Ω is indicted by the shape of the data point (from Ramberg and Niedzwecki, 1983).

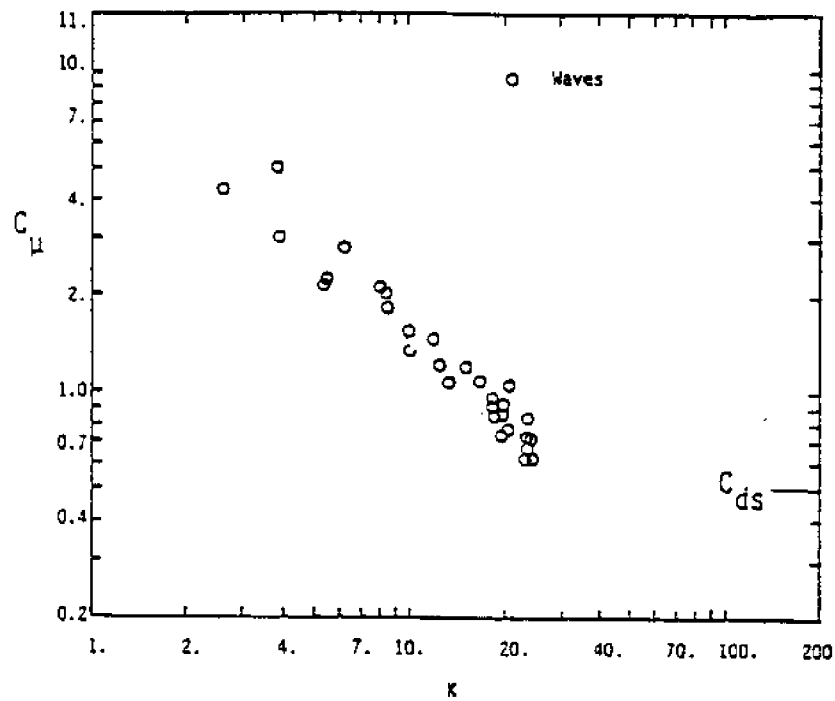

Fig. 1.2.2-7 C_μ versus K for a horizontal cylinder in waves (from Teng and Nath, 1984).

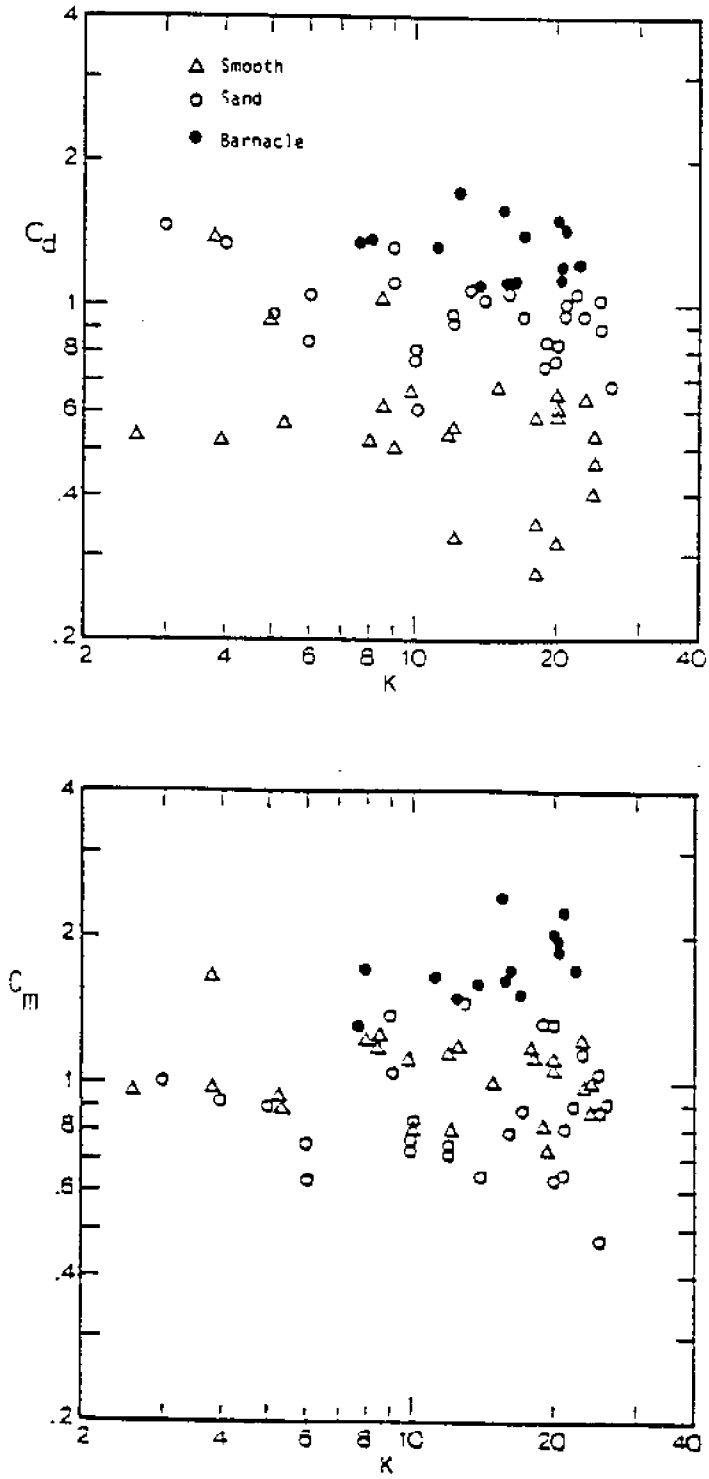

Fig. 1.2.2-8 C_d and C_m versus K for smooth and roughened horizontal cylinders in waves (from Teng and Nath, 1984).

cussed in Section 1.2.1 (Fig. 1.2.1-4). Note that the smooth cylinder diameter was used to compute the coefficients and K.

1.2.3 Cylinders in Waves and Current

Due to the mean flow of a current, the horizontal velocities toward the upstream side of a cylinder are stronger than those toward the downstream side. This causes a bias of the cylinder wake. The bias is greater if the current is stronger. If the current velocity (U) is larger than the maximum oscillatory velocity (u_μ), the horizontal velocity is always directed in the direction of the current.

Sarpkaya, et al. (1982 and 1984) studied the hydrodynamic forces on smooth and rough cylinders from combined shallow water waves and current by moving cylinders with a constant velocity in a planar oscillatory flow with the motion in-line with the flow. He evaluated C_d and C_m for the in-line force through Fourier analysis and the modified Morison equation as

$$F = \frac{\rho DL}{2} C_d(u+U)\left|u+U\right| + \frac{\rho\pi D^2 L}{4} C_m \frac{du}{dt} \qquad (1.2.3\text{-}1)$$

The coefficients correlated quite well with both K ($=u_\mu T/D$) and VM ($=UT/D$) as shown in Fig. 1.2.3-1 for $\beta=1594$. It is observed that the wake bias, resulting from the current, increases C_m and decreases C_d and, for K larger than 20, the effect of current on force coefficients and on the calculated in-line force is negligible.

Koterayama (1984) studied experimentally the forces on vertical cylinders with a constant forward velocity by using two experimental techniques. One was to move a cylinder in laboratory waves (wave

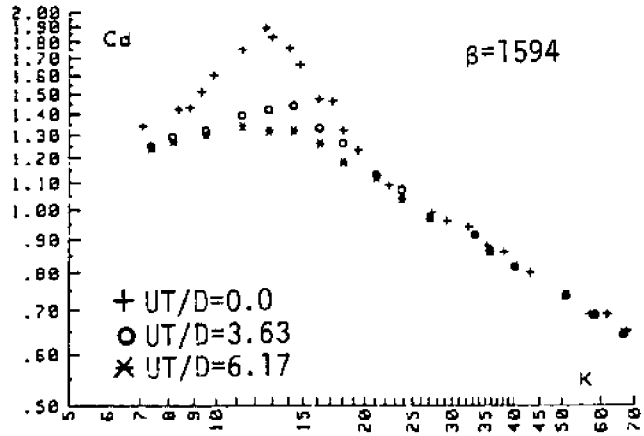

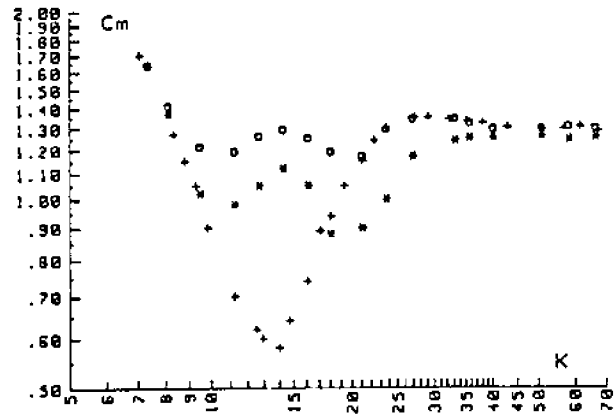

Fig. 1.2.3-1 C_d and C_m for a smooth cylinder in planar oscillatory flow and current for β=1594 (from Sarpkaya, 1984).

force test) and the other was to oscillate a cylinder moving with a steady translation in still water (surging test). He used Eq. (1.2.3-1) and a Fourier series expansion to analyze the in-line force. The steady drag coefficient (C_{do}), the oscillating drag coefficient (C_{d1}) , and the inertia coefficient (C_m) were obtained from the steady force, the harmonic force in phase with the velocity and the harmonic force in phase with the acceleration, respectively. The lift coefficients (C_ℓ), which was defined as 1/10 maximum values of lift forces divided by maximum total velocity square, was also estimated. Figure 1.2.3-2 shows these coefficients verse VM (=UT/D) for $3.8 < K < 6.1$. Koterayama concluded that the force coefficients depend mainly on VM, and the oscillatory drag coefficient is smaller than the steady drag coefficient and approaches it as VM increases. Matten (1976) obtained similar conclusions. Besides, the Fourier drag coefficients are generally smaller for the wave force tests than for the surging tests due to the 3-D effects, which reduced coherence and strength of vortices, of the wave tests.

Some researchers (Verley and Moe, 1979; Mercier, 1973; Kato et al., 1983; Bryndum et al.,1983) oscillated a cylinder in line with a steady flow which can be used to simulate a cylinder subjected to (shallow water) waves and current.

Verley and Moe (1979) conducted a sequence of experiments by oscillating a cylinder, which was attached to a pendulum, in line with a uniform and constant flow. In their study, the following two equations were used to analyze the data.

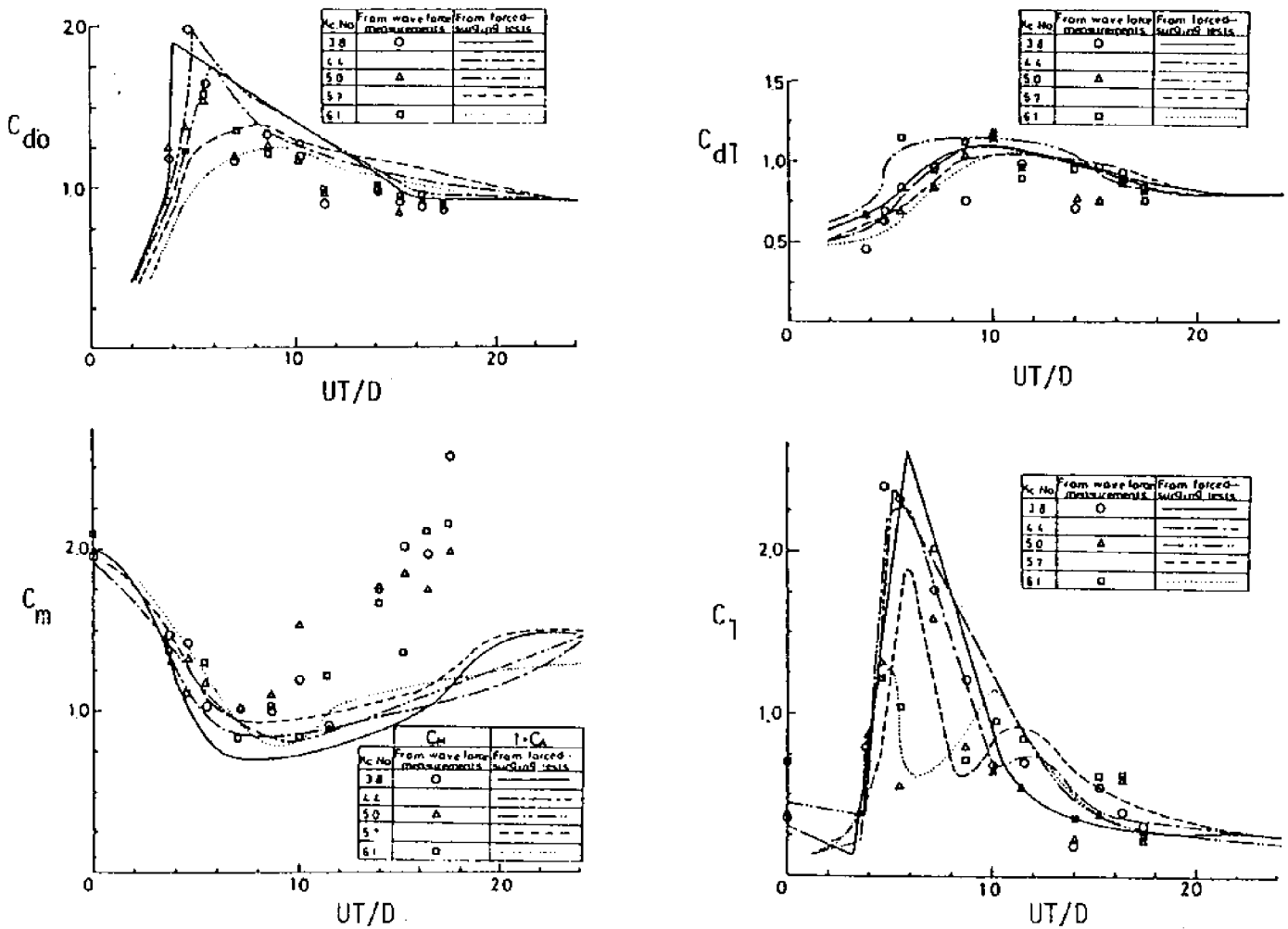

Fig. 1.2.3-2 Force coefficients versus UT/D for 6.1 > K > 3.8 for a vertical cylinder in waves and a cylinder oscillating with forward velocity (Koterayama, 1984).

$$F = \frac{\rho DL}{2} C_d(U-\dot{x})\left|U-\dot{x}\right| - \frac{\rho\pi D^2 L}{4}(C_m - 1)\ddot{x} \qquad (1.2.3\text{-}2)$$

and

$$F = \frac{\rho DL}{2} C_{do}U^2 - \frac{\rho DL}{2} C_{dl}\dot{x}\left|\dot{x}\right| - \frac{\rho\pi D^2 L}{4}(C_m - 1)\ddot{x} \qquad (1.2.3\text{-}3)$$

where $\dot{x}$ and $\ddot{x}$ are the velocity and acceleration of the cylinder. They studied the inertia coefficient (C_m), the steady drag coefficient (C_{do}) and the oscillatory drag coefficient (C_{dl}) for both equations, and found that Eq. (1.2.3-2) is the better formulation. Note that they split the drag coefficient in Eq. (1.2.3-2) into C_{do} and C_{dl} by using the similar definitions as just discussed in Koterayama's (1984) study. Figure 1.2.3-3 shows their results by using Eq. (1.2.3-2). The dependences of the force coefficients on VM (=U/TD) and x_o/D (=K/π) were observed. The x_o is the amplitude of the displacement.

Bryndum et al. (1983) used a least square method to quantify C_d and C_m in Eq. (1.2.3-2) and estimated the lift coefficients, C_ℓ. They concluded that C_d and C_ℓ decrease to as much as 60% and 40%, respectively, of the values found in wave motion when U/u_μ approaches 0.9.

Teng and Nath (1985) simulated the waves and current condition by towing horizontal cylinders (smooth and roughened) in waves and used the following modified Morison equation to describe the forces on a horizontal cylinder under waves and towing.

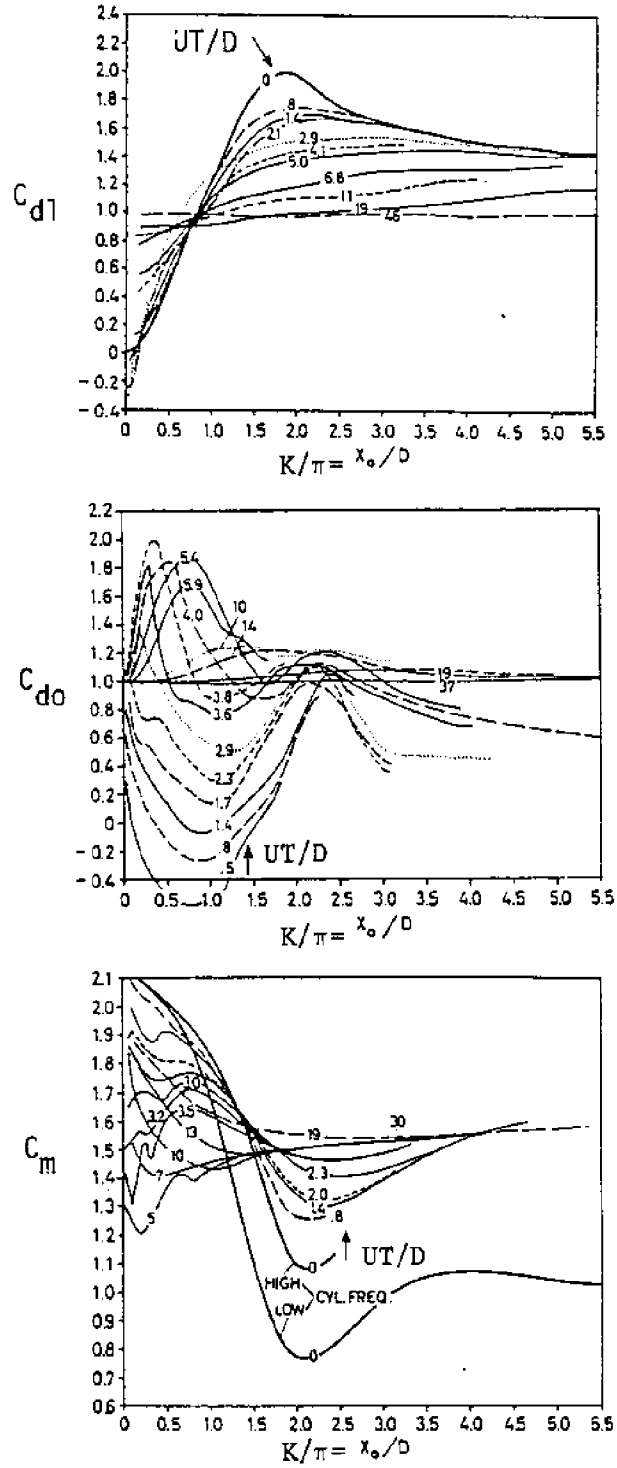

Fig. 1.2.3-3 Force coefficients for a smooth cylinder oscillating in a steady stream versus K for various UT/D (from Verley and Moe, 1979).

$$F_x = \frac{\rho DL}{2} C_d u|\vec{q}| + \frac{\rho \pi D^2 L}{4} C_m u' \qquad (1.2.3\text{-}4)$$

and

$$F_z = \frac{\rho DL}{2} C_d w|\vec{q}| + \frac{\rho \pi D^2 L}{4} C_m w' \qquad (1.2.3\text{-}5)$$

In the above equations, u is the sum of the wave-induced velocity (u_w) and the current velocity (U).

Figure 1.2.3-4 shows their C_d values for the smooth and the roughened cylinders against VM (=UT/D). They also found that C_d approaches that of steady flow as the current velocity increases. Teng and Nath (1984) studied the maximum total force coefficients (C_μ) for smooth and roughened horizontal cylinders and found the values of C_μ against K [$=(u_{w\mu}+U)T/D$] for the waves and current case agree quite well with those for the waves only case as shown in Fig. 1.2.3-5. From this figure, as K gets large, C_μ seems to approach the drag coefficient for steady flow, C_{ds}.

1.3 Scope of This Study

This thesis is about exterior hydrodynamic forces on horizontal circular cylinders which are slender and rigid.

The forces from laboratory periodic waves were measured for 4 horizontal cylinders with different surface roughnesses for Keulegan-Carpenter number (K) up to 25. The Reynolds number was in the range of $3\times10^4 < R < 2\times10^5$, and 5 orbital shape parameters (Ω) ranged from 0.42 to 0.85. The cylinders were smooth, sand-roughened, barnacle-roughened, and one with rigid artificial sea anemones.

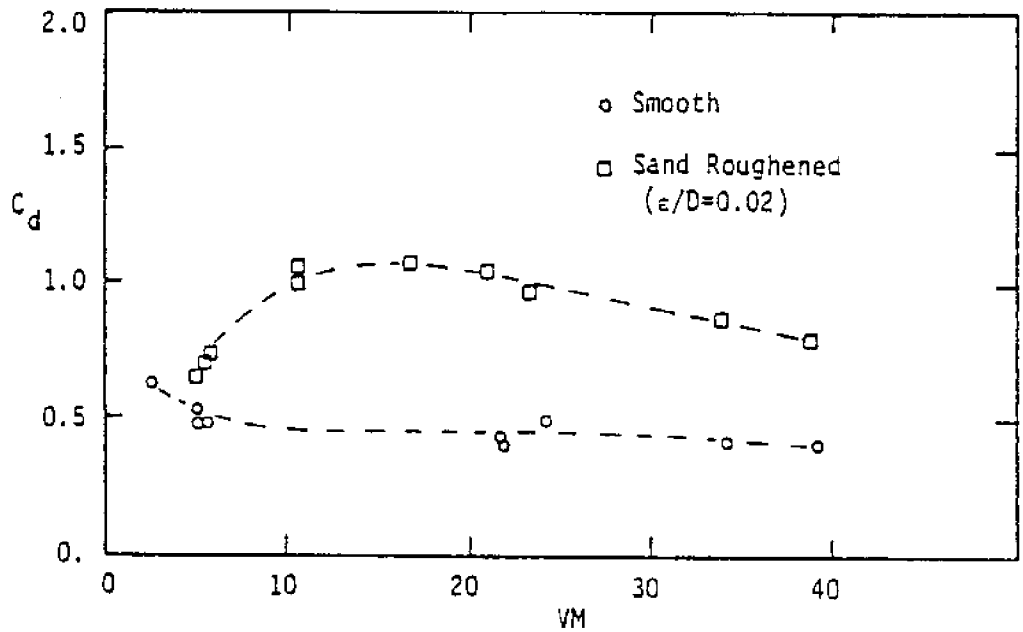

Fig. 1.2.3-4 C_d versus VM (=UT/D) for smooth and sand roughened horizontal cylinders in waves and towing (from Teng and Nath, 1985).

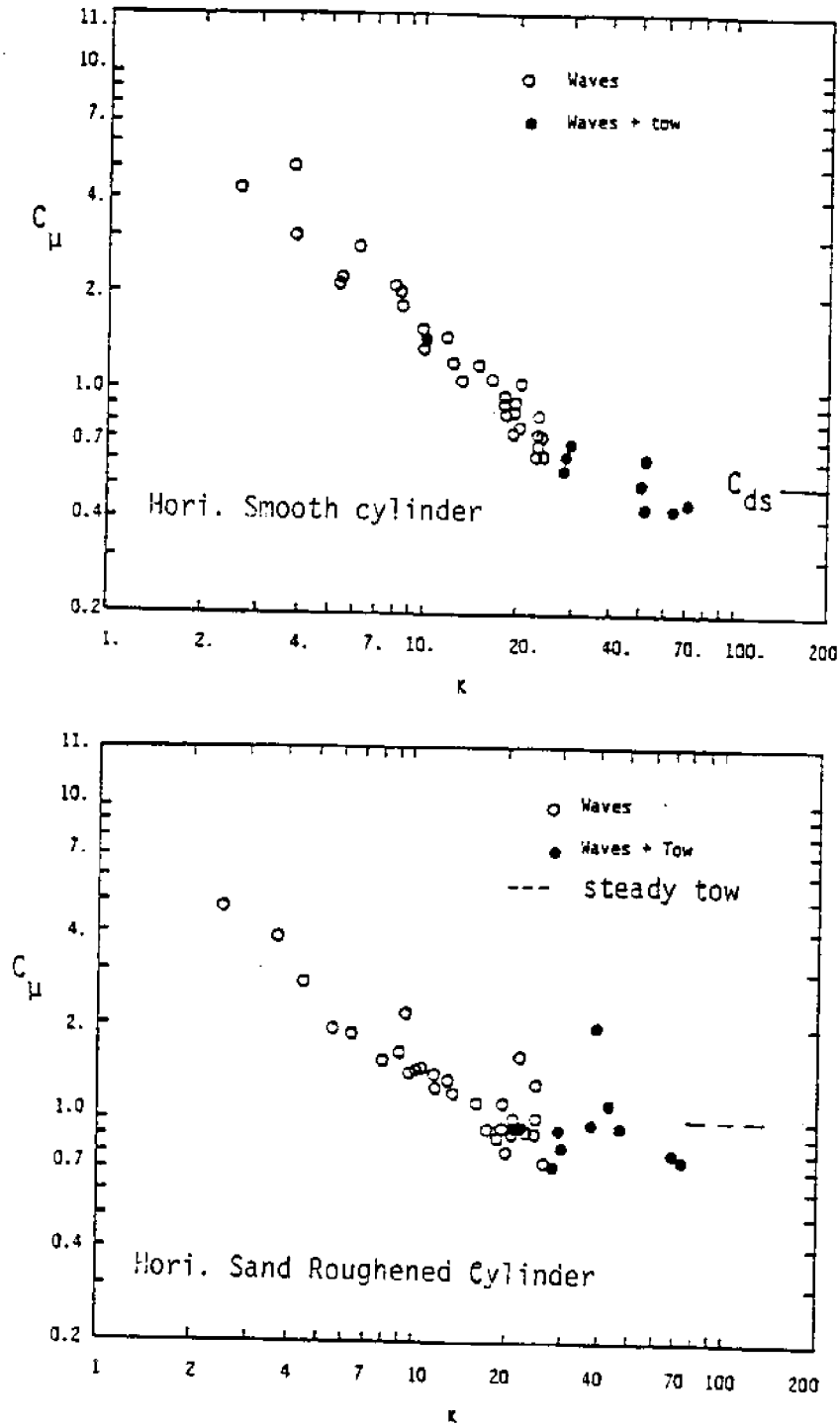

Fig. 1.2.3-5 C_μ versus K for smooth and sand roughened horizontal cylinders in waves only and in waves plus towing (from Teng and Nath, 1984).

In this thesis, both amplitudes and phases of harmonic components of measured forces are analyzed by using Fourier analysis. The force coefficients, C_d and C_m, based on the vector form of the Morison equation, the root-mean-square force coefficients, and the maximum force coefficients are utilized to illustrate the effects of roughness, K, and Ω.

The wave-to-wave variation of forces on horizontal cylinders in periodic waves is examined by means of the maximum forces, the root-mean-square forces and both the amplitudes and phases of harmonic components of forces.

Waves forces on vertical cylinders are compared with those on horizontal cylinders.

The cylinders were towed with steady speeds under a fixed wave condition, which simulates the superposition principle of waves and current, for the tow speeds up to 4.7 times the maximum wave-induced velocity. The towing (current) effect on force coefficients is examined.

Flow visualization experiments were conducted in a small wave flume to observe flow patterns around stationary horizontal smooth cylinders in periodic waves.

2. THEORY AND ANALYSIS

2.1 Governing Parameters

The force on a cylinder is a function of fluid viscosity (ν), cylinder diameter (D), fluid particle velocities (u and w), flow period (T), roughness height (e), etc. Through dimensional analysis, the dimensionless force coefficient is considered as a function of several dimensionless parameters. For horizontal cylinders in periodic waves and current, one possible set of important parameters is

$$C_f = f\left(\frac{u_\mu D}{\nu}, \frac{u_\mu T}{D}, \frac{e}{D}, \frac{w_\mu}{u_\mu}, \frac{UT}{D}, \frac{U}{u_{w\mu}}\right) \tag{2-1}$$

or

$$C_f = f(R, K, \varepsilon, \Omega, VM, U_r) \tag{2-2}$$

in which u_μ and w_μ are the maximum horizontal and vertical velocity respectively, U is current velocity, $u_{w\mu}$ is the maximum wave-induced horizontal velocity, R is the Reynolds number, K is the Keulegan-Carpenter number, ε is the relative roughness, Ω is the shape parameter of fluid particle orbit, VM is the Verley-Moe number, and U_r is the relative velocity. More details and discussion about this analysis can be found in Teng and Nath (1983).

The Reynolds number and Keulegan-Carpenter number for the combined field of waves and current may have several different definitions (see Sarpkaya, et al. 1984). The two dimensionless parameters used in the present study are defined in the following.

$$K = \frac{(u_{w\mu} + U)T}{D} \tag{2-3}$$

and

$$R = \frac{(u_{w\mu} + U)D}{\nu} \tag{2-4}$$

In the above dimensionless parameters, the maximum velocity is used to characterize the kinematics. But, this maximum velocity can not represent the nonlinearity of ocean waves. Thus, two different wave conditions could have the same maximum velocity (or the same dimensionless parameters). This will cause scatter in the data distributions when the data are plotted against these parameters.

2.2 The Vector Form of The Morison Equation

As discussed in Section 1.2.2, the forces on a horizontal cylinder can be predicted by the vector form of the Morison equation, which assumes the drag force is in line with the velocity vector and the inertia force is in line with the acceleration vector. That is,

$$\vec{F} = \frac{\rho DL}{2} C_d \vec{q}\left|\vec{q}\right| + \frac{\rho \pi D^2 L}{4} C_m \vec{q}' \tag{2-5}$$

In the above equation, $\vec{q}$ is the total velocity and the prime represents the associated Eulerian acceleration.

The total force thus described may be decomposed into the horizontal (x) and vertical (z) direction as

$$F_x = \frac{\rho DL}{2} C_d u\left|\vec{q}\right| + \frac{\rho \pi D^2 L}{4} C_m u' \tag{2-6}$$

and

$$F_z = \frac{\rho DL}{2} C_d w\left|\vec{q}\right| + \frac{\rho\pi D^2 L}{4} C_m w' \tag{2-7}$$

The vortex-induced force, which is not included in the above equation, is regarded as noise to the above forces.

2.3 Least-Squares Method

The time-invariant average force coefficients C_d and C_m in the vector form of the Morison equation are determined by using the least-squares method in this study. The least-squares method obtains the force coefficients by minimizing the total error between the measured forces and predicted forces. The details of this method can be found in Teng and Nath (1983). The force coefficients obtained are

$$C_d = \frac{(AA)(BB) - (DD)(EE)}{\frac{1}{2}\rho DL[(CC)(BB) - (DD)^2]} \tag{2-8}$$

and

$$C_m = \frac{(CC)(EE) - (AA)(DD)}{\frac{1}{4}\rho\pi D^2 L[(CC)(BB) - (DD)^2]} \tag{2-9}$$

in which

$$AA = \int_0^{2\pi} [F_{xm}u + F_{zm}w]\left|\vec{q}\right| d\theta \tag{2-10}$$

$$BB = \int_0^{2\pi} \left|\vec{q}'\right|^2 d\theta \tag{2-11}$$

$$CC = \int_0^{2\pi} \left|\vec{q}\right|^4 d\theta \tag{2-12}$$

$$DD = \int_0^{2\pi} [uu' + ww'] \left|\vec{q}\right| d\theta \tag{2-13}$$

$$EE = \int_0^{2\pi} [F_{xm}u' + F_{zm}w'] d\theta \tag{2-14}$$

In the above expressions, F_{xm} and F_{zm} are the horizontal and vertical measured force, respectively.

Under the same test condition, data of n wave cycles were recorded (see Section 4.4). The representative C_d and C_m may be determined from 3 ways: (a) Get C_d and C_m for each wave cycle, and then average these n pairs of coefficients to obtain an average pair; (b) Average these n cycles of wave data to obtain an average wave record, and then obtain coefficients for this mean wave; and (c) Get one pair of C_d and C_m by using the continuous n wave record as a whole. In Appendix A, it is proven that the representative pairs of C_d and C_m from these 3 ways are actually the same.

2.4 Harmonic Analysis

A periodic function f(t) with fundamental period T can be expressed with a Fourier series as

$$f(t) = a_o + 2 \sum_{n=1}^{\infty} (a_n \cos\omega_n t + b_n \sin\omega_n t) \tag{2-15}$$

in which $\omega_n = 2n\pi/T$,

$$a_n \quad = \frac{1}{T} \int_0^T f(t) \cos \frac{2n\pi t}{T} \, dt \tag{2-16}$$
$$n>0$$

and

$$b_{\substack{n\\ n\geq 1}} = \frac{1}{T}\int_{o}^{T} f(t)\sin\frac{2n\pi t}{T}\,dt \qquad (2\text{-}17)$$

using complex notation $F_n=a_n-ib_n$, the above coefficient expressions can be reduced to the following single equation

$$F_n = \frac{1}{T}\int_{o}^{T} f(t)e^{-i\left(\frac{2n\pi t}{T}\right)}dt \qquad (2\text{-}18)$$

If the continuous time series f(t) is not known and only equally spaced samples are given as a discrete time series, i.e. $\{f_j\}$, $j = 0, 1, 2, \ldots\ldots, (N-1)$, the following discrete Fourier transform may be used.

$$F_n = \frac{1}{N}\sum_{j=1}^{N-1} f_j e^{-i\left(\frac{2n\pi j}{N}\right)} \qquad (2\text{-}19)$$

and

$$f_j = \sum_{n=0}^{N-1} F_n e^{i\left(\frac{2n\pi j}{N}\right)} \qquad (2\text{-}20)$$

Since $F_n=a_n-ib_n$, we can obtain

$$F_n = |F_n|e^{-i\phi_n} \qquad (2\text{-}21)$$

in which $|F_n|$ $(=\sqrt{a_n^2+b_n^2})$ is the amplitude of the nth harmonic and $\phi_n(=\tan^{-1}(b_n/a_n))$ is associated phase angle. Thus,

$$f_j = \sum_{n=0}^{N-1} |F_n| \cos\left(\frac{2n\pi j}{N} - \phi_n\right) \qquad (2\text{-}22)$$

An FFT algorithm can be used to evaluate the amplitude and phase of each harmonic of a time series.

In the present study, this harmonic analysis is used to determine the amplitude and phase of each harmonic of the measured hydrodynamic forces (both the horizontal and the vertical), that will be studied in Sections 5.4 and 6.3.

From Eq. (2-22), the phase of each harmonic is related to a cosine curve, i.e., that means the phase is the shift between the profile of a harmonic and a cosine curve. In this study, a whole periodic wave is defined from peak (wave crest) to peak (see Section 4.3). The measured forces for the associated whole wave are taken from the same time interval. Thus, the phase of each harmonic of measured force is related to the wave crest (or the maximum of the horizontal velocity).

2.5 Kinematics of Fluid Particles

When analyzing the data, the ambient kinematics of fluid particles are needed. The seventh order stream function wave theory is used to predict the velocities and accelerations in the present study. Nath (1981) showed that the stream function theory compares quite well with the measured kinematics and is adequate for predicting velocities and accelerations of water particles at the center of a cylinder.

When a steady and uniform current (U) is introduced to the wave field, the linear superposition principle, which assumes the total

velocity is the linear combination of current velocity and wave-induced velocity, is used to predict the kinematics. According to the linear superposition principle (neglecting the interaction between waves and current), the water particle velocities under waves and current are expressed as

$$u(x,z,t) = u_w(x,z,t) + U \tag{2-23}$$

and

$$w(x,z,t) = w_w(x,z,t) \tag{2-24}$$

in which the subscript w represents the wave-induced velocity. Since the total acceleration is used in this study, the acceleration is modified due to the presence of the current as

$$u' = \frac{du}{dt} = \frac{\partial u_w}{\partial t} + (u_w + U)\frac{\partial u_w}{\partial x} + w_w \frac{\partial u_w}{\partial z} \tag{2-25}$$

and

$$w' = \frac{dw}{dt} = \frac{\partial w_w}{\partial t} + (u_w + U)\frac{\partial w_w}{\partial x} + w_w \frac{\partial w_w}{\partial z} \tag{2-26}$$

Teng and Nath (1983) showed that the stream function theory with linear superposition principle can predict the kinematics for a cylinder towed in a wave field (which is used to simulate a cylinder under waves and current in this study) quite well.

2.6 The Blasius' Equation

By using the unsteady form of the Blasius' equation, Maull and Milliner (1978) showed the horizontal and vertical forces, X and Z, on a cylinder due to the movements of the vortices are given by

$$X = \rho\Gamma\left\{w^* + \frac{D^2}{4(x^2+z^2)^2}\left[(z^2 - x^2)w^* + 2xzu^*\right]\right\} \qquad (2\text{-}27)$$

and

$$Z = -\rho\Gamma\left\{u^* + \frac{D^2}{4(x^2+z^2)^2}\left[(x^2 - z^2)u^* + 2xzw^*\right]\right\} \qquad (2\text{-}28)$$

in which Γ is the strength of the vortex (which is defined as positive when it is clockwise and negative when it is counter-clockwise), x and z are the coordinate of the vortex, u* and w* are the horizontal and vertical velocity of the vortex at point (x,z), and D is the diameter of the cylinder. Figures 2-1 shows the definitions of these variables.

From the above two expressions, the forces on the cylinder due to the moving vortices may be predicted. However, the magnitudes of these forces need precise and detailed values about the strength, location and velocity of the vortex. These values are almost impossible to obtain or measure until now. Thus, it is very difficult to quantify the forces. However, the direction of forces due to the motion of the vortex can be judged if the vortex motion can be roughly observed through experiments.

The force acting on a cylinder due to the motion of vortices is a summation of forces induced by each individual vortex. However, according to Eqs. (2-27) and (2-28), only a few vortices that are close to the cylinder are important. Contributions from most of the vortices can be neglected due to the weak strength, slow velocity or far distance from the cylinder.

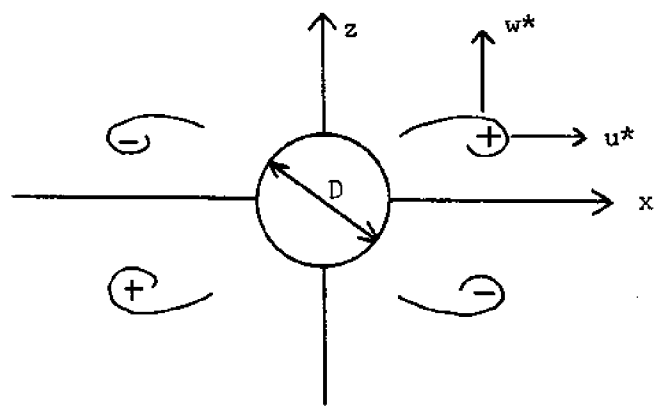

Fig. 2-1 Definition sketch for vortices around a horizontal cylinder in waves.

3. FLOW VISUALIZATION EXPERIMENTS OF HORIZONTAL CYLINDERS IN WAVES

3.1 Description of Experiment

In order to observe and study the vortex shedding patterns around a horizontal cylinder in waves, a series of flow visualization experiments were conducted at the wave flume in Graf Hall at OSU (see Fig. 3-1). This flume is 40 feet long, 24 inches wide and 26 inches in depth with a 18 feet long, 1/12 slope beach at one end. Two sidewalls of the flume are constructed of 1/2 inch clear Plexiglas. The waves, with the wave periods of from about 1 to 3 seconds and wave height up to 4 inches, depending on the water depth, are generated by a hinged flap type wavemaker. This wavemaker is driven by a 1/3 horsepower electric motor with an SCR speed control. The generator stroke is controlled by adjusting a linkage between the electric motor and the wave generating plate.

The smooth test cylinder, 1.5 inches in diameter and 24 inches long, is supported by two clear Plexiglas plates at two ends and is put in the flume horizontally. To avoid the boundary effect, the cylinder is located at least 4 diameters away from the free surface and solid bottom. This plastic cylinder has 8 equally-spaced passageways, that are 1 mm diameter holes drilled on the surface of the cylinder, around the circumference along the center cross section. These holes are connected by 8 plastic tubes, inside the cylinder, to two sets of glass columns, that contain dye and are located above the flume as shown in Fig. 3-2. The solution of potassium permanganate ($KMnO_4$) dye can be introduced into the

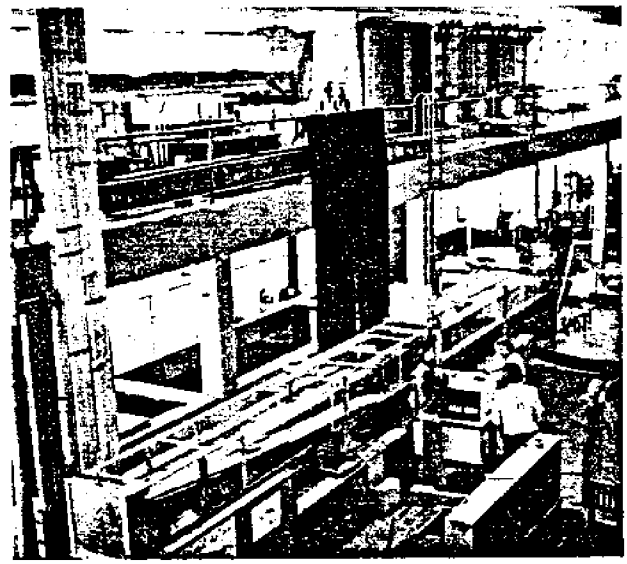

Fig. 3-1 Wave flume in Graf Hall at OSU.

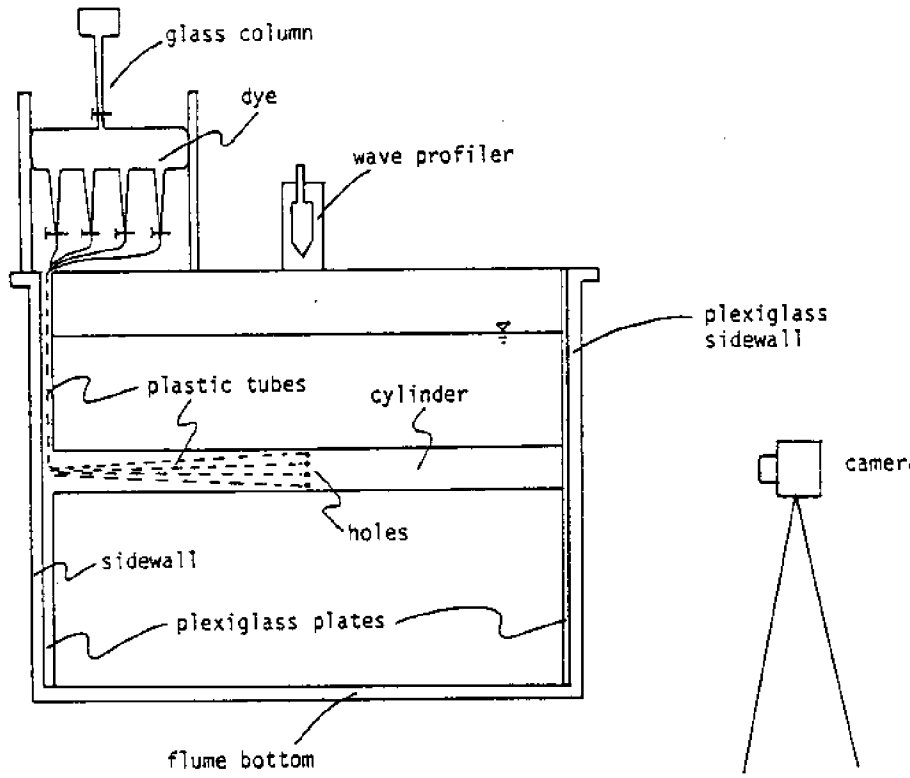

Fig. 3-2 Layout of flow visualization experiments.

boundary layer through the holes. Each set of glass columns contains 4 individual glass columns. A valve on each glass column controls the rate of dye released into the flow as necessary. A master control valve on each set of glass columns controls the ejection of dye from 4 different holes simultaneously.

A super 8 mm movie camera was used to record the continuous process of the flow pattern and vortex shedding. After development and processing, the movie film was examined frame by frame (or by slow motion) by using the Timelapse data analyzer projector. Also, still photos were made of the flow at the wave crest, trough and zero crossings. The layout of this experiment is sketched in Fig. 3-2.

Due to the limitation of the experiment facilities, only a limited range of experiments, characterized by some dimensionless parameters, could be conducted. They were:

R (Reynolds number): 1200-5000

K (Keulegan-Carpenter number): 2-13

Ω (shape parameter): 0.2-0.6

3.2 Results

It is possible to show only the influence of Ω (from 0.2 to 0.6) and K (from 3 to 12) on the patterns of vortex shedding. It is hoped this may give some insight to the flow process around horizontal cylinders in waves.

From consecutive observations of the flow visualization, the vortex shedding patterns sometimes vary from cycle to cycle under the same wave and cylinder conditions. It could have some kind of regularity over a long period. But, only several cycles were observed

because the water contaminated quickly with the dye (solution of potassium permanganate). The flow patterns presented here are the most possible and frequent patterns observed under the specific conditions.

Figure 3-3 shows some photos of the flow pattern around a horizontal cylinder from the experiment. In the following, the flow patterns are sketched from the continuous films taken by the movie camera.

Several typical cases, that contain two values of Ω (0.25 and 0.5) with different values of K for each Ω, are sketched and described in the following. To give a simple and clear presentation of the results for the flow visualization experiments, the periphery of the cylinder is divided into four quadrants as shown in Fig. 3-4. In this figure, the angular coordinate is also defined so that the location of formation and movement of a vortex can be easily described. In Figures 3-5 to 3-10, the arrow in the center of the cylinder represents the direction of the velocity vector at that moment. But, the length does not represent the magnitude of the velocity.

(1) <u>K=10 and Ω=0.25 (Fig. 3-5)</u>

At t=0, the vortices associated with quadrant I and II, namely vortex A and B respectively, start to form and grow with almost the same strength. The vortex D' from the previous cycle passes above the top of the cylinder counter-clockwise and moves with the newly formed A. After t=0, both A and B continue to grow and A is stronger and moves further than B. The vortex A detaches from the cylinder

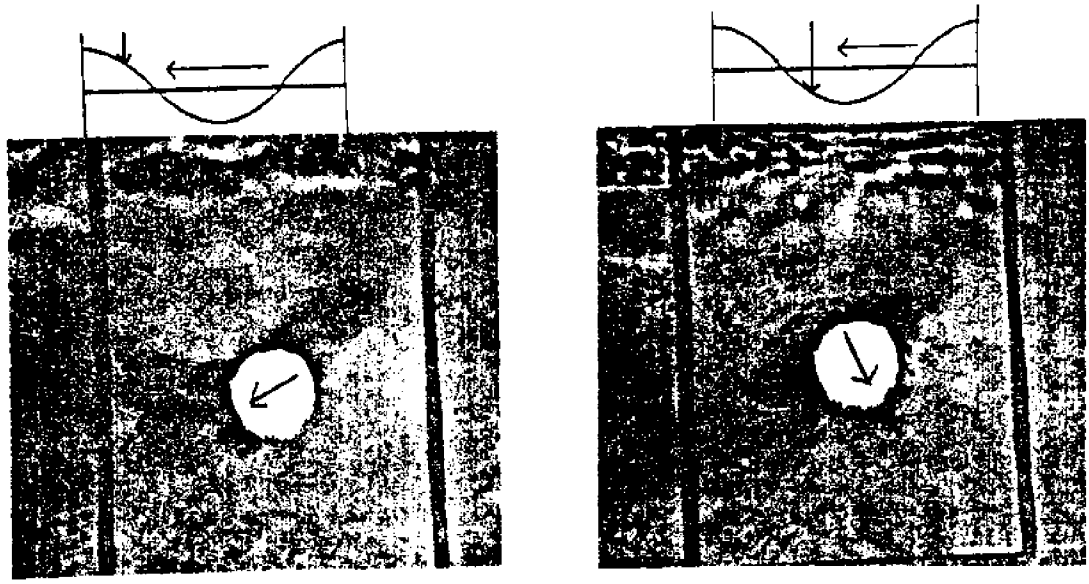

(a) K=10 Ω=.5 t=T/8

(b) K=10 Ω=0.5 t= $\frac{3}{8}$T

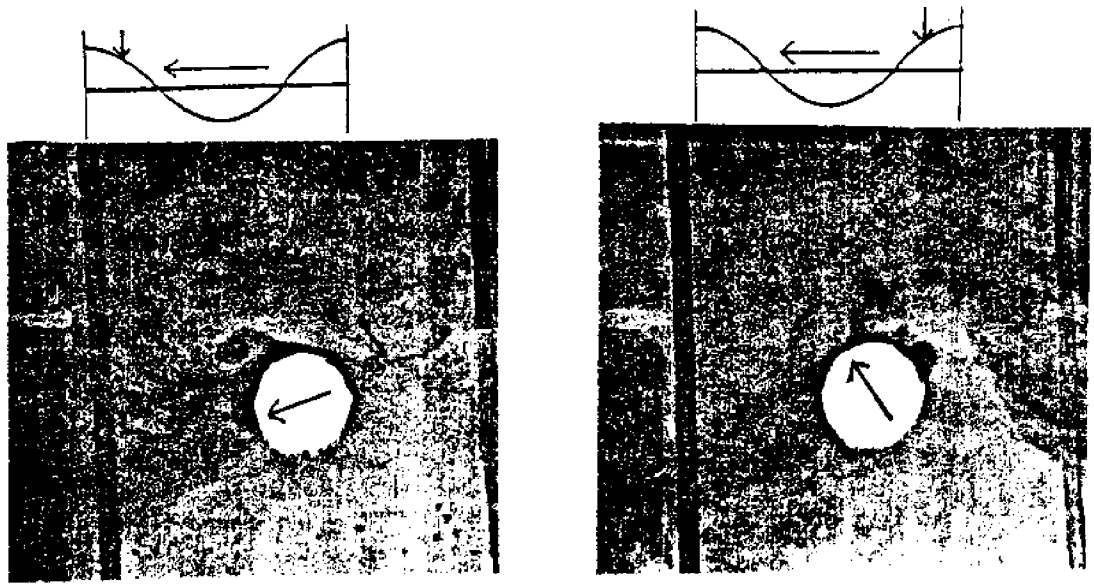

(c) K=12 Ω=0.25 t=T/8

(d) K=12 Ω=0.25 t= $\frac{7}{8}$T

Fig. 3-3 Photos of flow visualization around a horizontal cylinder in periodic waves. (The arrow at the cylinder center represents the velocity vector. The arrow at the above wave profile sketch points the phase that the wave passes the cylinder at that moment.)

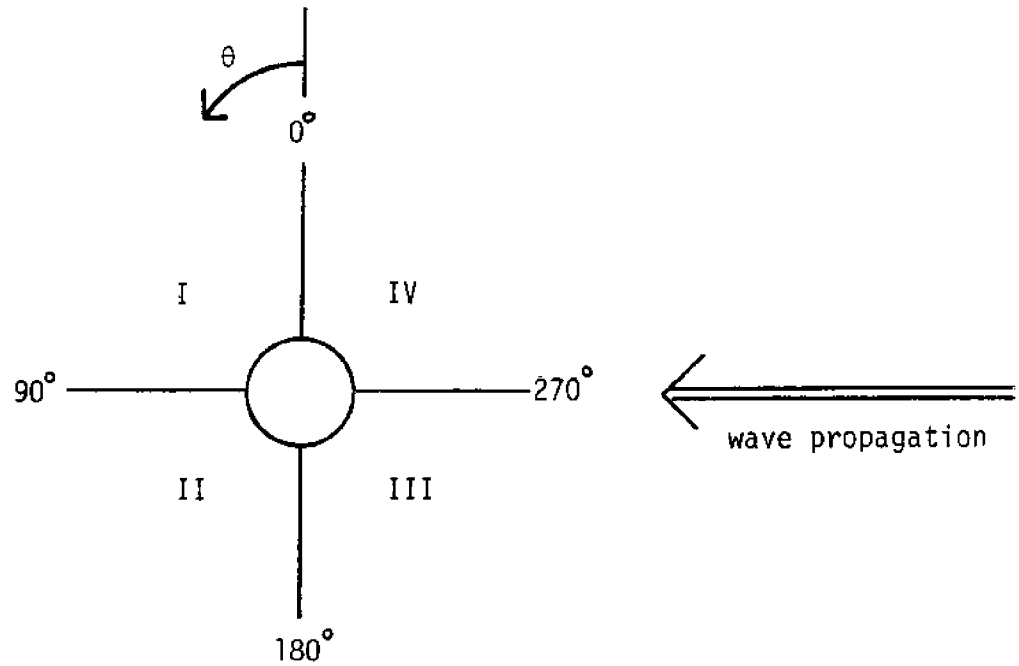

Fig. 3-4 Coordinate and quadrants around a horizontal cylinder.

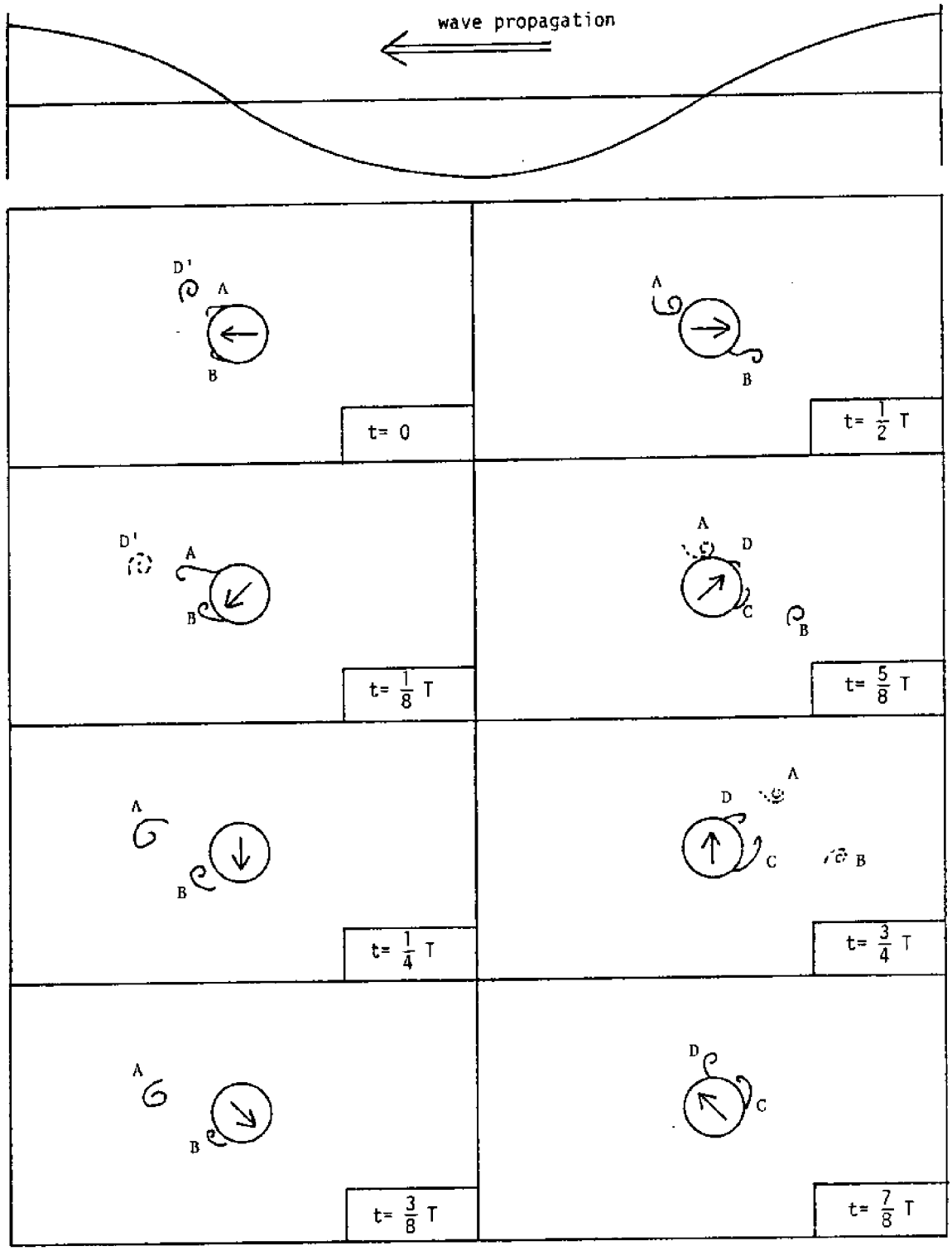

Fig. 3-5 Vortex shedding pattern around a horizontal cylinder in waves for K=10 and Ω=0.25.

between t=T/8 and t=T/4. The vortex A reaches the maximum distance, which varies from 2 to 3 diameter of the cylinder (measured from the center of the cylinder), at t=3/8T. B is always around the periphery of the cylinder. After t=3/8T, A and B start to reverse due to the increase of the rightward velocity. The vortex A is swept back and slightly touches the cylinder at $\theta=60°$. The vortex B, which did not detach during the forward half cycle, moves along the lower periphery from 150° to 210° during its reversal. Between t=T/2 and t=5/8T, the vortex A convects over the top of the cylinder and B detaches from the cylinder at $\theta=210°$. Then, both vortices continue to move to the right and diffuse rapidly. At t=5/8T, two vortices associated with quadrant III and IV, namely C and D, start to form and move upward slightly along the surface of the cylinder due to the presence of the vertical upward velocity. The vortices C and D grow and move counterclockwise along the surface of the cylinder (from 270° to 360°). At t=7/8T, D detaches the cylinder at $\theta=0°$ and will form a pair with the vortex formed at the next cycle at quadrant I. The vortex C becomes weaker and diffuses in the boundary at $\theta=0°$ by the end of this cycle.

(2) K=10 and $\Omega=0.5$ (Fig. 3-6)

At t=0, A and B have the same size and pattern of formation. After t=T/8, A detaches and B does not. At t=T/4, A and B start to reverse and move downward during the reversal due to the presence of the vertical water particle velocity. From a series of observation, the vortex A sometimes hits the cylinder at $\theta=150°$ and sometimes moves below the cylinder (does not hit it) at t=3/8T. The vortex B

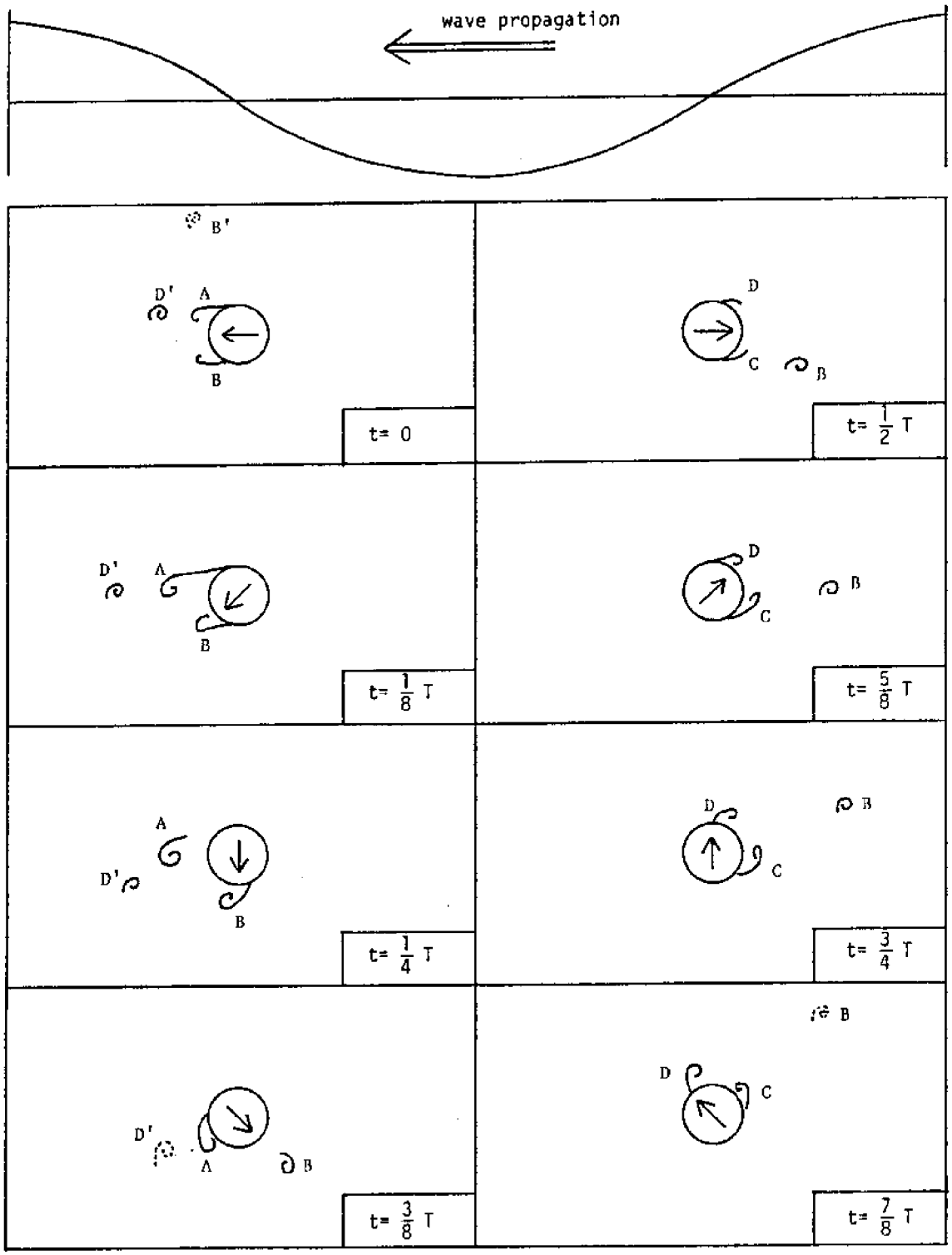

Fig. 3-6 Vortex shedding pattern around a horizontal cylinder in waves for K=10 and Ω=0.5.

detaches at θ=210° before t=3/8T. The vortices B and A (if A did not hit the cylinder) continue to move to the right and diffuse. The vortices C and D form at t=T/2. Both vortices move counterclockwise along the surface of the cylinder due to the vertical velocity. At t=7/8T, D detaches the cylinder at the top of the cylinder. The vortex C sometimes moves above the top of the cylinder (if A hit on the cylinder) and sometimes moves along the boundary of the cylinder near θ=0°. The vortex B moves upward with the vertical velocity after t=T/2 and diffuses gradually.

Comparing with Case (1), It is clear that vortices have more chance to move in the vertical direction due to the increase of Ω (or vertical fluid velocity) under the same K. For example, the vortex A convects away from the cylinder horizontally and reverses back over the upper half for Ω=0.25. For Ω=0.5, A moves downward gradually since its formation and reverses onto or under the lower half cylinder. Also, the developments of vortices in the horizontal direction are constrained as Ω becomes larger and the reversal of A and B occurs earlier for large Ω.

(3) K=5.5 and Ω=0.25 (Fig. 3-7)

At t=0, the vortices A and B form. A grows and moves to the left side and detaches at t=T/4. B grows slowly and stays around the periphery of the surface. Both A and B start to reverse after t=T/4. B is swept back along the lower surface of the cylinder (from 150° to 220°) and detaches the cylinder before t=T/2. Similar to case (1), A touches the upper surface of the cylinder (at θ=60°) at t=3/8T and moves over the top of the cylinder. After t=T/2, A almost dies out

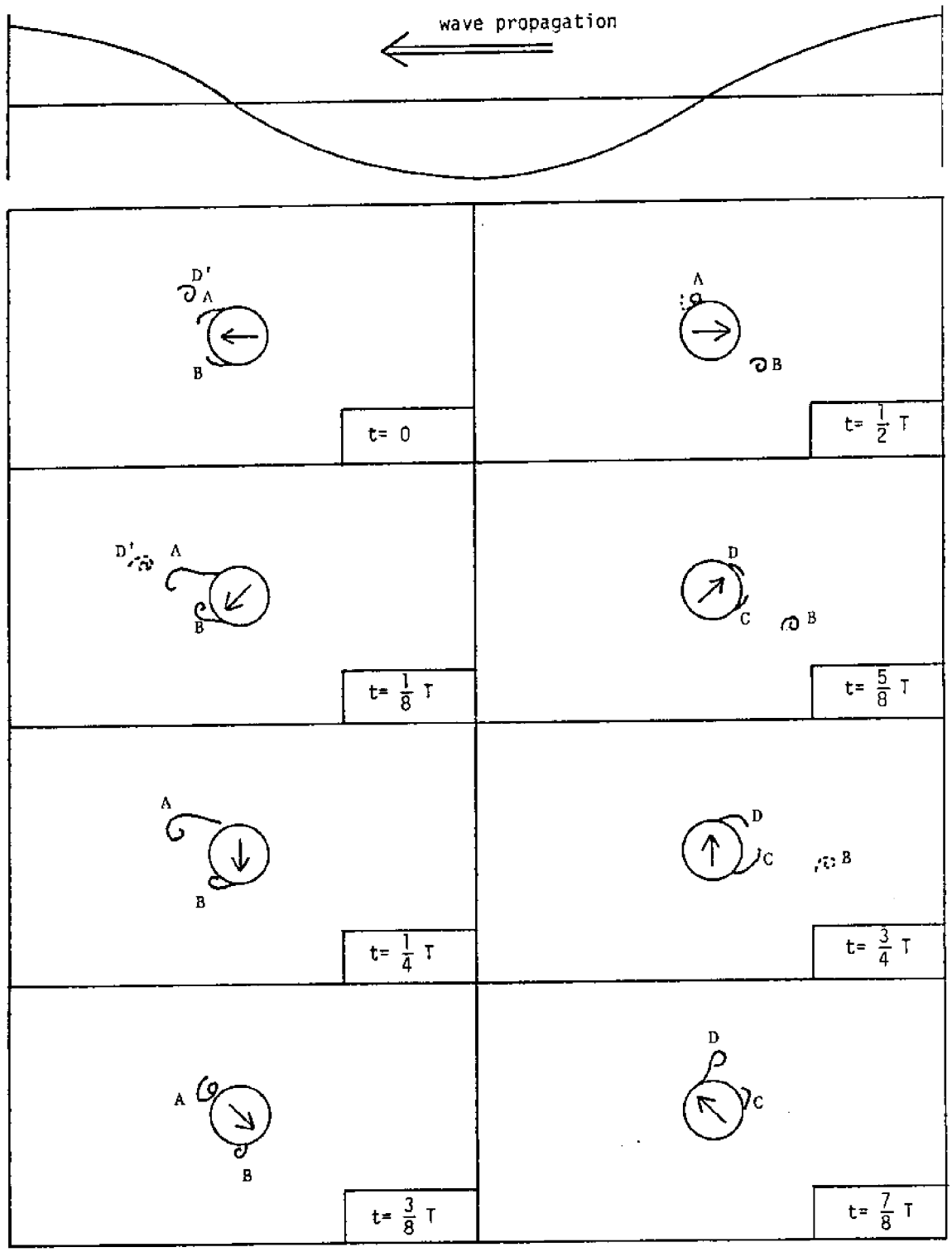

Fig. 3-7 Vortex shedding pattern around a horizontal cylinder in waves for K=5.5 and Ω=0.25.

and B continues to move to the right and diffuses gradually. The vortices D and C start to form after t=T/2 and move along the surface counterclockwise due to the upward velocity. D detaches from the surface after t=7/8T and continues to move to the left. C merges in the boundary of the surface at about 340°.

With the same Ω and smaller K, vortices (e.g., the vortex A) can not move as far as those with larger K in Case (1). Accordingly, it reverses back to the cylinder earlier during the flow reversal. The vortex A hits the cylinder at t=3/8T for K=5.5 and at t=T/2 for K=10.

(4) K=5.5 and Ω=0.5 (Fig. 3-8)

The vortices A and B form with significantly unequal size and strength at t=0. After formation, A grows and moves slightly downward and B does not grow too much due to the relatively strong vertical velocity. At t=T/4, A detaches from the cylinder and B still stays around the surface at θ=180°. After its reversal at t=T/4, A hits on the cylinder at θ=150° and dies out between t=3/8T and t=T/2. The vortex B detaches from the cylinder due to the reversal at t=3T/8 and moves to the right upper direction with the rotation of the velocity vector. D starts to form at t=T/2 and C starts to form at t=5/8T. D detaches the cylinder from the top (θ=0°) at t=3T/4. Note that the vortex B is at the right side of D and moves with D and diffuses. The smaller C, always moves around the surface of the cylinder from 270° to 360°, is mixed with the boundary at t=7T/8.

In this case, the flow pattern combines the characters of small K from Case (3) and large Ω from Case (2), that are the increase of

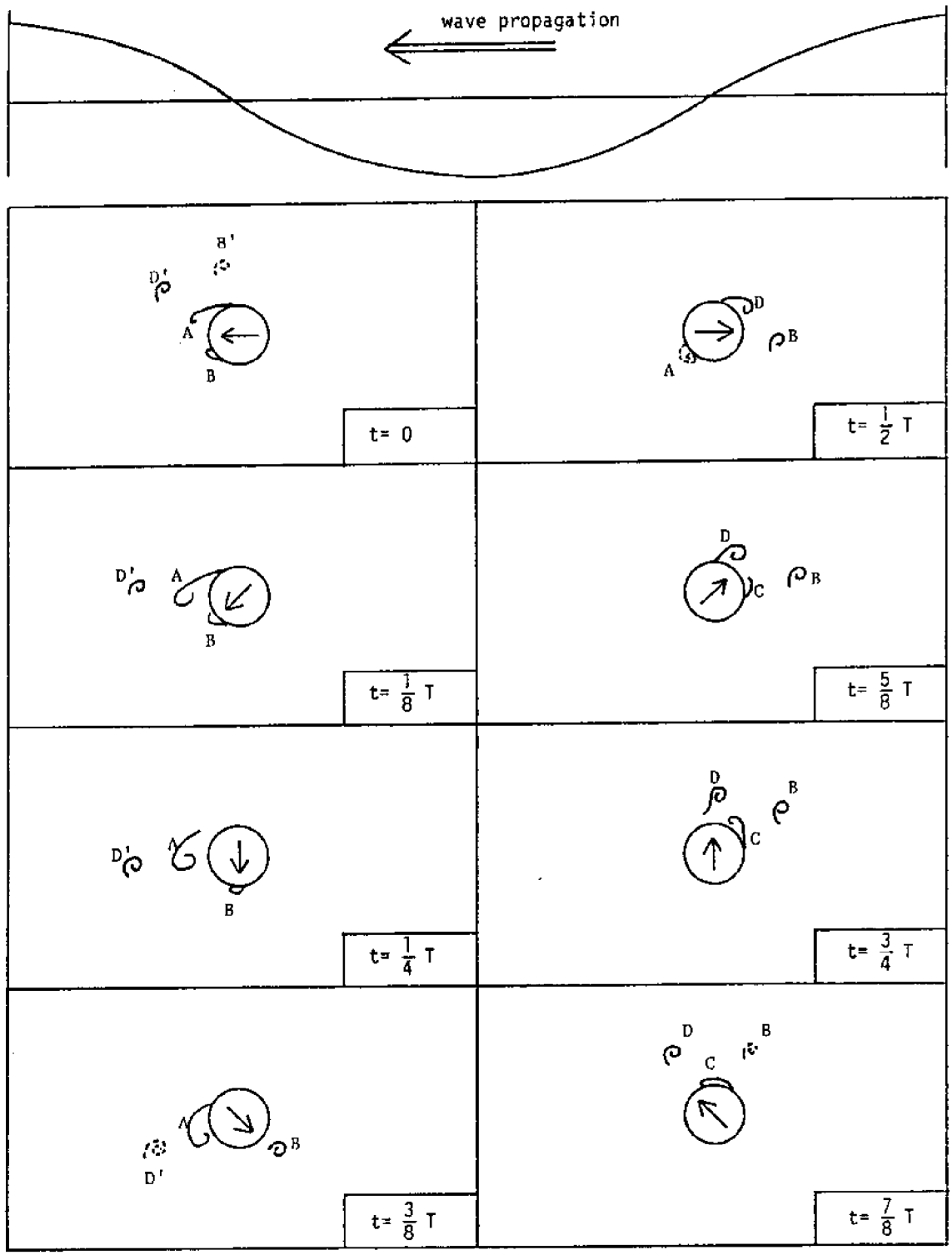

Fig. 3-8 Vortex shedding pattern around a horizontal cylinder in waves for K=5.5 and Ω=0.5.

vertical movements and decrease of horizontal movements. Thus, all vortices stay around the cylinder.

(5) For Ω=0.5 (the same as cases (2) and (4)) and smaller K(=3.5) (Fig. 3-9)

With smaller K, the vortex A does not detach from the cylinder. Before t=T/2, A hits the lower left surface (θ=150°) of the cylinder during its reversal. The B and D grow and detach due to the reversal of the flow. Both vortices rotate around the cylinder counter-clockwise for about 180°. The vortex A is much larger and stronger than the vortex B during the first half cycle.

(6) For Ω=0.25 (the same as cases (1) and (3)) and larger K(=12) (Fig. 3-10)

There exists a second vortex E at quadrant I right after the vortex A detached (at t=T/4). The vortex E reverses to the right hand side of the cylinder from the top of the cylinder. In this case, A reverses very slowly toward θ=90° and its strength is relatively weak as it approaches the surface. The formation and movement for vortices B, C, and D are almost the same as those for the same Ω and smaller K (=10).

Besides the cases sketched and described above, more cases were conducted. The flow patterns of the rest of the cases are similar to those just described. The general phenomena observed from all of the cases in the present study are summarized in the following.

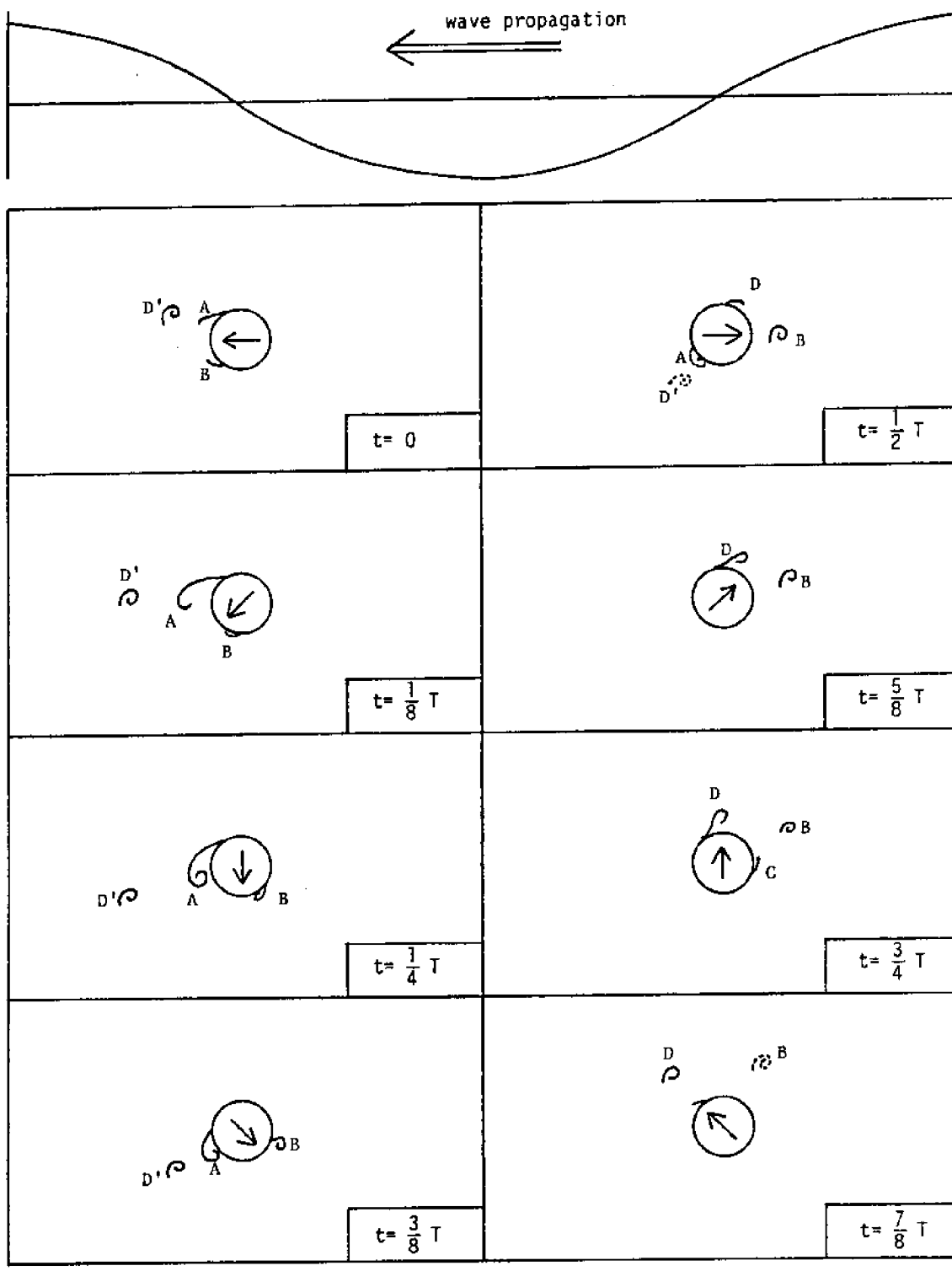

Fig. 3-9 Vortex shedding pattern around a horizontal cylinder in waves for K=3.5 and Ω=0.5.

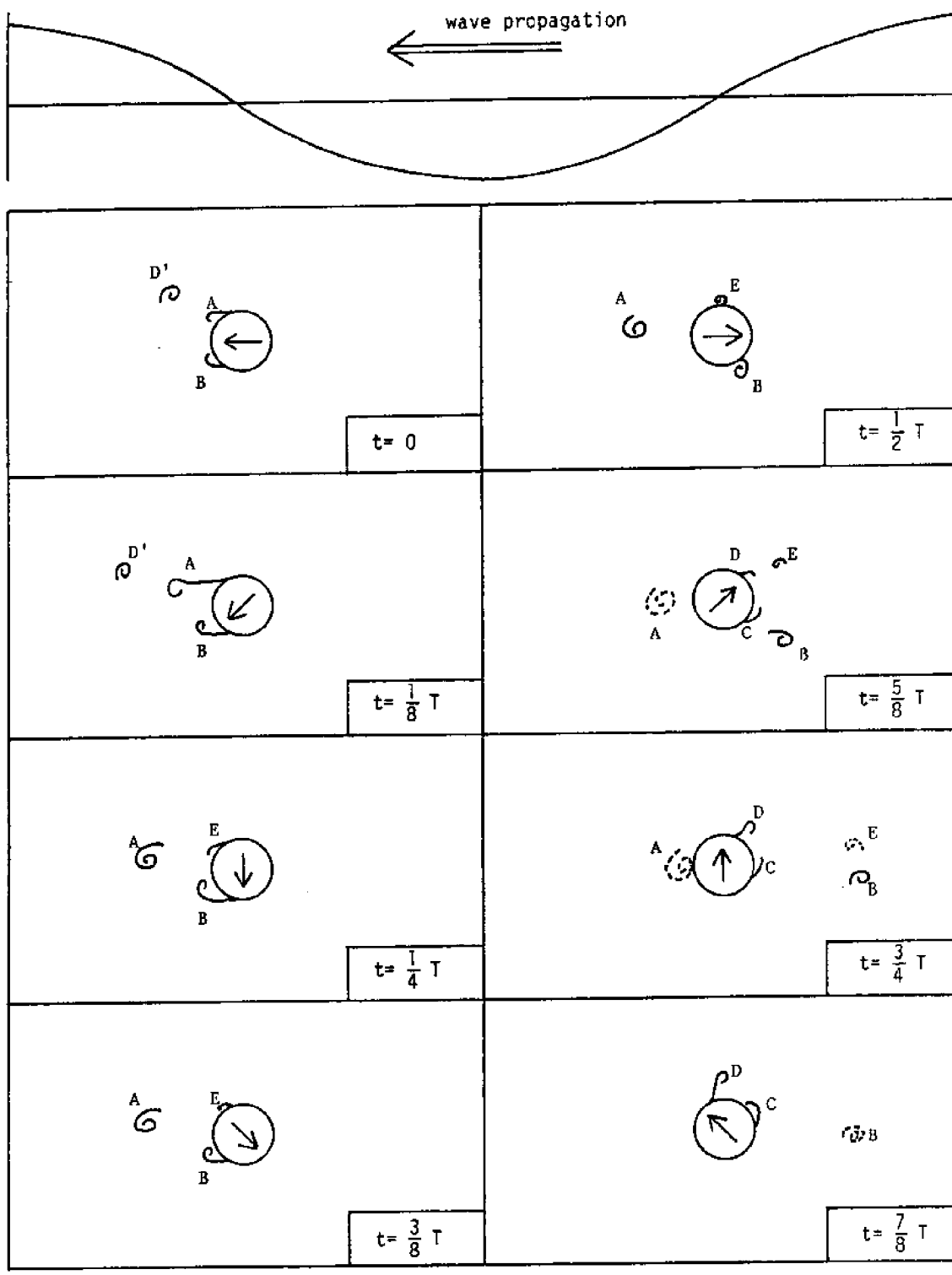

Fig. 3-10 Vortex shedding pattern around a horizontal cylinder in waves for K=12 and Ω=0.25.

(i) For all cases, the flow patterns are not symmetric about t=T/2. Usually, the vortices formed during the first half cycle (especially, the vortex A) are stronger than those formed during the second half cycle.

(ii) Basically, the 4 locations (one in each quadrant) of vortex formation are similar to those for planar oscillatory flow (Ω=0, see Fig. 1.2.1-9). The presence of the vertical velocity will shift the separation point a little and make the formed vortices move in the vertical direction in some degree.

(iii) For small values of Ω, the vortex A hits or passes over the cylinder at quadrant I (i.e., the upper half cylinder). For large Ω, the vortex A hits on or passes below the cylinder at quadrant II (i.e., the lower half cylinder). The value of Ω between these two conditions is approximately 0.35 in the present experiments. This value is thought to be function of R, K, and e/D.

(iv) The vortices B and D, formed at quadrant II and IV respectively, grow and detach from the cylinder mainly due to the reversal of the flow instead of the general detachment process as that in steady unidirectional flow.

(v) The vortex B formed at quadrant II always passes the the lower half of the cylinder during the reversal due to the downward vertical velocity. After detachment, B convects to the right (in quadrant III) for small Ω and convects upward (toward quadrant IV) for large Ω.

(vi) The vortices formed during the second half cycle, C and D, always move counter- clockwise over the top half of the cylinder. Then, D detaches from the top and moves with the newly formed A during the next cycle at quadrant I. The vortex C merges in the boundary at θ=330°-360° by the end of this cycle.

(vii) For large Ω, the vortex has more opportunity to move in the vertical direction. And the movement and growth of vortices in the horizontal direction are confined due to the relatively stronger vertical velocity of water particle.

(viii) For large K (note that K is based on the maximum horizontal velocity), the vortex has more opportunity to grow and move in the horizontal direction. Also, more vortices could form and grow with large K (e.g., $K > 12$ with Ω=0.25 in Fig. 3-10). For small K, the dominant vortex A does not detach and A is much larger and stronger than B (e.g., $K < 3.5$ with Ω=0.5 in Fig. 3-9).

(ix) Neither the wake nor the shed vortices rotate or move synchronously with the velocity vector, especially for small Ω.

Besides, it was observed that the diffused dye slowly moved toward the wave board during the flow visualization experiments. This phenomenon is thought to be due to the return current effect in a closed wave flume.

3.3 Discussion

(1) Comparison With Other's Observations

Comparing the present observations with those from Maull and Norman (1979) for horizontal cylinders in waves, the vortex shedding pattern they observed for K=8 and Ω=0.3 is almost the same as that for K=10 and Ω=0.25 in Section 3.2. They also presented the flow pattern for Ω=0.79, which is the highest Ω value they reached. The pattern they observed is similar to that observed with the highest value of Ω=0.6 in the present study.

(2) Comparison With Observations for Planar Oscillatory Flow

Comparing the present results with small Ω(=0.25) with those for planar oscillatory flow (Ω=0) shown in Fig. 1.2.1-9, it is clear that the differences are significant, especially for the second half cycle. The flow patterns for planar oscillatory flow (Ω=0) are symmetric, but those for horizontal cylinders in waves with $\Omega \neq 0$ are not. For Ω=0.25, the vortices formed in the first half cycle, A and B, are stronger and larger than C and D formed in the second half cycle. Also, during their reversal, A and B convect over the

cylinder from the upper and lower side respectively, but both C and D in the second half cycle move from the upper side.

The other important difference between $\Omega=0$ and $\Omega\neq0$ is that asymmetric vortices, that will cause the transverse (lift) force, for the horizontal cylinder cases ($\Omega\neq0$) occurs at smaller K than that for planar oscillatory flow ($\Omega=0$). Significant asymmetric vortices can be observed for $\Omega=0.5$ at $K=3.5$ for horizontal cylinders in waves. But, asymmetric vortices start to form at $K > 4$ for planar oscillatory flow as shown in Fig. 1.2.1-9. In other words, the presence of the vertical velocity will accelerate the occurrence of asymmetric vortices, which causes the unbalanced force called vortex-induced force.

It is believed that the flow pattern for horizontal cylinders in waves tends to be similar to that for planar sinusoidal flow as Ω approaches 0.

(3) Interaction Effects Between Vortices

The formation of the vortex D is at $t=5T/8$ for $\Omega=0.25$ and A reverses over the top of the cylinder in this case. The D forms at $t=T/2$ for $\Omega=0.5$ while A reverses under the lower half of the cylinder. It is clear that the formation of D is delayed if the vortex A convects over the upper half of the cylinder. In other words, the vortex A, which is defined as counterclockwise, will retard the formation of the clockwise D. The same for the lower half cylinder, the reverse vortex B retards the formation of C. Due to the delay of formation, the vortex C starts to form at the moment that the water particles start to move upward. Thus, the growth of C is confined

and the movement is usually along the surface. Before the end of a cycle, the vortex C is very close to the boundary of the top of the cylinder and tends to accelerate the growth of the vortex A in the next cycle. Note that the vortices A and C have the same sign (counterclockwise). This is considered as one of the reasons for A > B since there is no vortex will enhance the formation of B. Thus, it may be concluded when a vortex approaches a location where another vortex is going to form and grow, the former will enhance the latter if they have the same sign and the former will retard the latter if they have the opposite sign.

(4) Asymmetry of Flow Patterns

From all of the observations, the vortices form and grow during the first half cycle appear stronger than those observed in the second half one. The vortex A, associated with quadrant I and formed under the wave crest, is always strongest and thence the dominant one. The main reason is thought to be the nonlinearity of waves, which makes the horizontal velocity under the crest (t=0) greater than that under the trough (t=T/2). The enhancement and retardation between vortices (interaction effect) will enhance the asymmetry of the flow pattern around a horizontal cylinder in waves as discussed in the last paragraph.

The vortex A is always stronger and larger than the vortex B formed in the second quadrant. The main reason is that the downward vertical velocity retards the development of B. The interaction effect discussed in (3) and the small velocity gradient between the top and the bottom are thought to be possible reasons for A > B.

Thus, the fact that A > B is getting significant for small K (compare Fig. 3-6 with Fig. 3-9) and large Ω (compare Fig. 3-7 with Fig. 3-8).

(5) Effect of Vortex Formation and Movement on Forces

As discussed in Section 2.6, the forces induced by the formation and movement of vortices can be qualitatively estimated by the Blasius' equation, i.e., Eqs. (2-27) and (2-28).

From flow visualization and Figs. 3-5 to 3-10, only the vortices A and B (and E) dominate the flow field during the first half cycle. The D' from the previous cycle has a minor effect. Thus, the force induced by the movement of vortices is mainly the summation of the forces from these vortices. In the second half cycle, the vortices C and D dominate. The vortices from the previous cycle, i.e. A, B and E, have minor contributions.

From the observed flow patterns and Eqs. (2-27) and (2-28), the direction of forces induced by the movement of dominant vortices can be judged. For example, the vortex A induces downward forces and B induces upward forces. There exists a downward forces during the first half cycle as the effect of A is greater than that of B, and vice versa.

For large K, more vortices can form and move. These vortices will modify the induced force in both directions, especially in the vertical direction. Let us use the vortex E in Fig. 3-10 as an example. The newly formed E has the same effect as A. In the horizontal direction, A, B and E all induce forces to the left. Thus, the presence of E will enhance the magnitude of force in this direction (recall that total force induced by vortex movement is the

summation of the effects from each individual vortex). But, in the vertical direction, A induces downward forces and B induces upward forces. Then, E will induce downward forces again and might change the sign of the vertical force depending on the relative strength and velocity. Thus, the presence of the vortex E will change the pattern and increase the higher harmonics of forces in the vertical direction.

4. LARGE-SCALE LABORATORY EXPERIMENTS OF FORCE MEASUREMENTS

Actually, the experimental data of force measurements in the present study came from several research projects conducted at OSU from 1981 to 1985. Even though the experiment instruments and techniques were improved from time to time, the basic frame of the whole experimental system was unchanged. In this section, the important information about the experiments is described. For more details, the reader is suggested to refer to Nath (1981a, 1983b, 1983c, 1984a).

4.1 Wave Tank

The experiments of the present study were conducted at the O.H. Hinsdale Wave Research Laboratory (WRL) of Oregon State University. It is a wave flume 340 feet long, 12 feet wide and 15 feet deep in the test region. Water depths are usually 11.5 feet in the test region so that 3.5 feet of freeboard exists.

The wave board is a flap-type board which is hinged at the bottom and is activated by a 150-HP pump with a hydraulic servo mechanism. Good, repeatable periodic waves can be generated with periods of from about 1 second to 7 seconds. The wave height (trough to crest) are limited by incident breaking up to a period of 2.5 seconds, where the wave height is about 5 feet. For periods greater than 2.6 seconds, the maximum wave heights are limited by either the still water free board (3.5 feet) or the available energy from the wave generator. The maximum height for the 6.0 seconds waves is 3 feet. Random waves can also be generated using the on-site PDP-11

computer to generate the wave spectrum and the transfer function for the board motion.

A towing carriage, capable of towing up to 500 pounds at speeds ranging from 0.23 to 11.81 feet per second, is supported by the two side walls of the flume and is available for towing models. Figure 4-1 shows the carriage on the wave flume. In the present study, a cylinder subjected to waves and current is simulated by towing the cylinder with steady velocity in a wave field.

4.2 Test Cylinders

All test cylinders in this study have a nominal diameter of 8 inches (actual diameter is 0.719 feet) and 8.7 feet long. Each cylinder includes a two-foot long test section at the center portion and two dummy sections at both ends to minimize the end effect. The outer shell of each section is made up of two aluminum semi-cylinders. The shells were drilled for bolt holes (which were flush bolted) so that the shells with different roughness could be easily changed by removal of these bolts.

The test section is suspended from two 5/8-inch diameter aluminum rods that were milled on the ends to receive strain gauges in such a manner as to measure the total horizontal and vertical forces on the test section. The gauging length of each rod is 8 inches, and the construction resulted with this gauge length being a fixed ended beam. There are four beams total and the strain gauges are arranged to eliminate any influences from torsion or from off-centered loadings of the hydrodynamic forces.

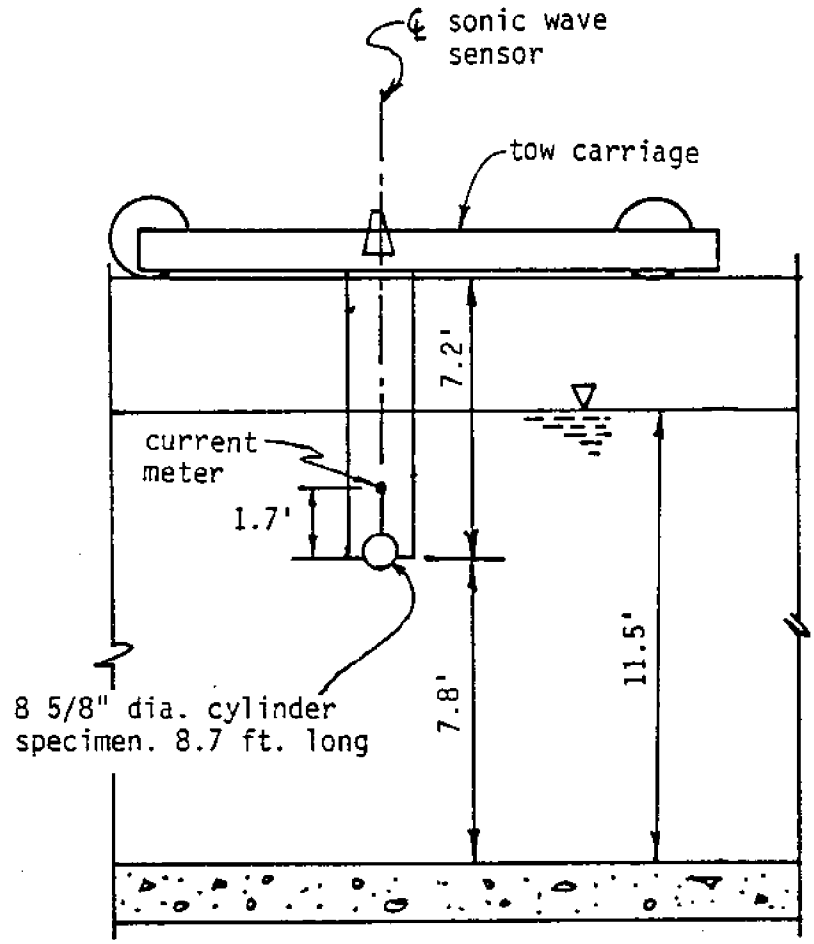

Fig. 4-1 Cross section of specimen set-up in the OSU Wave Research Facility.

In this study, four sets of cylinders with different roughness were examined: (1) the smooth cylinder (abbreviated as HSMC8); (2) the sand-roughened cylinder (HSRC.02); (3) the barnacle-roughened cylinder (HBRC.2); (4) the artificially rigid sea anemone cylinder (HRAN). Figure 4-2 shows the skins of these four types of cylinders. The smooth cylinder has a smooth aluminum surface. The sand-roughened cylinder was made by gluing sands uniformly on the smooth aluminum surface and is characterized by relative roughness e/D = 0.023 (e = sand size and D = diameter of the smooth cylinder). The barnacle-roughened cylinder had dried barnacles randomly glued on and the e/D = 0.19 is determined by circumferential measurements. The artificially rigid sea anemone cylinder was constructed by gluing 1-5/16 inches in diameter and 3-3/4 inches wood rods on. It is a 1/3 scale ratio model to the typical structures and anemone in seas. The spacing between artificially rigid anemones (rods) in a row, which is parallel to the cylinder axis, is 3 inches. The distance between rows is 3 inches and there is 1.5 inches distance shift between two consecutive rows. The details of this model cylinder can be found in Nath (1984a) and observed in Fig. 4-2. The relative roughness e/D, which was determined by area projections, is 0.315 for the rigid anemone cylinder. Table 4-1 summarizes the abbreviation, relative roughness, effective diameter and name of project of these four test cylinders. In this table, the effective diameter factor, δ, is defined as the ratio of the effective diameter to the smooth diameter. The effective diameters for the HBRC.2 and HRAN were obtained

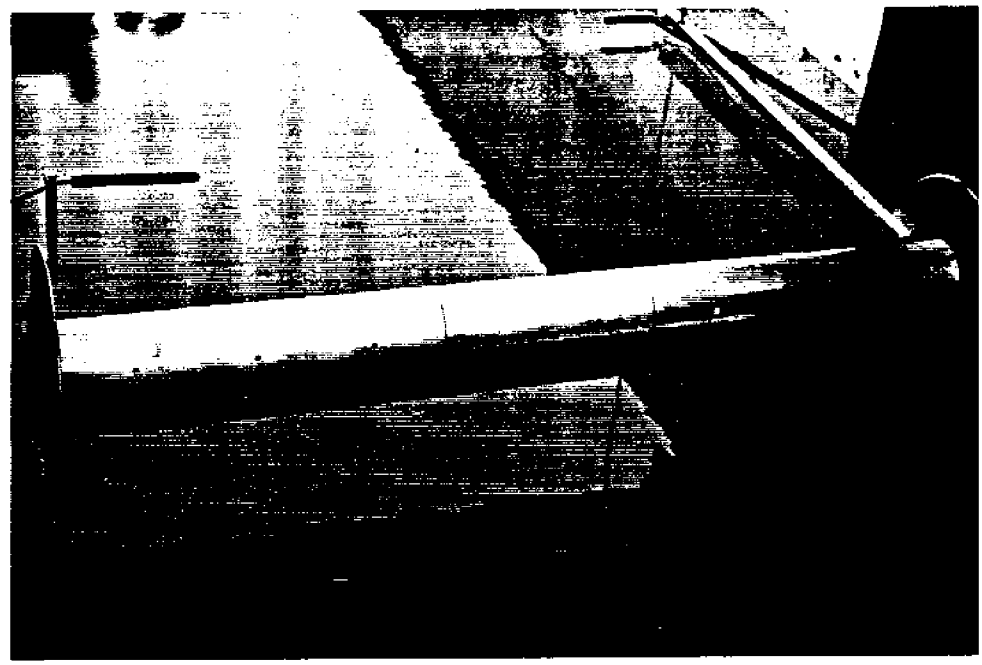

Horizontal smooth cylinder (HSMC8)

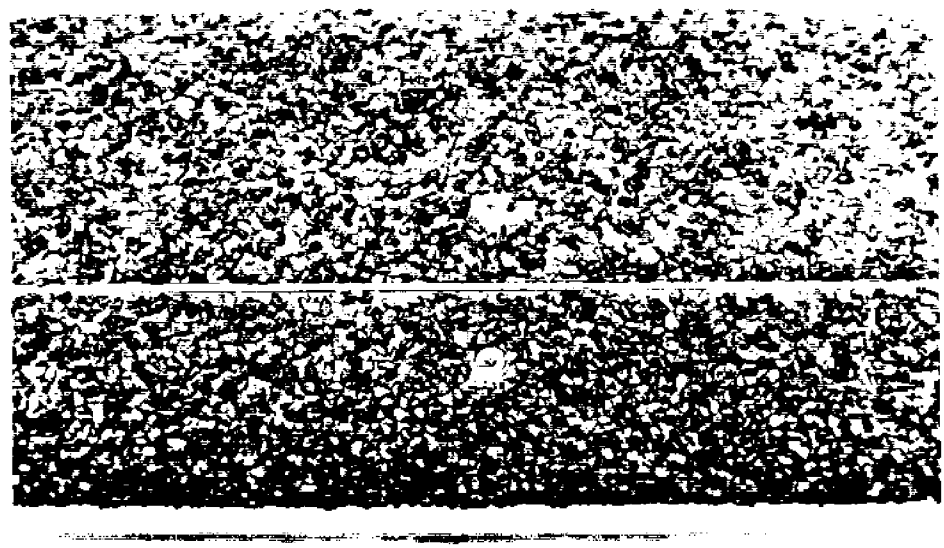

Horizontal sand roughened cylinder (HSRC.02)

Fig. 4-2 Test cylinders in this study.

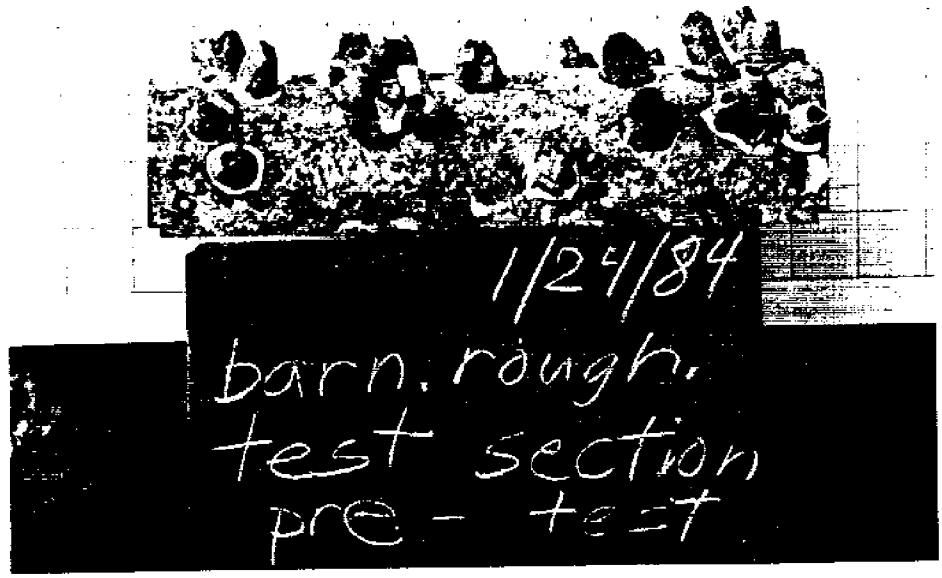

Horizontal barnacle roughened cylinder (HBRC.2)

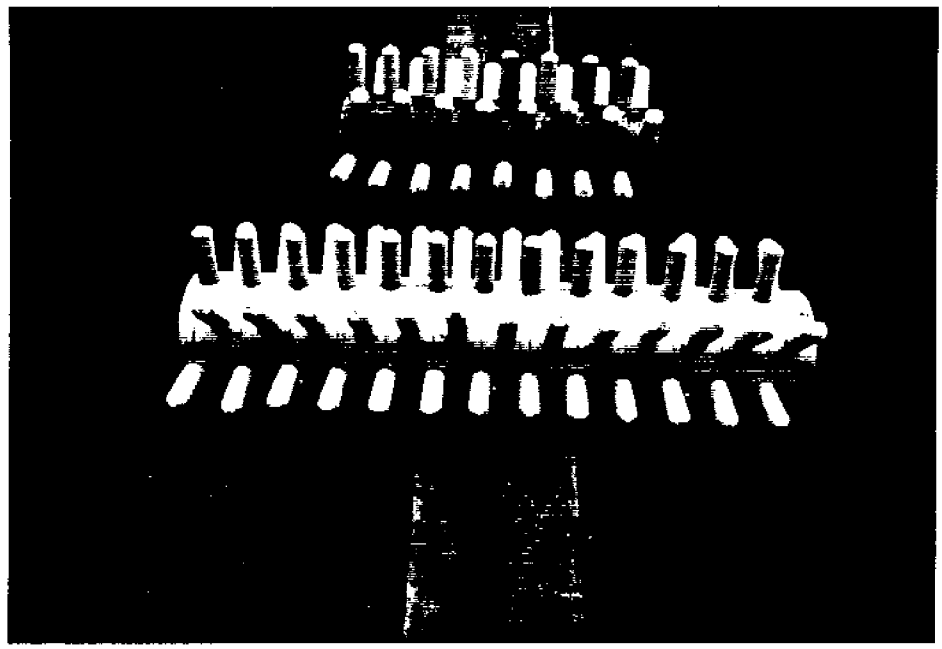

Horizontal artificially rigid sea anemone cylinder (HRAN)

Fig. 4-2 Test cylinders in this study (continued).

Table 4-1. Information about test cylinders studied in this thesis.

Test Cylinder	Abbreviation	e/D	Effective Diameter δD*	δ	Project (Year)
Hori. SMooth Cylinder	HSMC8	-	0.72 (0.72)**	1.00	API (1981)
Hori. Sand Roughened Cylinder	HSRC.02	0.023	0.75 (0.72)	1.046	API (1984)
Hori. Barnacle Roughened Cylinder	HBRC.2	0.19	0.88 (0.72)	1.22	NSF.SG (1984)
Hori. Artificially Rigid Sea ANemone Cylinder	HRAN	0.315	0.99 (0.72)	1.38	API (1984)

* The smooth diameter is D. The effective diameter is δD.
The symbol δ is called the effective diameter factor.
** Values in the parentheses are the smooth diameter D.

by measuring the projection area. The effective diameter for the HSRC.02 was calculated by the grain size of uniform sand.

4.3 Measurements and Recording

The horizontal and vertical forces were measured together with the wave profile and water kinematics for each test run.

The water surface profile was measured with a sonic profiler mounted in an opening of the carriage directly above the test cylinder. The water velocities were measured for each cylinder with Marsh McBirney current meters. Due to the presence of the cylinder, it is impossible to measure water velocities at the same position of the center of the cylinder. Thus, the current meter was placed 1.87 diameters clear of the top of the cylinder to minimize effects on the current meter from the presence of the cylinder.

The force transducers were carefully calibrated by means of providing known forces before and after the test. The details of calibrations can be found in Nath (1981a, 1984a, and 1985b).

Experimental outputs were recorded on digital magnetic tape and strip chart records. A PDP-11 minicomputer provided software for multiplexing and initial recording on disk. After the experiment, data were transferred from disk to tape.

The original approach to digitize the data is to keep the time interval small enough to avoid aliasing in the frequency domain with respect to the fundamental wave frequency and the higher harmonics for any frequencies under consideration. Because the Fast Fourier Transform (FFT) algorithm was used for processing the data, each fundamental wave period was digitized at 2N (where N is integer)

intervals. After complete processing, the data were reduced to 32 increments (with equal spacing) per wave, from which the force coefficients and other desired quantities were calculated.

Because the data in the present study came from different projects, some of the data were recorded for 10 waves, from which 7 peak-to-peak waves were chosen and used for data analysis. For some data, only 4 waves were recorded, from which 3 peak-to-peak waves were used. The details about waves recorded and used are reported in the next section.

4.4 Test Conditions

The test conditions of force measurements for the smooth and roughened cylinders, periodic waves and waves plus current (towing) are summarized in Table 4-2.

The ranges of governing parameters for the present study are:

R : 0.3×10^5 - 1.8×10^5 (up to 5×10^5 if including current),

K : 2-25 (up to 60 if including currents),

e/D: 0.(HSMC8), 0.02(HSRC.02), 0.19(HBRC.2), 0.315(HRAN),

Ω : 0.85, 0.67, 0.55, 0.47, 0.42,

VM : 0-40, and

U_r : 0-4.7.

In this study, horizontal cylinders were towed with steady velocity U toward the waves. This simulates that the current is in the direction of wave propagation, i.e., the current velocity is positive and is added to the wave-induced velocity.

Table 4-2. Test conditions for force measurements.

Cylinders	Periodic Waves			Waves Plus Towing		
	test conditions	No. of runs	No. of waves	test conditions	No. of runs	No. of waves
HSMC8	T=2.5,3.7,4.6, 5.3,6. sec. H=.8–4.7 ft. depends on T	50	3	———	—	—
HSRC.02	" "	17	7	T=4.6 sec. H=4.0 ft U=0–9.6 ft/sec.	22	3–7*
HBRC.2	" "	14	7	T=3.7 sec. H=3.5 ft U=.9–9.2 ft/sec	8	3–7*
HRAN	" "	14	7	T=3.7 sec. H 3.5 ft U=2.5–8.5ft/sec	8	3–7*

* depending on tow speed

Since cylinders were towed into waves, the period experienced by the cylinder is different from the actual wave period, T, and is called the apparent period, T_{ap}.

$$T_{ap} = \frac{T}{1 - \frac{U}{C}} \tag{4-1}$$

in which C is the wave celerity. Thus, the apparent wave period should be used in the dimensionless parameters K (Eq. 2-3) and VM instead of the actual period. However, the wave-induced kinematics must still be predicted by using the actual wave period (see Teng and Nath 1985).

5. FORCES ON HORIZONTAL CYLINDERS IN PERIODIC WAVES

In this chapter, the forces on horizontal cylinders in laboratory periodic waves are studied in several respects. First, the variations of measured forces, from wave to wave in a train of periodic waves, are examined. Then, the forces based on the Morison equation, the maximum and the rms forces, and the harmonic components of forces are studied. Finally, the forces between horizontal and vertical cylinders are compared.

In this study, because the water depth and cylinder elevation are fixed for all runs, the shape parameter, Ω, is mainly determined by the wave period, T. The nonlinearity of waves has a negligible effect on the determination of Ω. Herein, the runs with the same wave period are considered to have the same Ω. Note that values of $\beta(=D^2/T\nu)$ are also the same for runs with the same T. Thus, Ω and β are related. Table 5-1 presents the Ω and β values for the associated wave periods used in the present experiments.

Table 5-1. Values of Ω and β with respect to T.

T(sec.)	Ω	β*
2.5	0.85	1.47×10^4
3.7	0.67	0.99×10^4
4.6	0.55	0.80×10^4
5.3	0.47	0.69×10^4
6.0	0.42	0.61×10^4

*based on D = 8" and temperature = 50°F

5.1 Wave-to-Wave Variations of Forces

From flow visualization experiments (Chapter 3), it is observed that the wake and the vortex pattern may vary from wave to wave in a train of periodic waves. Accordingly, the flow induced forces in both the horizontal and vertical directions may vary from wave to wave. Besides, in the laboratory, waves can not be repeated perfectly in a train of periodic waves. For example, for the wave heights, the ratios of the standard deviation (σ) to the mean value (m) over a train of periodic waves in this study have values up to 3%. (Note that this ratio (σ/m) of measured forces will be used to show the wave-to-wave variation of forces.) In addition, there could be other un-identified or unknown reasons for wave-to-wave variation of forces, e.g., coherence effect.

Figures 5.1-1 and 5.1-2 show two records of wave profile and force measurements under 7 consecutive waves. From these two examples, it is clear that wave-to-wave variations exist for both amplitude and phase. In the following sections, the mean values of measurements of a record of 7 waves are used to quantify the force coefficients and their tendencies are studied at that time. (For the smooth cylinder, only 3 waves were recorded for each test run. See Table 4-1.)

In this section, the wave-to-wave variations of the maximum force, the root-mean-square (rms) force and the harmonic component of forces are examined to see whether there is any tendency for these variations. The standard deviation (σ) and the ratio of the standard deviation to the mean value (σ/m) of these forces are used to examine

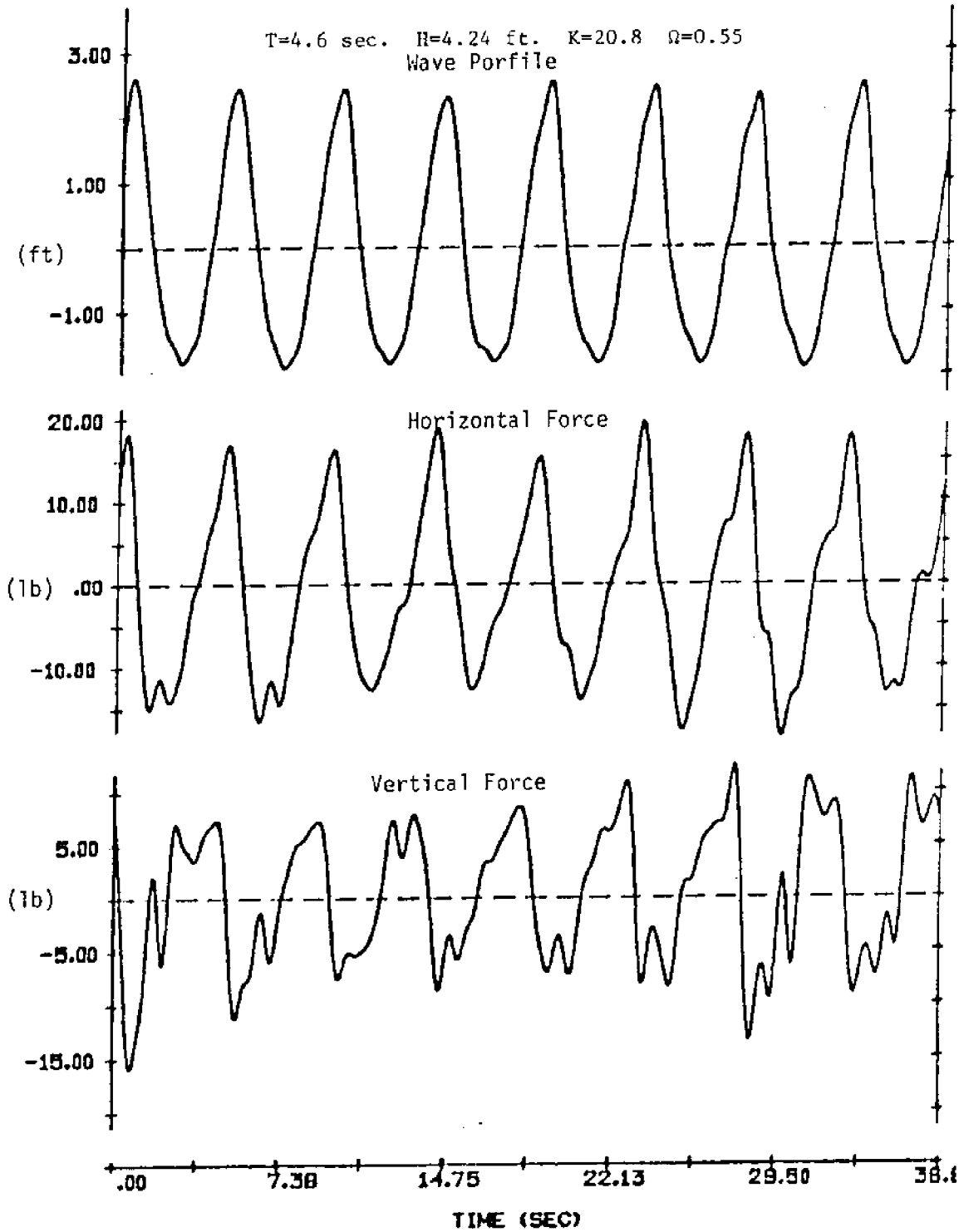

Fig. 5.1-1 Force measurements of a horizontal cylinder under 7 consecutive waves (T = 4.6 sec., H = 4.24 ft).

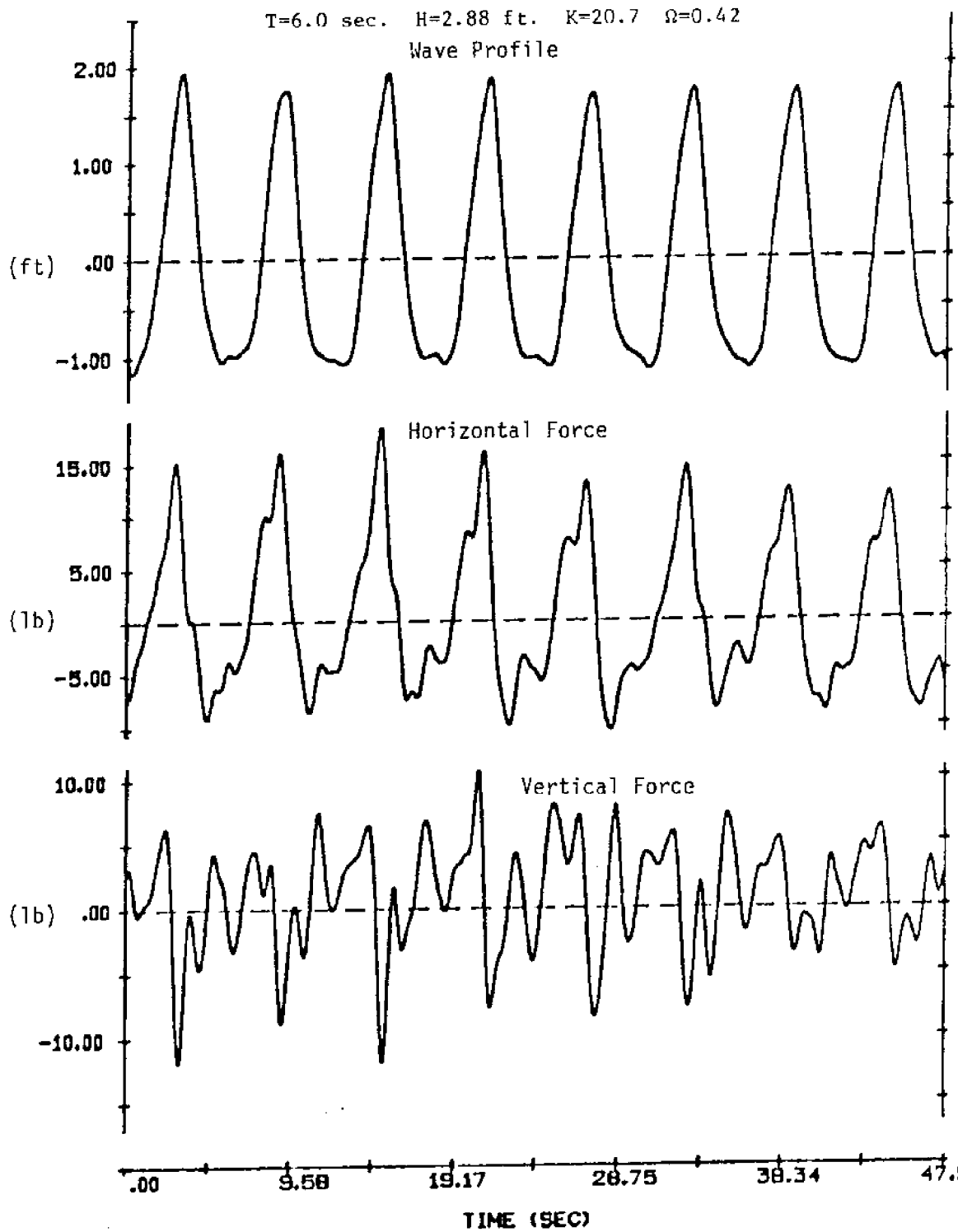

Fig. 5.1-2 Force measurements of a horizontal cylinder under 7 consecutive waves (T = 6.0 sec., H = 2.88 ft).

the variations. The mean values of these forces will be studied in Sections 5.3 and 5.4.

In this study, data for the smooth cylinder (HSMC8) only were recorded for 3 wave cycles. Thus, three roughened cylinders (HSRC.02, HBRC.2 and HRAN) with 7 waves data are used to analyze the variations.

Figures 5.1-3 and 5.1-4 present the σ/m values of the maximum force and rms force in both directions for the sand-roughened cylinder (HSRC.02). In Fig. 5.1-3, the variations of the maximum horizontal force (empty symbols) are all below 15%. No clear trend on Ω can be observed. The variations of the maximum vertical force (solid symbols) are higher and seem to increase as K increases or Ω decreases. Variations of rms forces in both directions (Fig. 5.1-4) are smaller than those of maximum forces. The σ/m values of rms vertical forces are all smaller than 0.24 and are higher than those of rms horizontal forces except the one with the smallest K and largest Ω. For larger K, the variations of horizontal rms forces are all below 10%.

For both rougher cylinders (HBRC.2 and HRAN), the trend is almost the same as that for the HSRC.02 as shown in Figs. 5.1-5 and 5.1-6 for the HRAN. One very important difference is that the variations for the rougher cylinder (HRAN) are clearly smaller than those for the HSRC.02. The results for the HBRC.2 (which are tabulated in Appendix B and not shown here for space saving) have the same trend.

The harmonic components of forces in the horizontal and vertical directions are calculated by using Fourier analysis described in

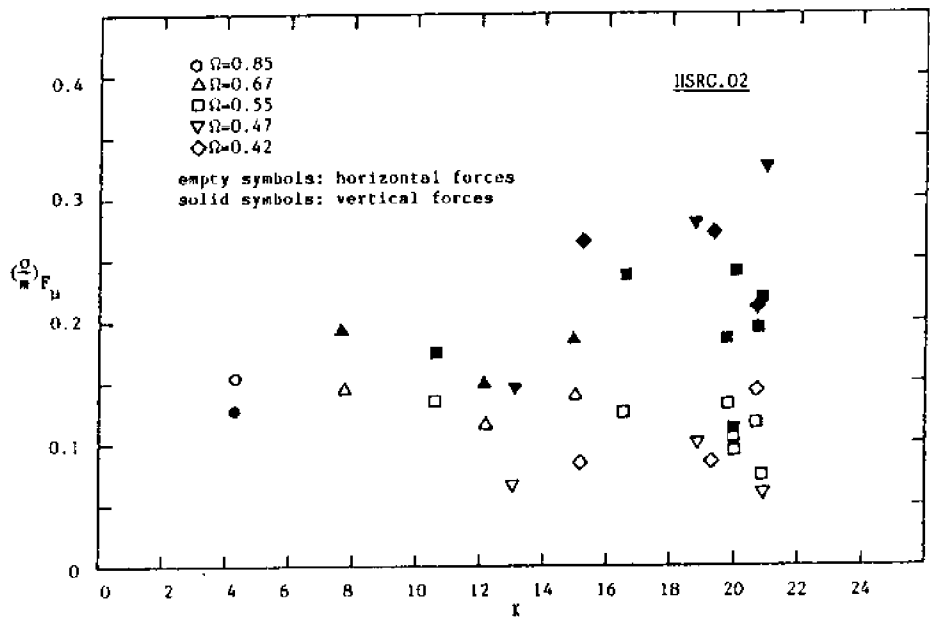

Fig. 5.1-3 σ/m values of maximum forces versus K for HSRC.02.

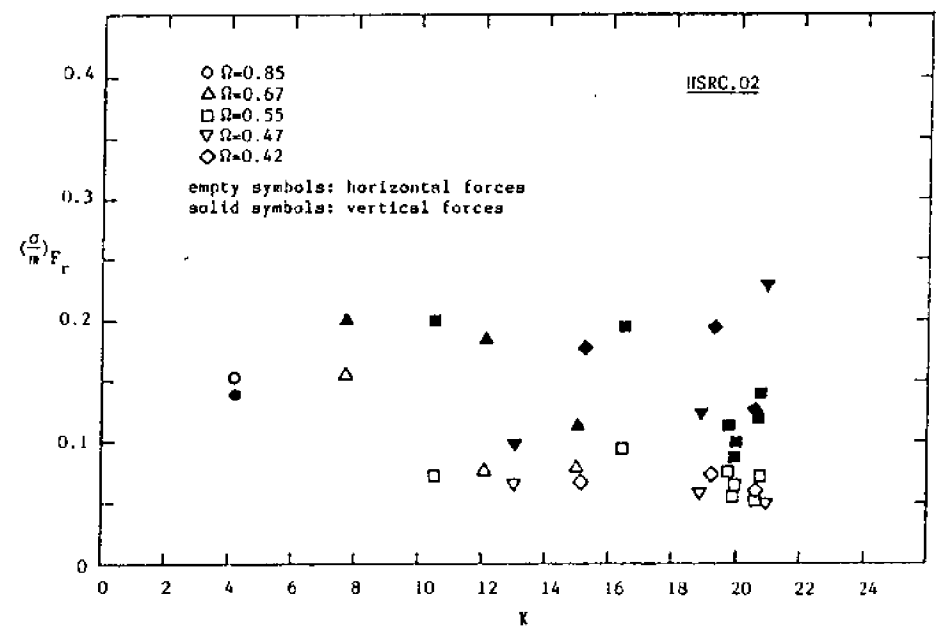

Fig. 5.1-4 σ/m values of rms forces versus K for HSRC.02.

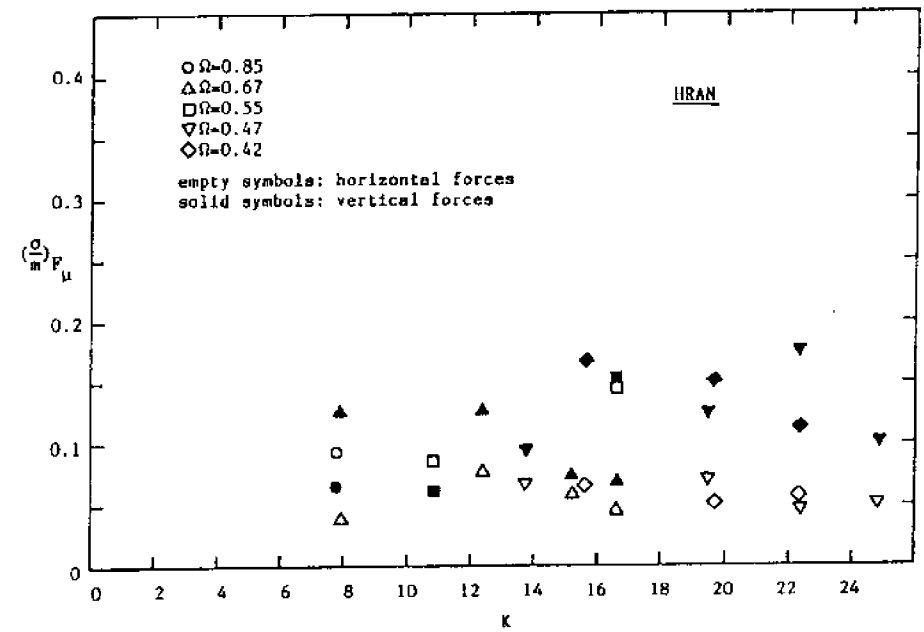

Fig. 5.1-5 σ/m values of maximum forces versus K for HRAN.

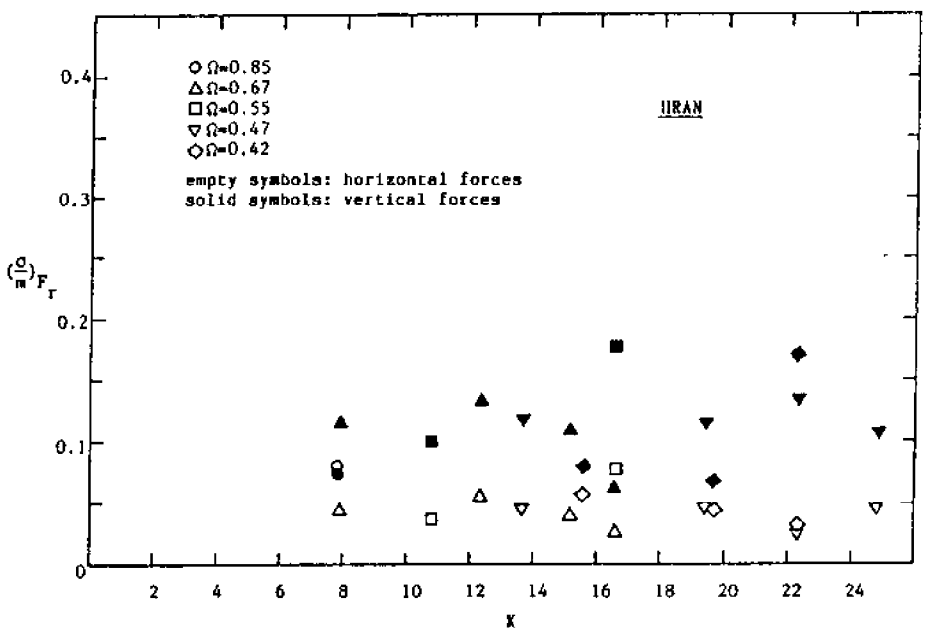

Fig. 5.1-6 σ/m values of rms forces versus K for HRAN.

Section 2.4. Their mean values will be studied in Section 5.4 and the wave-to-wave variations of each harmonic force are analyzed here. The σ/m values of the amplitude of the fundamental and the second harmonic forces for HSRC.02 and HRAN are plotted in Figs. 5.1-7 and 5.1-8, respectively. For large K, the σ/m values of the fundamental harmonic horizontal force for HSRC.02 and HRAN are less than 0.1. In the vertical direction, the σ/m values of the fundamental harmonic of forces are higher than those in the horizontal direction and the trend that variations with smaller Ω are greater than those with larger Ω is observed.

In Fig. 5.1-8, the σ/m values for the second harmonic forces are much higher than those for the first harmonic force and the values of variations in both directions seem to have the same order. The σ/m values of the second harmonic horizontal force for small $\Omega(< 0.47)$ are smaller than those for large $\Omega(> 0.55)$. This is true for all three roughened cylinders. Variations of the second harmonic vertical force do not have clear trend on Ω.

The standard deviations (σ) of the phase angles (see definition in Section 2.4) of the fundamental harmonic force in the horizontal and the vertical direction, $\phi_x(1)$ and $\phi_z(1)$, are shown in Fig. 5.1-9. The $\phi_x(1)$ values are all smaller than 10° and the $\phi_z(1)$ has greater variations (up to 20°). Combining the variations of phase angles with amplitude variations discussed above, it is concluded that the fundamental harmonic forces in the horizontal direction have less variation than those in the vertical direction. Furthermore, the phases for the second harmonic force are extremely scattered. Thus,

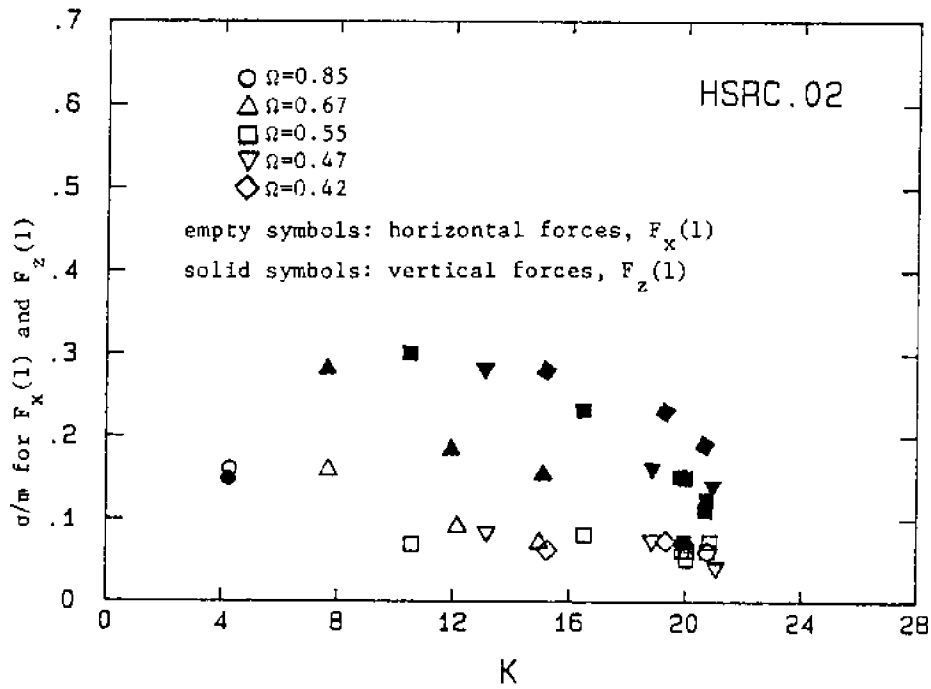

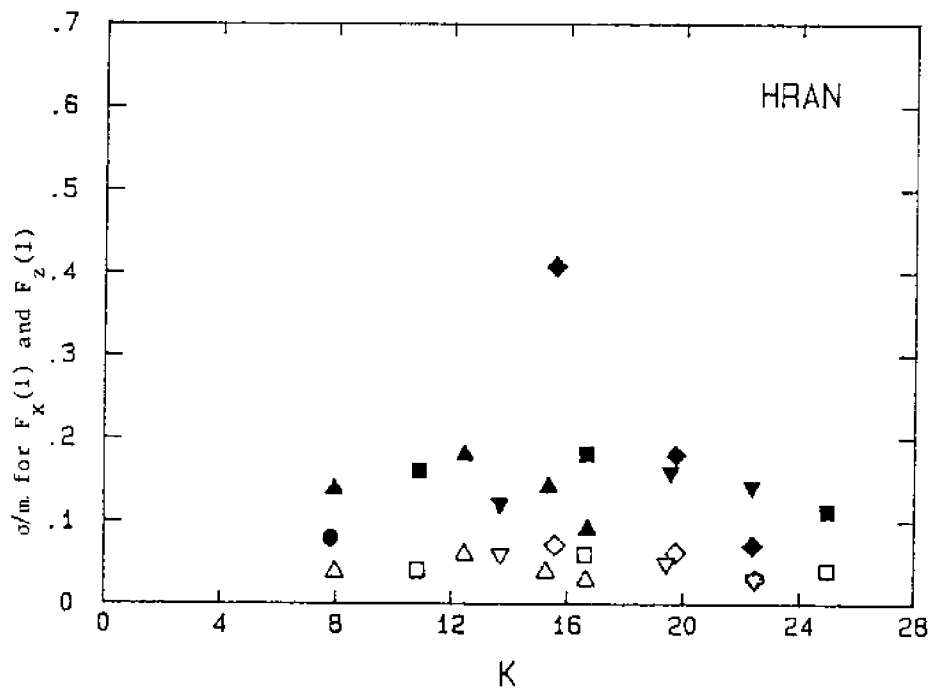

Fig. 5.1-7 σ/m values of the fundamental harmonic forces versus K for various Ω.

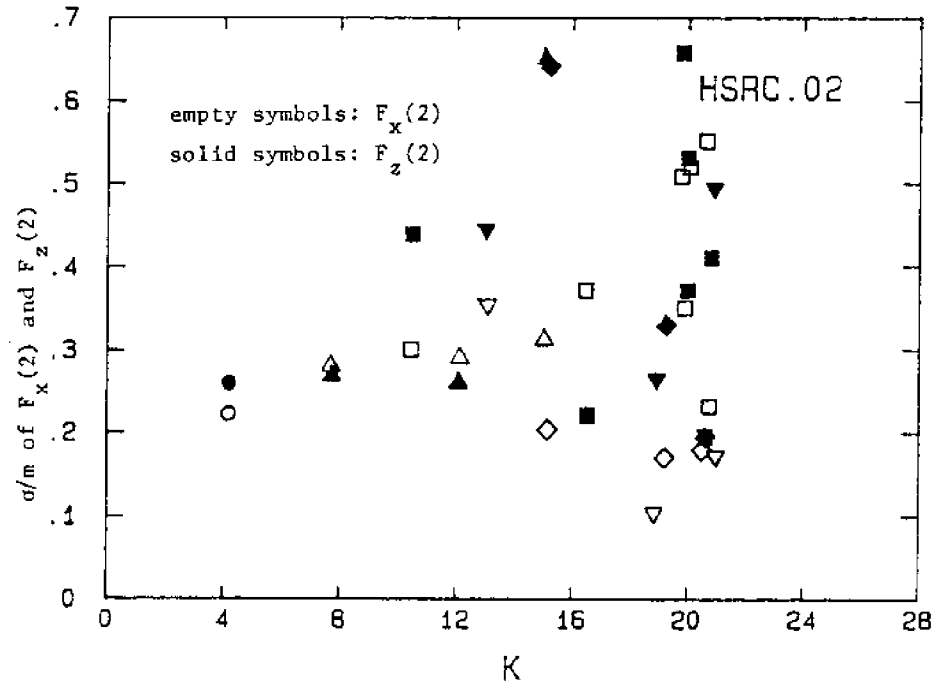

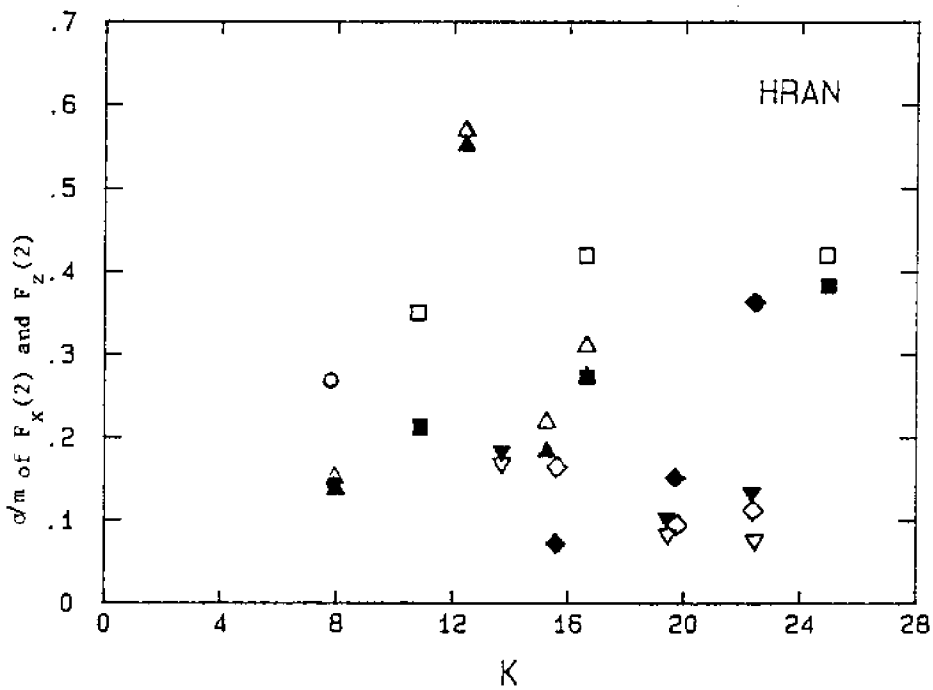

Fig. 5.1-8 σ/m values of the second harmonic forces versus K for various Ω.

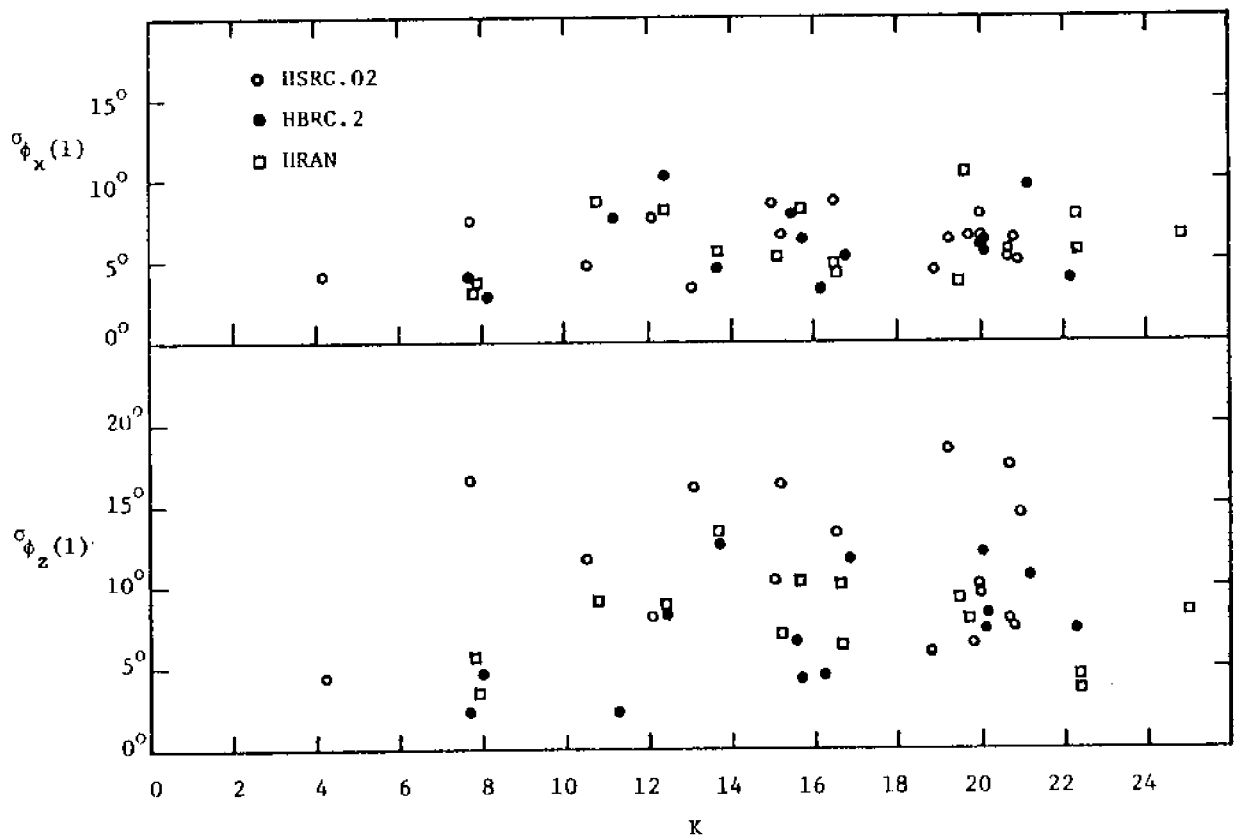

Fig. 5.1-9 Standard deviation of phase angles of the fundamental harmonic forces versus K for roughened cylinders.

the wave-to-wave variations of the second harmonic forces (both amplitude and phase) are much greater than those of the fundamental harmonic forces, especially for the phase. Since the second harmonic forces come mainly from the effect of vortex shedding, a relatively large amount of variations of forces comes from the vortex shedding phenomena.

From the flow visualizations in Chapter 3, the principle formation and movement of vortices are in the horizontal direction for a horizontal cylinder in waves. Thus, their induced forces are mainly in the vertical direction. Compared with the horizontal forces, the vertical forces contain more vortex-induced forces and less the first harmonic forces depending on Ω. It is one of the reasons that the variations of the maximum and rms forces in the vertical direction are greater than those in the horizontal direction as shown in Figs. 5.1-3 to 5.1-6 (because the vortex-induce forces contain more variations).

Besides the wave-to-wave variation of measured forces, Nath (1986) examined the variability of force coefficients, C_d and C_m, from wave to wave for vertical cylinders in waves. He reported that the wave-to-wave variation of C_d and C_m is probably due to subtle differences in the phase between the ambient flow conditions and the force measurements, which are due to the vagaries of vortex shedding.

According to the above discussions, the wave-to-wave variation of forces from the present data has the following characteristics:

(1) The vortex shedding phenomena have great contribution to the wave-to-wave variation of forces.

(2) The variation of the horizontal force is smaller than that of the vertical force, partly because the vortex shedding effect in the horizontal direction is smaller than in the vertical direction.

(3) The variations of forces for the rougher cylinders (HBRC.2 and HRAN) are smaller than those for the sand-roughened cylinder (HSRC.02).

(4) In general, as Ω decreases, the variation of horizontal forces decreases and the variation of vertical forces increases.

In spite of the variations discussed in this section, the mean values of forces are used and studied in the later sections.

5.2 Forces Predicted by The Morison Equation

The force coefficients, C_d and C_m, for the HSMC8, HSRC.02, HBRC.2 and HRAN are shown in Figs. 5.2-1 to 5.2-4. The results for the smooth cylinder have considerable scatter. However, it seems that C_d values with the smallest shape parameter (Ω=0.42) are greater than those with larger Ω. Bearman, et al. (1985a) also presented the values of C_d and C_m for a smooth horizontal cylinder in waves from a larger wave tank. The upper and lower bound of their data are shown as dashed lines in Fig. 5.2-1. In spite of the similar scatter, their C_d values are in the same range of the present data and C_m values are a little higher. The possible reason for the difference is the different β values between these two studies. The β values for Bearman, et al.'s data are higher than those for the present

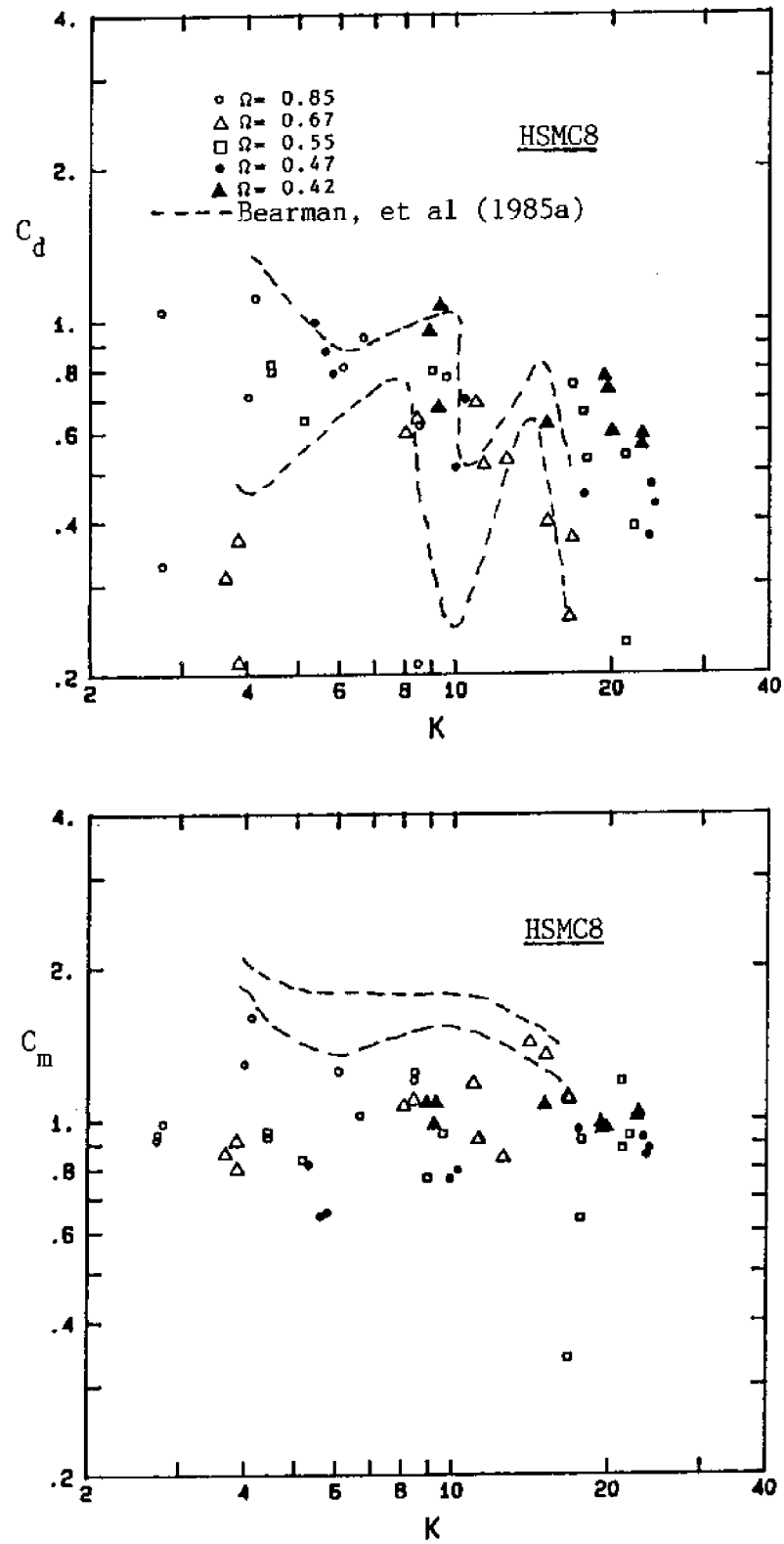

Fig. 5.2-1 C_d and C_m versus K with various Ω for HSMC8 in periodic waves.

data. For planar oscillatory flow (Ω=0), Sarpkaya (1976) also showed that the C_m values were higher for larger β values.

The force coefficients for roughened cylinders shown in Figs. 5.2-2 to 5.2-4 have fewer data points and seem to have less scatter. The data with smaller Ω are greater than those with large Ω, especially for C_m and smallest Ω. Both C_d and C_m increase as the relative roughness, e/D, increases. Note that the smooth cylinder diameter is used to evaluate force coefficients for roughened cylinders here. If the effective diameters (see Section 4.2.) are desired to use, the C_d values should be divided by the effective diameter factor δ (Table 4-1) and the C_m values are divided by δ^2.

By examining the force traces of measured data and values predicted by the vector form of the Morison equation with the best fitted C_d and C_m, it seems that the vector form of the Morison equation can not predict the forces on a horizontal cylinder (both the phase and magnitude) quite well, especially for large K and small Ω. Figures 5.2-5 and 5.2-6 show two examples of the comparison between measured and predicted forces.

To examine the forces predicted by the vector form of the Morison equation, the root-mean-squared error, which is defined as Eq. (5.2-1), and the ratio of the maximum predicted total force to the maximum measured total force $[(F_p)_\mu/(F_m)_\mu]$ are used.

$$E_{rms} = \frac{\sqrt{\frac{1}{T}\int_0^T [(F_{xm} - F_{xp})^2 + (F_{zm} - F_{zp})^2]dt}}{(F_\mu)_{measured}} \qquad (5.2\text{-}1)$$

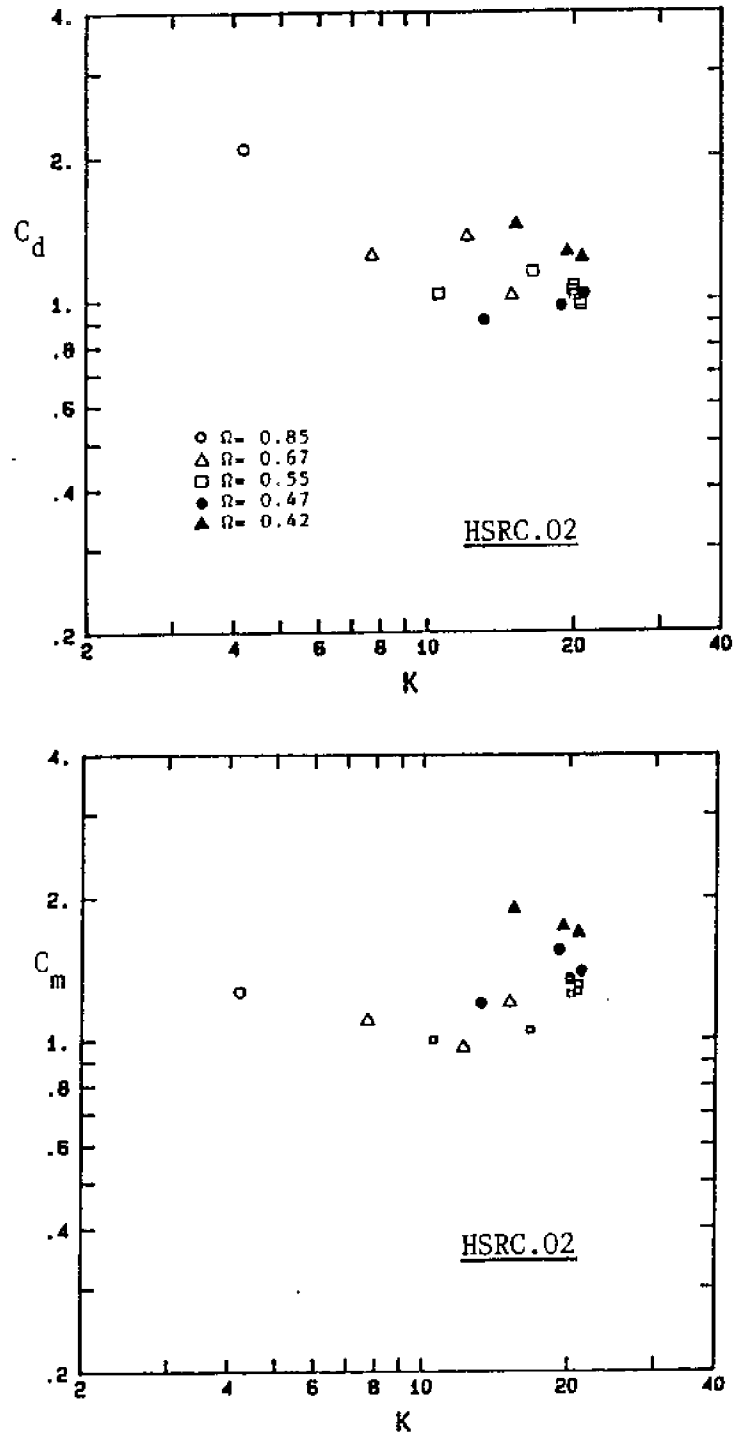

Fig. 5.2-2 C_d and C_m versus K with various Ω for HSRC.02 in periodic waves (all values based on the smooth cylinder diameter).

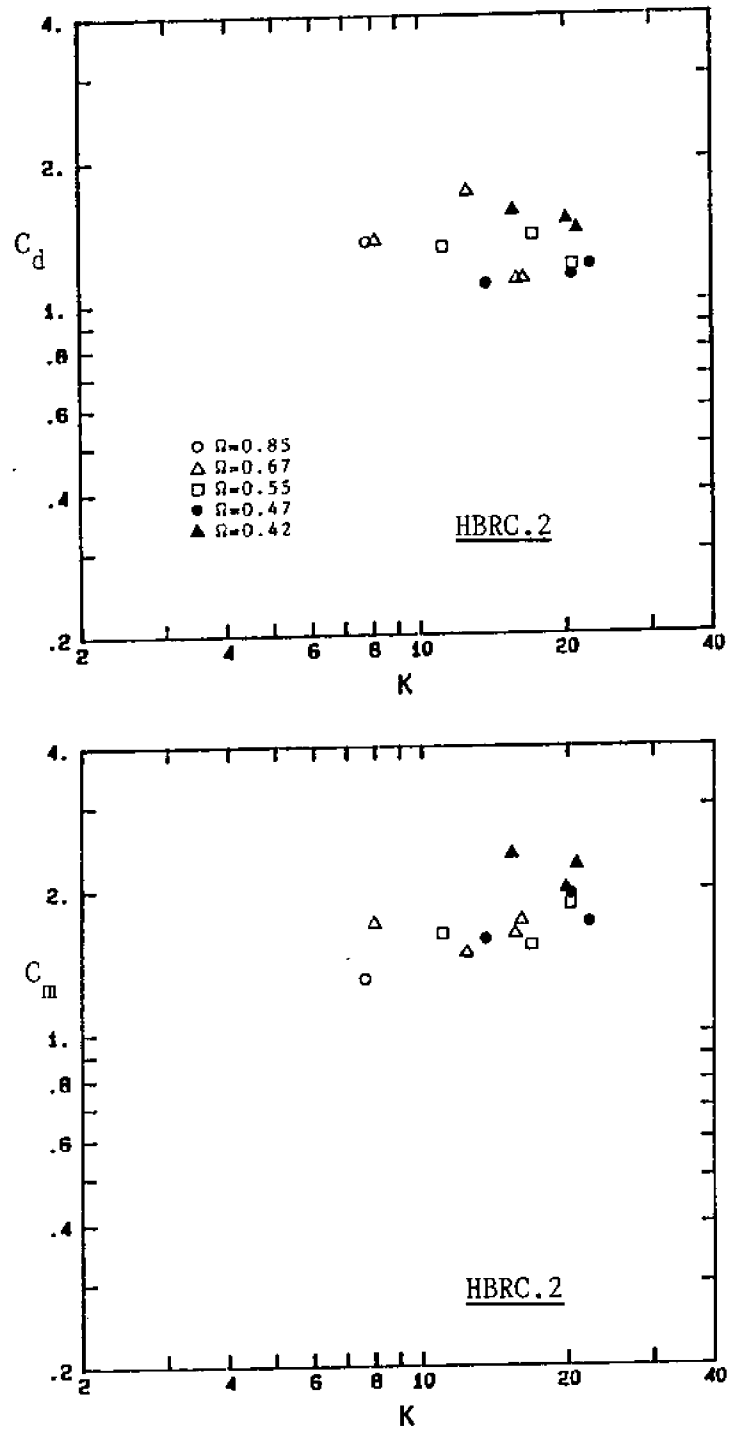

Fig. 5.2-3 C_d and C_m versus K with various Ω for HBRC.2 in periodic waves (all values based on the smooth cylinder diameter).

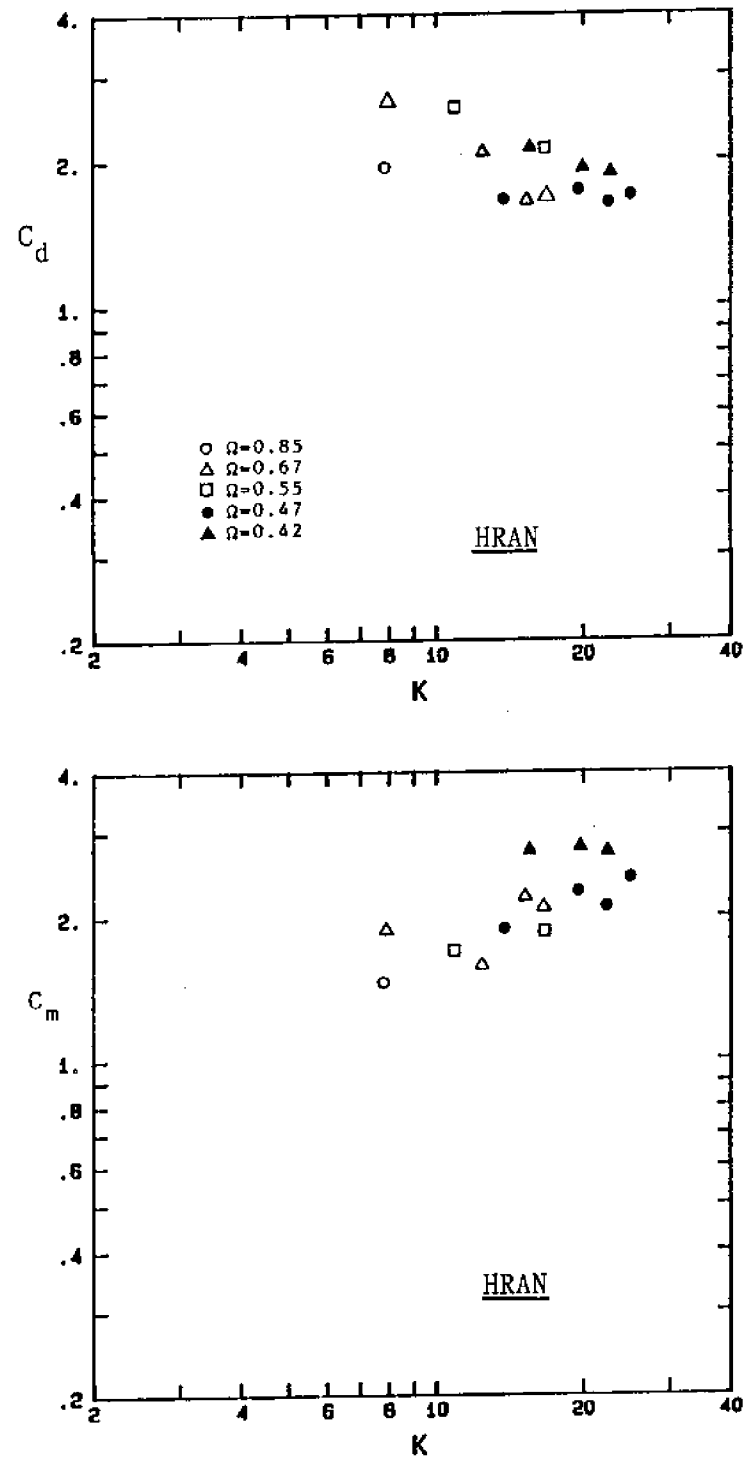

Fig. 5.2-4 C_d and C_m versus K with various Ω for HRAN in periodic waves (all values based on the smooth cylinder diameter).

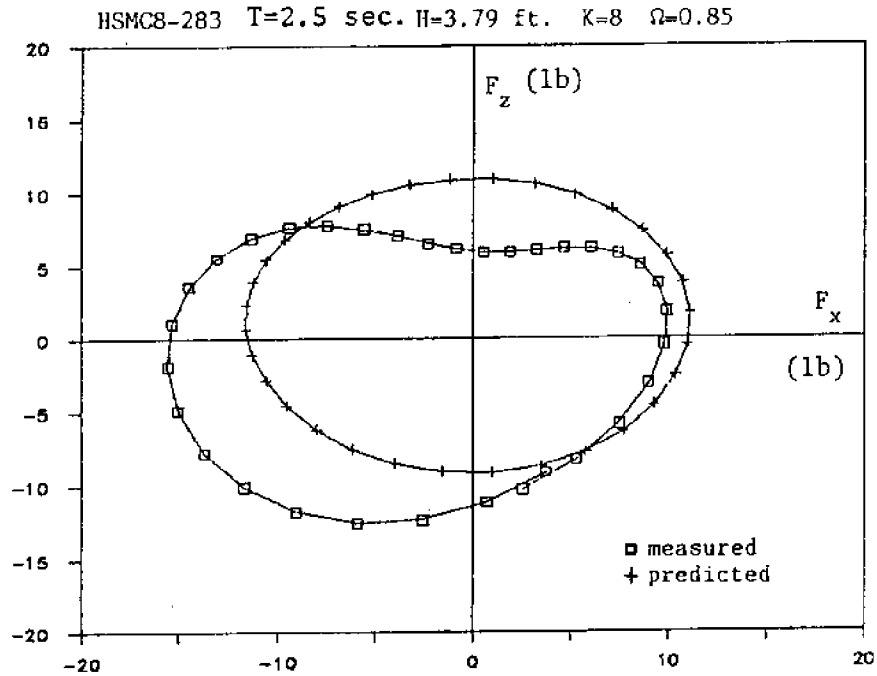

Fig. 5.2-5 Comparison between measured and predicted forces for K=8 and Ω=0.85.

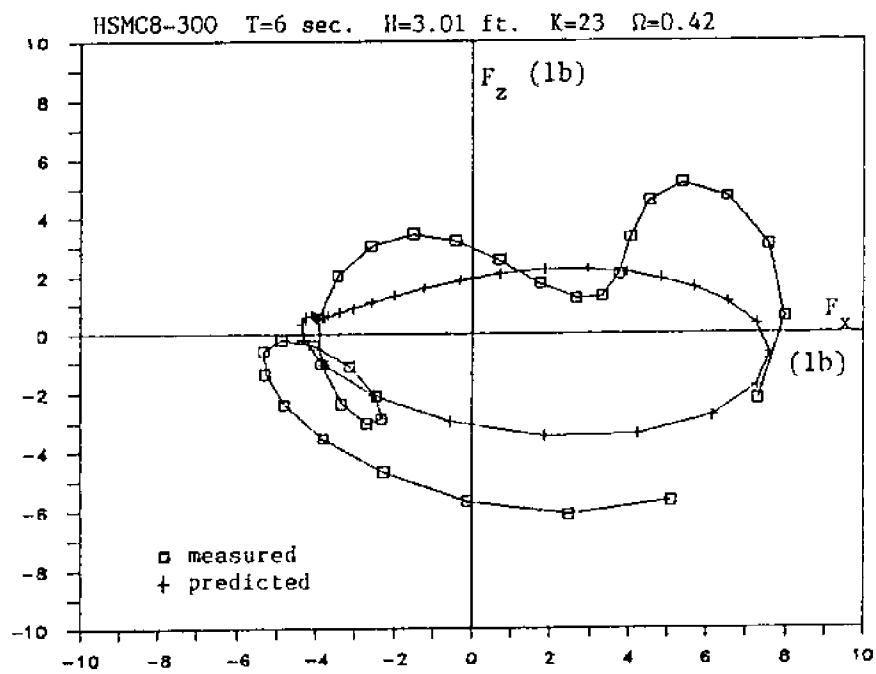

Fig. 5.2-6 Comparison between measured and predicted forces for K=23 and Ω=0.42.

in which F_{xm} is the measured horizontal force, F_{xp} is the predicted horizontal force, F_{zm} and F_{zp} are the vertical measured and predicted forces, and $(F_{\mu})_{measured}$ is the maximum total (horizontal + vertical) measured force.

Table 5-2 shows the range, mean and standard deviation of these two parameters over all the test runs for each test cylinder. From this table, the Morison equation underpredicted the maximum total force and generated relatively large root-mean-square errors. Also, it seems that predictions for the roughened cylinders are a little better than those for the smooth cylinder.

The main weakness of the vector form of the Morison equation in predicting forces on a horizontal cylinder in waves is the lack of a term to take the force due to the vortex shedding into account. Thus, when determining C_d and C_m, this vortex induced force is introduced into the drag and inertia term as noise and makes the force coefficient scattered. From flow visualization experiments (Chapter 3) and Section 5.1, the vortex shedding affects the vertical force more severely than the horizontal force. Thus, predictions of forces in the vertical direction are usually worse than those in the horizontal direction. One extreme example is the prediction for Ω=0. Under this condition, the horizontal force can be predicted by the Morison equation quite well, but the vertical force, which now is mostly an asymmetric vortex-induced force, cannot be predicted by this equation at all.

As mentioned in section 1.2.2, the vortex-induced force (with unknown magnitude, angle and sign) on a horizontal cylinder in waves

Table 5-2. rms error and maximum force ratio for forces predicted by the vector form of the Morison equation in waves.

test cylinder	E_{rms} (rms error)			$(F_p)_\mu / (F_m)_\mu$		
	range	mean	standard deviation	range	mean	standard deviation
Smooth Cylinder (HSMC8)	0.14-0.44	0.303	0.062	0.66-0.97	0.79	0.08
Sand Cylinder (HSRC.02)	0.20-0.35	0.259	0.034	0.69-0.93	0.82	0.06
Barnacle Cylinder (HBRC.2)	0.16-0.30	0.217	0.043	0.72-1.00	0.88	0.07
Anemone Cylinder (HRAN)	0.21-0.26	0.222	0.031	0.80-0.99	0.88	0.06

is mixed with the drag and inertia force. Generally, it is almost impossible to separate the vortex induced force from the drag and inertia force. However, for $\Omega=0$ (cylinders in shallow water waves or planar oscillatory flow), the vortex induced transverse force is independent of the in-line (drag and inertia) force that is predicted by the Morison equation. In this case, the drag and the inertia force associated with the force coefficients will not be contaminated by the vortex-induced transverse force. That is the main reason why the reported data for $\Omega=0$ (e.g. Sarpkaya 1976, Chakrabarti 1980) possess less scatter and the in-line force can be predicted better than those for the present study ($0 < \Omega < 1$) and those from Bearman, et al. (1985a).

If the vector form of the Morison equation is used, only a relatively small amount of second harmonic forces can be predicted due to the nonlinearity of the flow. Figures 5.2-7 and 5.2-8 show the spectral plots of the measured forces, related to the time plots of Figs. 5.2-5 and 5.2-6, for the smooth cylinder. From these two examples, it is clear that both the second harmonics of the horizontal and vertical force are relatively significant. In other words, the vector form of the Morison equation fails to predict the second harmonic forces which are thought to be mainly due to the vortex shedding phenomena. The significance of the second harmonics will be studied in detail in Section 5.4.2.

From the results of the flow visualization experiments, it is clearly observed that the rotation of the wake around a horizontal cylinder in waves is not always synchronized with the velocity

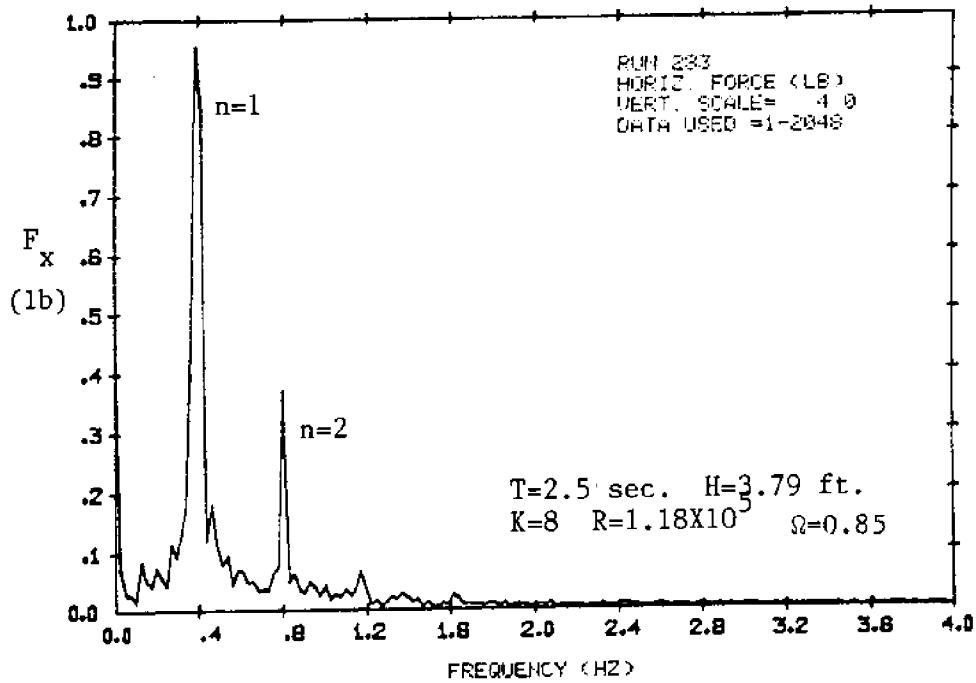

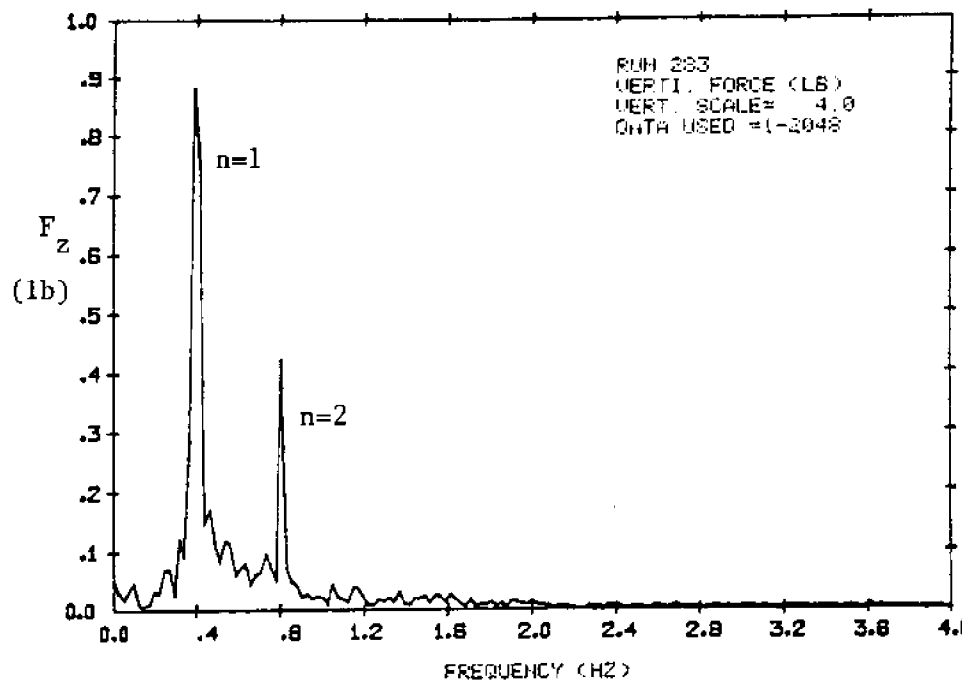

Fig. 5.2-7 Spectra of measured forces for HSMC8 in waves for K=8 and Ω=0.85.

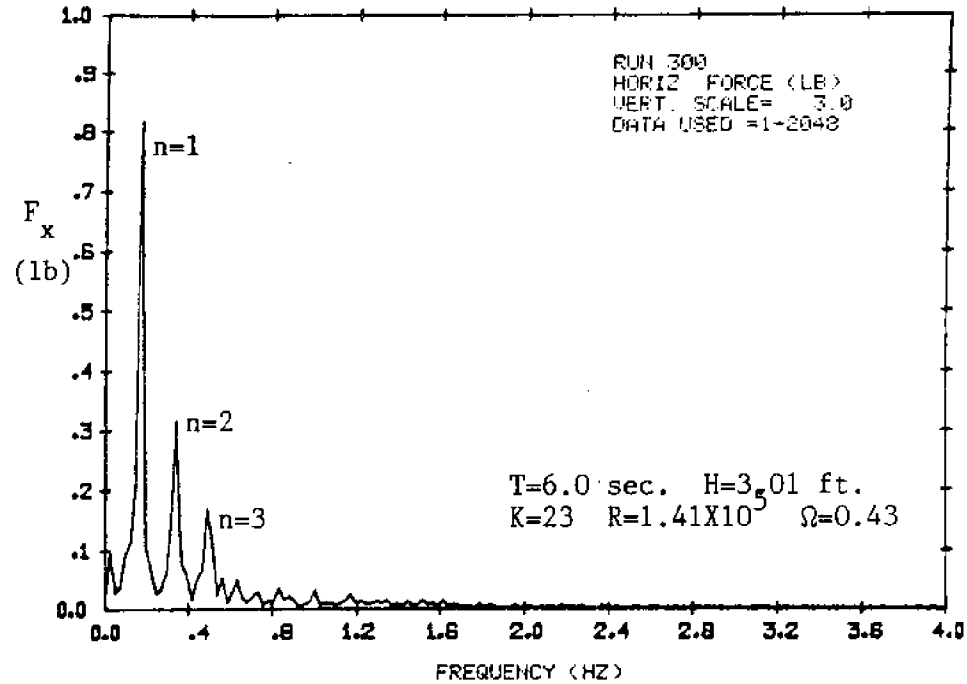

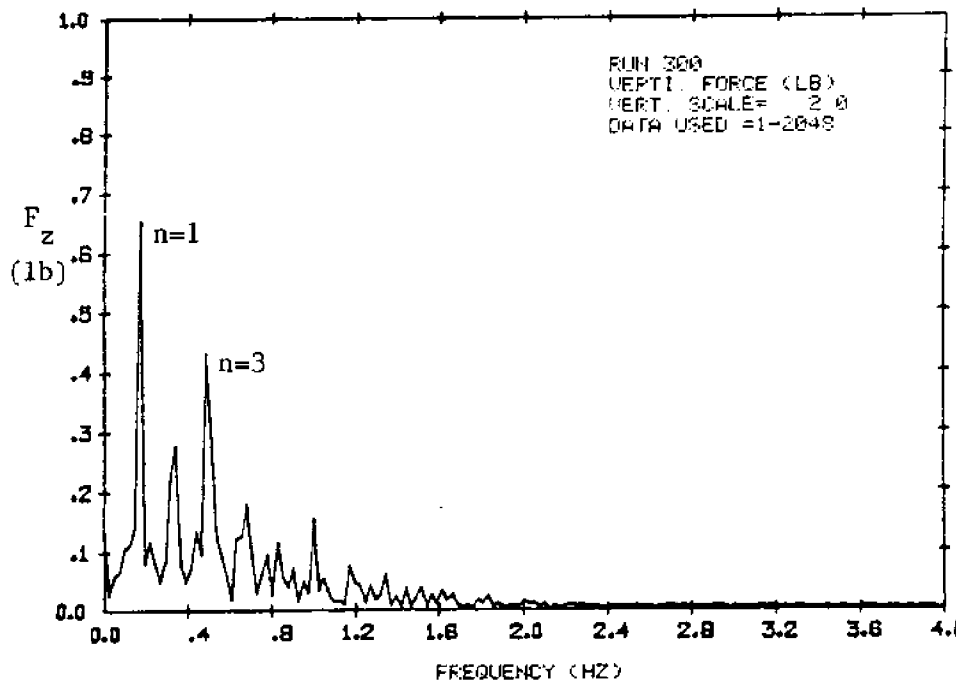

Fig. 5.2-8 Spectra of measured forces for HSMC8 in waves for K=23 and Ω=0.43.

vector. For small Ω, the wakes do not truly rotate around the cylinder. They just fluctuate in a small region on one side of the cylinder due to the relatively small vertical velocity during the first half cycle of the wave motion and then fluctuate in a small region on the other side of the cylinder during the second half cycle. Similar results can be found from the flow visualization experiments of Maull and Norman (1979). Chaplin (1984) and Grass, et al. (1984) also concluded that there is a time lag between the rotation of the wakes and the velocity vector.

The vector form of the Morison equation assumes the force on a horizontal cylinder is the vector combination of drag force (which is in-line with the velocity vector) and inertia force (which is in-line with the acceleration vector). Due to the lag and un-synchronization between the wake rotation and the velocity vector, the vector form of the Morison equation can not accurately describe the drag and inertia force. As sketched in Fig. 5.2-9, when the rotation of the wake and the velocity vector are not synchronized, the instantaneous drag force (mostly form drag due to the wake) will have a component perpendicular to the velocity vector. This component will be counted as the inertia force instead of the drag force according to the vector form of the Morison equation and will contaminate the determination of force coefficients.

Rodenbusch and Gutierrez (1983) used the forces projected in the instantaneous velocity direction (that include all the drag force and a portion of the inertia force) and the least square technique to determine C_d and C_a ($=C_m-1$) for horizontal cylinders in orbital

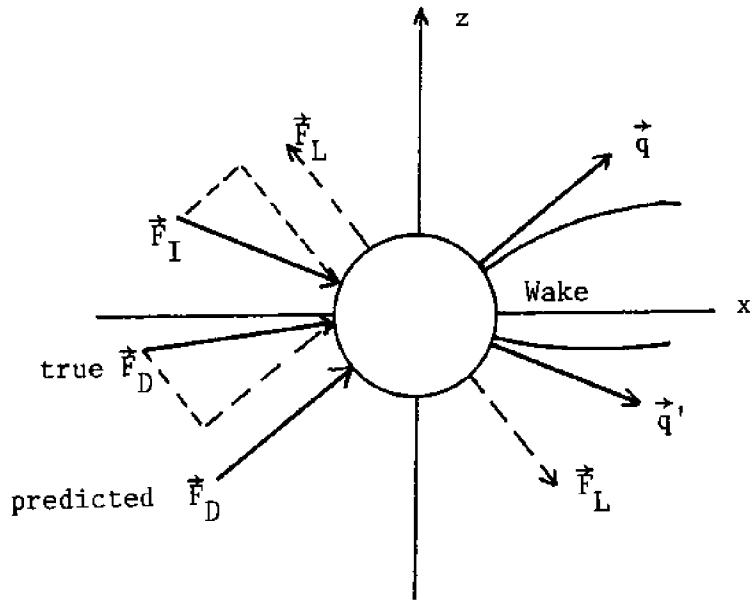

Fig. 5.2-9 Forces and kinematics on a horizontal cylinder in periodic waves.

oscillatory flow (see Section 1.2.2 for more details). Due to the unsynchronization between the velocity vector and the wake, the C_d and C_m they obtained should be contaminated more or less as discussed above and shown in Fig. 5.2-9.

From the above discussion, it may be concluded that the vector form of the Morison equation underpredicts the maximum force on a horizontal cylinder up to 20% and produces rms errors of from 15% to 40% due to the lack of a term taking the vortex induced force into account and due to the unsynchronization between the wake and the velocity vector. Because of the above weaknesses, even if good correlations between forces coefficients and governing parameters are obtained, the force predictions (both amplitude and phase) by using the vector form of the Morison equation will not be much better in a wide range of conditions. For example, if the correlation between parameters (K and Ω) and force coefficients (C_d and C_m) is very good in Fig. 5.2-1, the prediction of forces shown in Fig. 5.2-5 and Fig. 5.2-6 will not improve too much.

However, the vector form of the Morison equation is widely used in the practical engineering design and research work. From an engineering point of view, this equation is still an acceptable approximation providing an appropriate factor of safety is also applied in order to approximate the maximum forces well, on a statistical basis.

Sarpkaya (1984) and Grass, et al. (1984) calculated C_d and C_m from the horizontal force (they called it in-line force) of a horizontal cylinder in simulated orbital flow (see Section 1.2.2 for details). Their C_d and C_m cannot be compared directly with the

present data because the present data are obtained from the total (horizontal and vertical) force. It is known that the vertical force sometimes has the same magnitude as the horizontal force, depending on Ω. Thus, it is very important to consider the vertical force and include it into the total force.

Grass, et al. (1984) and Chaplin (1985b) oscillated a cylinder in an elliptic or circular path in still water to simulate a horizontal cylinder in waves (see Section 1.2.2). One very important difference between these simulations and large, real wave conditions is the nonlinearity of the waves. Besides, in the real waves, the wake and vortices rotate more or less around the cylinder as observed in the flow visualizations (Chapter 3) for a large enough Ω. That means that the wake encounter effect is weak, especially for deep water waves. But, for a cylinder oscillating elliptically in still water, the cylinder will encounter its own wake or vortices due to its own motion in the still water. These differences could cause the difference of the induced forces between these two cases.

5.3 Maximum and Root-Mean-Square Forces

From the last section and Table 5-2, it is shown that the vector form of the Morison equation underpredicts the maximum force and generates large rms error. The maximum force and the root-mean-square (rms) force are very important for the practical engineering design. In this section, these two forces will be studied directly from the measured forces. Besides their importance in design, these two values have the advantage that they are relatively insensitive to the phase or phase shift between two different components. It is well

known that the C_d and C_m in the Morison equation are very sensitive to the phase (see Nath 1986) and, thus, they always have considerable scatter.

The rms force coefficients in the horizontal and in the vertical direction, the total rms coefficient, and the maximum total force coefficient are designated as C_{xr}, C_{zr}, C_{tr} and C_{μ}, respectively, and are defined in the following.

$$C_{xr} = \frac{F_{xr}}{\frac{1}{2}\rho DLu_r^2} \tag{5.3-1}$$

$$C_{zr} = \frac{F_{zr}}{\frac{1}{2}\rho DLu_r^2} \tag{5.3-2}$$

$$C_{tr} = \frac{(F_{xr}^2 + F_{zr}^2)^{1/2}}{\frac{1}{2}\rho DL(u_r^2 + w_r^2)} \tag{5.3-3}$$

$$C_{\mu} = \frac{F_{\mu}}{\frac{1}{2}\rho DLu_{\mu}^2} \tag{5.3-4}$$

in which the subscripts μ and r represent the maximum and the root-mean-square value respectively. The F_{μ} is the maximum of the total force (the vector sum of the horizontal and vertical force). Because the above coefficients all contain the first power of the diameter, D, in the denominators, the coefficients are modified by dividing the effective diameter factor, δ, (see Table 4-1 for δ values for roughened cylinders) if the effective diameters are desired to be used.

Figures 5.3-1 to 5.3-4 present the above coefficients versus K for the smooth cylinder (HSMC8) in waves. In Fig. 5.3-1, the C_{xr}

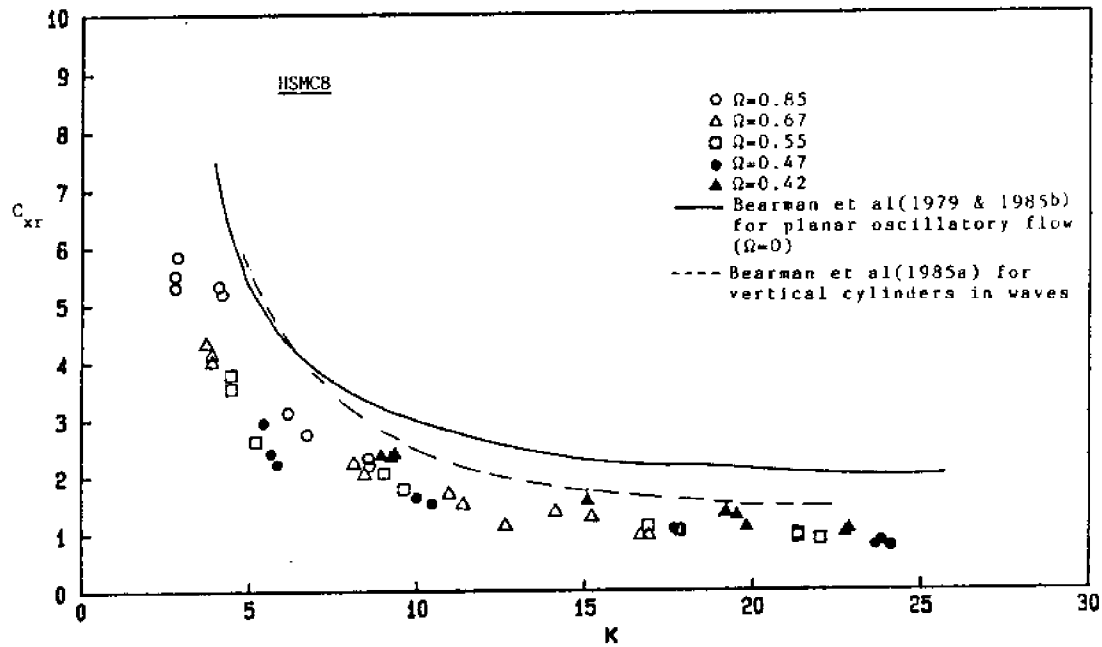

Fig. 5.3-1 C_{xr} versus K for various Ω for HSMC8 in waves.

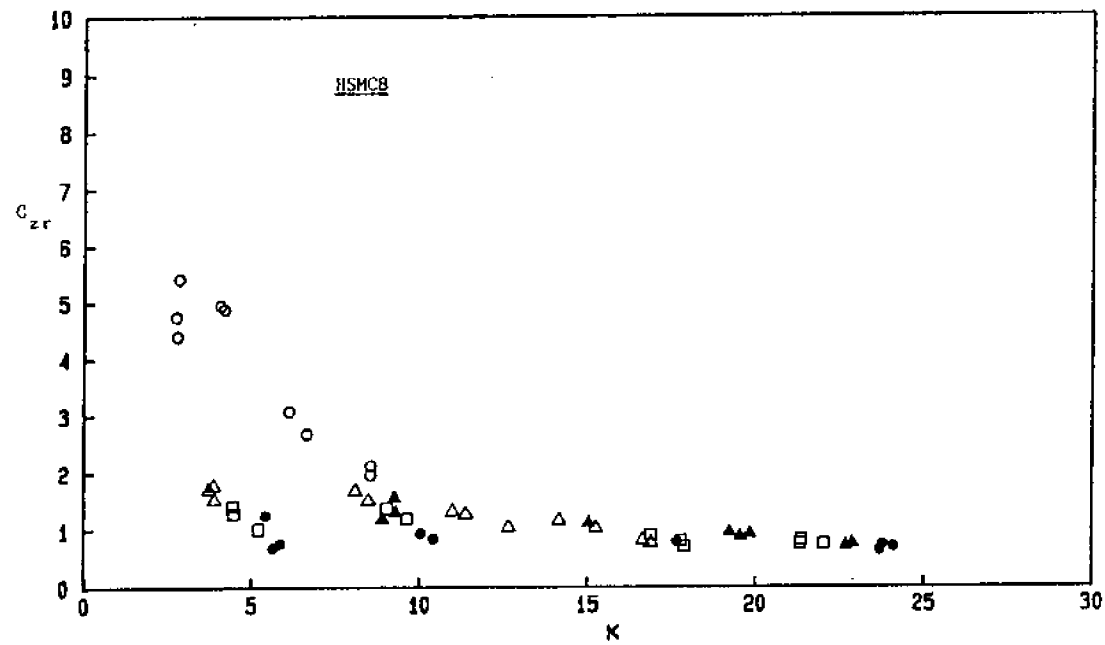

Fig. 5.3-2 C_{zr} versus K for various Ω for HSMC8 in waves.

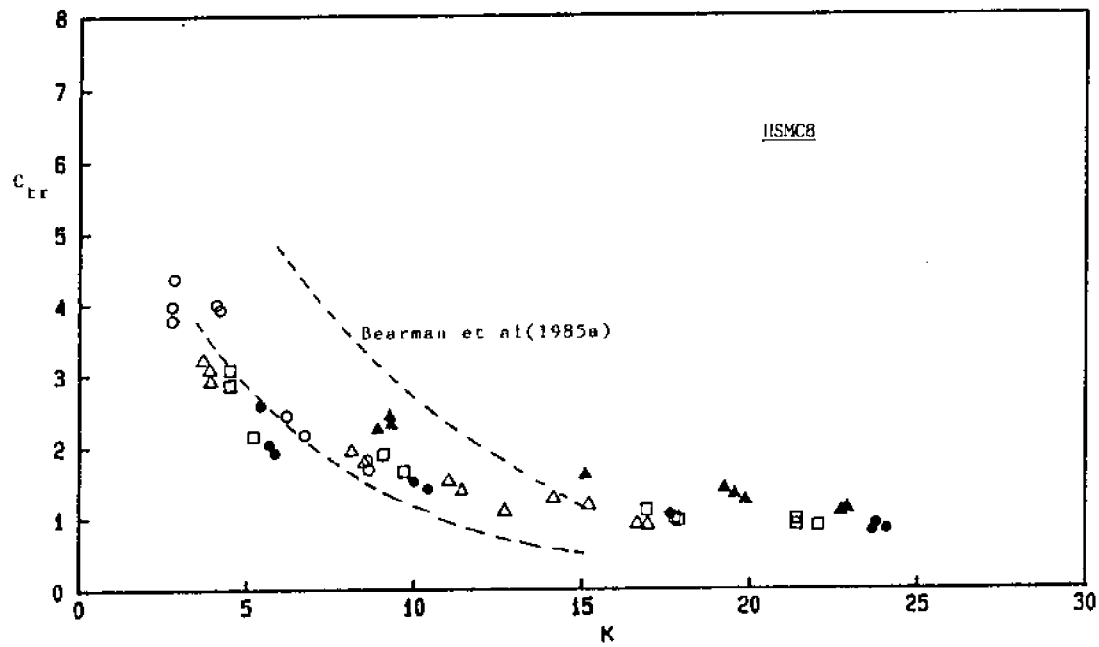

Fig. 5.3-3 C_{tr} versus K for various Ω for HSMC8 in waves.

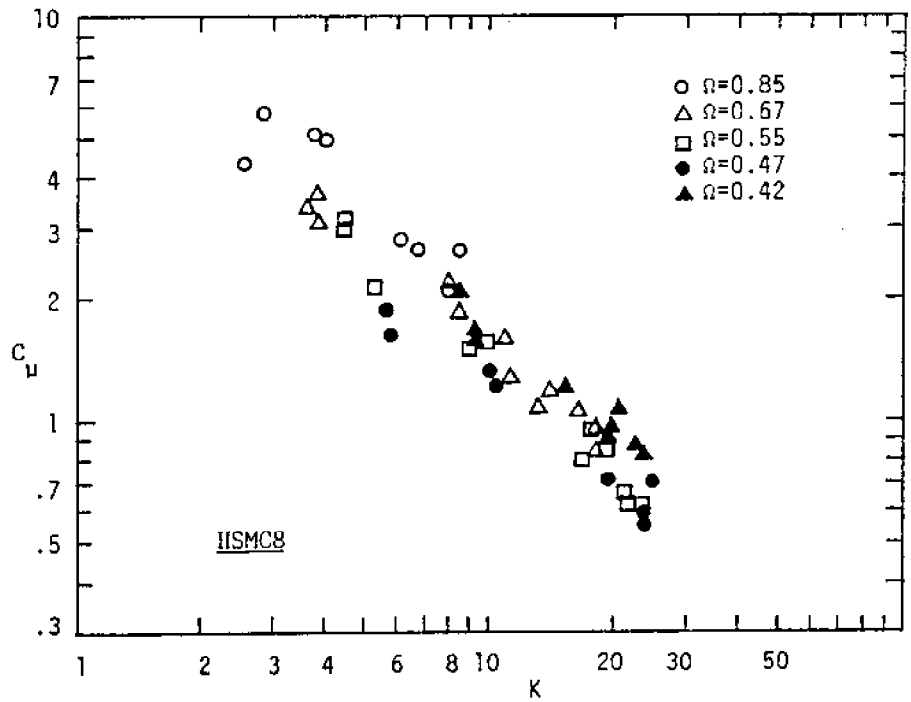

Fig. 5.3-4 C_μ versus K for various Ω for HSMC8 in waves.

fits well with K. The values of C_{xr} with the smallest Ω(=0.42, solid triangles) are higher than the rest of the data. For $\Omega > 0.42$, the trend of C_{xr} on Ω is not distinguishable. The solid line represents the values of C_{xr} from Bearman et al. (1979 and 1985b) for planar oscillatory flow (Ω=0) and the dashed line is the C_{xr} from Bearman, et al (1985a) for vertical cylinders in waves. The differences between cylinders in planar oscillatory flow and vertical cylinders in waves were discussed in Section 1.2.1. The present data for a horizontal cylinder in waves are smaller than those for planar oscillatory flow (Ω=0) and vertical cylinders in waves. It is believed that the values of C_{xr} for $\Omega \neq 0$ approach those for Ω=0 as Ω approaches 0.

For C_{zr}, all data match well for $K > 10$. For $K < 10$, the data for the largest Ω(=0.85, open circles) are clearly higher than those with smaller Ω. It is reasonable because the vertical velocity is relatively large for larger Ω and the vertical force increases accordingly. Comparing C_{xr} with C_{zr}, the former is a little larger than the latter for $K > 10$. For $K < 10$, the difference increases with decreasing K for Ω smaller than 0.85. The reason is that, for small K and Ω, the vertical velocity is too small to make the wake move in the vertical direction and the form drag in the vertical direction is small. Because the vertical velocity almost has the same order as the horizontal velocity for Ω=0.85, the difference between C_{xr} and C_{zr} is small, even for small K.

The total rms force coefficient, C_{tr}, has the same trend as C_{xr} and the tendency that the values for the smallest Ω(=0.42) are higher

is clearer for C_{tr} than that for C_{xr}. In Fig. 5.3-3, the two dashed lines represent the upper and lower bound of the data from Bearman et al. (1985a). The present data fit their data for $K > 5$, but are lower for $K < 5$. Again, the difference is probably due to the different β values as discussed in Section 5.2.

In Fig. 5.3-4, the maximum total force coefficient, C_μ, correlates with K and does not have clear trend on Ω. Note that C_μ includes the vortex-induced force which contains great variations in both amplutides and phases (as discussed in Section 5.1).

Due to limitations of experiments, the smallest Ω obtained in the present study is 0.42. This value is not small enough to make the flow approach planar oscillatory flow (i.e. Ω=0). It is believed that the data would approach those for planar oscillatory flow if Ω approaches zero.

Figures 5.3-5 to 5.3-8 show the above four force coefficients against K for three roughened horizontal cylinders (HSRC.02, HBRC.2 and HRAN).

The values of C_{xr} (Fig. 5.3-5) and C_{tr} (Fig. 5.3-7) increase significantly as the relative roughness (e/D) increases. If the effective diameter is used instead of the smooth diameter, the values for those with larger relative roughness are still higher. This shows the effect of roughness on forces (force coefficients). The trend that the values of Cxr and Ctr with smallest Ω(=0.42, solid triangles) are higher than the rest of the data is clearer for roughened cylinders.

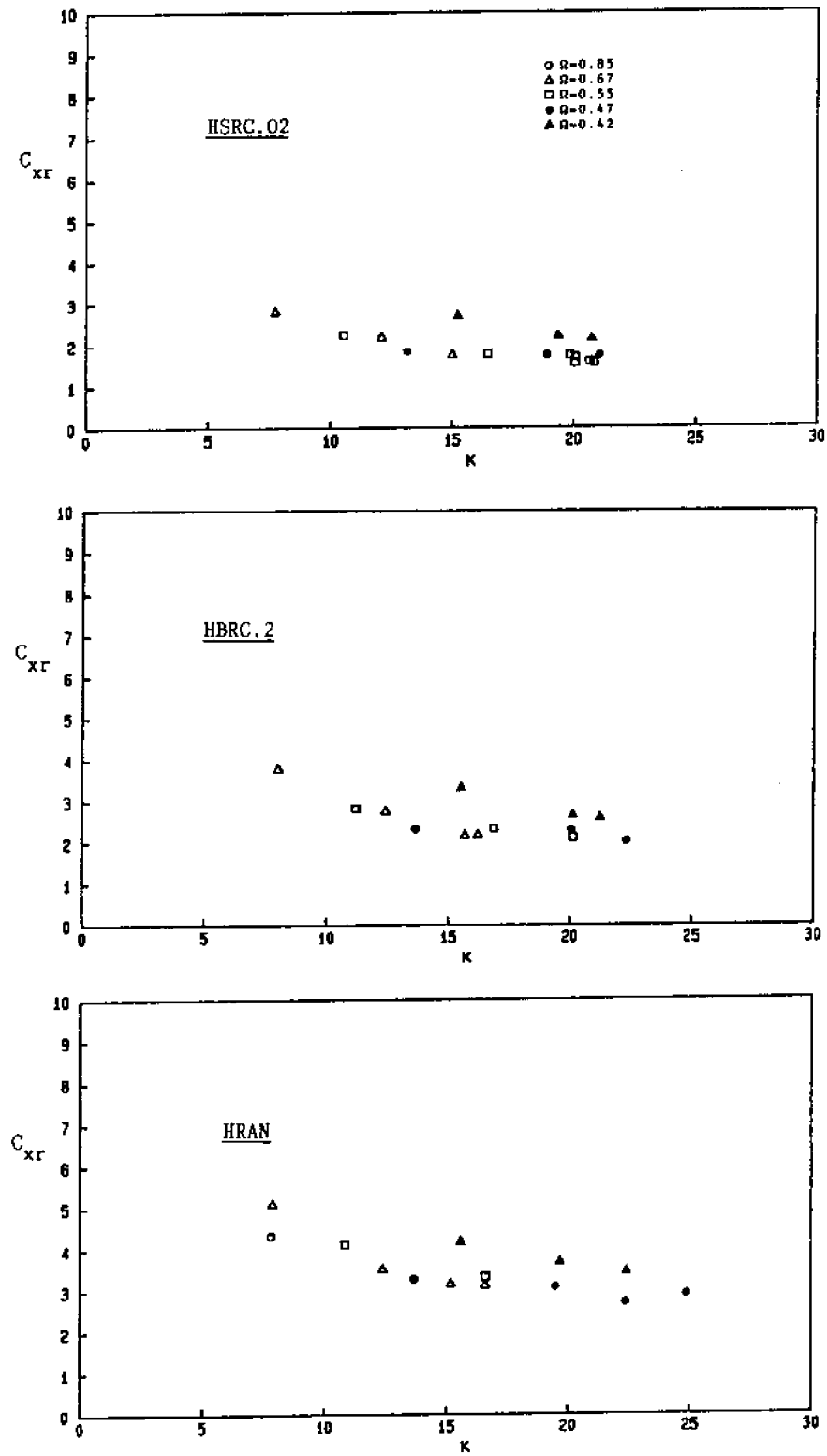

Fig. 5.3-5 C_{xr} versus K for various Ω for roughened cylinders in waves (all values based on the smooth cylinder diameter).

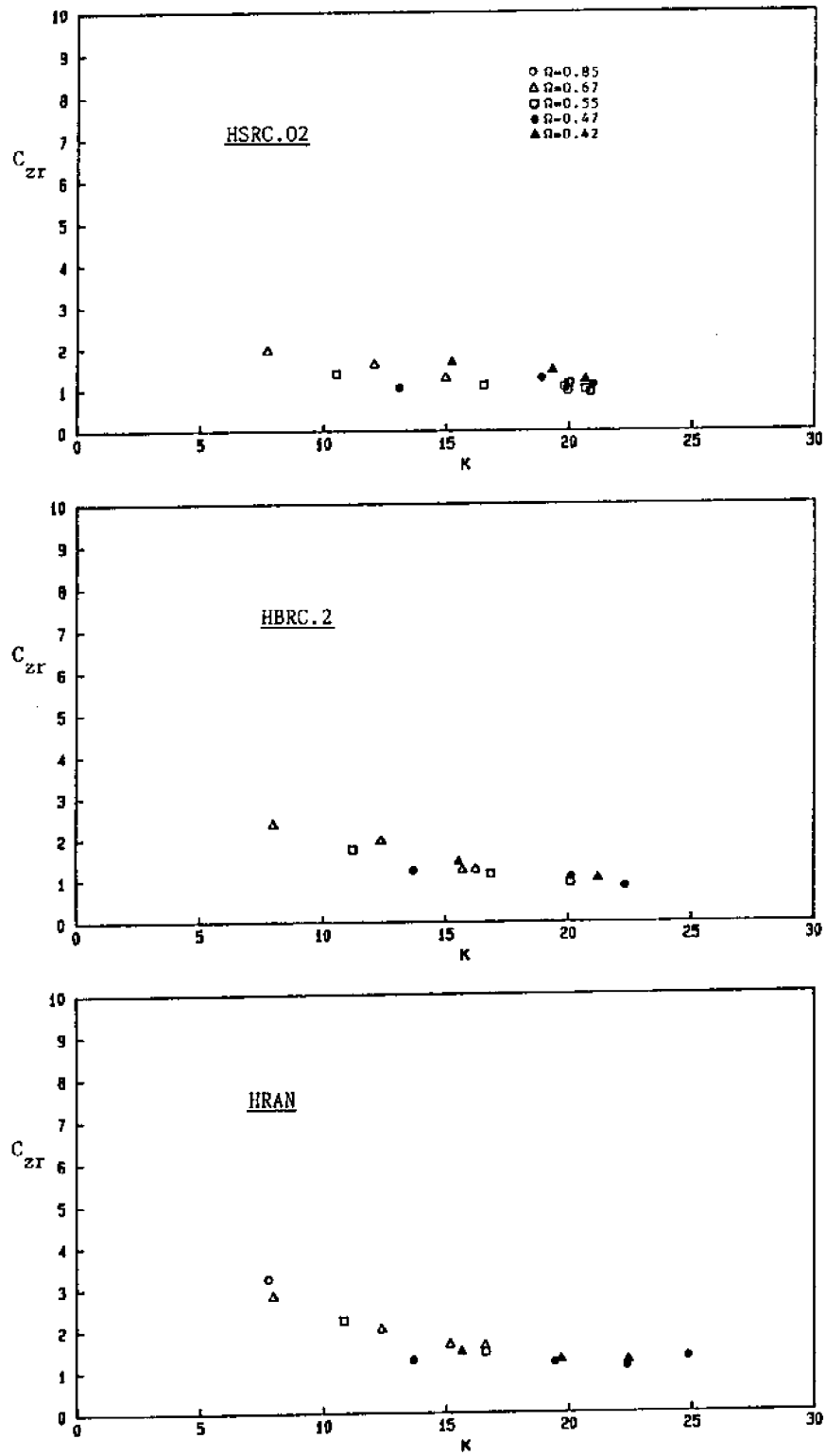

Fig. 5.3-6 C_{zr} versus K for various Ω for roughened cylinders in waves (all values based on the smooth cylinder diameter).

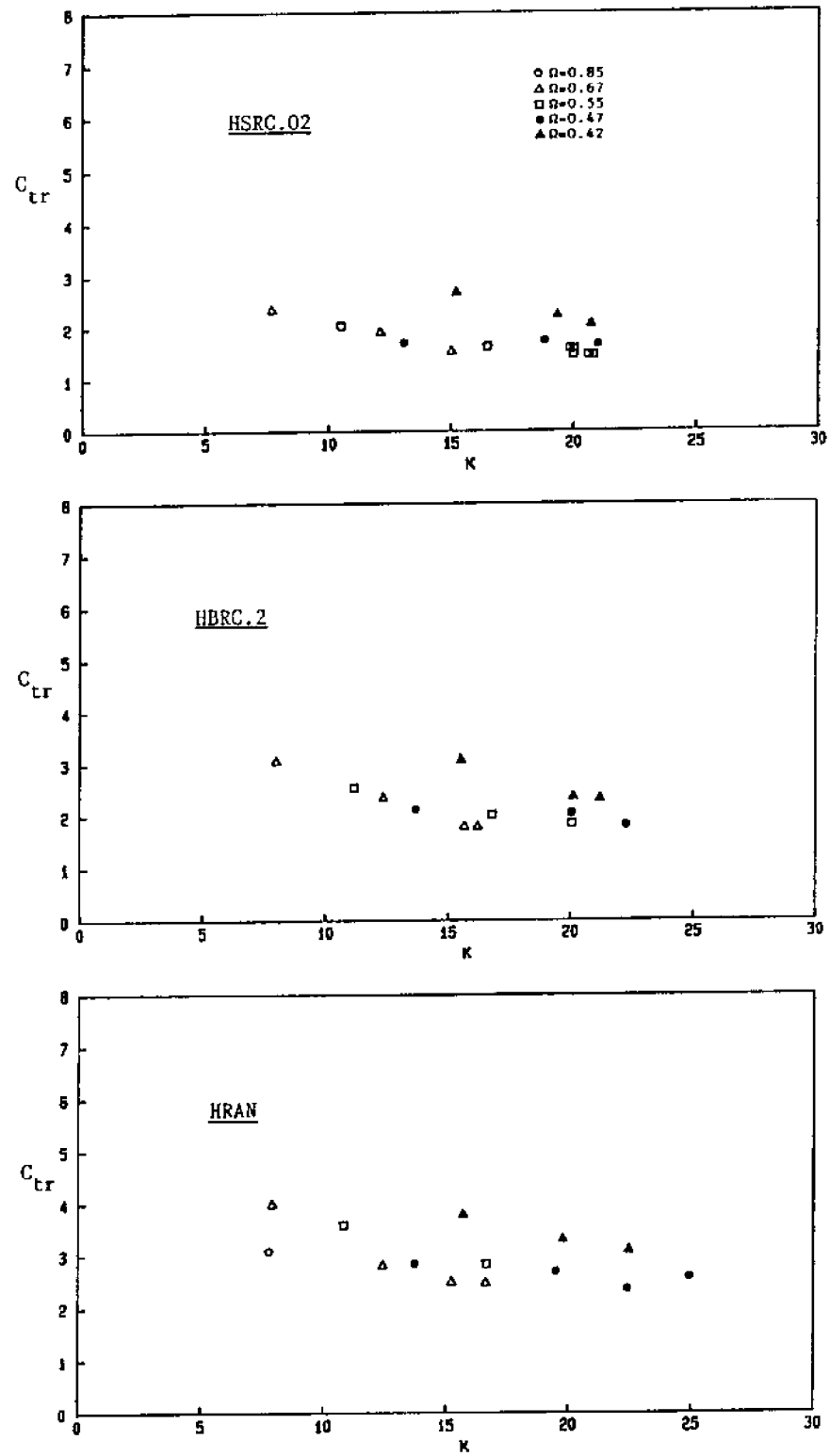

Fig. 5.3-7 C_{tr} versus K for various Ω for roughened cylinders in waves (all values based on the smooth cylinder diameter).

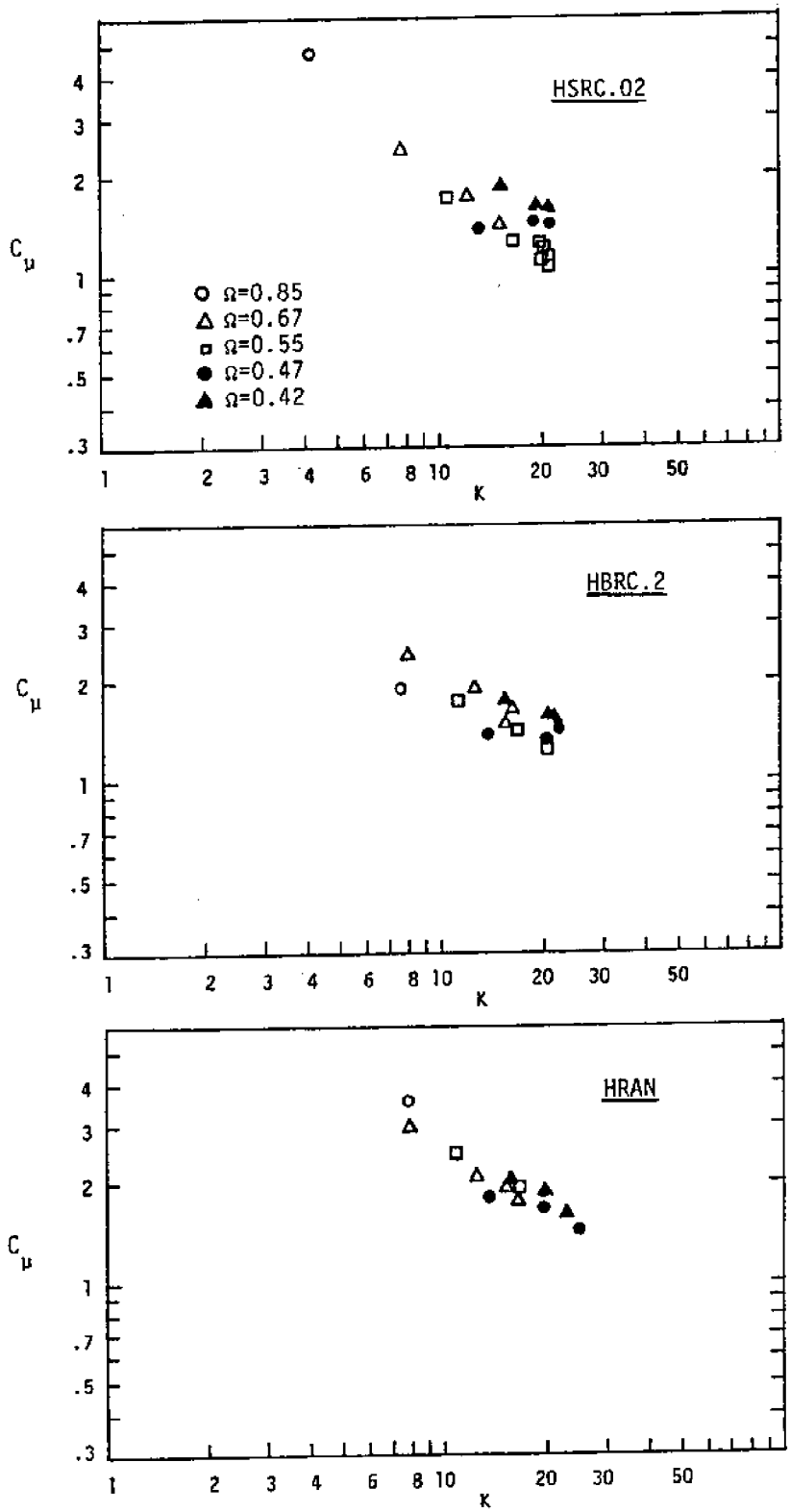

Fig. 5.3-8 C_μ versus K for various Ω for roughened cylinders in waves (all values based on the smooth cylinder diameter).

From Fig. 5.3-6, the values of C_{zr} correlate well with K for each cylinder, but no clear trend on Ω can be observed (Note that there is only one data point for Ω=0.85 for all roughened cylinders). Unlike those for C_{xr} and C_{tr}, C_{zr} seems not to increase significantly as e/D increases, especially for those with small Ω (solid symbols). That means, from the present data, the C_{zr} does not vary significantly among different e/D. One notable phenomenon is that the C_{zr} for HBRC.2 (with larger roughness) is a little smaller than that for HSRC.02. From Fig. 4-2, the roughness of HSRC.02 is uniform and organized, but the roughness of HBRC.2 is nonuniform and unorganized. Thus, the spanwise coherence and the induced forces on HBRC.2 are reduced. This is thought to be the reason that causes Czr of HSRC.02 is greater than that of HBRC.2 in spite of its smaller relative roughness. Comparing Fig. 5.3-6 with Fig. 5.3-2, it is observed that C_{zr} increases from the smooth cylinder to the roughened cylinders. Thus, the rms vertical force coefficient increases from smooth cylinders to roughened cylinders, but it does not have a pronounced increase among different roughened cylinders. For planar oscillatory flow (Ω=0), Sarpkaya (1976) reported the maximum lift coefficients (i.e., the maximum vertical force coefficient for Ω=0) do not vary among different e/D and he (1986) showed the rms lift force coefficients increase from the smooth to the rough cylinder (see Figs. 1.2.1-7 and 1.2.1-8). This phenomenon and possible reasons will be studied further in the following section.

Compared with the results of the smooth cylinder (Fig. 5.3-4), the C_{μ} values for the roughened cylinders presented in Fig. 5.3-8 are

much higher. No clear difference of C_μ values between the HSRC.02 and HBRC.2 is observed. The values of C_μ for the HRAN are clearly higher than the HSRC.02 and HBRC.2. It is observed for all three roughened cylinders that the values of C_μ for the smallest Ω(=0.42) are greater than the rest of the data.

5.4 Harmonic Analysis of Forces

In this section, the amplitude and phase of each harmonic component (the wave frequency is the fundamental frequency) of the horizontal and vertical forces are analyzed by using Fourier analysis described in Section 2.4.

Basically, the fundamental harmonic of the forces comes mainly from the inertia force and the drag force. The higher harmonics of the forces are composed of the vortex-induced force (due to the asymmetric vortex motion) and a relatively small amount of nonlinear Morison force coming from the nonlinearity of waves and the nonlinear drag term. By conducting a harmonic analysis of the horizontal and vertical forces, the structure of these forces can be examined.

The amplitudes of each harmonic are normalized by the square of the maximum horizontal velocity as follows.

$$C_x(n) = \frac{F_x(n)}{\frac{1}{2}\rho D L u_\mu^2} \tag{5.4-1}$$

amd

$$C_z(n) = \frac{F_z(n)}{\frac{1}{2}\rho D L u_\mu^2} \tag{5.4-2}$$

in which n (an integer) represents the order of harmonics. In addition to the amplitudes, the phase angles of each harmonic are studied. These angles are designated as $\phi_x(n)$ and $\phi_z(n)$, that represent the phase angles of the nth harmonic force in the horizontal and vertical direction, respectively. Equations (5.4-1) and (5.4-2) contain the first power of D. If the effective diameters are considered, these coefficients should be divided by δ.

5.4.1 Fundamental Harmonic

The values of $C_x(1)$ for HSMC8 with various values of Ω are plotted against K in Fig. 5.4.1-1. It is clear that $C_x(1)$ correlates well with K and, except for Ω=0.85, the trend of $C_x(1)$ on Ω is not very clear. The best fit lines for Ω=0.85 and Ω=0.67 are drawn by eye for the comparison with the following figure. In Fig. 5.4.1-2, the relation between $C_z(1)$ and Ω can be drawn, especially for small K. The $C_z(1)$ decreases as Ω decreases because the Morison-type force (inertia plus drag) in the vertical direction decreases as the Ω decreases (i.e., the relative vertical velocity decreases). For $K < 10$, there is a clear discrepancy of $C_z(1)$ between data for Ω=0.85 (open circles) and the rest of the data. Similar trend was observed for C_{zr} in Section 5.3.

In Fig. 5.4.1-2, the best fit lines of $C_x(1)$ for Ω=0.85 and Ω=0.67 from Fig. 5.4.1-1 are also drawn. It is clear that, for $K < 10$, the $C_z(1)$ with Ω=0.85 is very close to $C_x(1)$. However, $C_z(1)$ with smaller Ω is much smaller than the associated $C_x(1)$ for small K. The reason is, for small K and Ω, the vertical velocity might be too small to make the wake move in the vertical direction. It is

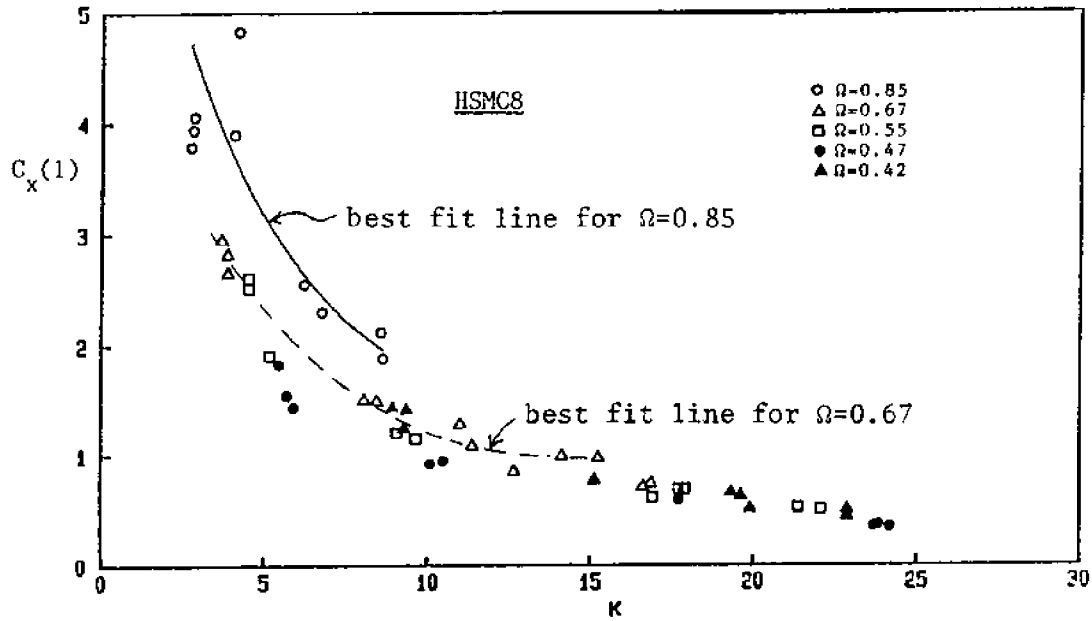

Fig. 5.4.1-1 $C_x(1)$ versus K for various Ω for HSMC8 in waves.

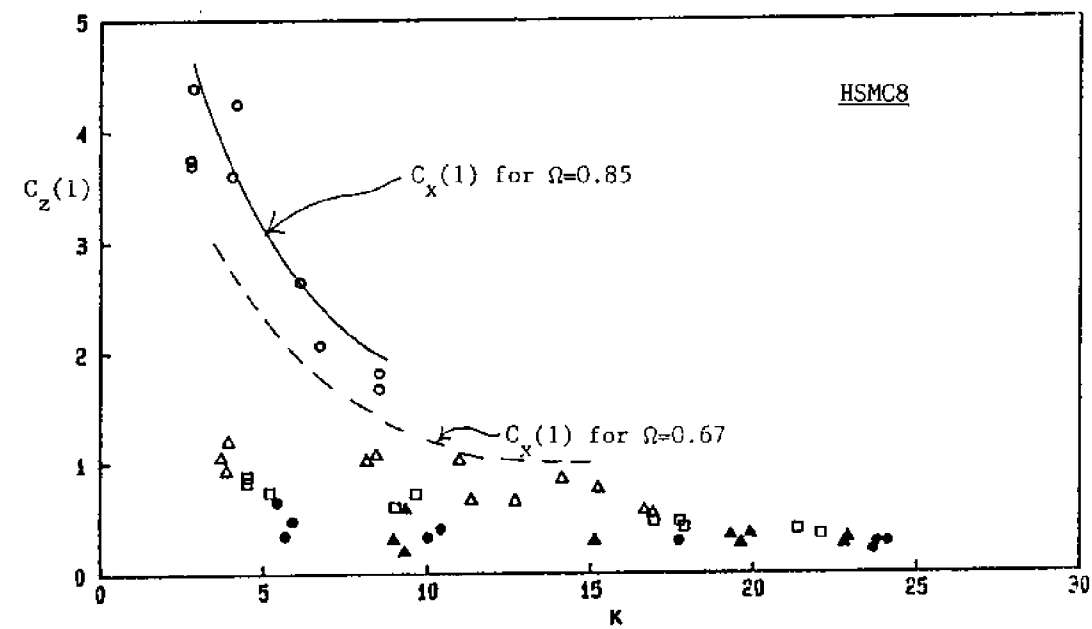

Fig. 5.4.1-2 $C_z(1)$ versus K for various Ω for HSMC8 in waves.

thought that, for $K < 10$, there is an Ω value between 0.67 and 0.85 that has the vertical velocity strong enough to make the wake rotate around the cylinder. For $K > 10$, the values of $C_z(1)$ for all Ω in this study are just a little lower than those of $C_x(1)$.

Maull and Norman (1979) used the rms horizontal velocity to quantify K and $C_x(1)$ and found the dependence of $C_x(1)$ on Ω. In Fig. 5.4.1-3, the present data were recalculated and plotted with Maull and Norman's data. Although the present data fall between the upper and the lower limit of their data, the dependence on Ω is still not clear. Bearman et al. (1985a) also reported their data fell between these limits but no trend on Ω could be observed. Now, the question is why Maull and Norman can find the dependence of $C_x(1)$ on Ω, but this trend can not be clearly found from the present data and Bearman, et al's data? The difference of $\beta(=D2/T\nu)$ values is thought to be one of the possible reasons. Although β and Ω are closely related for the same test cylinder and cylinder elevation as discussed at the beginning of this chapter, for the same Ω, the β values may vary between different experiments and should be considered as an important parameter. Maull and Norman conducted the experiment in a relative small wave flume and the β values were about 200. The experiments of the present study and of Bearman, et al. were conducted in a large wave tank and β values for both studies were over 5000. From the data of planar oscillatory flow from Sarpkaya (1976), it is also observed that force coefficients (C_d, C_m and rms force coefficient) for different β values are distinguishable for small β. However, these coefficients are very close to each other between

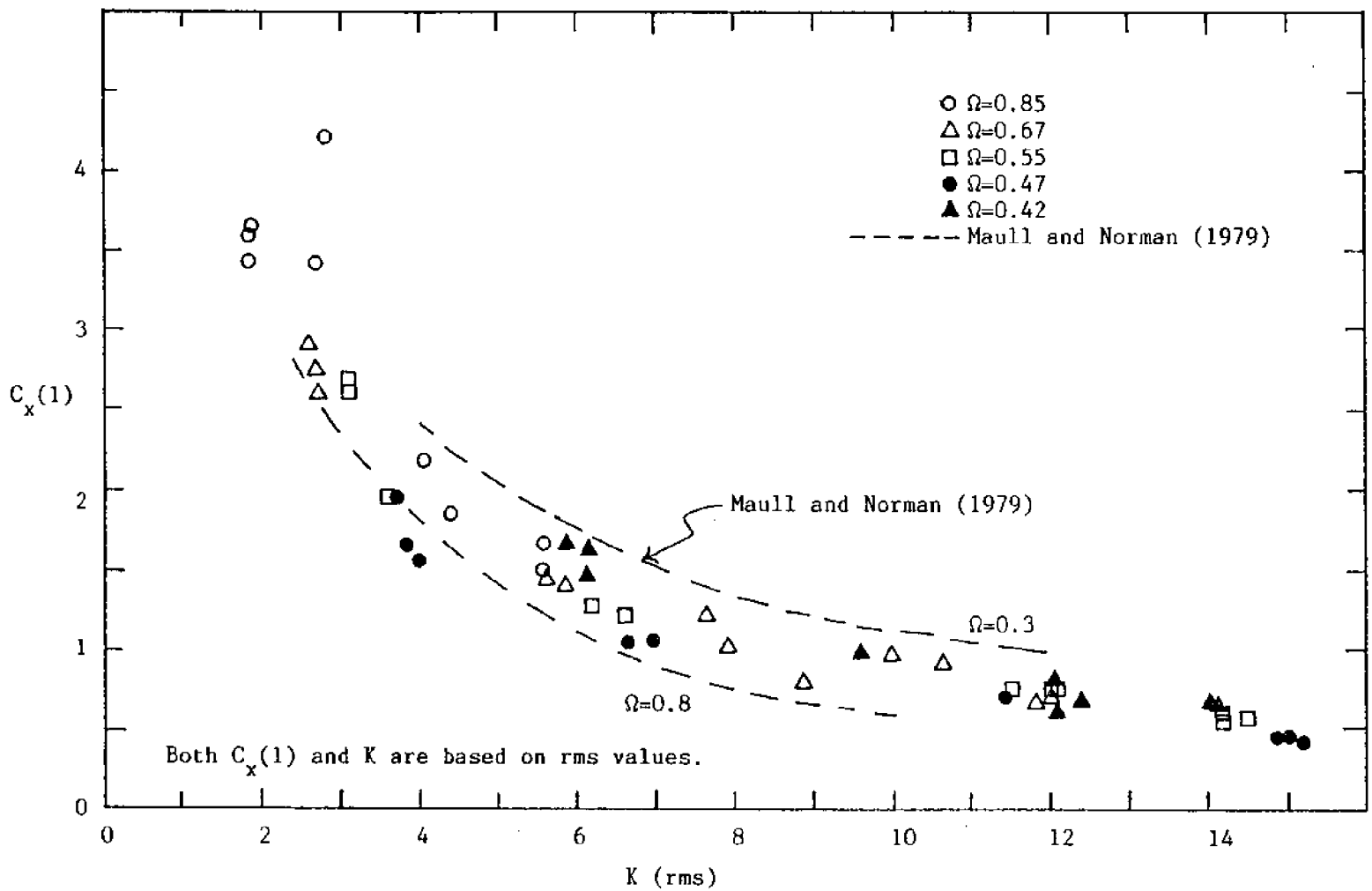

Fig. 5.4.1-3 $C_x(1)$ versus K (values are based on rms velocity) for various Ω for HSMC8 in waves with those from Maull and Norman (1979).

different β values for $\beta > 3000$. That means, for large β values, the force coefficients under the same K are very close and the dependence on other parameters is hard to distinguish.

The phase angles (see definition in Section 2.4) for the fundamental harmonic of the horizontal and vertical forces for HSMC8 are plotted in Figs. 5.4.1-4 and 5.4.1-5. The phase angles for the first harmonic of horizontal forces, $\phi_x(1)$, only vary in a small range. The trend that $\phi_x(1)$ for small Ω (e.g. solid symbols) is smaller than that for large Ω (e.g. open symbols) is roughly observed. The $\phi_x(1)$ seems to decrease slightly as K increases. It is reasonable because the drag force tends to dominate as K increases. The $\phi_x(1)$, containing mostly the drag and inertia force, should approach 0° as the drag component becomes very large. The scatter of the phase angle for the fundamental harmonic of the vertical force ($\phi_z(1)$) is more significant. However, it is visible that the $\phi_z(1)$ values for smaller Ω are smaller.

The values of $C_x(1)$ and $C_z(1)$ for three roughened cylinders (HSRC.02, HBRC.2 and HRAN) against K for various values of Ω are shown in Figs. 5.4.1-6 and 5.4.1-7. The $C_x(1)$ increases considerably as the relative roughness increases and dependence on Ω is not clear. In Fig. 5.4.1-7, the increase of $C_z(1)$, due to the increase of roughness, is not as rapid as that of $C_x(1)$. The $C_z(1)$ increases from the smooth cylinder to the sand-roughened cylinder. But, the $C_z(1)$ does not increase significantly from HSRC.02, HBRC.2 to HRAN, especially for those with small Ω (solid symbols). The similar trend was found for C_{zr} in the previous section. For small Ω, the vertical

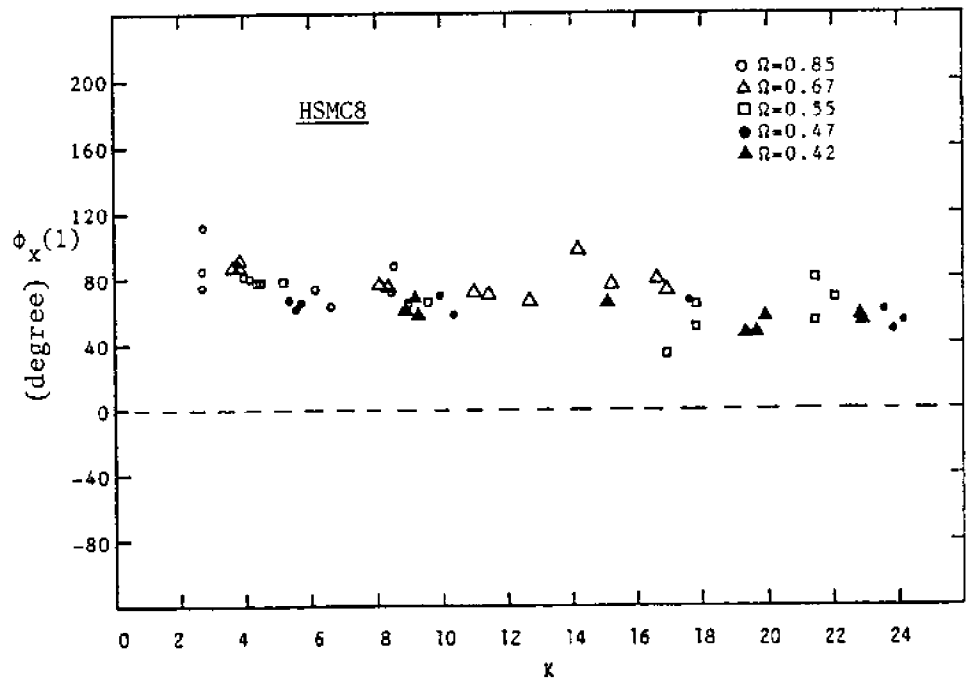

Fig. 5.4.1-4 $\phi_x(1)$ versus K with various Ω for HSMC8 in waves.

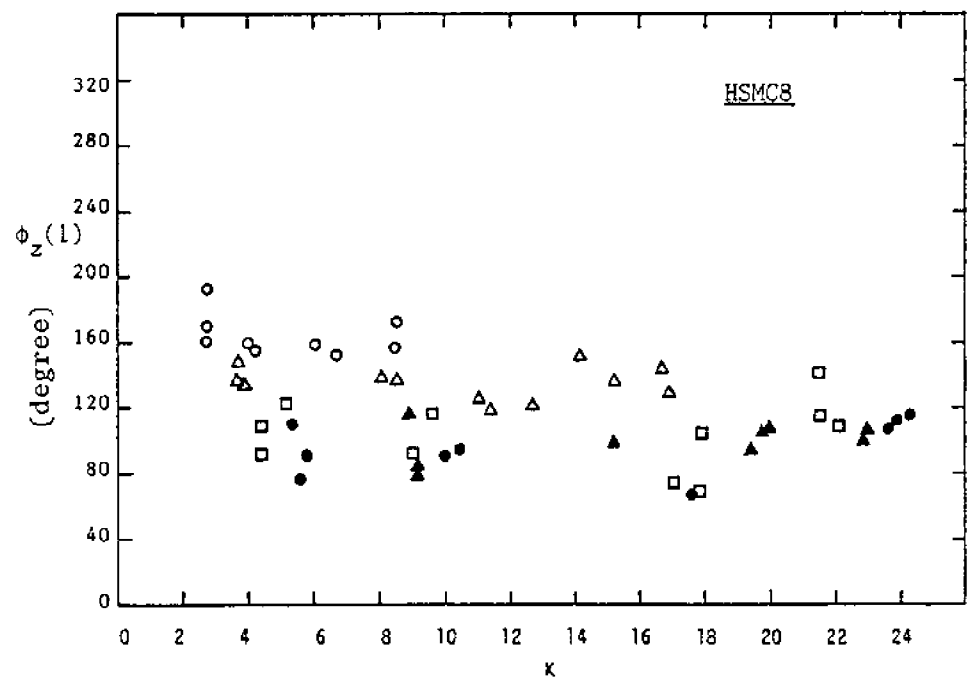

Fig. 5.4.1-5 $\phi_z(1)$ versus K with various Ω for HSMC8 in waves.

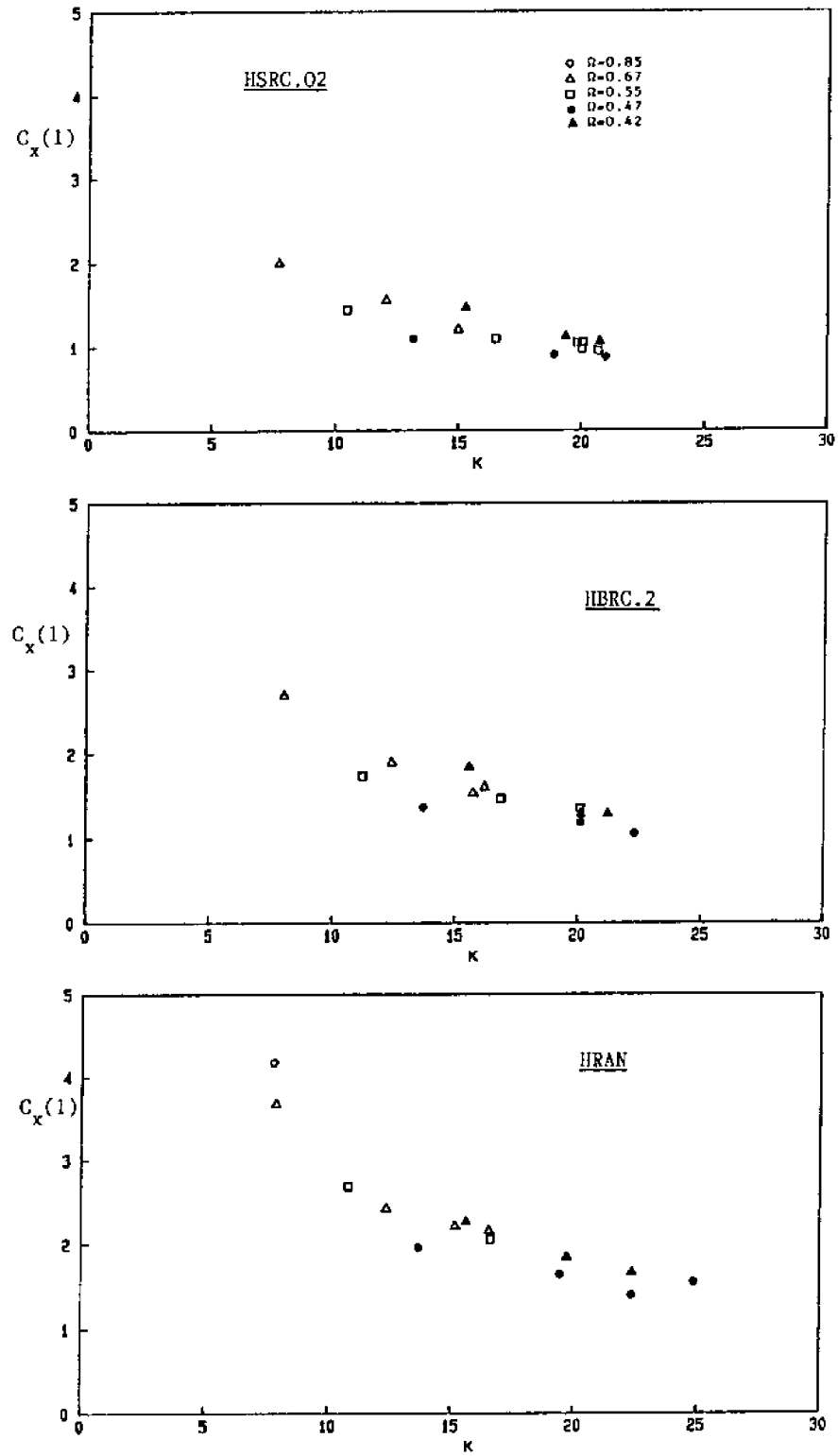

Fig. 5.4.1-6 $C_x(1)$ versus K for various Ω for roughened cylinders in waves (all values based on the smooth cylinder diameter).

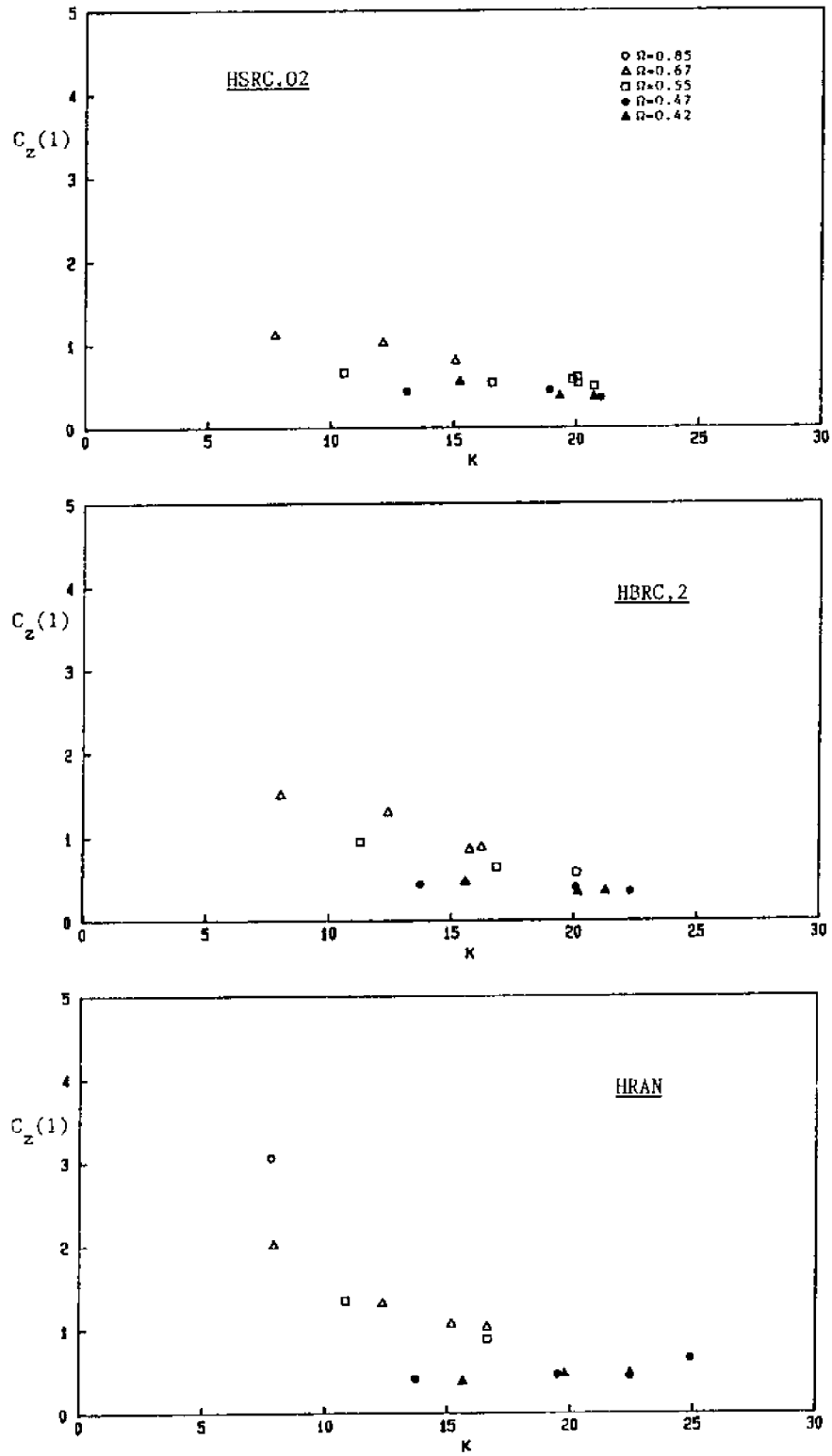

Fig. 5.4.1-7 $C_z(1)$ versus K for various Ω for roughened cylinders in waves (all values based on the smooth cylinder diameter).

velocity might be too small to make the wake move toward the vertical direction. Thus, for small Ω, the fundamental harmonic vertical force coefficients does not vary between different roughened cylinders. However, for the smooth cylinder, the wake is easier to move due to the smooth boundary of the cylinder. Besides, the tendency that $C_z(1)$ decreases with decreasing Ω is more clear as the relative roughness increases.

Because no clear dependence of $\phi_x(1)$ and $\phi_z(1)$ on Ω for the roughened cylinders is observed, only one symbol is used to represent each cylinder in Figs. 5.4.1-8 and 5.4.1-9. Values of $\phi_x(1)$ for three different roughened cylinders agree quite well with one another (Fig. 5.4.1-8). That means, in this study, the phase angle of the fundamental horizontal force does not vary due to the change of relative roughness. Comparing to Fig. 5.4.1-4, the $\phi_x(1)$ for roughened cylinders is slightly lower than that of the smooth cylinder. That means, under the same K, forces on roughened cylinders are more drag-dominant than those on the smooth cylinder.

Although the values of $\phi_z(1)$ for the roughened cylinders have a little more scatter than those of $\phi_x(1)$, the values of $\phi_z(1)$ are still in a small range as shown in Fig. 5.4.1-9. The $\phi_z(1)$ values for three roughened cylinders have less scatter than those for HSMC8.

From the present data, the scatter of $\phi_x(1)$ and $\phi_z(1)$ for the roughened cylinders is less than that for the smooth cylinder. Combining this result with the result of $C_x(1)$ and $C_z(1)$, it can be said that the fundamental harmonic force (mainly the inertia and drag

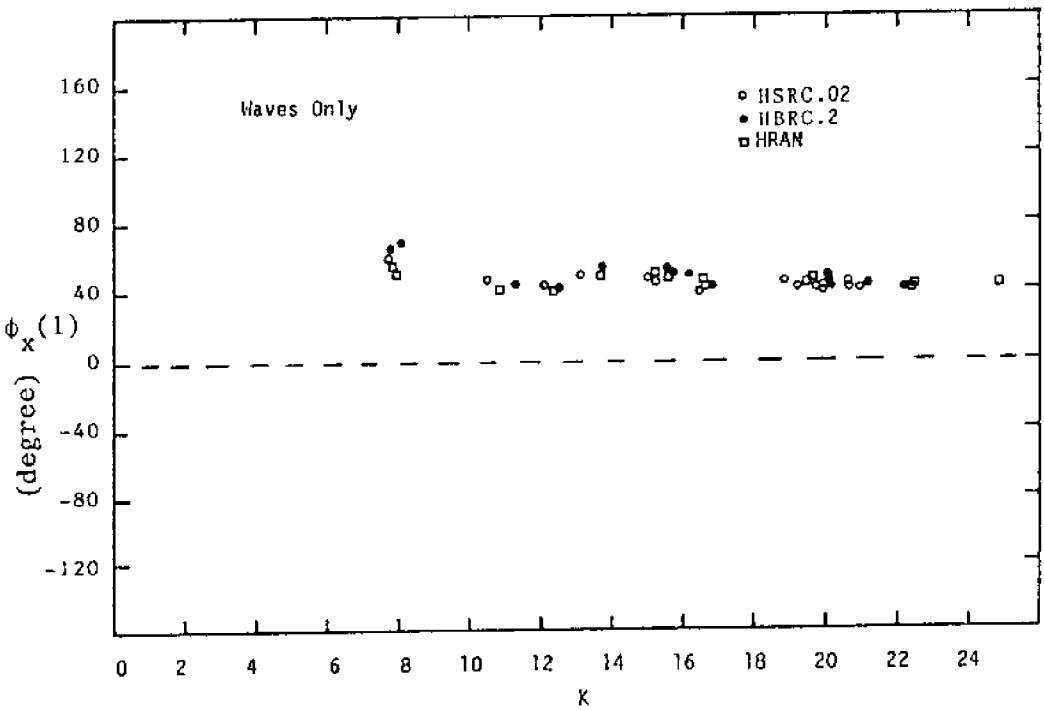

Fig. 5.4.1-8 Phase angle of the fundamental horizontal forces for roughened cylinders in waves.

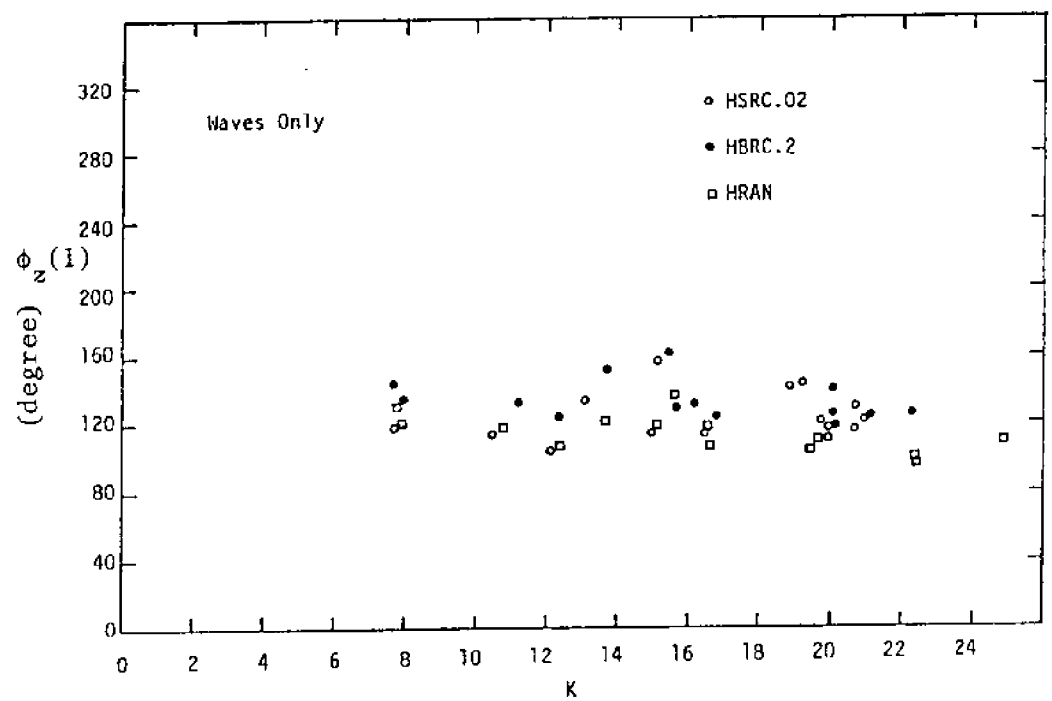

Fig. 5.4.1-9 Phase angle of the fundamental vertical forces for roughened cylinders in waves.

force) on the roughened cylinders has less variation than on the smooth cylinder.

From the above discussions, the characteristics of the fundamental harmonic forces of the present data can be summarized as follows.

(1) Both force coefficient (amplitude) and phase of the fundamental harmonic horizontal force correlate quite well with K and the dependence on Ω is roughly observed. In the vertical direction, the fundamental harmonic force (both coefficient and phase) decreases as Ω decreases.

(2) As the relative roughness increases, the fundamental harmonic horizontal force increases even if the effective diameter is used. It reveals that the roughness significantly increases the fundamental harmonic of horizontal forces.

(3) The fundamental harmonic vertical force coefficient increases significantly from the smooth cylinder to the roughened cylinders. However, this force coefficient does not have pronounced increase between roughened cylinders.

(4) The fundamental harmonic forces (especially the phase) for the roughened cylinders in both directions have less scatter than those for the smooth cylinder.

As mentioned at the beginning of this chapter, the fundamental forces are mainly from the inertia and the drag components. Because the fundamental forces (force coefficiients and phases) do not have pronounced scatter, the drag and inertia force should not have great variation. Thus, the scatter of C_d and C_m shown in Section 5.2. is thought mainly from the higher harmonic forces.

5.4.2 Higher Harmonics

In this study, only the second and the third harmonic of measured forces are investigated. To compare the relative importance, the force coefficients for these higher harmonics (i.e., $C_x(n)$ and $C_z(n)$, n=2 and 3) are normalized by dividing by the related fundamental harmonic force coefficients ($C_x(1)$ and $C_z(1)$). These coefficients are designated as $C'_x(n)$ and $C'_z(n)$, respectively and are called the relative nth harmonic horizontal and vertical force coefficients. The original values of $C_x(n)$ and $C_z(n)$ are listed in Appendix B.

Figures 5.4.2-1 to 5.4.2-4 present these relative horizontal and vertical force coefficients of the second and third harmonic for the smooth cylinder (HSMC8). From Figs. 5.4.2-1 and 5.4.2-2, it is clear that both relative force coefficients in the horizontal direction, $C'_x(2)$ and $C'_x(3)$ increase as K increases. That coefficients with smaller Ω (solid symbols) are greater than those with larger Ω (open symbols) is roughly observed. Because none of $C'_x(2)$ or $C'_x(3)$ is greater than 1.0 in this study, none of the second harmonic force exceeds the fundamental harmonic force and none of the third harmonic force exceeds the second harmonic force in the horizontal direction.

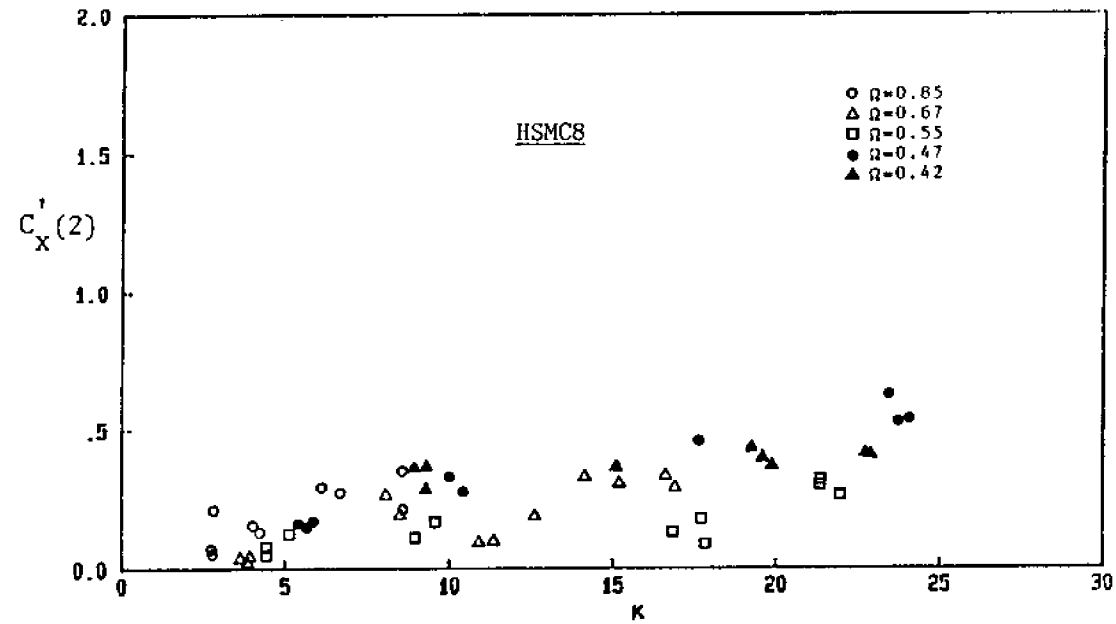

Fig. 5.4.2-1 $C_X'(2)$ versus K for various Ω for HSMC8 in waves.

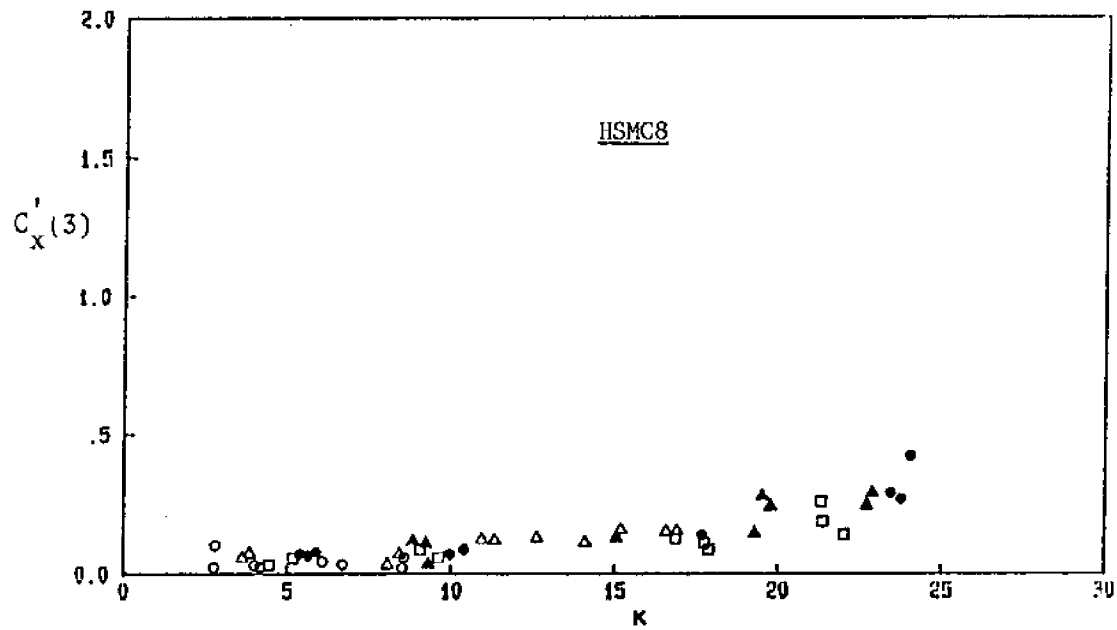

Fig. 5.4.2-2 $C_X'(3)$ versus K for various Ω for HSMC8 in waves.

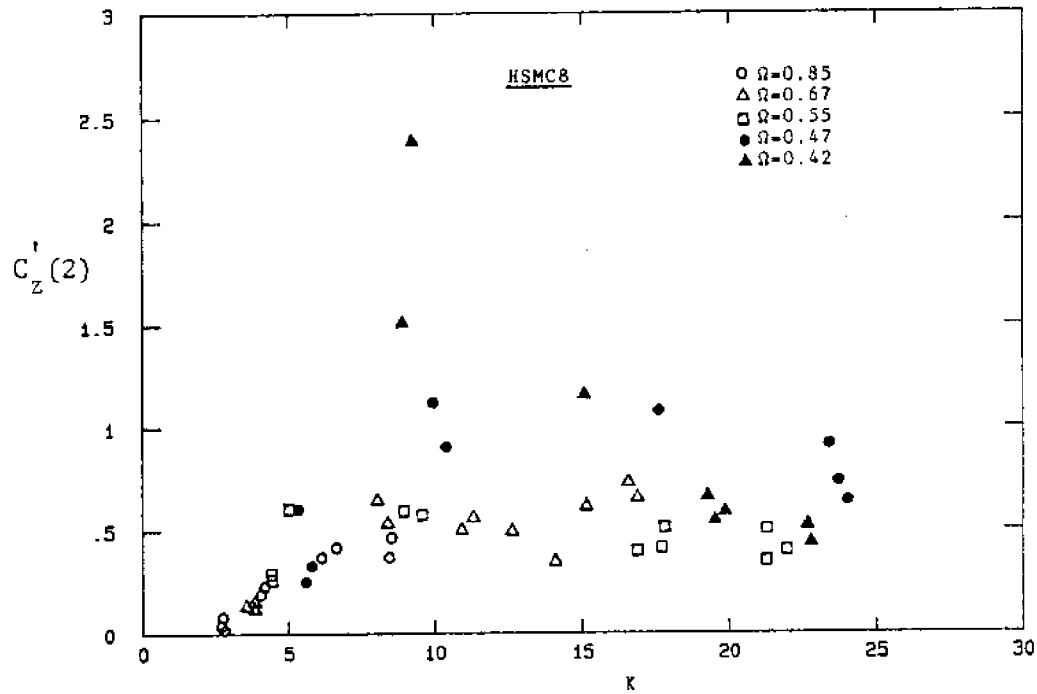

Fig. 5.4.2-3 $C_z'(2)$ versus K for various Ω for HSMC8 in waves.

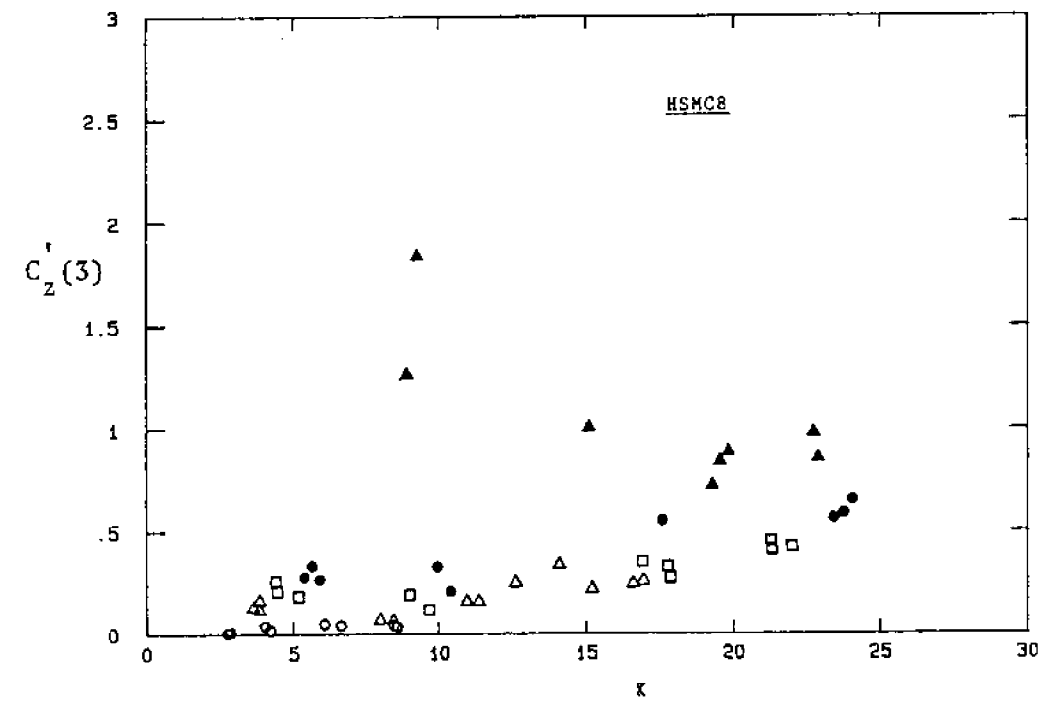

Fig. 5.4.2-4 $C_z'(3)$ versus K for various Ω for HSMC8 in waves.

When studying the transverse force on a cylinder under planar oscillatory flow (which is the effect of asymmetric vortex shedding), several researchers (e.g., Sarpkaya 1976) found the transverse coefficient possess a maximum at K around 10. The $C_x'(2)$, which counts the vortex shedding effect in the horizontal direction, also has a local maximum at K=9 as shown in Fig. 5.4.2-1.

In the vertical direction, $C_z'(2)$ increases rapidly from K=2.5 and also reaches the maximum at K=9 as shown in Fig. 5.4.2-3. The $C_z'(2)$ for the smaller Ω (solid symbols) is clearly greater than that for the larger Ω (open symbols). After the maximum value at K=9, $C_z'(2)$ with small Ω decreases. The $C_z'(2)$ with larger Ω decreases mildly and, then, reaches another peak value at K=16. This trend is similar to the transverse force of a cylinder under planar oscillatory flow as reported by Ikeda and Yamamoto (1981). Actually, the original data from Sarpkaya (1976) also have this character.

For $\Omega > 0.5$, none of $C_z'(2)$ or $C_z'(3)$ exceed 1.0. In other words, the second and the third component will not be larger than the fundamental force in the vertical direction for large Ω. For $\Omega < 0.5$, some of the $C_z'(2)$ are greater than 1.0 and that means the second harmonic force exceeds the fundamental force. It is believed that $C_x'(2)$ will increase rapidly as Ω decreases below the lowest Ω value here (=0.42) because the fundamental harmonic vertical force decreases and the second harmonic force increases rapidly with decreasing Ω (decreasing vertical velocity). Note that $C_z'(2)$ approaches zero at K=2.5. This result confirms that the asymmetric vortex shedding starts earlier for horizontal cylinders in waves than

in planar oscillatory flow (i.e. K=4) as observed in the flow visualization experiments (see Chapter 3).

In Fig. 5.4.2-4, the values of $C_z'(3)$ for Ω= 0.42 are much greater than those for other values of Ω including Ω=0.47 which is just a lot higher than 0.42. Thus, a value between 0.42 and 0.47 is thought to be the critical value of Ω that makes the third harmonic force significant. Comparing with $C_z'(2)$ in Fig. 5.4.2-3, $C_z'(3)$ for Ω=0.42 is greater than $C_z'(2)$ as $K > 18$. This implies the stronger third harmonic force (due to the formation and motion of the third vortex in one half cycle with relatively stronger strength) exists for small Ω and $K > 18$.

The phase angles of the second harmonic force ($\phi_x(2)$ and $\phi_z(2)$) for the smooth cylinder (HSMC8) are plotted in Figs. 5.4.2-5 and Fig. 5.4.2-6. No clear trend on Ω can be observed. The scatter in these plots is expected because (i) vortex shedding forces are not so regular even under planar oscillatory flow as reviewed in Section 1.2, (ii) the second (or higher) harmonic force includes a portion of the nonlinear force, coming from the wave nonlinearity and nonlinear drag term (the square of the velocity), and (iii) the phase is very sensitive even with a small disturbance. However, the rough trend that these two angles increase with increasing K for $K < 10$ and then keep constant is still observable. The phase angles for the third harmonic force are more scattered than those for the second harmonic force and are listed in Appendix B.

The relative second and third harmonic force coefficients in the horizontal direction, $C_x'(2)$ and $C_x'(3)$, for roughened cylinders do not

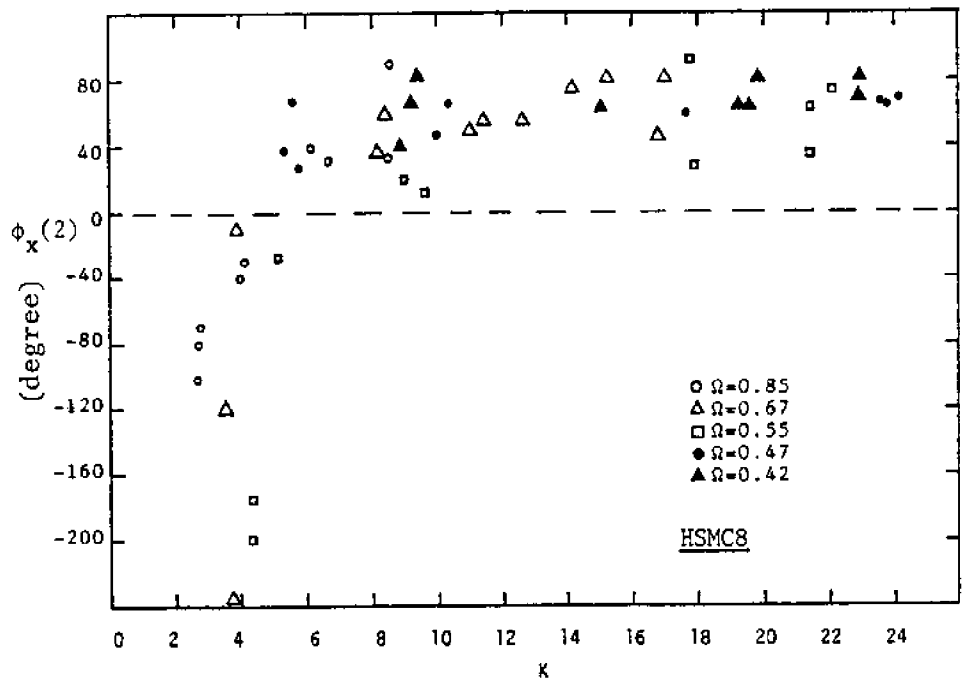

Fig. 5.4.2-5 $\phi_x(2)$ versus K with various Ω for HSMC8 in waves.

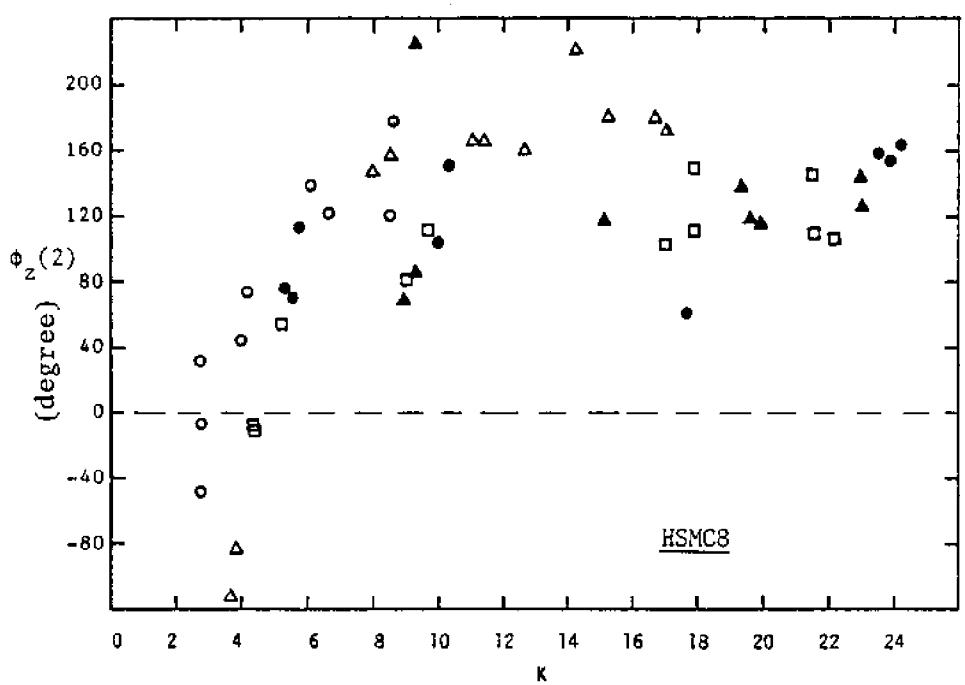

Fig. 5.4.2-6 $\phi_z(2)$ versus K with various Ω for HSMC8 in waves.

increase with the increase of roughness as shown in Figs. 5.4.2-7 and 5.4.2-8. That means the higher harmonic horizontal forces increase at the same rate as the fundamental harmonic horizontal force due to the increase of e/D. Note that the fundamental harmonic horizontal force coefficient increases significantly as e/D increases (see Section 5.4.1). Besides, the $C'_x(2)$ with smaller Ω is greater than that with larger Ω, but this tendency does not hold for $C'_x(3)$.

Similar to those for the smooth cylinder (Figs. 5.4.2-3 and 5.4.2-4), the $C'_z(2)$ and $C'_z(3)$ for the roughened cylinders with small Ω are higher than those with large Ω as shown in Fig. 5.4.2-9 and 5.4.2-10. None of the second and the third harmonic vertical forces exceed the fundamental vertical force for large Ω (open symbols). In general, $C'_x(2)$ and $C'_x(3)$ do not vary significantly between different e/D values except the data with small Ω near K=15. From the last section, it was observed that the fundamental vertical force does not significantly increase due to the increase of e/D. Thus, the higher harmonic vertical forces are still at the same range between different e/D except near K=15. Because no data for roughened cylinders with small Ω are at K=9, the peak value at K=9 found for the HSMC8 can not be verified for the roughened cylinders.

Similar to the smooth cylinder, $\phi_x(2)$ and $\phi_z(2)$ for the roughened cylinders have no clear relation with Ω and scatter exists somewhat as shown in Figs. 5.4.2-11 and 5.4.2-12.

In summary, the following characteristics of the higher (second and third) harmonic forces from the present data can be stated.

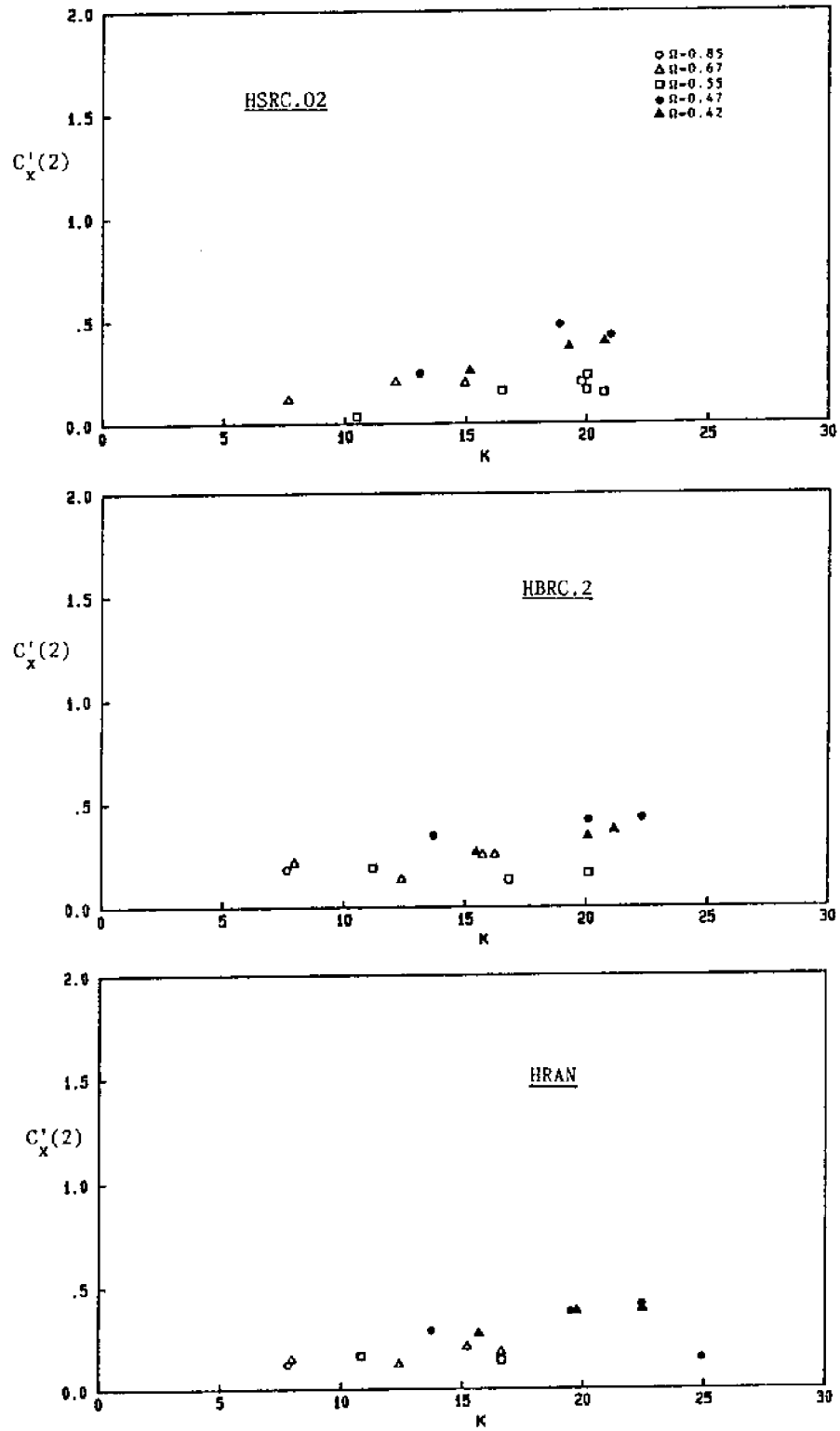

Fig. 5.4.2-7 $C_x'(2)$ versus K for various Ω for roughened cylinders in waves (all values based on the smooth cylinder diameter).

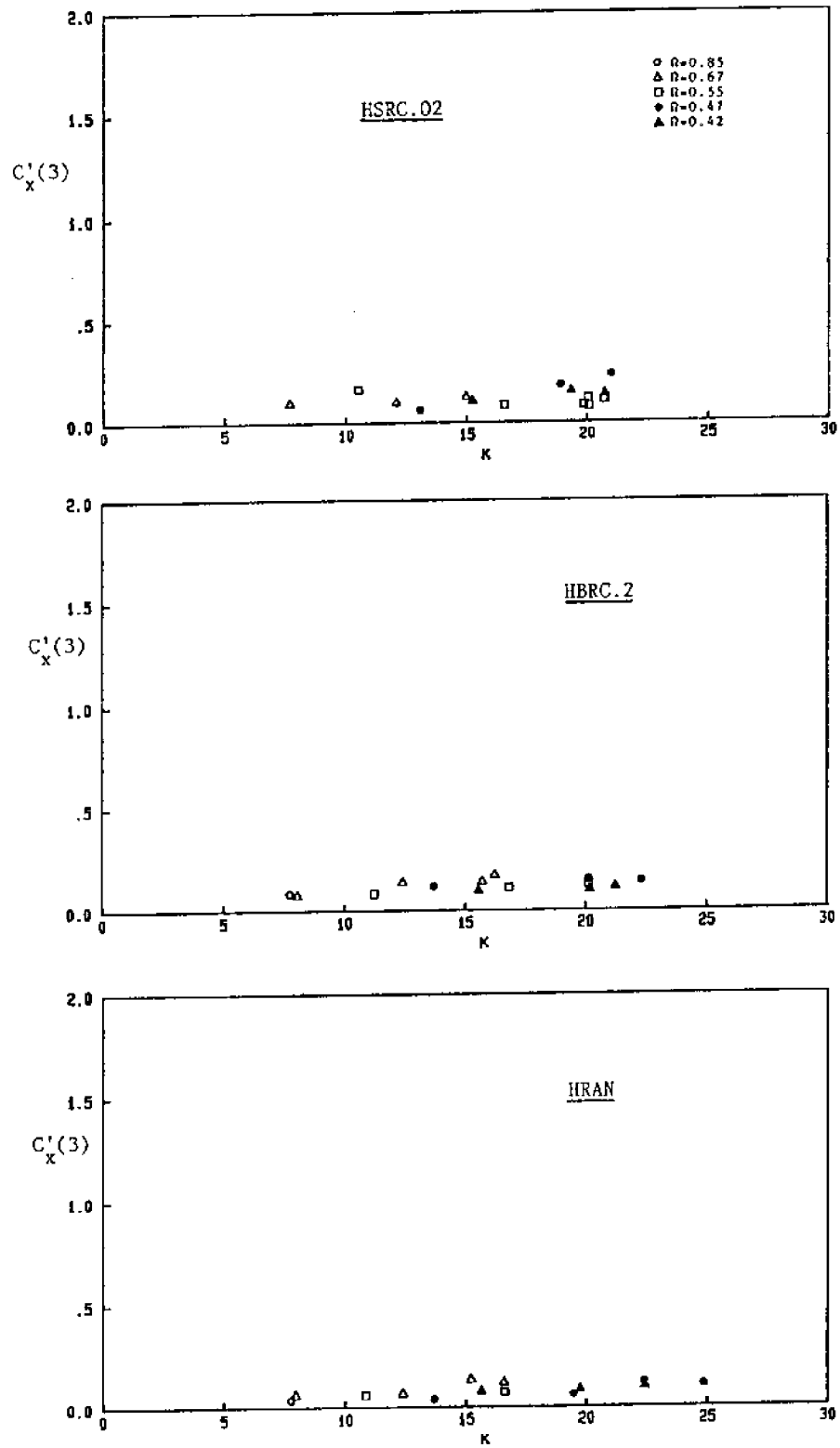

Fig. 5.4.2-8 $C_x'(3)$ versus K for various Ω for roughened cylinders in waves (all values based on the smooth cylinder diameter).

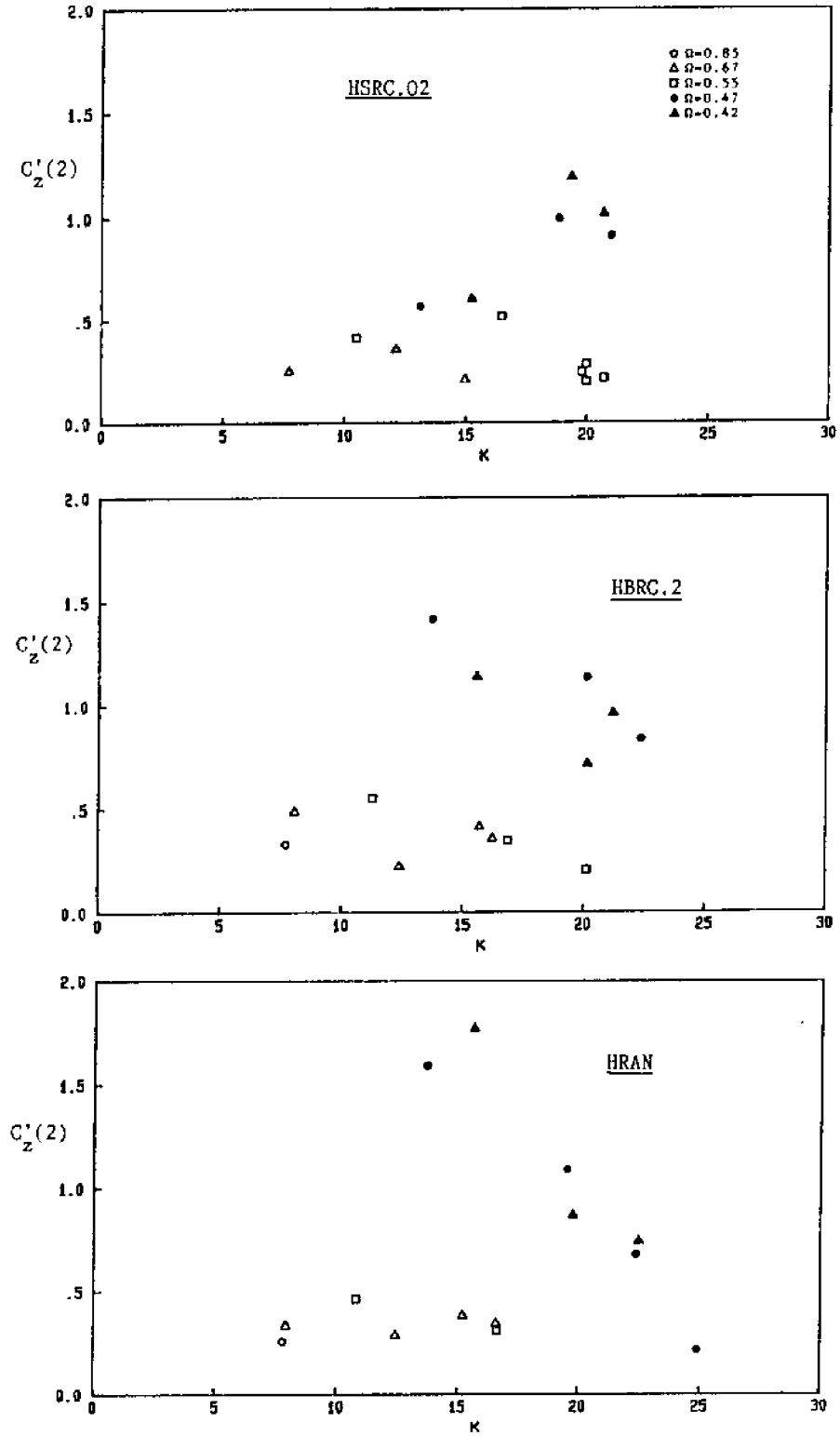

Fig. 5.4.2-9 $C_z'(2)$ versus K for various Ω for roughened cylinders in waves (all values based on the smooth cylinder diameter).

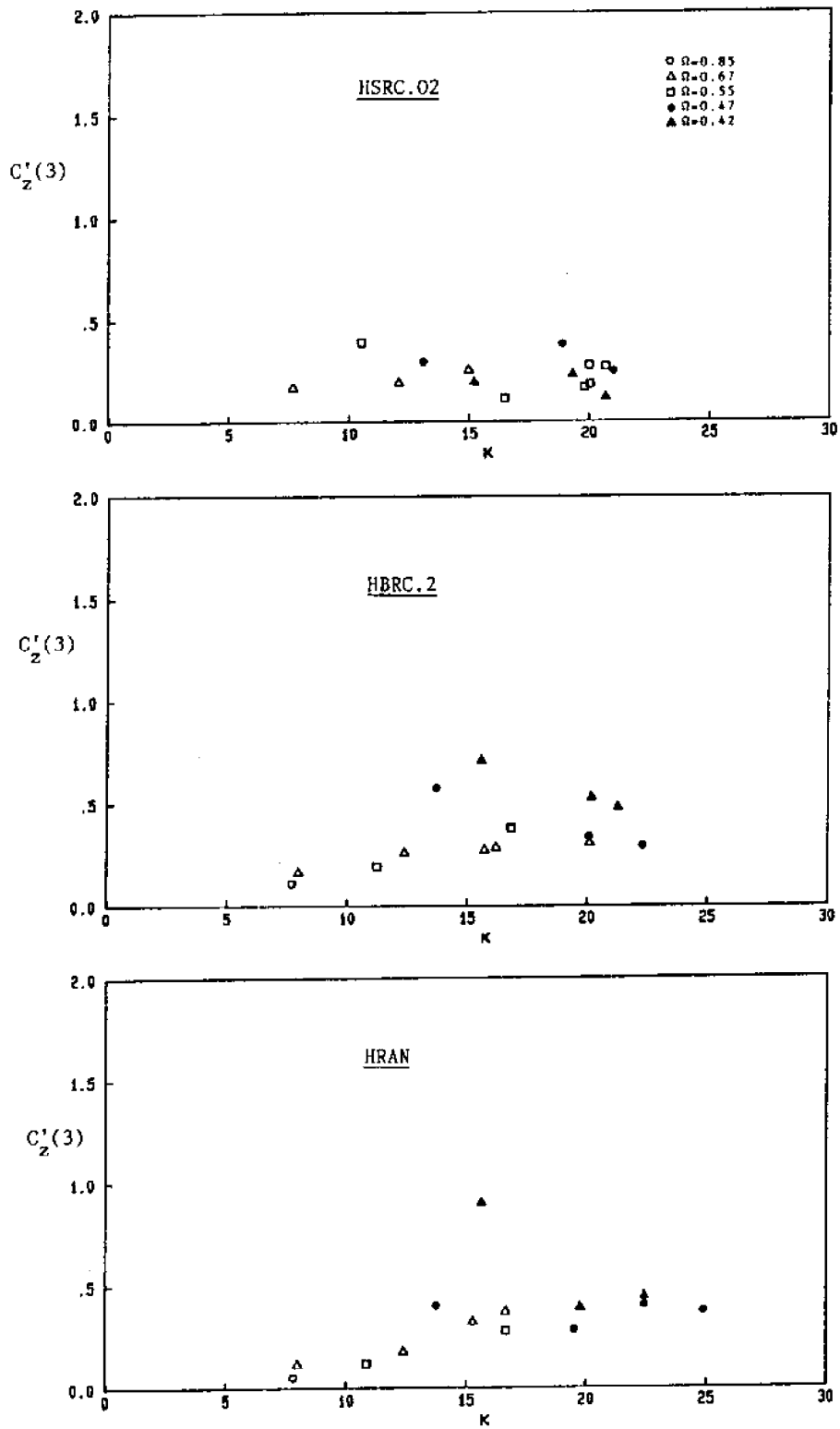

Fig. 5.4.2-10 $C_z'(3)$ versus K for various Ω for roughened cylinders in waves (all values based on the smooth cylinder diameter).

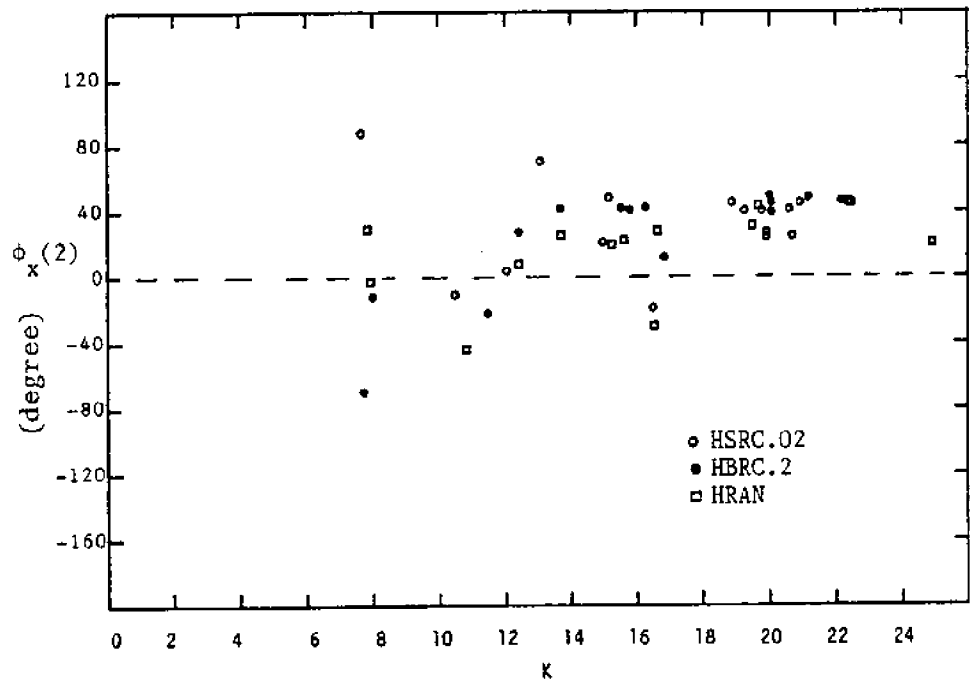

Fig. 5.4.2-11 $\phi_x(2)$ versus K for roughened cylinders in waves (K based on the smooth cylinder diameter).

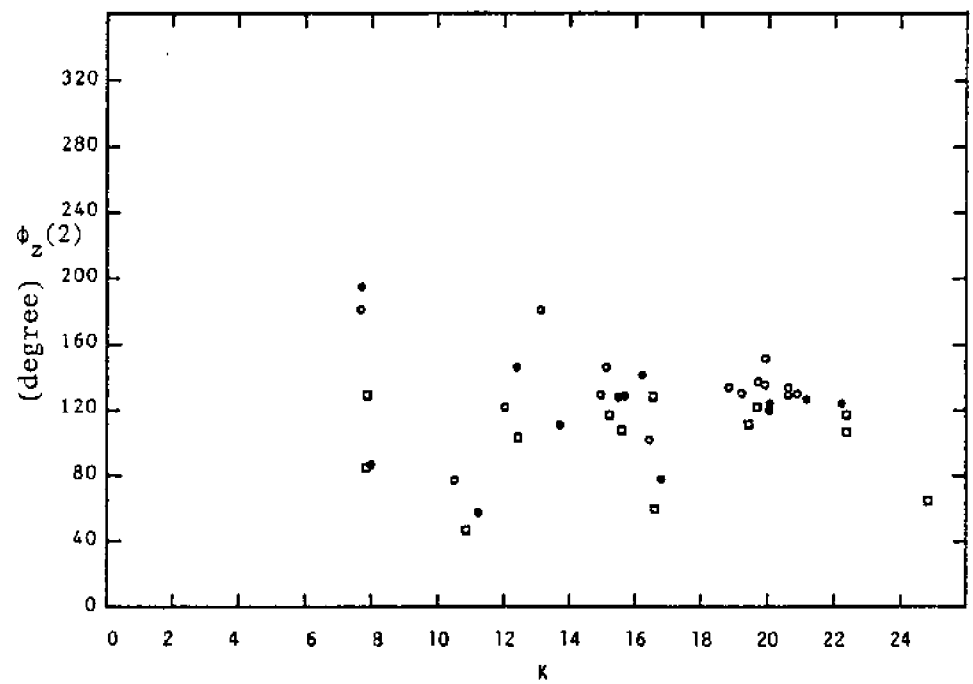

Fig. 5.4.2-12 $\phi_z(2)$ versus K for roughened cylinders in waves (K based on the smooth cylinder diameter).

(1) As K increases or Ω decreases, the importance of the higher harmonic forces in both directions increase.

(2) In the horizontal direction, the higher harmonic forces are all smaller than the fundamental forces. In the vertical direction, the higher harmonic forces exceed or approach the fundamental harmonic forces for small Ω and large K.

(3) The higher harmonic horizontal force increase with the increase of e/D at the same rate as the fundamental harmonic horizontal forces.

(4) The relative second and the third harmonic vertical force coefficients have a maximum at K=9 and K=15. This is similar to the characteristics of transverse force coefficients from planar oscillatory flow (Ω=0).

(5) Phase angles of the higher harmonic forces are relatively more scattered than those for the fundamental harmonic forces due to, mainly, the random nature of the vortex shedding force.

5.4.3 Steady Component

The steady component (D.C. component) of forces on a cylinder is considered as the result of the flow around the cylinder (see Chaplin 1984) in an open environment or return currents if experiments are conducted in a closed wave flume (see Nath 1982). According to Kim (1983), the return current in a closed wave flume has the following characteristics:

(i) For a specified wave period T, the return current increases with the increase of the wave height H.

(ii) With the same wave heights, the return current for shorter period waves is greater than that for longer period waves.

The steady components of the measured horizontal and vertical forces for the HSMC8 in this study are shown in Fig. 5.4.3-1. To show the influence of H and T directly, steady forces in these figures are not normalized by any factor.

Because most of the horizontal steady forces are negative, it reveals that the horizontal steady force in this study is strongly affected by the presence of return currents that cause negative horizontal steady forces. The steady force with the longer wave period (or small Ω) is smaller than that with shorter period (or large Ω). This tendency is due to the character (ii) of the return current indicated above. According to the character (i), with the same period (the same symbol), the horizontal steady force should increase if the wave height increases (i.e., K increases). From Fig. 5.4.3-1, the force just increases a little as H (or K) increases, especially for those with longer periods (solid symbols).

For small waves ($K < 7$), most of the vertical steady force are positive. One possible reason for this is the viscous effect around the horizontal cylinder as presented by Chaplin (1984). For $K > 7$, the vertical steady forces for longer wave periods are very small and do not increase with increasing H. For shorter waves, the forces are negative and the magnitudes are larger than those for longer waves.

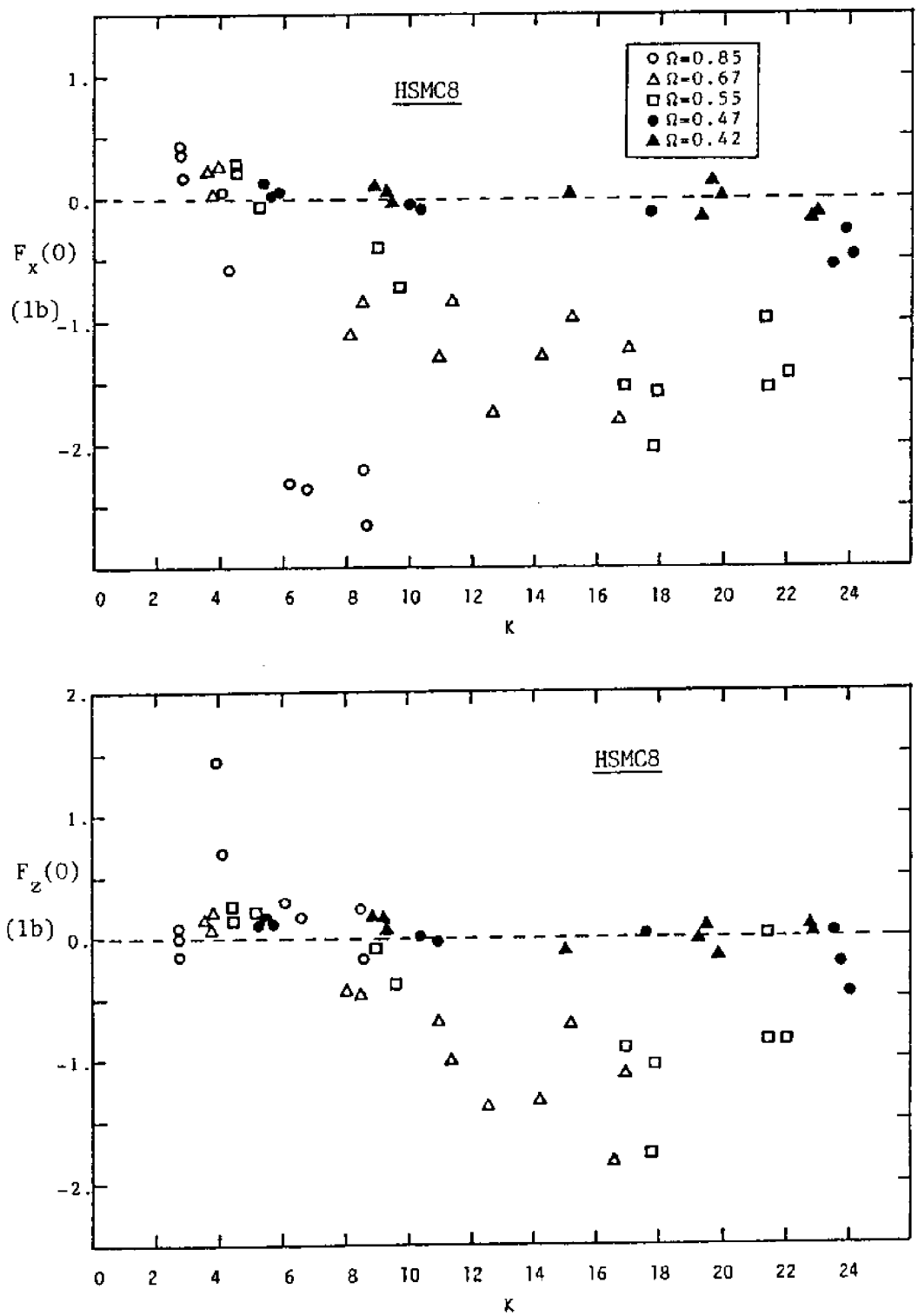

Fig. 5.4.3-1 Steady horizontal and vertical forces for HSMC8 in waves.

For large K, the vertical steady force is the result of the mean of the asymmetric vortex-induced force. Because the details of the asymmetric vortex shedding were not clearly known until now, the vertical steady force induced by them can not be predicted accordingly.

For the sand-roughened cylinder (as shown in Fig. 5.4.3-2), the horizontal steady forces with small T are in the same level as that of the smooth cylinder. That means the presence of the roughness does not have a clear influence on it. The steady forces with larger T (solid symbols) all become positive, but those with smaller T are still negative.

Comparing with the result from HSMC8 (Fig. 5.4.3-1), the vertical steady forces for HSRC.02 become positive due to the presence of the roughness as shown in Fig. 5.4.3-2. The same results hold for the other two roughened cylinders (HBRC.2 and HRAN) that are tabulated in Appendix B. Thus, the steady vertical forces are mostly negative for the smooth cylinder but are positive for the roughened cylinders. The reason for this phenomenon is unknown.

From the present data, the steady component of forces can be characterized as:

(1) In this study, the horizontal steady force is mainly due to the return current in the closed wave tank.

(2) Both horizontal and vertical steady force for the smooth cylinder are smaller for smaller Ω (or larger T).

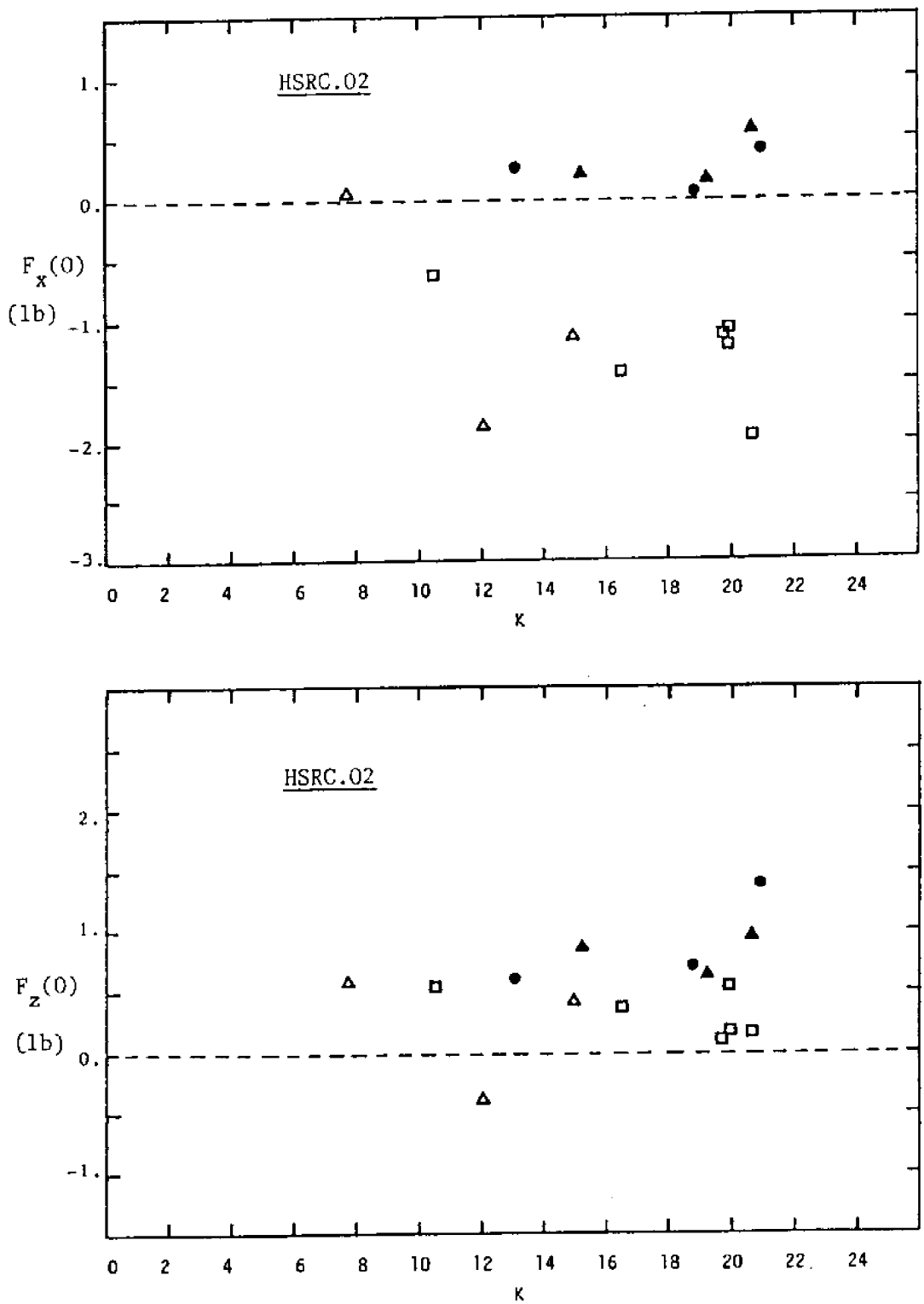

Fig. 5.4.3-2 Steady horizontal and vertical forces on HSRC.02 in waves (K based on the smooth cylinder diameter).

(3) The vertical steady forces are strongly affected by the roughness. For large K, these forces are mostly negative for the smooth cylinder. They become positive for the roughened cylinders.

5.5 Horizontal vs. Vertical Cylinders

As indicated in Section 1.1 and 1.2, horizontal cylinders and vertical cylinders in waves have some significant differences in flow patterns around them and in the induced forces. In this section, differences and similarities of forces acting on these two cylinders (horizontal and vertical) in periodic waves are compared and examined. Note that the forces on vertical cylinders considered here were measured on a small segment of the cylinders (i.e., local forces).

Nath (1983a) has reported that both C_d and C_m for the vertical cylinder are larger than those for the horizontal cylinder for the smooth and roughened cylinders except that values of C_d between smooth horizontal and smooth vertical cylinders do not have appreciable differences. Recall that the hydrodynamic forces acting on a fixed cylinder due to the unsteady flow consist of three components: the drag, the inertia and the vortex-induced forces. For vertical cylinders, C_d and C_m are evaluated from in-line forces which include the drag, inertia and a small portion of vortex-induced force (which is neglected in the Morison equation). The vortex-induced force normal to the in-line force is called the transverse force for vertical cylinders and is not involved in determining C_d and C_m. But, the values of C_d and C_m for the horizontal cylinder are determined from

all three components (drag, inertia and vortex-induced) as discussed in Section 5.2. When comparing the C_d and C_m between these two cylinders, one must keep this difference in mind.

The following data of vertical cylinders used to compare with those of horizontal cylinders are from Nath (1983b, 1984a). Because the in-line force on a vertical cylinder and the horizontal force on a horizontal cylinder are in line with the wave propagation, the term "in-line force" is used for both cylinders here. Both the transverse force on a vertical cylinder and the vertical force on a horizontal cylinder are normal to the direction of wave propagation and the cylinder axis. Thus, these two forces are called "transverse force" for simplicity of comparison.

Nath (1983a) defined the maximum in-line force coefficient, Cx_μ, as

$$C_{x\mu} = \frac{F_{x\mu}}{\frac{1}{2}\rho D L u_\mu^2} \tag{5.5-1}$$

He reported this coefficient is higher for vertical cylinders than for horizontal ones.

The rms in-line, transverse and total (in-line + transverse) force coefficients are designated as C_{xr}, C_{zr}, and C_{tr}, respectively, and their definitions are the same as Eqs. (5.3-1) to (5.3-3). Values of these coefficients for the smooth vertical cylinder are plotted together with those for the smooth horizontal cylinder (HSMC8) in Figs. 5.5-1 to 5.5-3. The C_{xr} values of the vertical cylinder are higher than those of the horizontal cylinder. On the

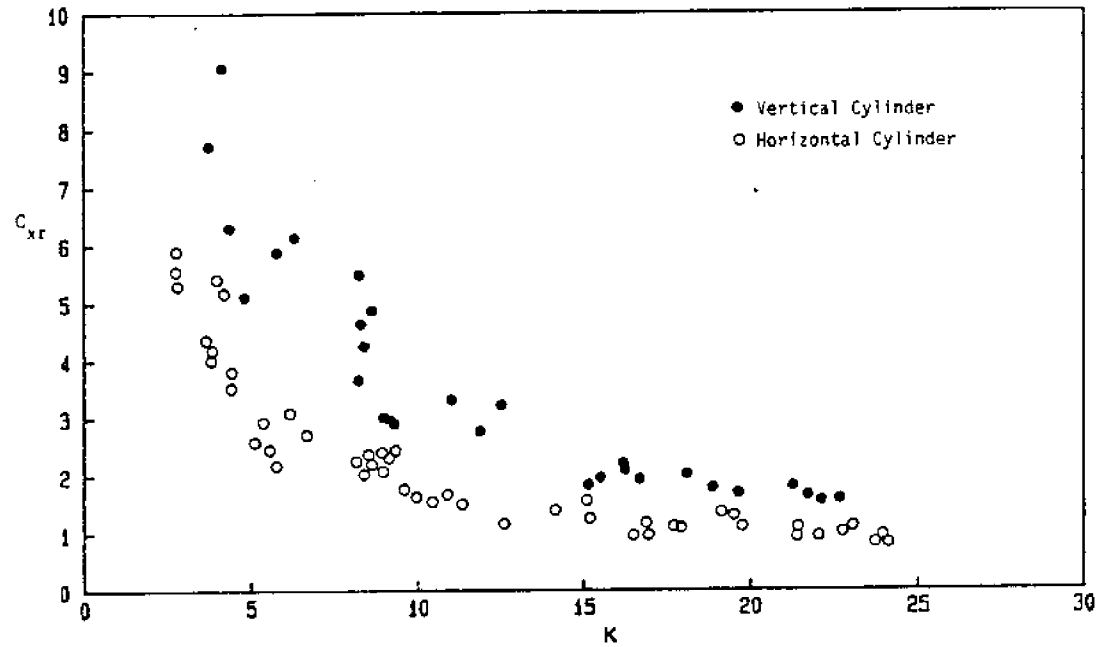

Fig. 5.5-1 Comparison of C_{xr} between horizontal and vertical smooth cylinders in waves.

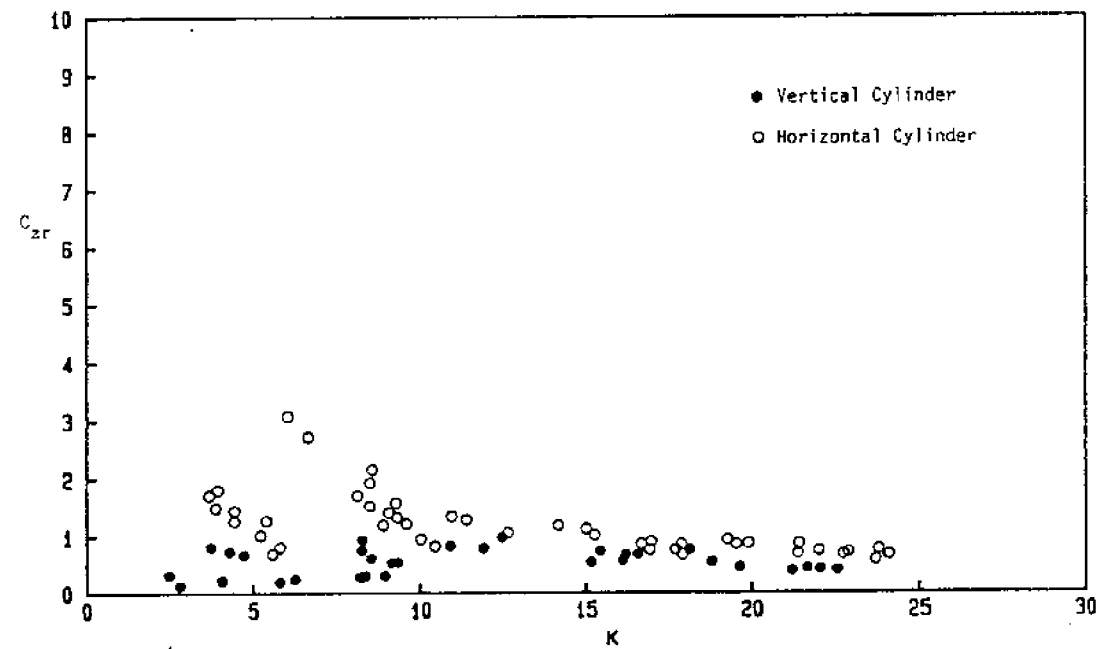

Fig. 5.5-2 Comparison of C_{zr} between horizontal and vertical smooth cylinders in waves.

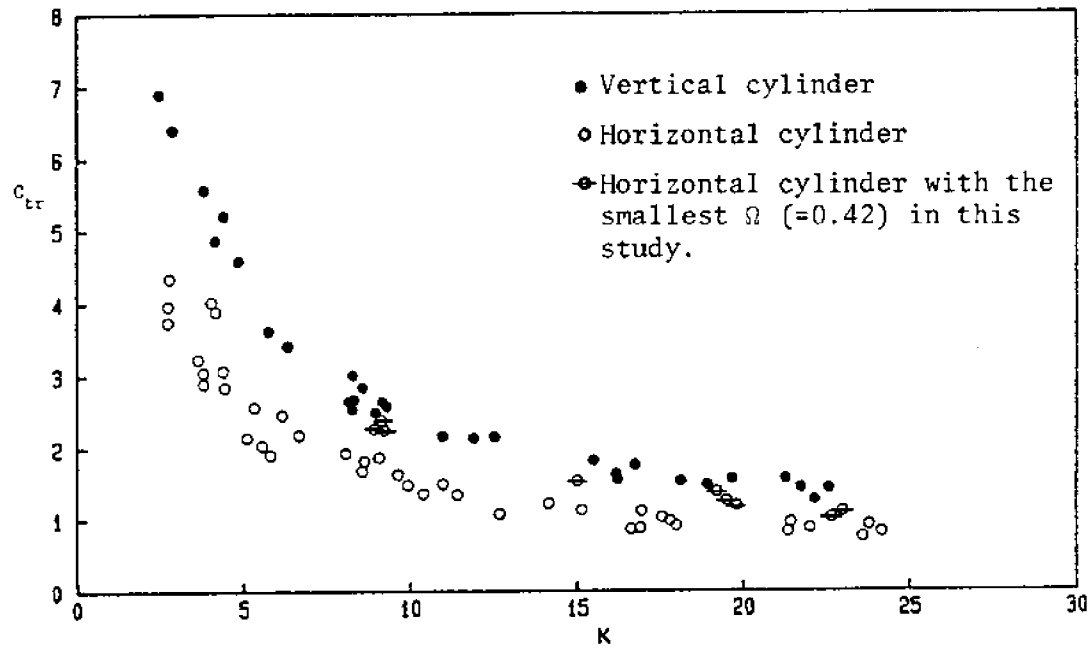

Fig. 5.5-3 Comparison of C_{tr} between horizontal and vertical smooth cylinders in waves.

other hand, C_{zr} values of the vertical cylinder are smaller than those of the horizontal one. Thus, the total rms force coefficient (drag + inertia + vortex-induced) is needed to compare the total forces between them. In Fig. 5.5-3, the values of C_{tr} for the vertical cylinder correlate very well with K. These values are higher than those for the horizontal cylinder and form an upper bound. In other words, the total rms force acting on the vertical cylinder is larger than that on the horizontal cylinder. The C_{tr} values for the horizontal cylinder with the smallest Ω(=0.42) in this study, that have a cross bar on the representative symbols in Fig. 5.5-3, are very close to the values of the vertical cylinder at K = 9, 15, 19, and 23. This implies C_{tr} values for these two cylinders are getting closer if Ω for the horizontal cylinder becomes smaller.

The maximum total force coefficients for the horizontal cylinder together with the maximum in-line force coefficients for the vertical cylinder from Nath (1985a) are shown in Fig. 5.5-4. Note that the maximum in-line force coefficients, $C_{x\mu}$, for the vertical cylinder are evaluated from in-line forces only and the transverse force (induced by vortex shedding) is not included. But, the C_{μ} for the horizontal cylinder is evaluated from the total (drag, inertia and vortex-induce force) force. Although the transverse force is not included, the $C_{x\mu}$ for the vertical cylinder is still higher and forms an upper bound of C_{μ}. For vertical cylinders in waves, several studies (e.g. Chakrabarti, et al. 1976; Sawaragi, et al. 1976) reported that the maximum transverse force might exceed the maximum in-line force and the total resultant force might be 1.4 to 1.6 times

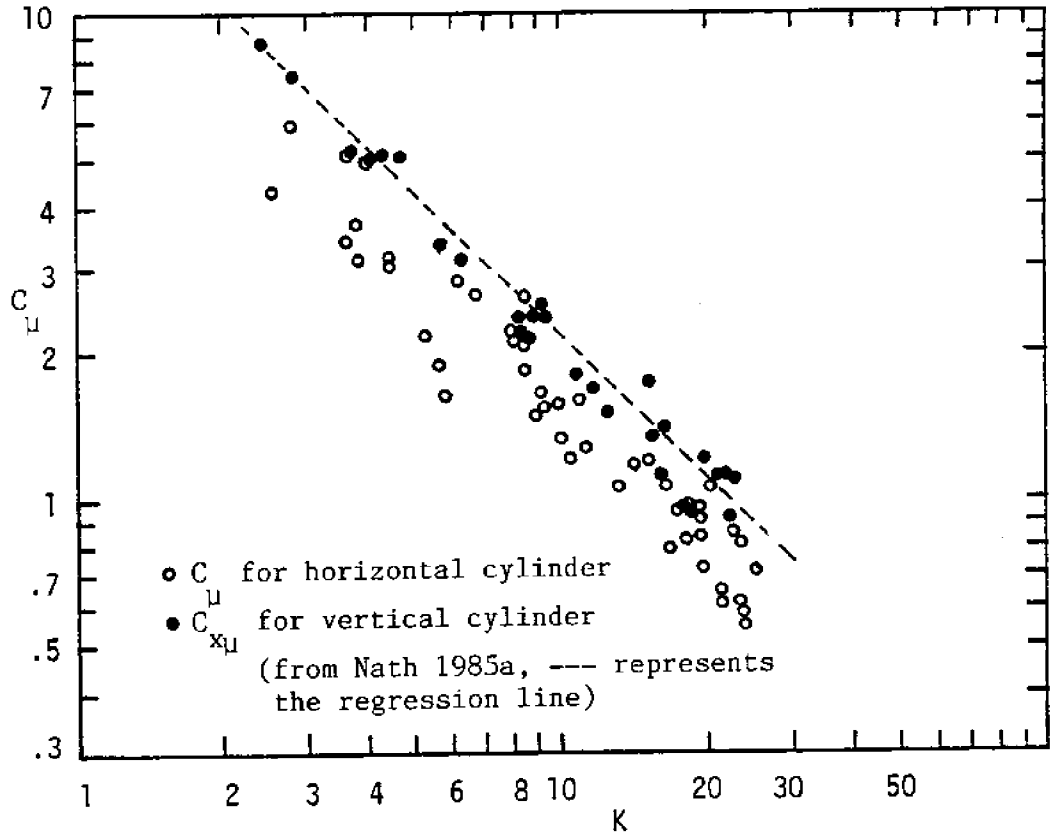

Fig. 5.5-4 Comparison of maximum force coefficients between horizontal and vertical smooth cylinders in waves.

of the in-line force. Sawaragi et al (1976) also reported the phases between the maximum in-line force and the maximum transverse force are close to or, sometimes, coincide with each other. With the transverse force included, the maximum total force coefficient for the vertical cylinder in periodic waves is, naturally, higher than that for the horizontal one. It can be concluded that the maximum total force coefficient for the horizontal cylinder in periodic waves is smaller than either the maximum in-line or the maximum total force coefficient for the vertical cylinder. Thus, the in-line maximum force coefficients for a vertical cylinder can be used to calculate the total maximum force on a horizontal cylinder for engineering design and this will be a conservative design for most cases with $\Omega \neq 0$.

The force coefficients of the first and the second harmonic force for both cylinders in both directions are shown in Figs. 5.5-5 and 5.5-6. In the horizontal direction, $C_x(1)$ values for the vertical cylinder are higher than those for the horizontal cylinder and the values of $C_x(2)$ are at the same level for both cylinders. However, in the perpendicular direction, both $C_z(1)$ and $C_z(2)$ for the horizontal cylinder are greater than those for the vertical cylinder.

From the above discussions, the horizontal force on a vertical cylinder is greater than that on a horizontal cylinder. In the perpendicular direction, the force on a vertical cylinder is smaller than on a horizontal cylinder. Over all, the total force on vertical cylinders is greater than that on horizontal cylinders. This is also true for the sand-roughened cylinders. Figure 5.5-7 shows the C_{tr}

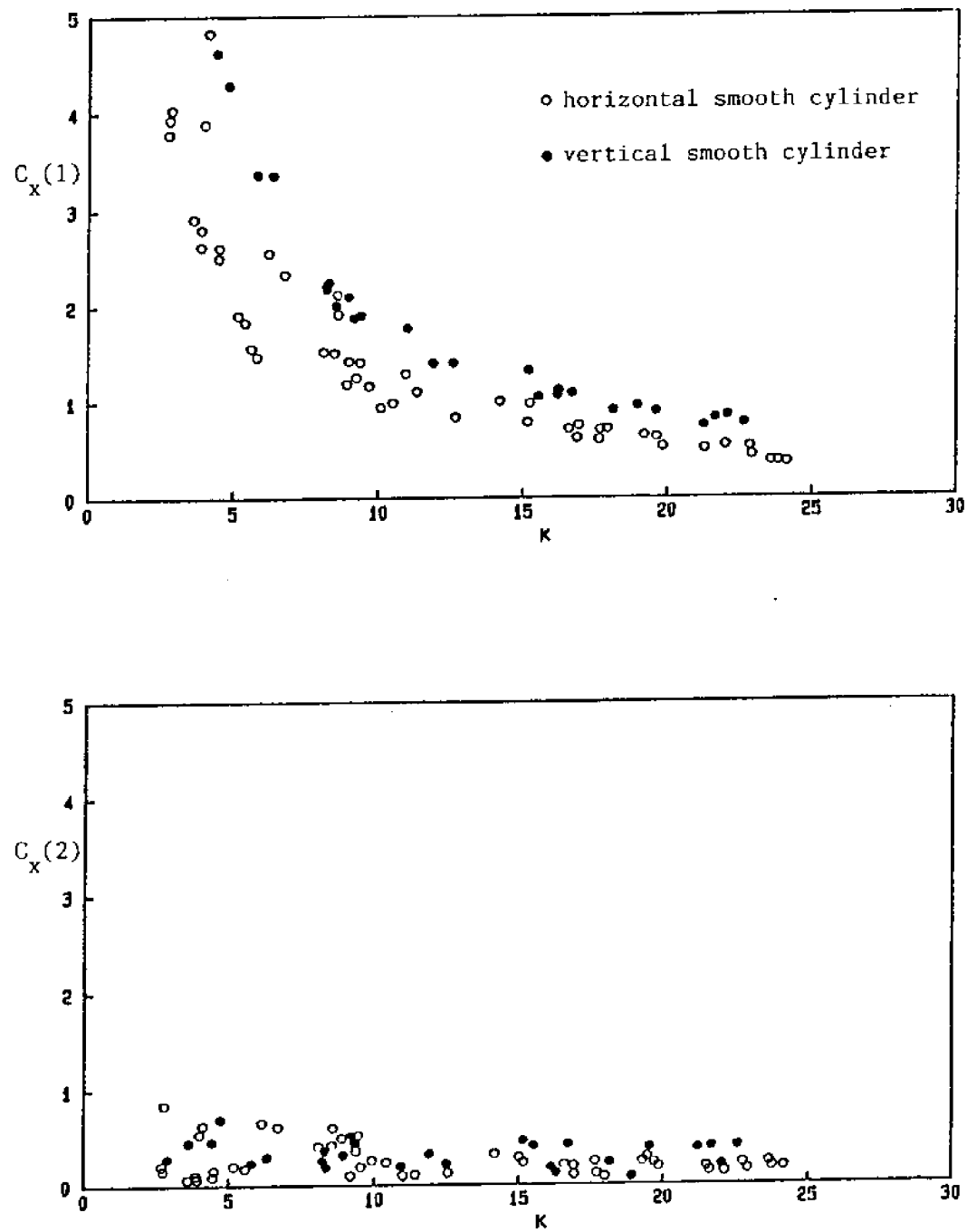

Fig. 5.5-5 Comparison of $C_x(1)$ and $C_x(2)$ between horizontal and vertical smooth cylinders in waves.

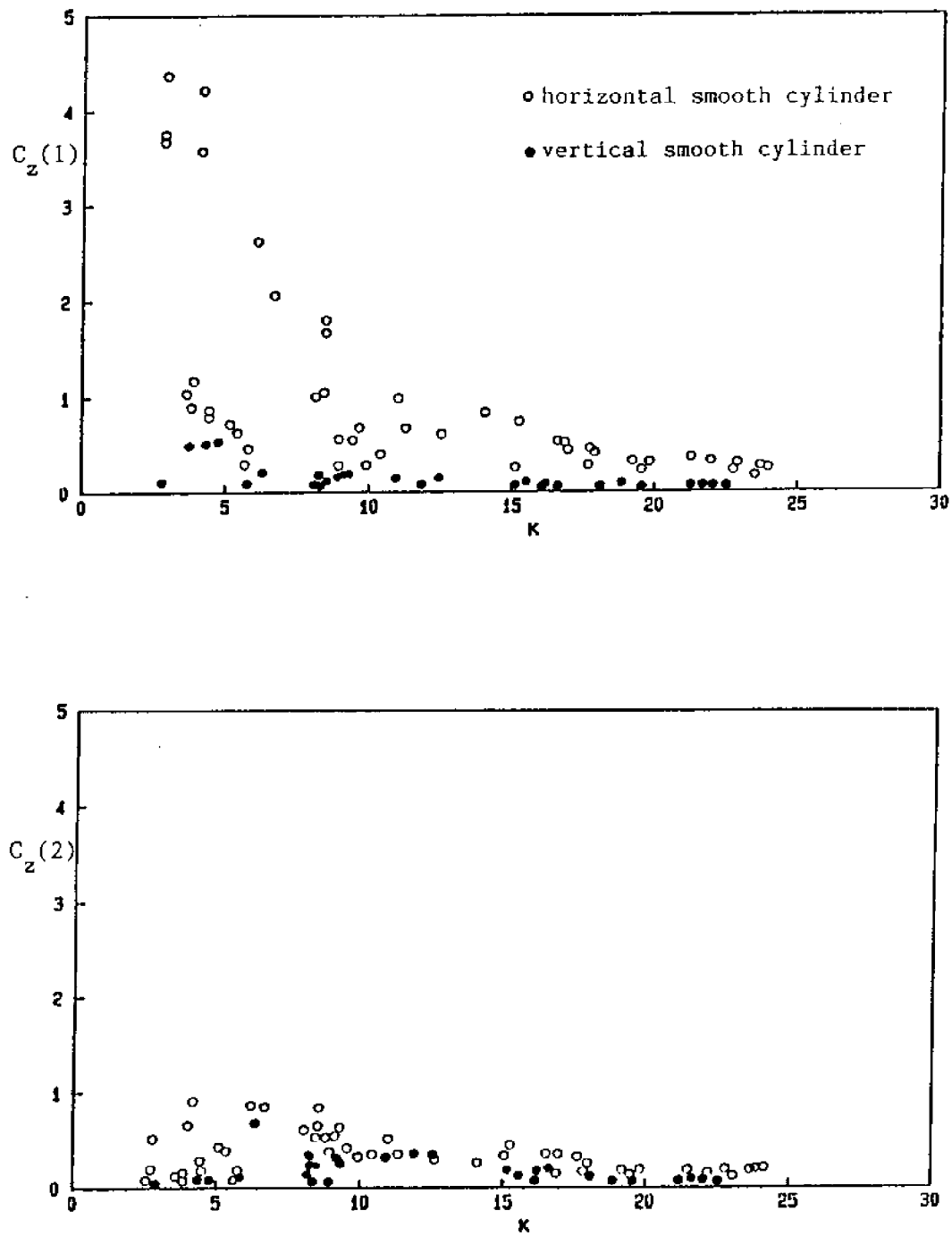

Fig. 5.5-6 Comparisons of $C_z(1)$ and $C_z(2)$ between horizontal and vertical smooth cylinders in waves.

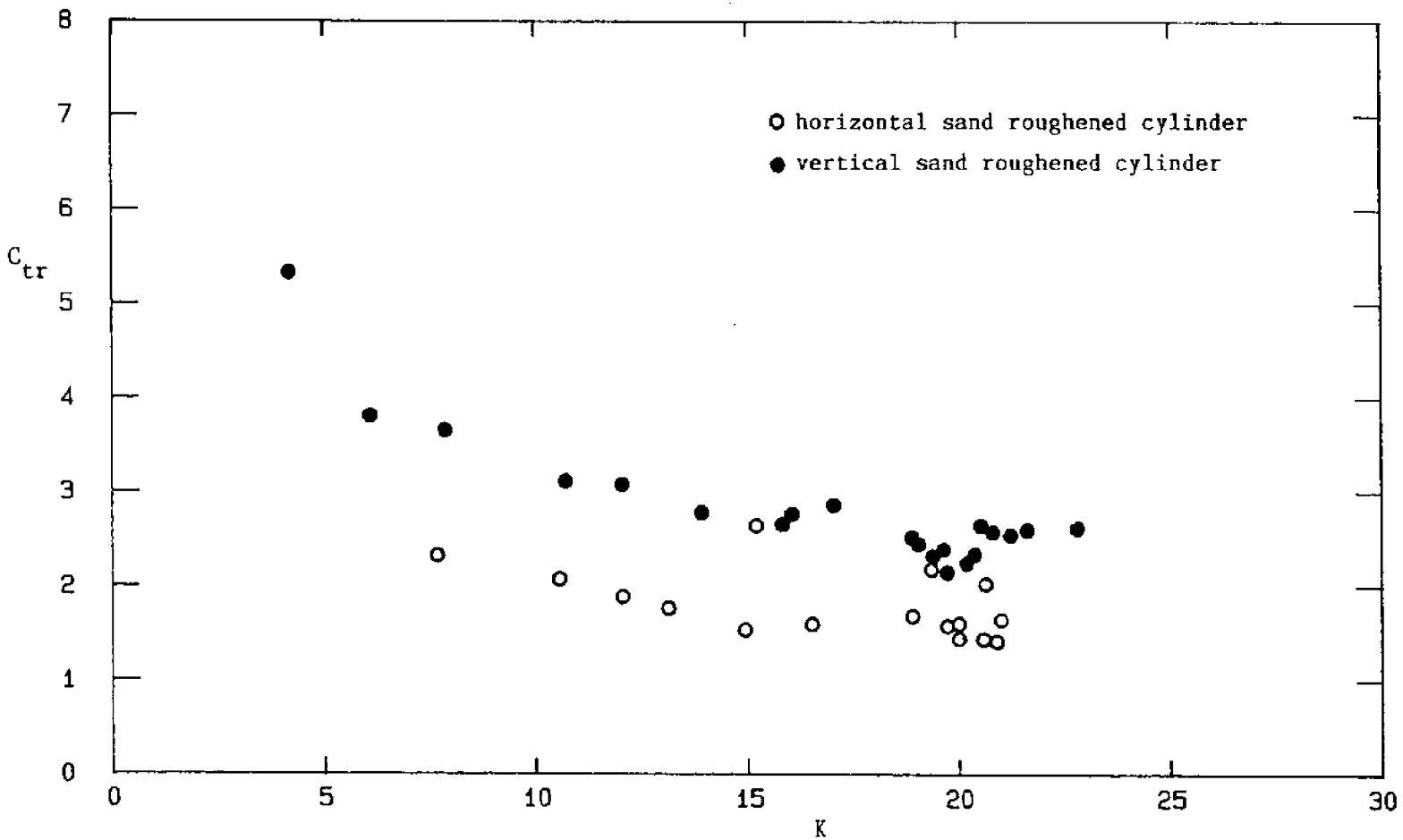

Fig. 5.5-7 Comparison of C_{tr} between horizontal and vertical sand roughened cylinders in waves (all values based on the smooth cylinder diameter).

values for both the horizontal and the vertical sand-roughened cylinder.

From the flow visualization results in Chapter 3, it is seen that the wake formed around a horizontal cylinder rotates or moves around the cylinder (depending on Ω) and the chance that the wake is washed back on to the cylinder (wake encounter effect) reduces as Ω increases. Besides, the formation and movement of wake and vortices around a horizontal cylinder are confined in the horizontal direction and increase in the vertical direction due to the increase of Ω (or vertical velocity). These are thought to be the main reasons that cause the difference of forces between vertical and horizontal cylinders discussed above.

6. FORCES ON HORIZONTAL CYLINDERS UNDER WAVES AND TOWING

As pointed out in Chapter 1, the existence of a current will bias the flow pattern around a cylinder and, thence, affect the hydrodynamic force on it. In this study, a horizontal cylinder in the superposition principle of waves and current is simulated by towing the horizontal cylinder in waves (see Chapter 4). In this chapter, the towing (current) effect on wave forces on horizontal cylinders is studied based on the forces on horizontal cylinders in waves only (as discussed in Chapter 5) and based on the linear superposition principle (as described in Section 2.5).

From the test conditions listed in Section 4.4, the sand-roughened cylinder (HSRC.02) in waves and towing has more data points and is studied here as a base. The data from the rougher cylinders (HBRC.2 and HRAN) are compared to those for HSRC.02.

6.1 Forces Predicted by the Morison Equation

The vector form of the Morison equation, Eq. (2-5), with the linearly superimposed kinematics shown in Eqs. (2-23) to (2-26) is used to predict forces on horizontal cylinders in waves and towing. Again, the least square method (Section 2.3) and the smooth cylinder diameter (D=0.72 ft) were used to determine C_d and C_m. If the effective diameters are desired to be used, C_d and C_m are modified by dividing by the effective diameter factor δ and δ^2, respectively.

Figure 6.1-1 shows the C_d and C_m of the sand-roughened cylinder against K for the waves and towing case together with those for the waves only case. The values of C_d seem to fit quite well between

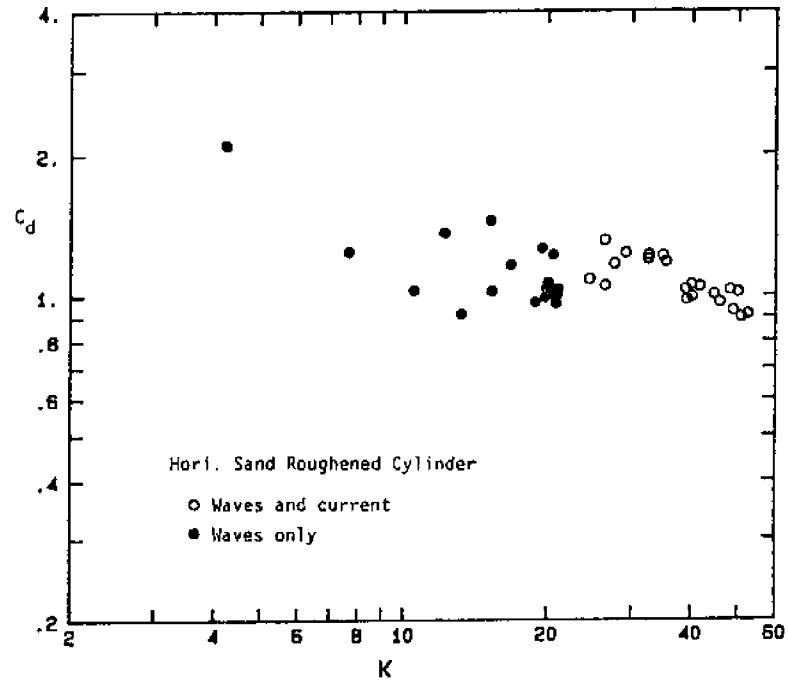

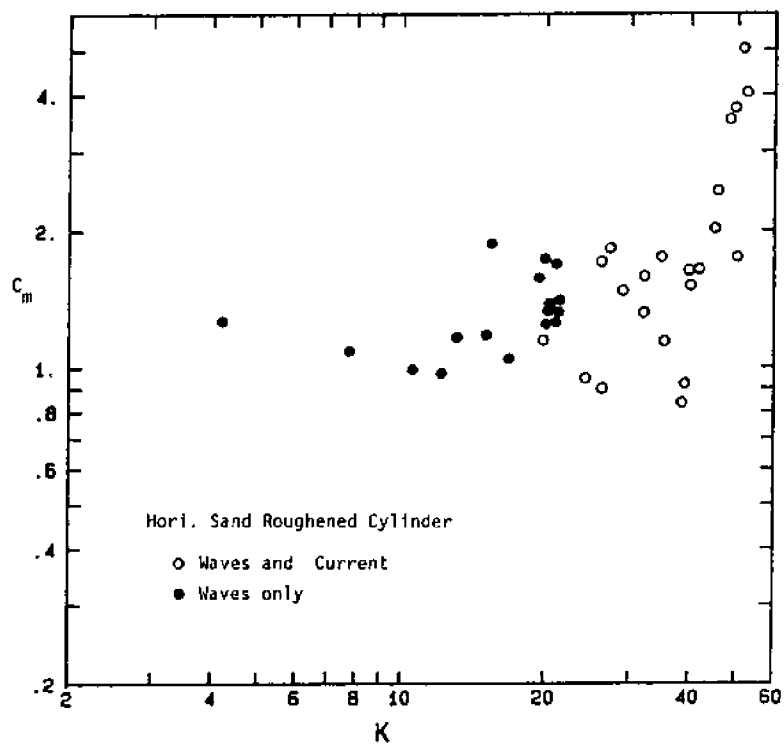

Fig. 6.1-1 C_d and C_m versus K for HSRC.02 under waves and towing (all values based on the smooth cylinder diameter).

these two cases, although they do not overlap. The C_m values for the waves and towing case are widely scattered, especially for those with larger tow (current) velocity (equivalently, with larger K). As indicated by Dean (1976), if the drag forces tend to dominate, the data are better conditioned for determining C_d, and the C_m values tend to be contaminated by errors and are scattered. When a cylinder is towed with steady speed in a wave field, the drag force on the cylinder increases rapidly as the tow velocity increases and the inertia force becomes less and less important. Thus, C_m values for waves and towing are not reliable and are not so important. The C_m values for the HSMC8 are included here only for interest's sake. A more detailed discussion about this point can be found in Teng and Nath (1983).

The values of C_d for HBRC.2 and HRAN are plotted against K in Figs. 6.1-2 and 6.1-3. As seen, these data all fit well with those for the waves only case. Thus, the K defined in Eq. (2-3) for waves and towing [$=(U+u_{w\mu})T/D$, in which $u_{w\mu}$ is the maximum wave-induced velocity] seems to be acceptable when it is considered as an extension of the waves only case.

Similarly to the question raised in Section 5.2, how does the vector form of the Morison equation with the above empirical coefficients, C_d and C_m, predict the measured forces for the waves and towing case? Figures 6.1-4 and 6.1-5 show two examples of comparison between measured forces and forces predicted by the Morison equation for U=1.80 and 4.94 ft/sec ($U/u_{w\mu}$ = 0.56 and 1.42, respectively. From these two examples, it can be seen that predictions in both

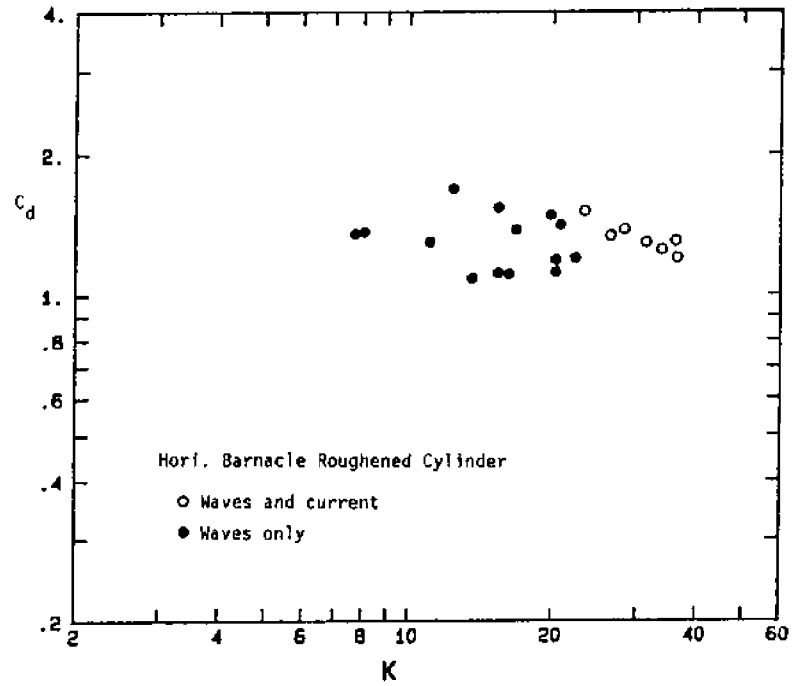

Fig. 6.1-2 C_d versus K for HBRC.2 under waves and towing (all values based on the smooth cylinder diameter).

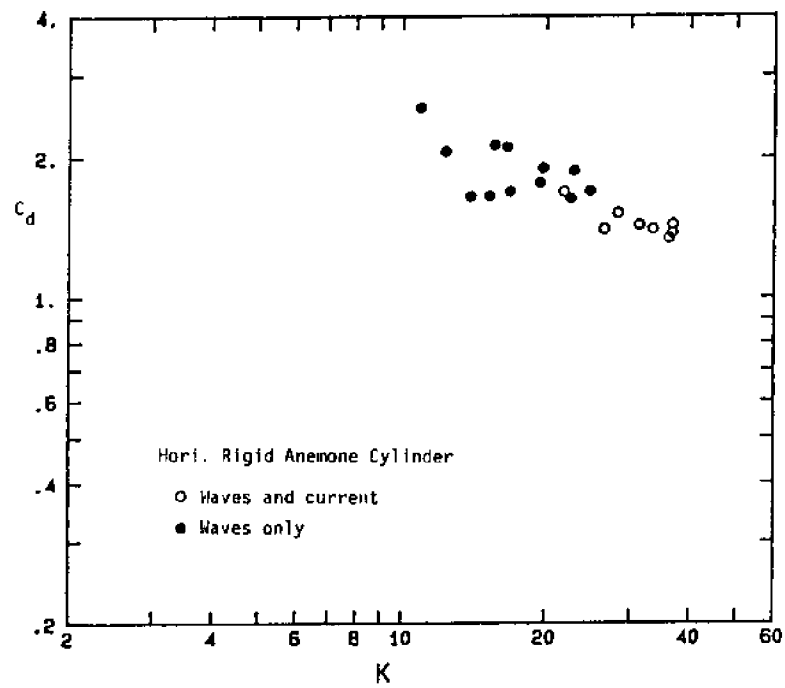

Fig. 6.1-3 C_d versus K for HRAN under waves and towing (all values based on the smooth cylinder diameter).

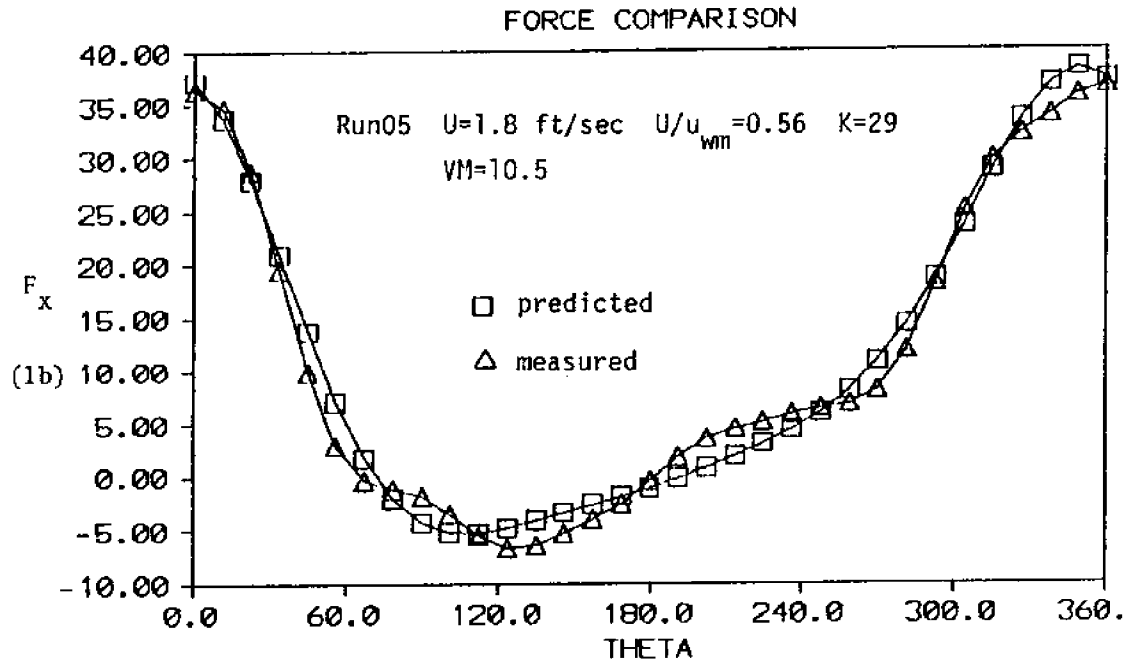

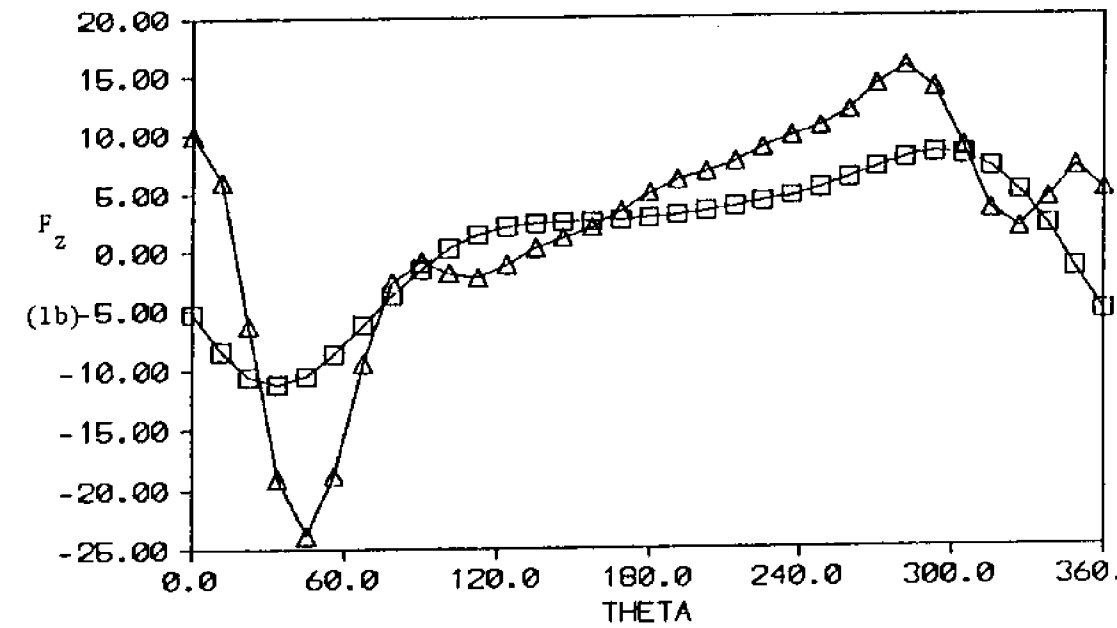

Fig. 6.1-4 Comparison between measured and predicted forces under waves and towing ($U/u_{w\mu}$ = 0.56).

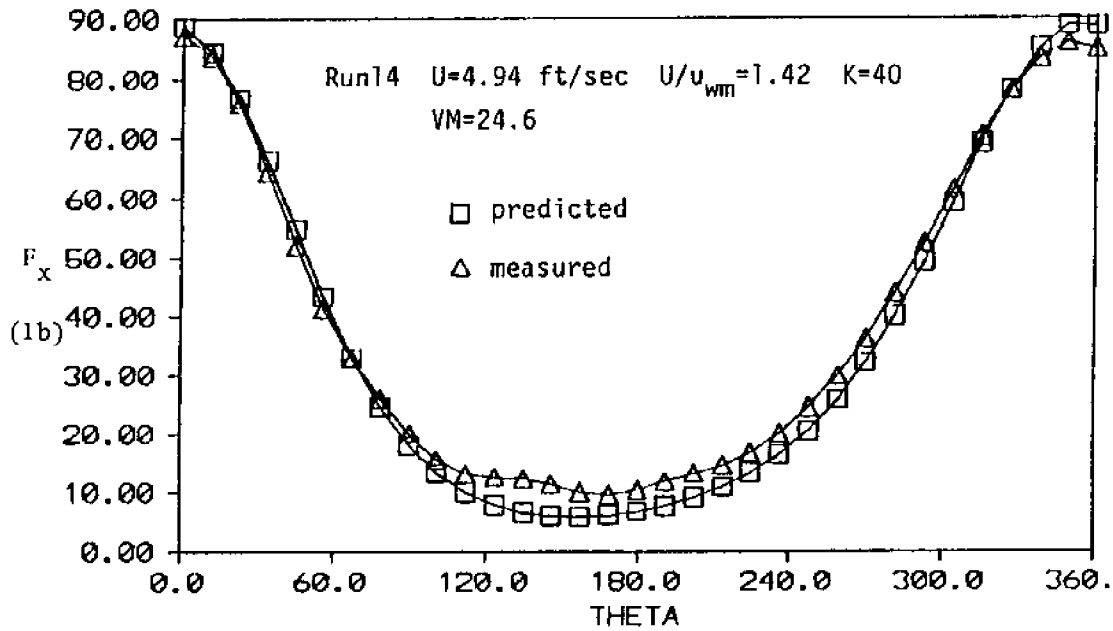

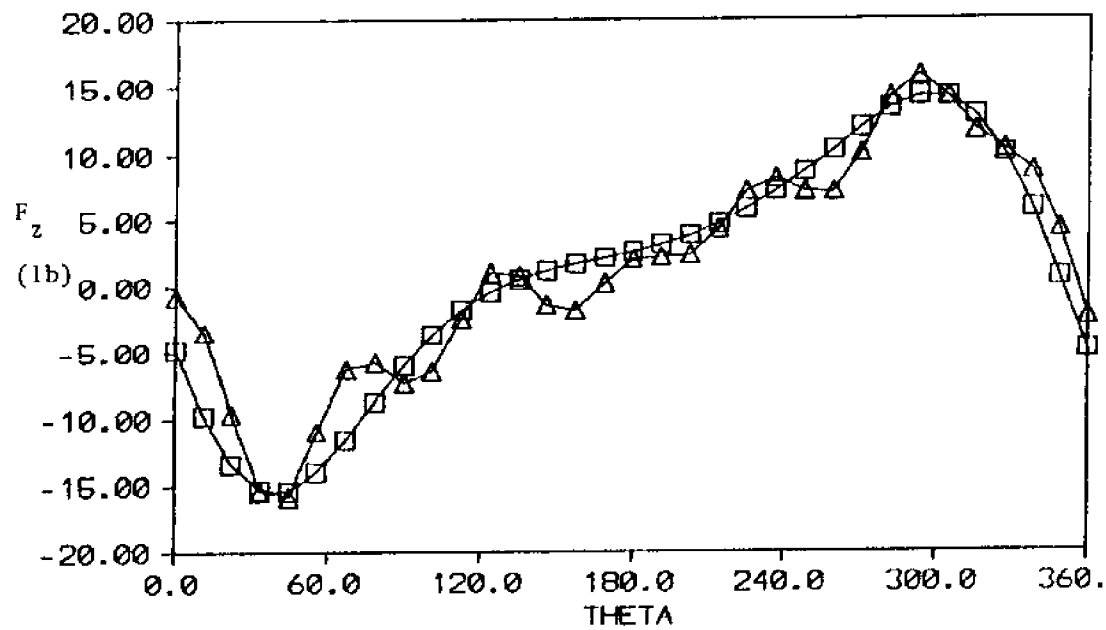

Fig. 6.1-5 Comparison between measured and predicted forces under waves and towing ($U/u_{wμ}$ = 1.42).

directions for larger U match the measurements better than those for smaller U. Table 6-1 presents the values of the ratio of the maximum predicted total force to the maximum measured total force, $(F_p)_\mu/(F_m)_\mu$, and the rms error as defined in Eq. (5.2-1) for three roughened cylinders (HSRC.02, HBRC.2 and HRAN) in waves and towing. Based on these two indicators, it seems predictions of forces on horizontal cylinders for the waves and towing case by using the vector form of the Morison equation are much better than those for the waves only case (see Table 5-2).

The C_d values for all three cylinders are plotted against the relative velocity, $U/u_{w\mu}$, in Fig. 6.1-6. Note that test runs for each cylinder have almost the same wave conditions (see Table 4-2) with different tow velocities. For the sand roughened cylinder (HSRC.02), the C_d value for the waves only case with the same wave condition is around 1.0 (from Section 5.2). As a cylinder is towed in the wave field, C_d values become larger than those for the waves only case for $U/u_{w\mu} < 1.2$ and they drop quickly as $U/u_{w\mu} > 1.2$. For HBRC.2 and HRAN, only one data point is below $U/u_{w\mu} = 1.2$, however, the values of C_d for $U/u_{w\mu} > 1.2$ are all smaller than that point.

For $U/u_{w\mu} > 1.0$, the horizontal velocity, which is always positive and varies from $U-u_{w\mu}$ to $U+u_{w\mu}$, is in the opposite direction of the towing and does not reverse. This flow may be called the "uni-directional oscillatory flow." If the wake and vortices are washed back upon the cylinder, the actual velocity around the cylinder increases and, thence, the induced force increases (it is called wake encounter effect, see Heideman, et. al 1979). For $U/u_{w\mu} > 1.0$, the

Table 6-1. RMS errors and maximum force ratios for forces predicted by the vector form of the Morison equation under waves and towing.

Cylinder	U	K	VM	U/u_{wu}	rms error	$\frac{(F_p)_u}{(F_m)_u}$
HSRC.02 (T=4.6sec H=4.0ft)	1.22	26.55	7.30	0.34	0.251	1.01
	1.27	26.33	7.58	0.36	0.280	0.91
	1.16	24.53	6.96	0.36	0.236	0.91
	1.80	29.10	10.44	0.56	0.208	0.93
	1.80	27.36	10.44	0.55	0.181	0.98
	2.96	32.35	16.18	0.90	0.186	0.91
	2.99	32.28	16.32	0.92	0.159	0.97
	3.69	34.76	19.46	1.14	0.153	0.92
	3.73	35.38	19.63	1.12	0.170	0.91
	4.37	39.03	22.32	1.20	0.114	0.99
	4.33	38.68	22.15	1.20	0.140	0.94
	4.93	39.84	24.53	1.44	0.115	0.93
	4.94	39.86	24.44	1.42	0.081	1.01
	5.74	41.71	27.55	1.74	0.088	0.98
	6.95	45.48	31.69	2.06	0.091	0.97
	6.91	44.95	31.55	2.11	0.078	1.00
	8.00	48.09	34.95	2.38	0.079	1.01
	8.44	48.96	36.23	2.55	0.082	1.00
	8.52	49.94	36.46	2.43	0.116	1.10
	9.05	51.18	37.94	2.57	0.103	1.15
	9.59	52.02	39.39	2.80	0.116	1.15
				mean =	0.14	0.98
				standard deviation =	0.06	0.07
HBRC.2 (T=3.7sec H=3.5ft)	2.41	23.39	11.73	1.01	0.18	1.02
	3.61	26.49	15.16	1.34	0.12	1.00
	4.57	28.18	18.31	1.85	0.09	0.99
	5.94	31.33	22.31	2.47	0.06	1.00
	7.07	33.86	25.17	2.90	0.05	1.01
	8.28	36.23	28.10	3.46	0.08	0.99
	9.14	36.23	29.87	3.80	0.08	0.96
				mean =	0.09	1.00
				standard deviation =	0.04	0.02
HRAN (T=3.7sec H=3.5ft)	2.49	21.95	11.22	1.05	0.10	0.98
	3.57	26.68	15.14	1.31	0.12	0.98
	4.60	28.37	18.55	1.89	0.08	0.98
	5.95	31.36	22.26	2.45	0.11	0.98
	6.82	33.39	24.57	2.78	0.11	0.98
	8.00	36.29	27.37	3.07	0.14	1.11
	8.55	36.87	28.66	3.49	0.14	1.10
	8.52	37.07	28.56	3.36	0.12	1.02
				mean =	0.12	1.02
				standard deviation =	0.02	0.06

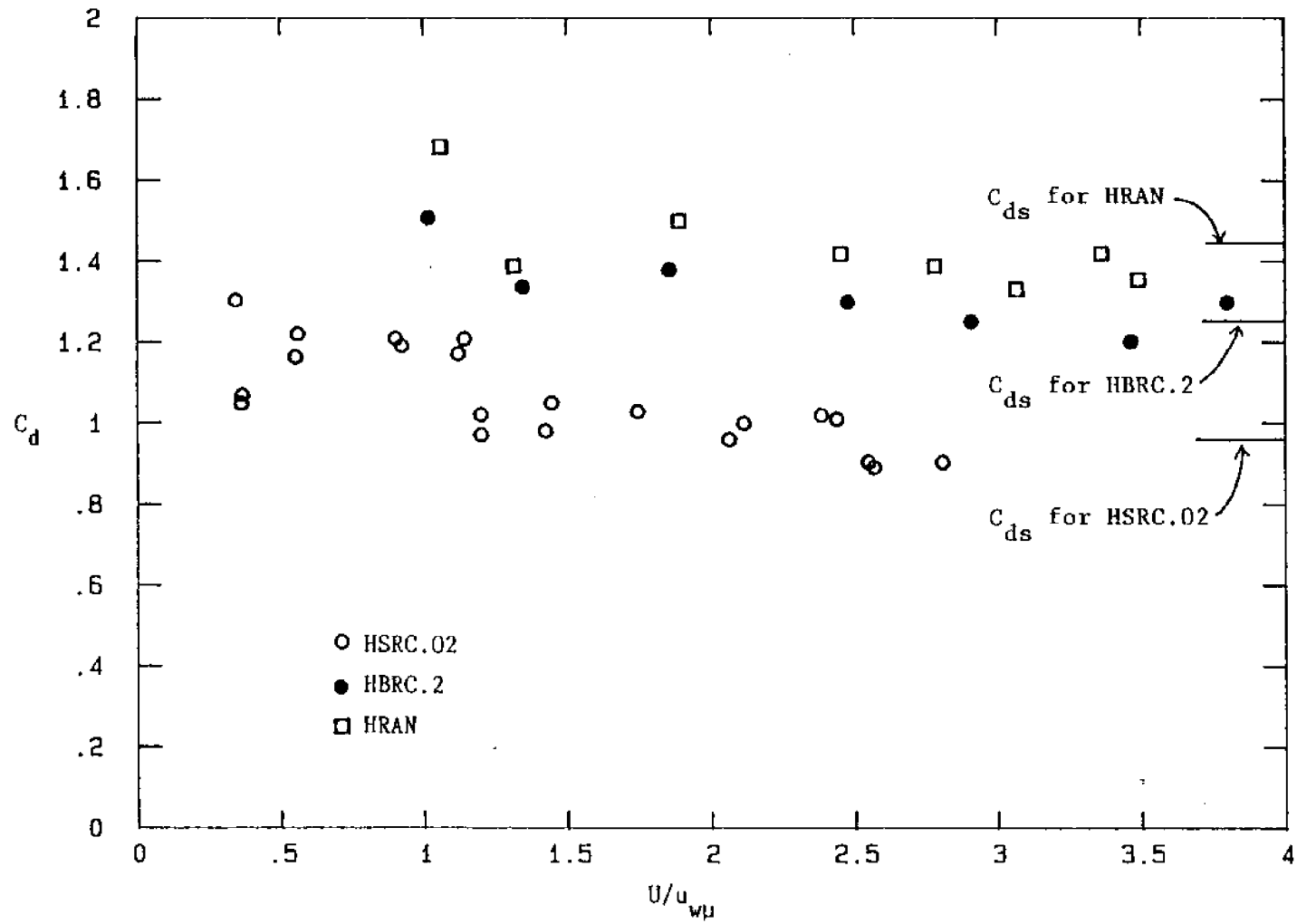

Fig. 6.1-6 C_d versus U/u_{wu} for roughened cylinders in waves and towing (all values based on the smooth cylinder diameter).

wake and vortices are not washed back upon the cylinder. Under this circumstance, the wake encounter effect vanishes and the force drops down.

One might wonder why the C_d does not drop down exactly at $U/u_{w\mu} = 1.0$. For $U=u_{w\mu}$, there is an instant that the combined velocity is zero. Due to deceleration of flow, a portion of formed vortices and wake might have a chance to move back on to the cylinder. For $U/u_{w\mu} > 1.2$, the smallest relative velocity is $0.2\ u_{w\mu}$ and the chance for the vortices and wake to move back on to the cylinder is nil. This needs to be verified in some way; possibly by a flow visualization experiment.

For large $U/u_{w\mu}$, C_d for waves and towing approaches the value of the steady flow drag coefficient, C_{ds}. Note that C_{ds} is 0.95 for the HSRC.02, 1.25 for the HBRC.2 and 1.45 for the HRAN (Nath 1984a and 1985b) as marked in Fig. 6.1-6.

Figure 6.1-7 shows the values of C_d for all three roughened cylinders versus Verley-Moe number (VM = UT/D, see Section 2.1). The data for the smooth and sand-roughened cylinder from Teng and Nath (1983, 1985) are plotted in this figure as dashed and solid lines, respectively. For the HSRC.02, our new data (1984 API project) fit well with our old data (1982 API project), especially for large VM. The old data with small tow velocity (VM < 5) decrease and are smaller than those for the waves only case (C_d=1.0). Matten (1976) reported that C_d decreases for a very small current, and then increases as the current increases. Our old data with very small

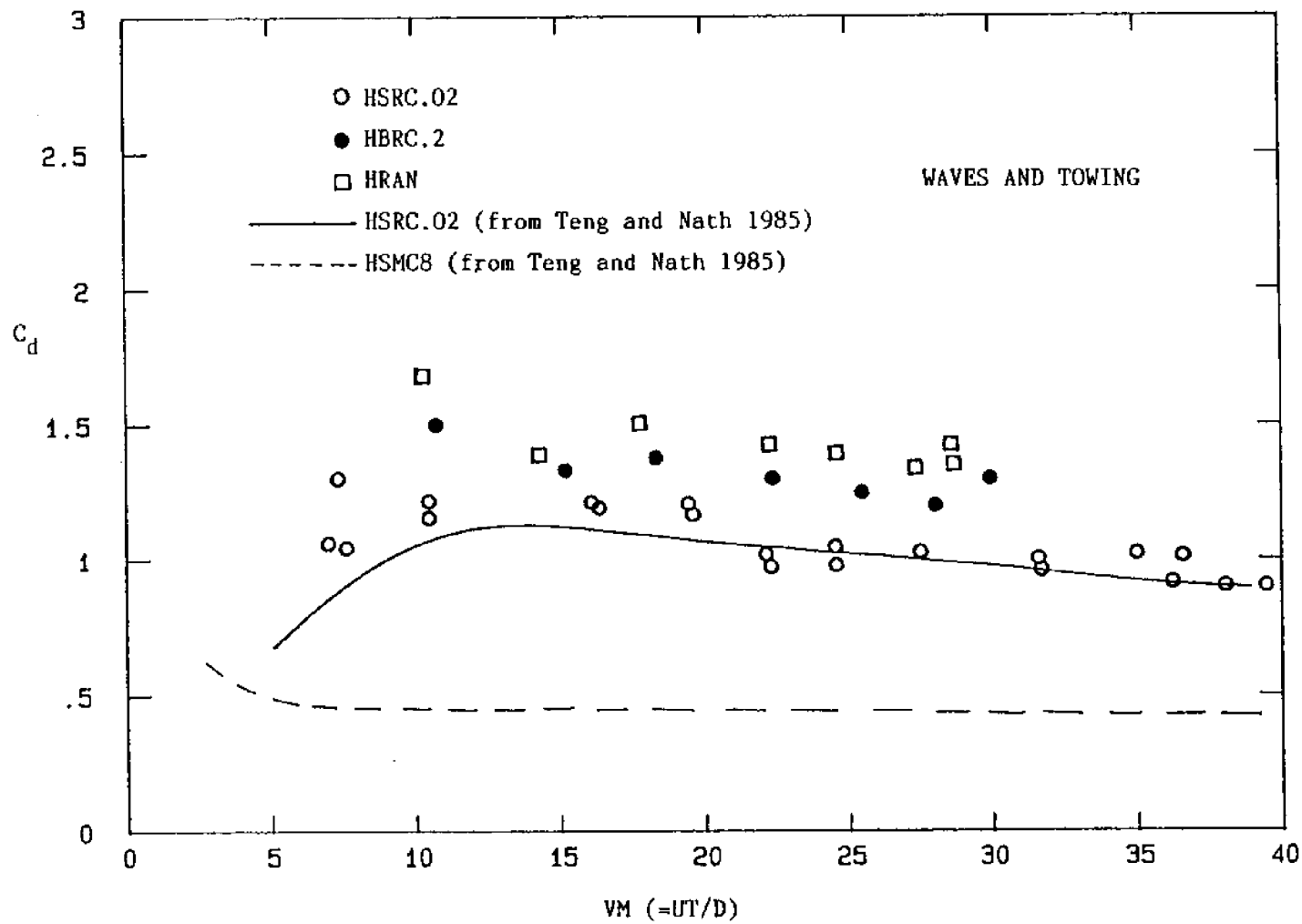

Fig. 6.1-7 C_d versus VM for cylinders in waves and towing (all values based on the smooth cylinder diameter).

currents (about VM=5) seem to have the same trend but the data points are not enough to support this result.

6.2 Maximum and Root-Mean-Square Forces

The root-mean-square and the maximum force coefficients, i.e., C_{xr}, C_{zr}, C_{tr}, and C_{μ}, used in this section have similar definitions as in Section 5.3, i.e., Eqs. (5.3-1) to (5.3-4). The only modification is that the total velocity (tow velocity + wave-induced velocity) is used as the normalization factor instead of the wave-induced velocity.

Figure 6.2-1 presents the values of the horizontal rms force coefficient, C_{xr}, for the sand roughened cylinder (HSRC.02) in waves and towing. The data for the same cylinder in waves only from Section 5.3 are plotted as circles. The solid circles represent the data for waves only that have the same wave period T (equivalently, the same Ω or β) as those for waves plus towing. Recall that all data of the HSRC.02 in waves and towing have the same wave period (T = 4.6 sec.) and similar wave height (H = 4 ft). The ranges of relative velocity, $U/u_{w\mu}$, are also marked in this figure. Considering the data with the same T (or Ω), it is clear that the horizontal rms force coefficient increases as towing is introduced. As tow velocity continues to increase, it starts to decrease. When the relative velocity is greater than 1.2, this force coefficient decreases rapidly. This trend is similar to that for C_d as presented in Section 6.1.

The vertical and the total rms force coefficients for HSRC.02 in waves and towing are shown in Figs. 6.2-2 and 6.2-3 with the same

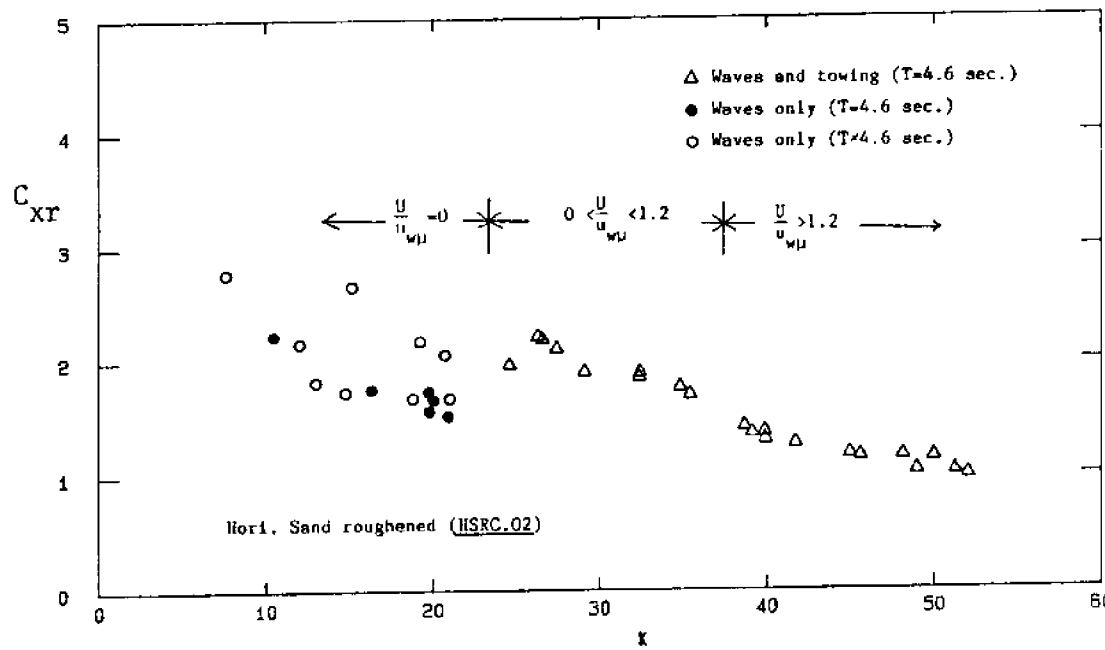

Fig. 6.2-1 C_{xr} versus K for HSRC.02 under waves and towing (all values based on the smooth cylinder diameter).

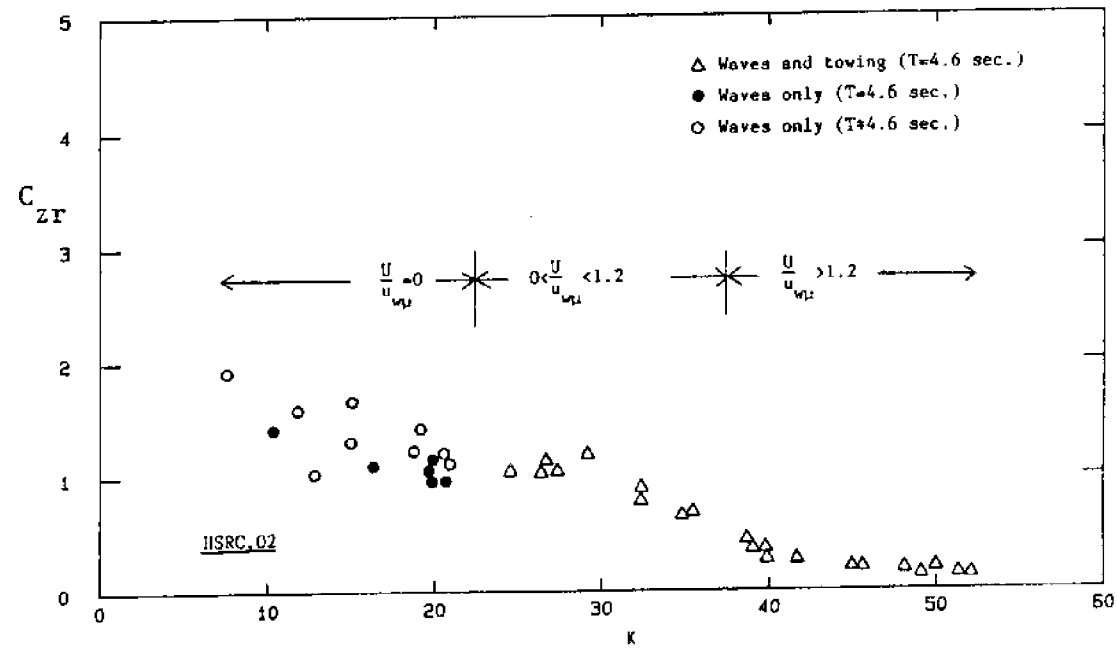

Fig. 6.2-2 C_{zr} versus K for HSRC.02 under waves and towing (all values based on the smooth cylinder diameter).

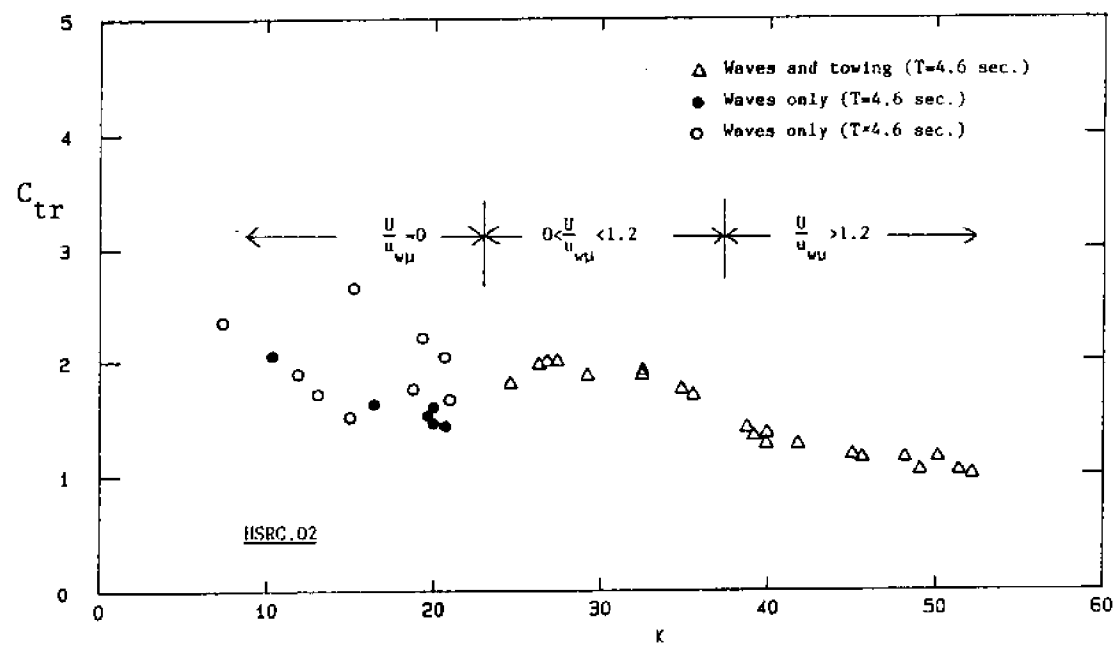

Fig. 6.2-3 C_{tr} versus K for HSRC.02 under waves and towing (all values based on the smooth cylinder diameter).

format as in Fig. 6.2-1. The same trend as C_{xr} is observed for C_{tr}. The C_{zr} just increases a little as the towing is introduced. As tow velocity increases, it decreases. After $U/u_{w\mu}$=1.2, it drops down rapidly and becomes very small. Over all, it can be said the rms force coefficients increase as the cylinder is towed into the wave field, and then they decrease rapidly as the tow velocity is greater than the maximum wave-induced velocity. A reasonable conjecture is that the same behavior would be in evidence for waves plus current, using the linear superposition principle.

The values of C_{xr} versus K for two rougher cylinders (HBRC.2 and HRAN) with those for the HSRC.02 are presented in Fig. 6.2-4 and they correlate well with K. The C_{xr} for the HRAN is a little higher than that for HBRC.2, but no difference can be observed if the effective diameters are used. The values of C_{xr} for the HSRC.02 seems a little higher than those for the rougher HBRC.2 and HRAN. The reason is thought to be the different T (Ω or β) used for these cylinders (T = 4.6 sec. for HSRC.02 and T = 3.7 sec. for HBRC.2 and HRAN). Thus, some other parameters should be considered when studying horizontal cylinders under waves and towing (current).

Actually, the K for waves plus towing [$=(U+u_{w\mu})T/D$] contains VM ($=UT/D$) and K for wave only case ($u_{w\mu}T/D$). Figure 6.2-5 shows the values of C_{xr} versus VM. The C_{xr} values for these three cylinders decrease as VM increases. From this figure, it seems that C_{xr} values for HSRC.02 are equal to or just a little smaller than those for HBRC.2 and HRAN although the e/D value for HSRC.02 is much smaller than for HBRC.2 and HRAN. Note that, for the waves only case, C_{xr}

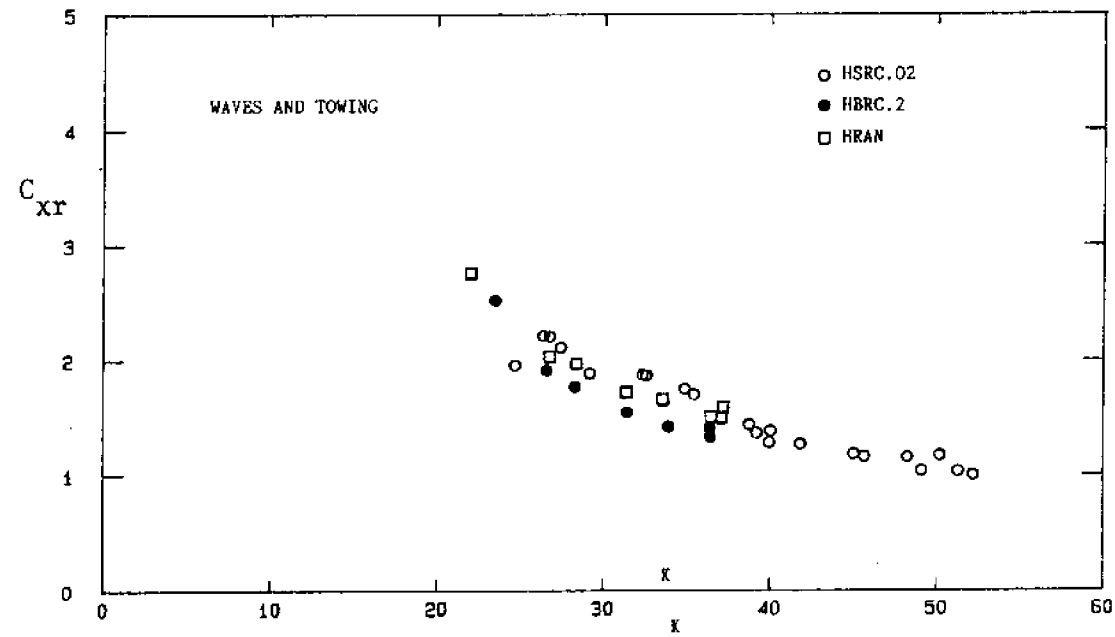

Fig. 6.2-4 C_{xr} versus K for horizontal cylinders under waves and towing (all values based on the smooth cylinder diameter).

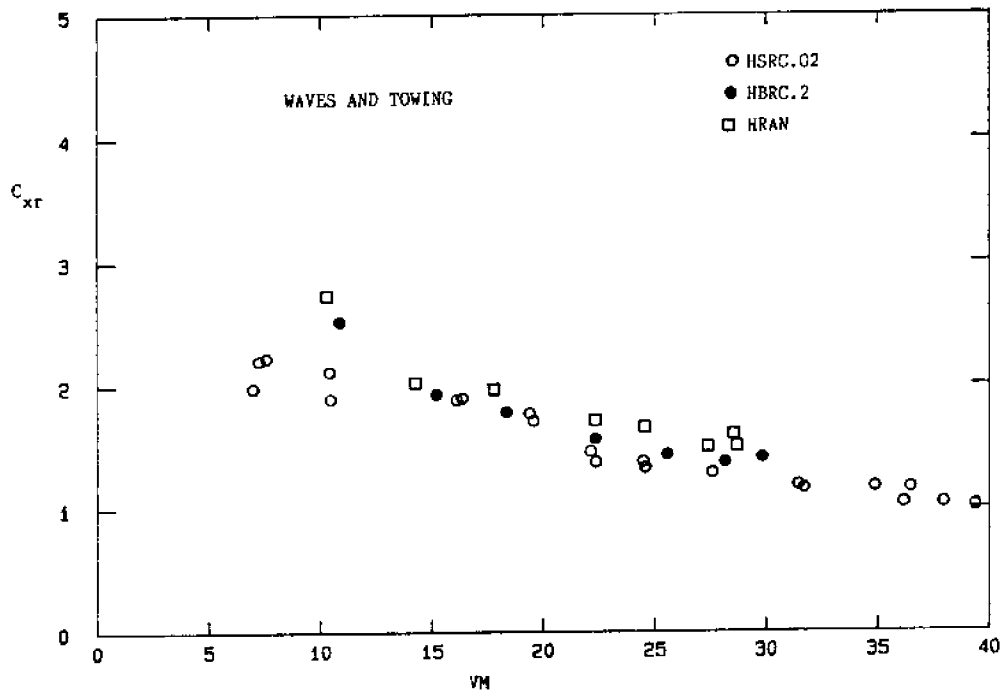

Fig. 6.2-5 C_{xr} versus VM for horizontal cylinders under waves and towing (all values based on the smooth cylinder diameter).

values for HSRC.02 are much smaller than those for the other two cylinders as shown in Fig. 5.3-5.

Figure 6.2-6 shows these data against relative velocity, $U/u_{w\mu}$. In this figure, the data for HSRC.02, unlike in Figs. 6.2-4 and 6.2-5, are clearly smaller than those for HBRC.2 and HRAN. The parameter $U/u_{w\mu}$ indicates the degree of the bias of a wake, i.e., the larger the $U/u_{w\mu}$, the greater the bias. If the U is greater than the $u_{w\mu}$ (it is called "uni-directional oscillatory flow," see Section 6.1), the wake forms on the lee side of the cylinder only. Thus, this parameter is important when the towing (current) effect for a fixed wave condition is considered.

The values of C_{zr} for three roughened cylinders versus $U/u_{w\mu}$ are shown in Fig. 6.2-7. The differences of C_{zr} between different roughened cylinders are clear. Again, the C_{zr} values drop down significantly for $U/u_{w\mu} > 1.2$. The total rms force coefficients (C_{tr}) for the HBRC.2 and HRAN have the same tendency as C_{xr} and are not repeatedly reported here.

The maximum force coefficients, C_μ for both the waves only case and the waves plus towing case are plotted in Figs. 6.2-8 to 6.2-10 for three roughened cylinders, respectively. The data for the waves only case and for the waves and towing case connect well. Combining this result with that of C_d in Section 5.1, it is thought the use of K defined in Eq. (2-3) and the use of $U+u_{w\mu}$ to estimate kinematics are acceptable for determining C_d and C_μ when the waves and towing case is considered as an extension of the waves only case. The results of C_μ for the rougher cylinders HBRC.2 and HRAN seem to

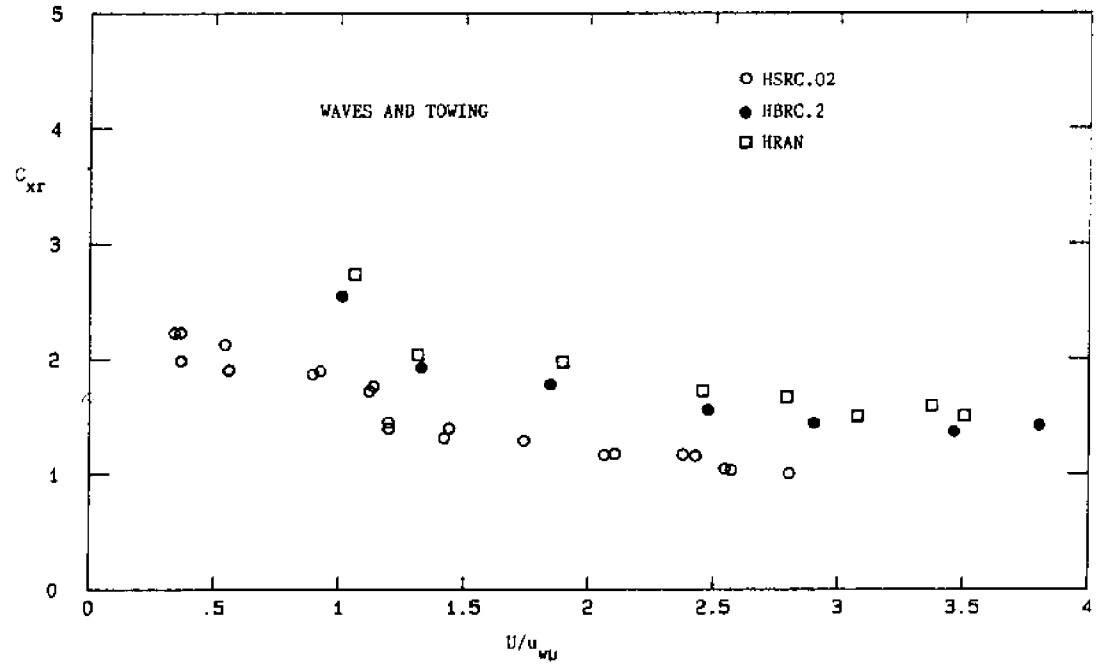

Fig. 6.2-6 C_{xr} versus U/u_{wu} for horizontal cylinders under waves and towing (all values based on the smooth cylinder diameter).

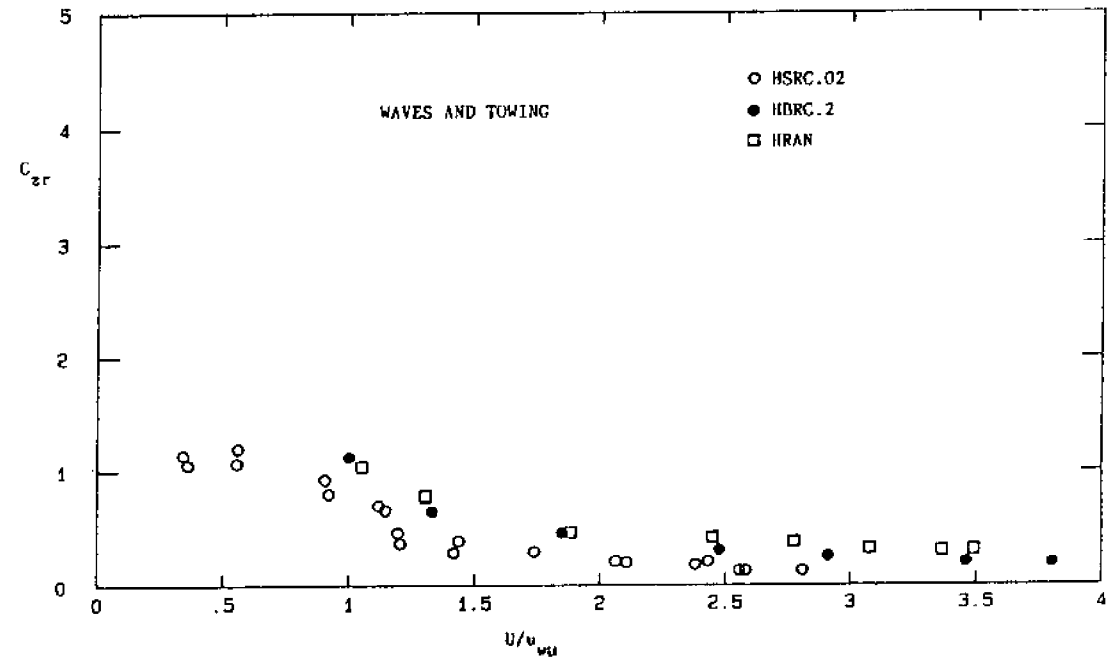

Fig. 6.2-7 C_{zr} versus U/u_{wu} for horizontal cylinders under waves and towing (all values based on the smooth cylinder diameter).

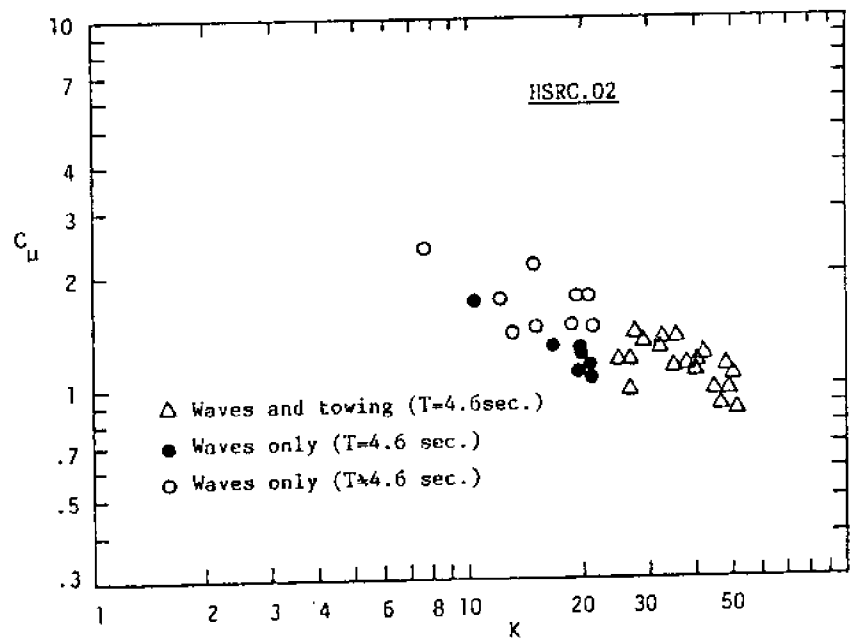

Fig. 6.2-8 C_μ versus K for HSRC.02 under waves and towing (all values based on the smooth cylinder diameter).

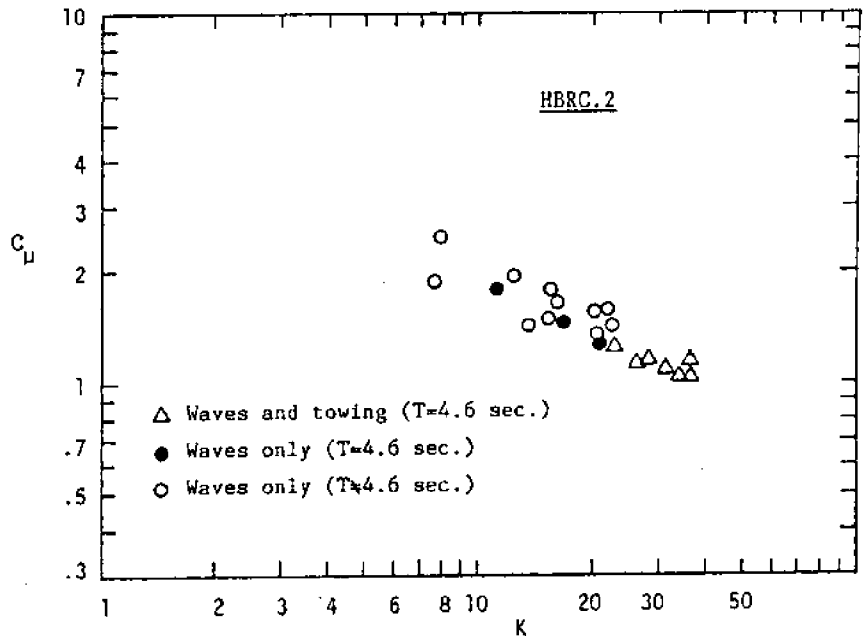

Fig. 6.2-9 C_μ versus K for HBRC.2 under waves and towing (all values based on the smooth cylinder diameter).

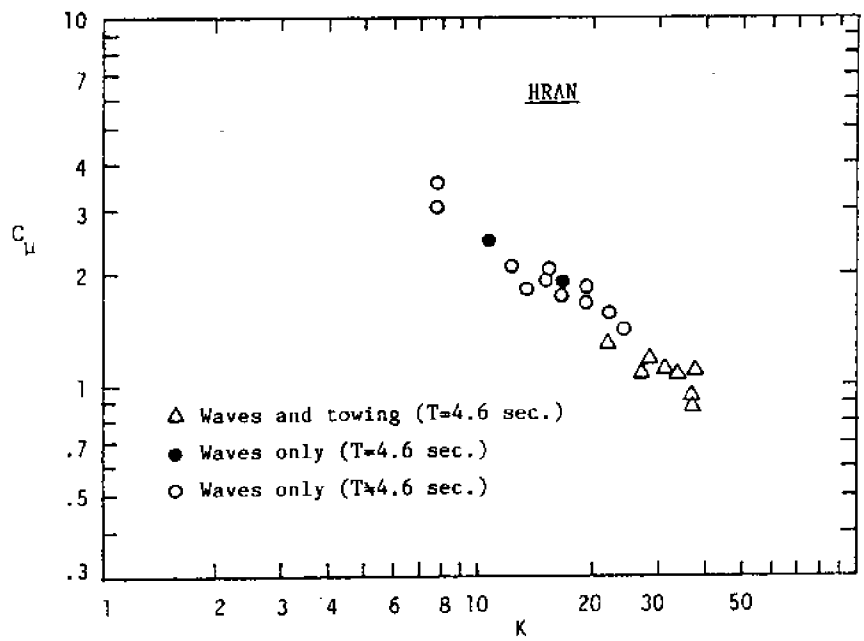

Fig. 6.2-10 C_μ versus K for HRAN under waves and towing (all values based on the smooth cylinder diameter).

posses less scatter than those for the HSRC.02 as shown in Figs. 6.2-8 to 6.2-10. It is also observed that dC_μ/dK (the slope of the best fit line) becomes steep as e/D increases. But, the C_μ for the waves only case increases as e/D increases. Thus, the C_μ for the waves and towing case does not have pronounced increase due to the increase of e/D.

Figure 6.2-11 shows the C_μ values for all three cylinders versus relative velocity, $U/u_{w\mu}$. It seems that C_μ values for three roughened cylinders under waves and towing are at the same range and no clear difference is observed. Note that the smooth cylinder diameter is used to evaluate C_μ and K.

6.3 Harmonic Analysis of Forces

In this section, the forces on horizontal cylinders under waves and towing are decomposed into harmonic components by using Fourier Analysis to study towing (current) effect on wave forces.

Intuitively, the steady horizontal force increases rapidly as the tow (current) velocity increases. The steady horizontal force coefficients, which are normalized by the square of the towing velocity ($=U^2$, which is also the maximum of the steady component of the total velocity square), for all three cylinders (HSRC.02, HBRC.2 and HRAN) are shown in Fig. 6.3-1. Values of this coefficient correlate well with $U/u_{w\mu}$ and decrease rapidly for $U/u_{w\mu} > 1.2$. As the tow velocity becomes very large, the $C_x(0)$ for each cylinder approaches their associated steady flow drag coefficient, C_{ds}. The steady flow drag coefficients for these three cylinders marked on the figure were reported by Nath (1984a,1985b). Thus, for large tow

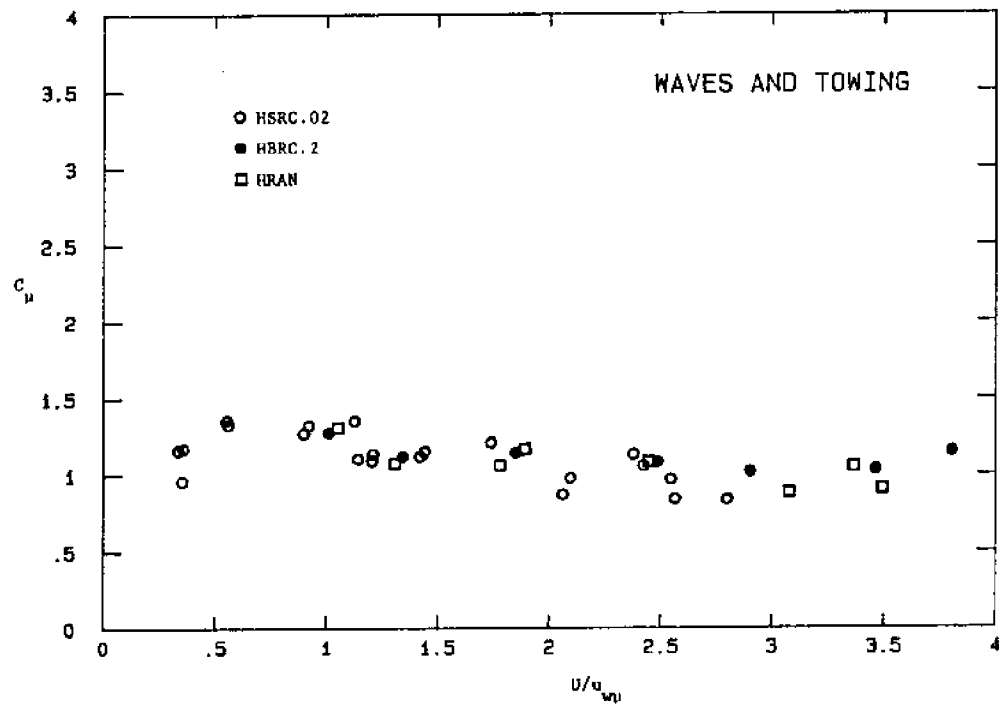

Fig. 6.2-11 C_μ versus $U/u_{w\mu}$ for roughened horizontal cylinders under waves and towing.

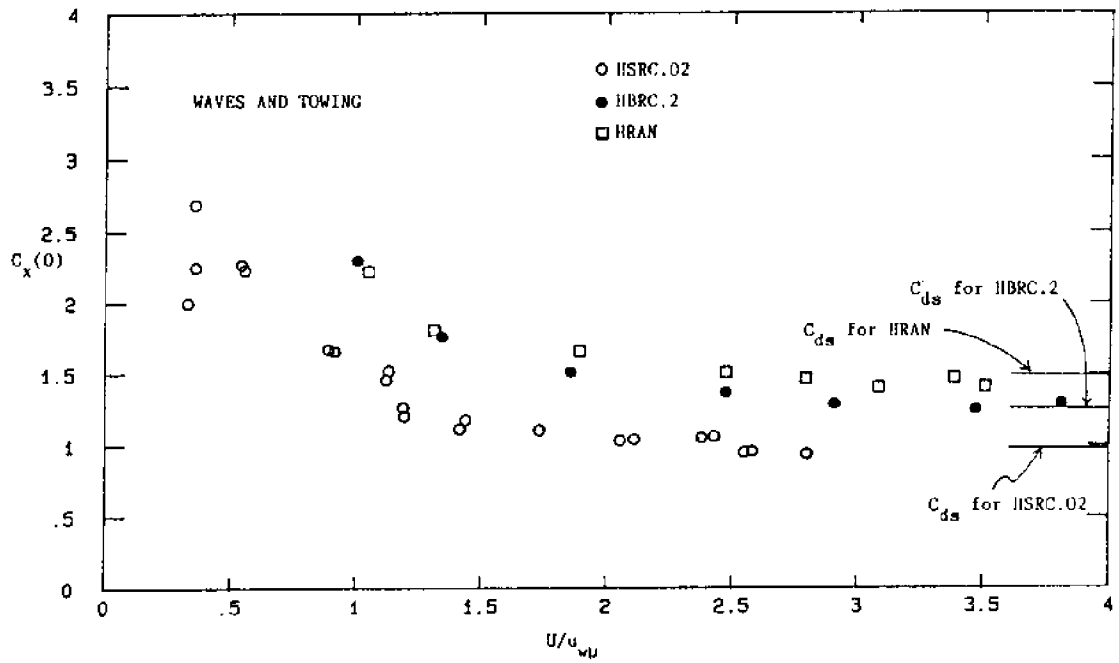

Fig. 6.3-1 $C_x(0)$ (based on U^2) versus U/u_{wu} for horizontal cylinders under waves and towing (all values based on the smooth cylinder diameter).

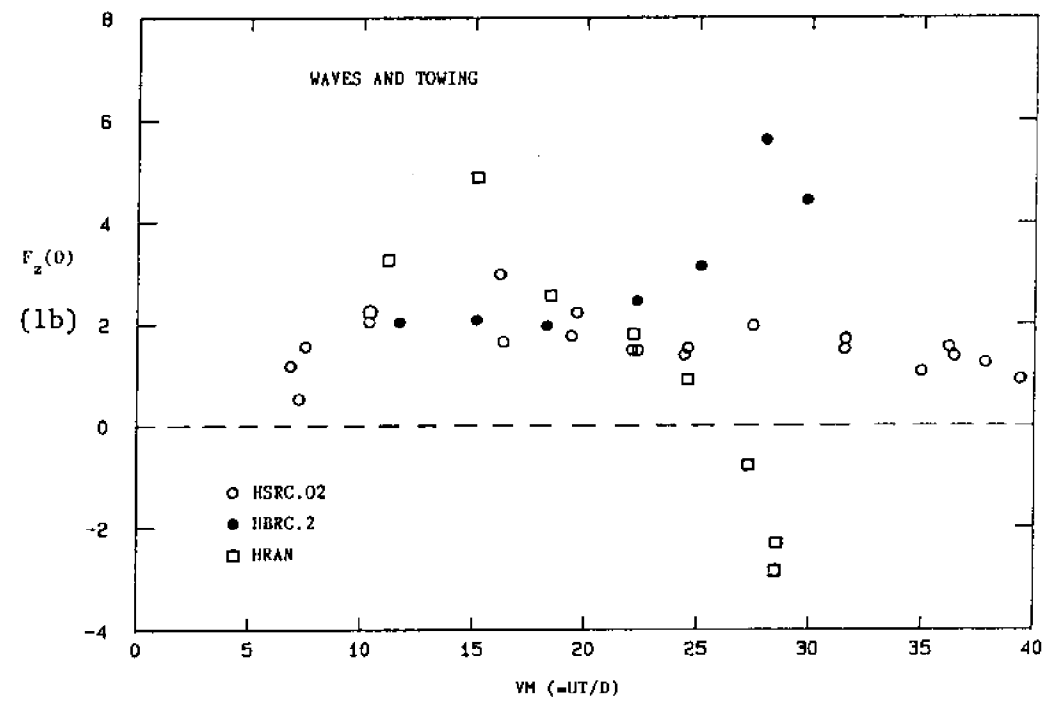

Fig. 6.3-2 Steady vertical forces versus VM for horizontal cylinders under waves and towing.

velocity, the steady horizontal force for the wave and towing case is mainly due to the towing and the contributions from waves (u_w^2) and the cross term between waves and towing (i.e., $2u_wU$) are very small and unimportant.

Figure 6.3-2 shows the vertical steady forces (note: it is dimensional) for all three cylinders. The steady vertical forces, $F_z(0)$, for the HSRC.02 are all positive and do not increase as U increases. The values of $F_z(0)$ for the HBRC.2 are also positive and increase for VM > 20. But, these forces for the HRAN vary from positive to negative as U increases. It seems that $F_z(0)$ does not increase with increase of tow velocity (at most there is a minor increase) and no general trend for $F_z(0)$ can be found. The reason for the vagarious trend of $F_z(0)$ between different roughened cylinders is unknown.

In Fig. 6.3-3, the fundamental harmonic horizontal force coefficient of the HSRC.02, normalized by the maximum wave-induced velocity (i.e. $u_{w\mu}$), increases rapidly as K (or U) increases. That means the presence of the towing significantly increases the fundamental harmonic of the horizontal force. Therefore, the square of the total maximum velocity, $(U+u_{w\mu})^2$, which includes the tow velocity square (U^2) and the cross term ($2Uu_{w\mu}$), is used as the normalization factor in Figure 6.3-4. It is clear that $C_x(1)$ in this figure correlates quite well with K and seems to connect well with that for the waves only case.

The fundamental harmonic horizontal force coefficients, $C_x(1)$, for rougher cylinders (HBRC.2 and HRAN) are plotted in Fig. 6.3-5

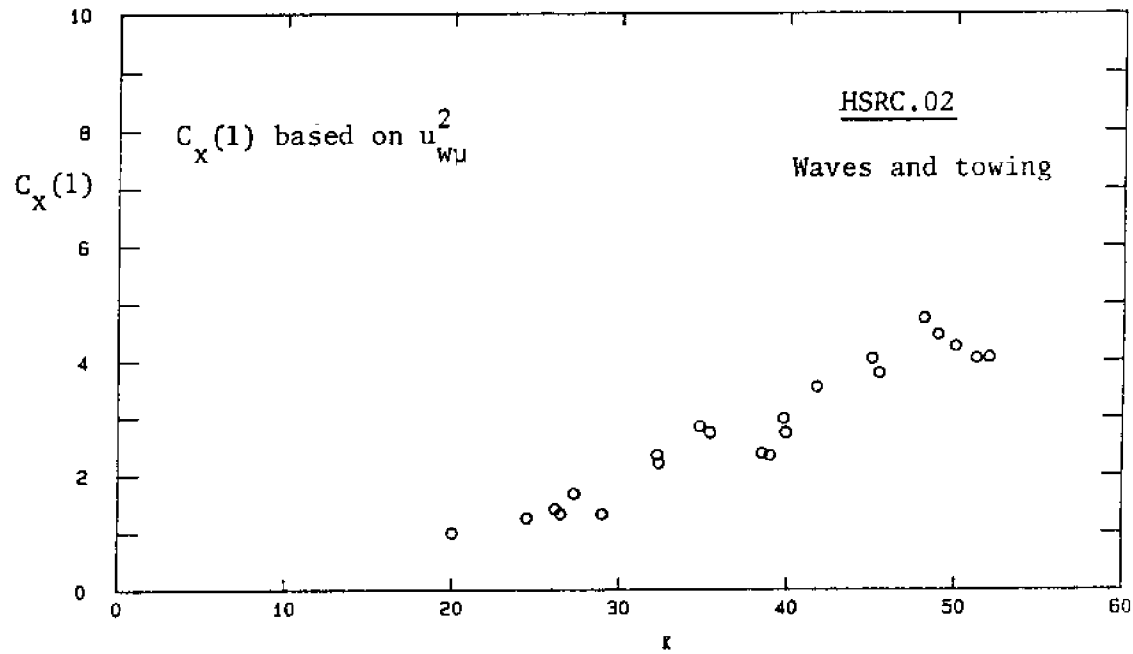

Fig. 6.3-3 $C_x(1)$ (based on $u_{w\mu}^2$) versus K for HSRC.02 under waves and towing (all values based on the smooth cylinder diameter).

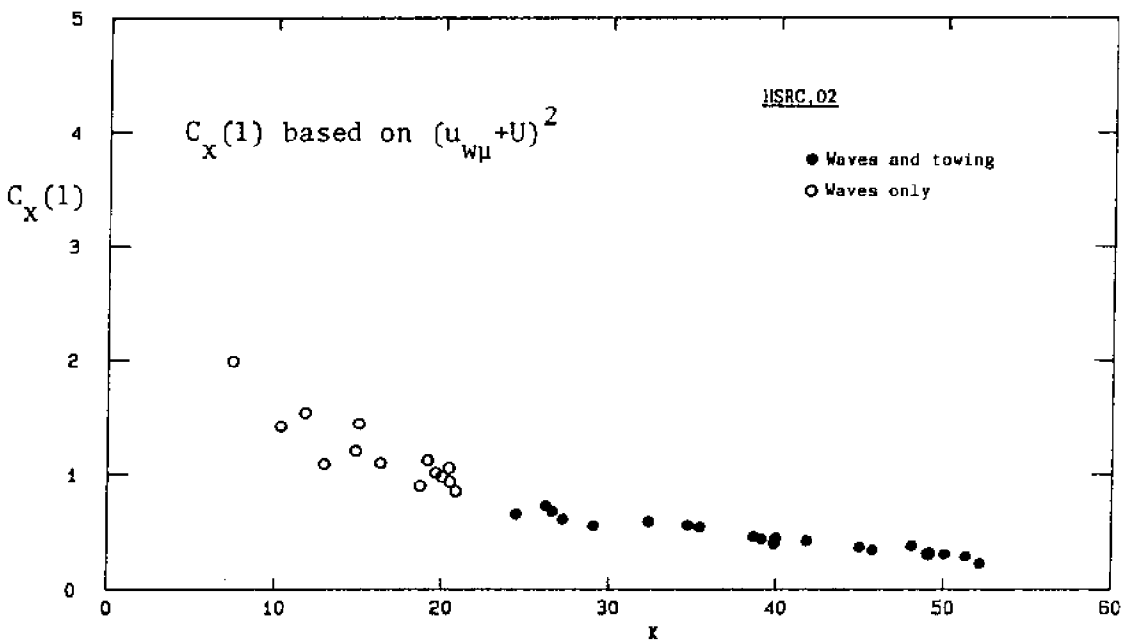

Fig. 6.3-4 $C_x(1)$ (based on $(U+u_{w\mu})^2$) versus K for HSRC.02 under waves and towing (all values based on the smooth cylinder diameter).

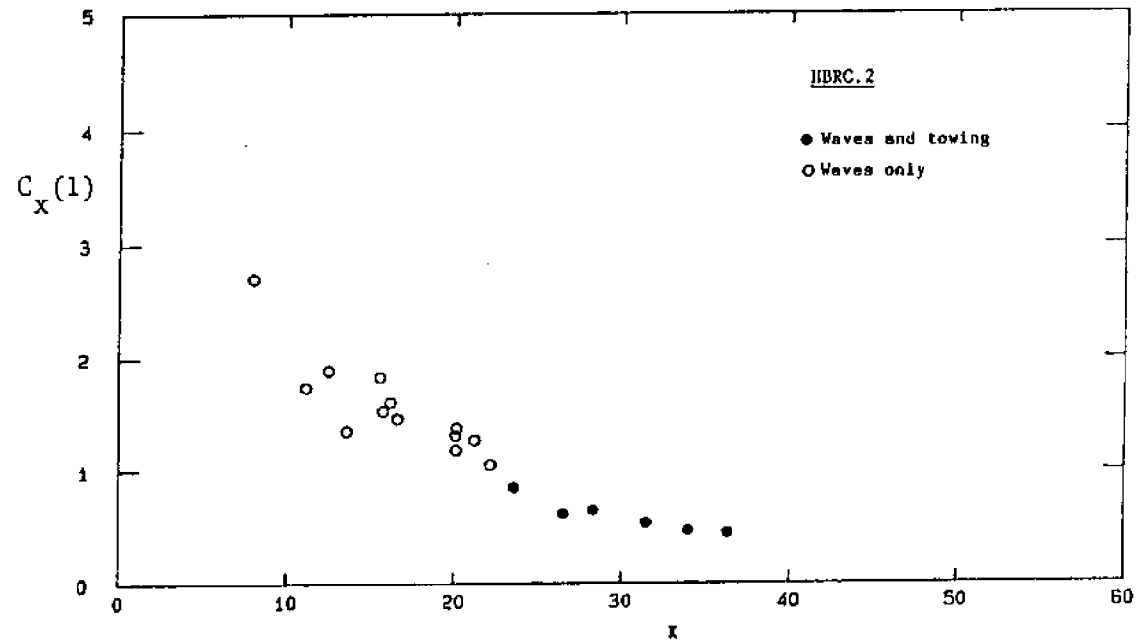

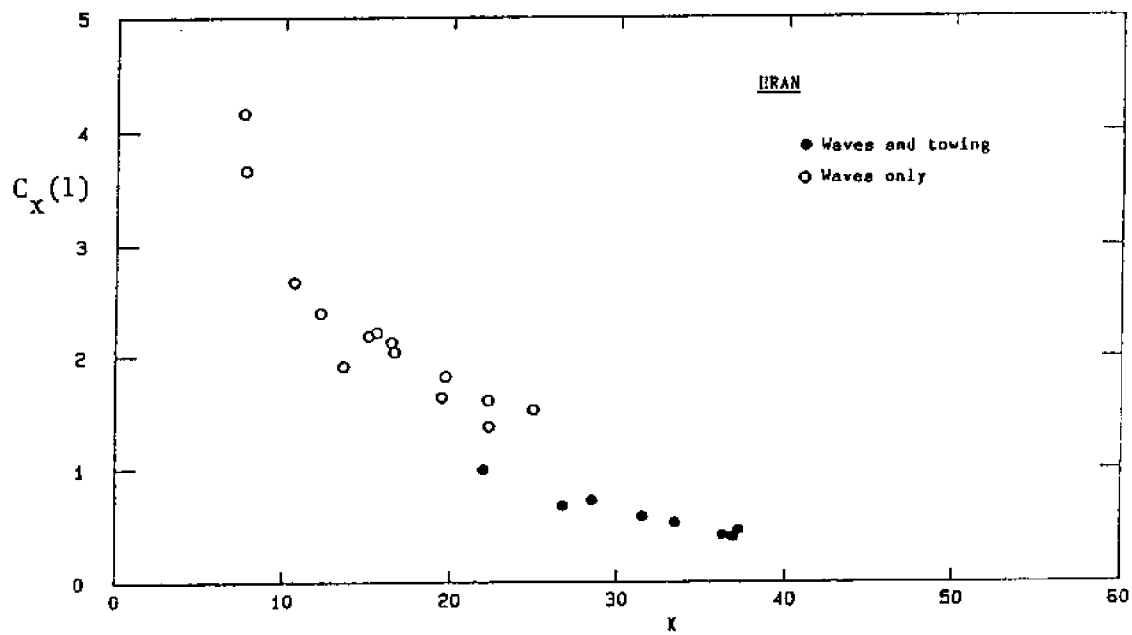

Fig. 6.3-5 $C_x(1)$ (based on $(U+u_{wu})^2$) versus K for HBRC.2 and HRAN under waves and towing (all values based on the smooth cylinder diameter).

with the data for waves only. The values of $C_x(1)$ for the waves and towing case still correlate well with K, but can not connect well with those for waves only, especially for the HRAN. From Figs. 6.3-4 and 6.3-5, the $C_x(1)$ values for the waves only case do increase with increasing e/D, but the values for the waves and towing case do not increase as significantly as those for the waves only case. However, when these values are plotted against $U/u_{w\mu}$ as shown in Fig. 6.3-6, the increase of $C_x(1)$ with increaseing e/D is clear. This implies that (i) the $U/u_{w\mu}$ is an important parameter for determining the towing (current) effect; and (ii) one had better consider more parameters to determine the force coefficients under waves and towing (current).

From the above studies, both the steady horizontal force and the fundamental harmonic horizontal forces increase as the tow velocity increases. The ratios of the amplitude of the fundamental harmonic horizontal force to the steady horizontal force, $F_x(1)/F_x(0)$, for all three cylinders are plotted against the relative velocity, $U/u_{w\mu}$, in Fig. 6.3-7 and they all fit well. From this figure, the fundamental harmonic force is dominant for $U/u_{w\mu} < 1$ and, then, its importance decreases as the tow velocity increases. This ratio approaches a constant (about 0.25) for large U. In other words, the rate of increase of the fundamental harmonic horizontal force is the same as that of the steady horizontal force for large U. This also implies that the fundamental harmonic of horizontal forces have a pronounced increase due to the presence of steady tow.

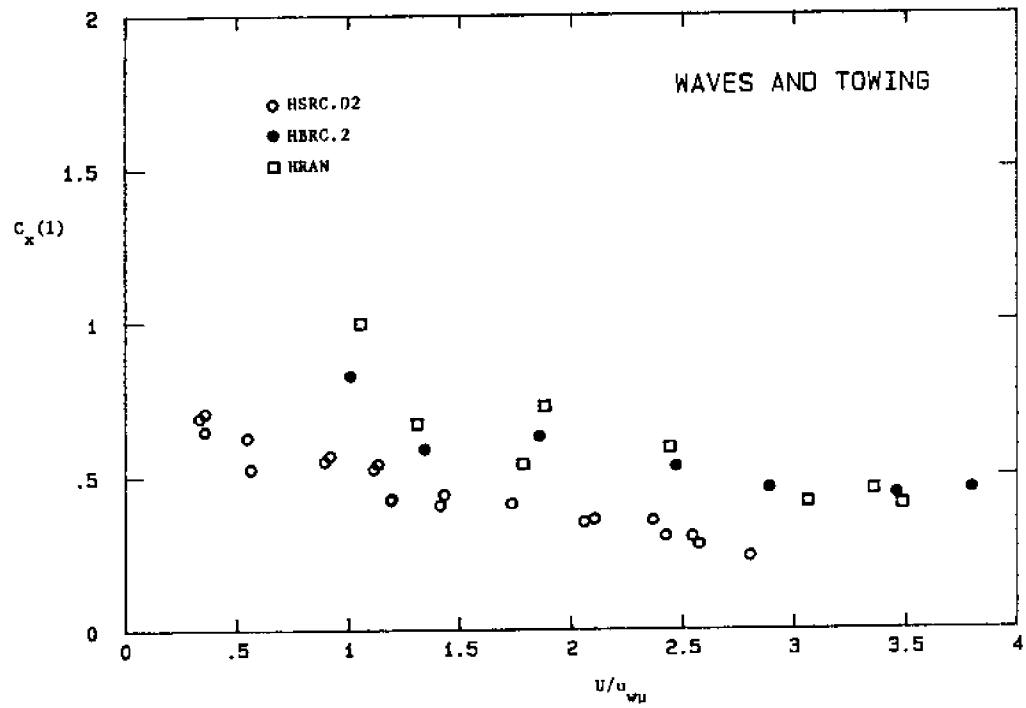

Fig. 6.3-6 $C_x(1)$ versus $U/u_{w\mu}$ for roughened horizontal cylinders under waves and towing (all values based on the smooth cylinder diameter).

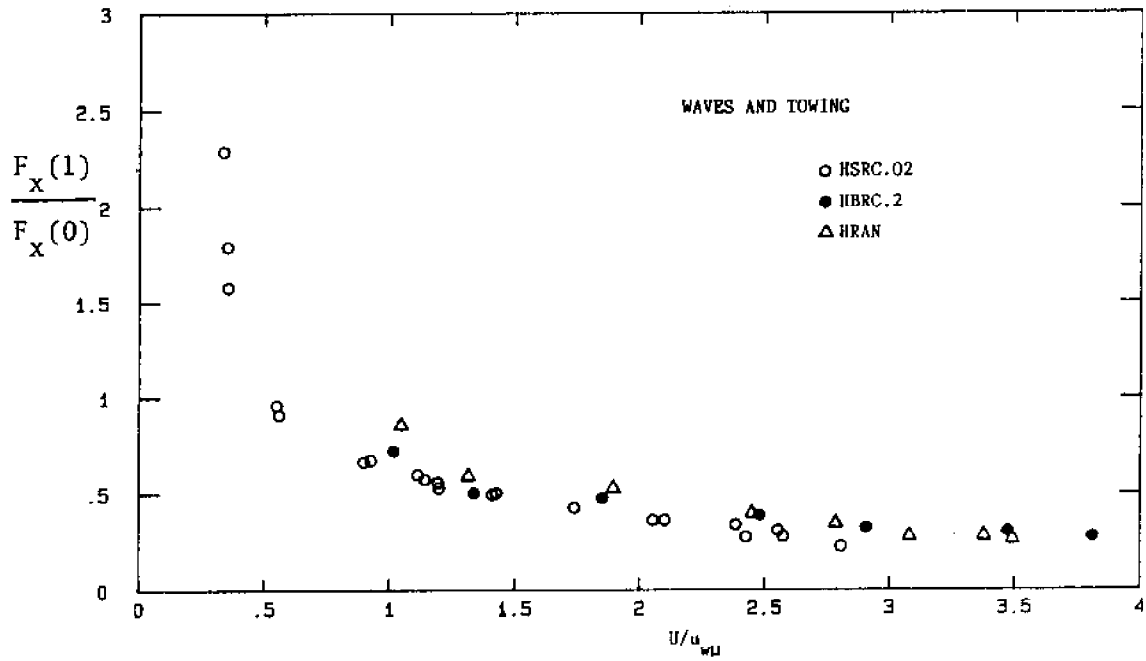

Fig. 6.3-7 Ratio of fundamental harmonic to steady horizontal force versus $U/u_{w\mu}$ for horizontal cylinders under waves and towing.

The values of $C_z(1)$, which are normalized by dividing by $(u_{w\mu}+U)^2$, of the sand roughened cylinder for waves and towing are plotted in Fig. 6.3-8 and their correlation with K is good. It seems the connection of $C_z(1)$ between the waves only case and the waves plus towing case is smooth. The $C_z(1)$ is very small for large tow velocity. That means the towing does not siginificantly increase the fundamental harmonic of vertical forces (note the normalization factor of $C_z(1)$ includes U^2 and $2Uu_{w\mu}$).

Figure 6.3-9 shows the values of $C_z(1)$ versus $U/u_{w\mu}$ for three roughened cylinders. It is clear that the values are higher for the rougher cylinders. Again, this trend is hard to find if these values are plotted against K.

The phase angles of the fundamental harmonic of horizontal and vertical forces, $\phi_x(1)$ and $\phi_z(1)$, for all three cylinders are plotted against K in Fig. 6.3-10. These two phase angles correlate very well with K, especially for large K (or U). Comparing with the results for waves only case (Figs. 5.4.1-8 and 5.4.1-9), it seems that phase angles in both directions decreases a little due to the increase of tow velocity, i.e., the increase of K (or U). For large K, the $\phi_x(1)$ approaches 0° and $\phi_z(1)$ approaches 90°. This means the forces are dominated by the drag component because these angles show the forces are in phase with the velocity components.

By examining the magnitudes of the second harmonic force in both directions for all three cylinders, it seems these forces do not increase too much as the tow velocity increases. That means the towing of a cylinder (or the presence of a current) in a wave field does not

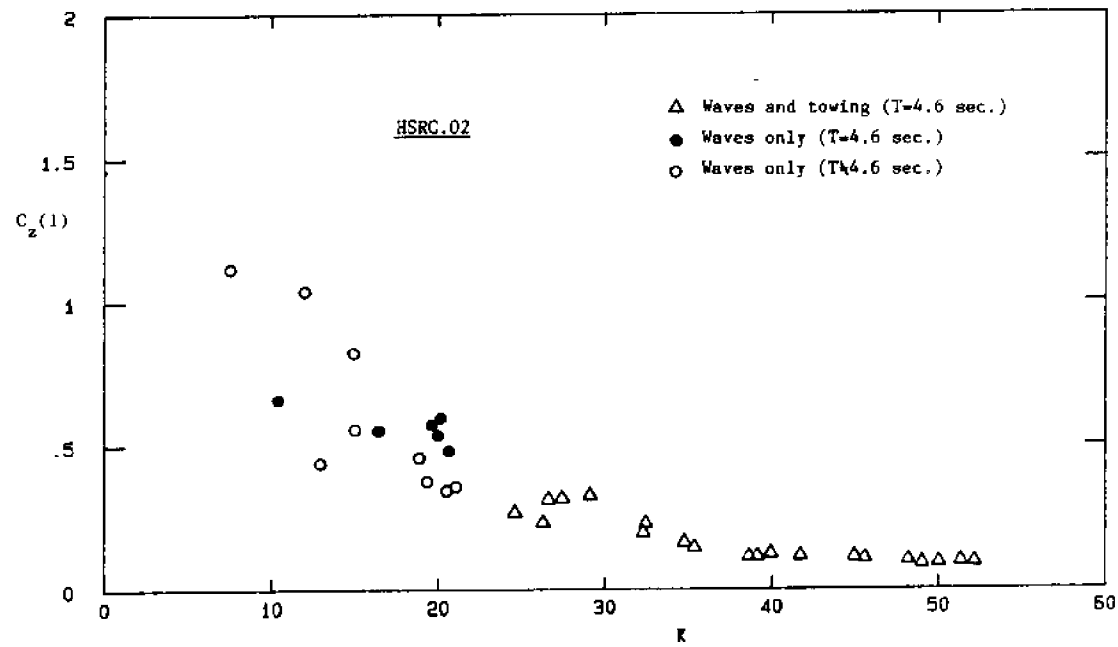

Fig. 6.3-8 $C_z(1)$ versus K for HSRC.02 under waves and towing (all values based on the smooth cylinder diameter).

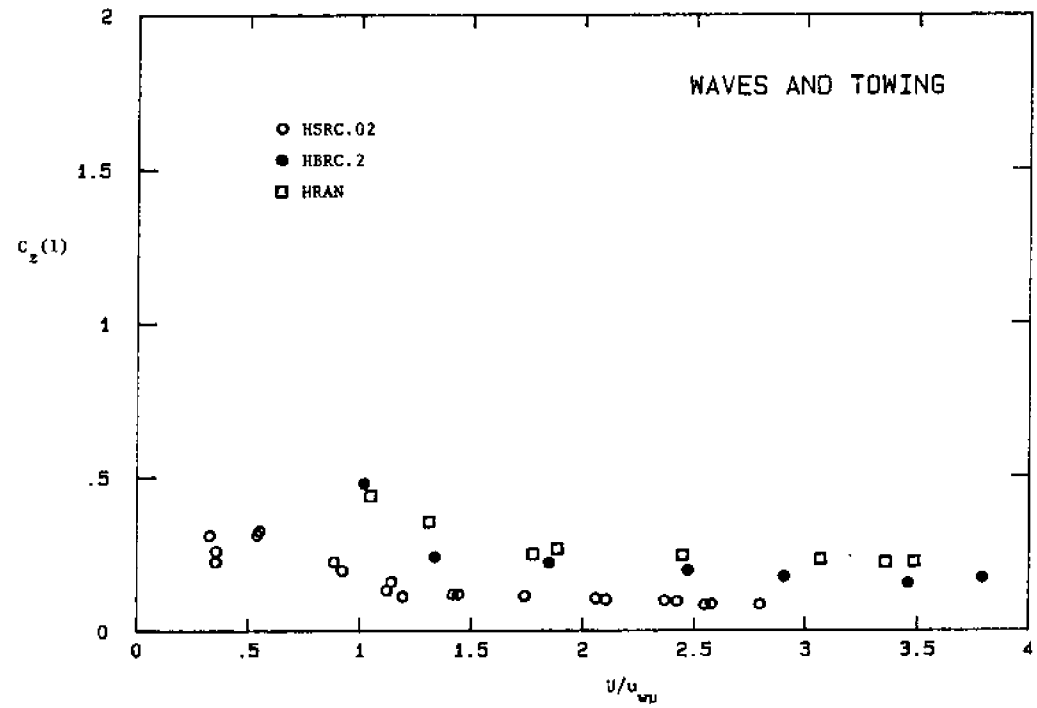

Fig. 6.3-9 $C_z(1)$ versus U/u_{wu} for roughened horizontal cylinders under waves and towing (all values based on the smooth cylinder diameter).

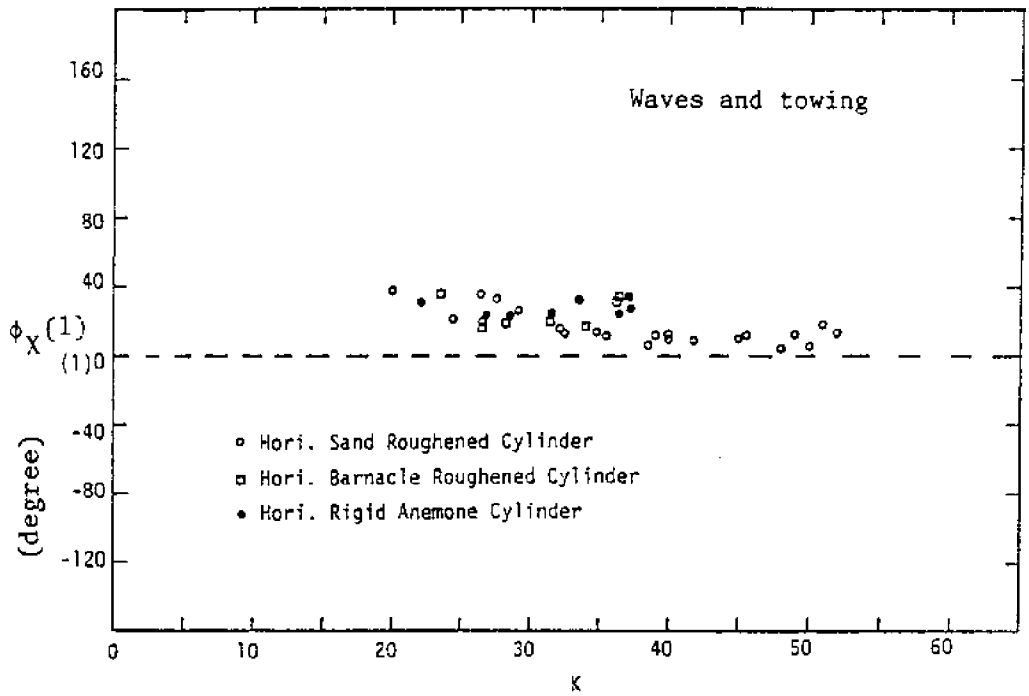

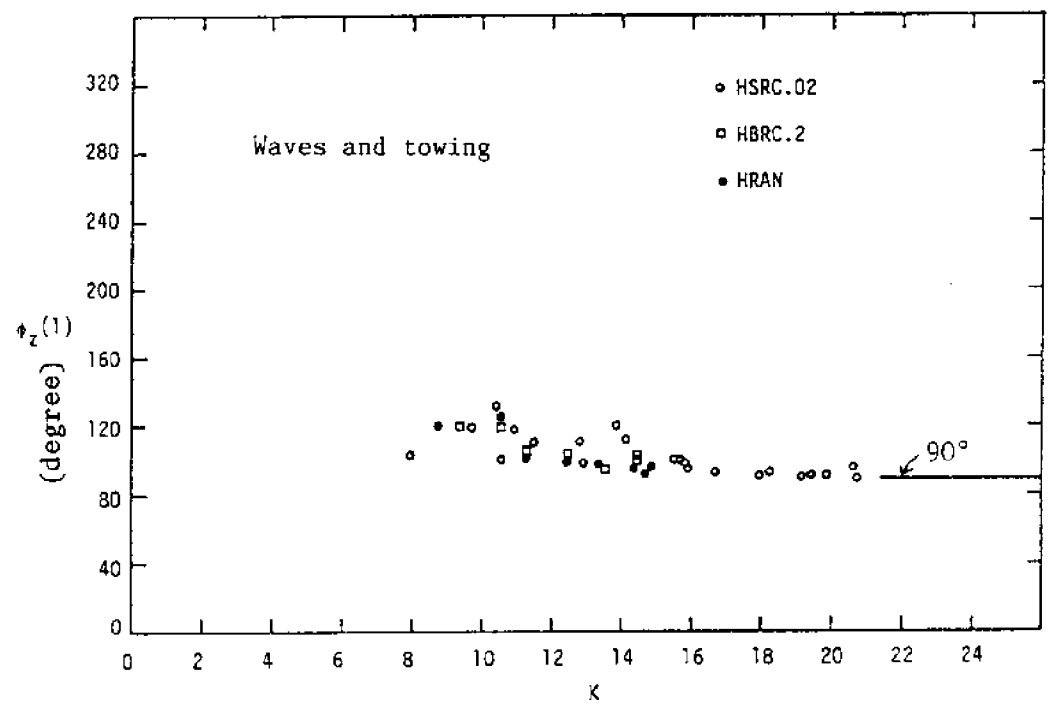

Fig. 6.3-10 Phase angles of the fundamental harmonic forces for horizontal cylinders under waves and towing.

significantly increase the second harmonic forces (mostly vortex-induced force).

The second harmonic force coefficients are normalized by the associated fundamental force coefficients and are designated as $C_x'(2)$ and $C_z'(2)$. Figures 6.3-11 and 6.3-12 present these two coefficients versus $U/u_{w\mu}$ for all three cylinders. The $C_x'(2)$ decreases as U increases. It seems that the values of $C_x'(2)$ for the HRAN and HBRC.2 are smaller than those for the HSRC.02. Note that $C_x'(2)$ is normalized by $C_x(1)$. From Fig. 6.3-6, $C_x(1)$ values for the HRAN and HBRC.2 are greater than those for the HSRC.02. Thus, values of $C_x(2)$ do not have significant increase due to the increase of e/D.

In the vertical direction, $C_z'(2)$ for the HSRC.02 (Fig. 6.3-12) reaches the maximum near $U/u_{w\mu}=1.2$, and then decreases for $U/u_{w\mu} > 1.2$. Data points for the HBRC.2 and HRAN are not enough to support this result. Except for $U/u_{w\mu}=1.2$, $C_z'(2)$ values do not increase as U increases. Since towing of the cylinder does not make great increase of $C_z(1)$, $C_z(2)$ does not significantly increase. Note that $C_z'(2)=C_z(2)/C_z(1)$. No clear difference of $C_z'(2)$ between different roughened cylinders can be observed for large tow velocities.

From Figs. 6.3-11 and 6.3-7, the second harmonic of the horizontal force, comparing with the steady horizontal force, is relatively unimportant as the tow velocity increases (e.g., not over 5% for $U/u_{w\mu}=2.5$) and can be neglected. Meanwhile, from Figs. 6.3-8 and 6.3-12, the second harmonic of the vertical force is relatively small for large U if compared with the horizontal steady force.

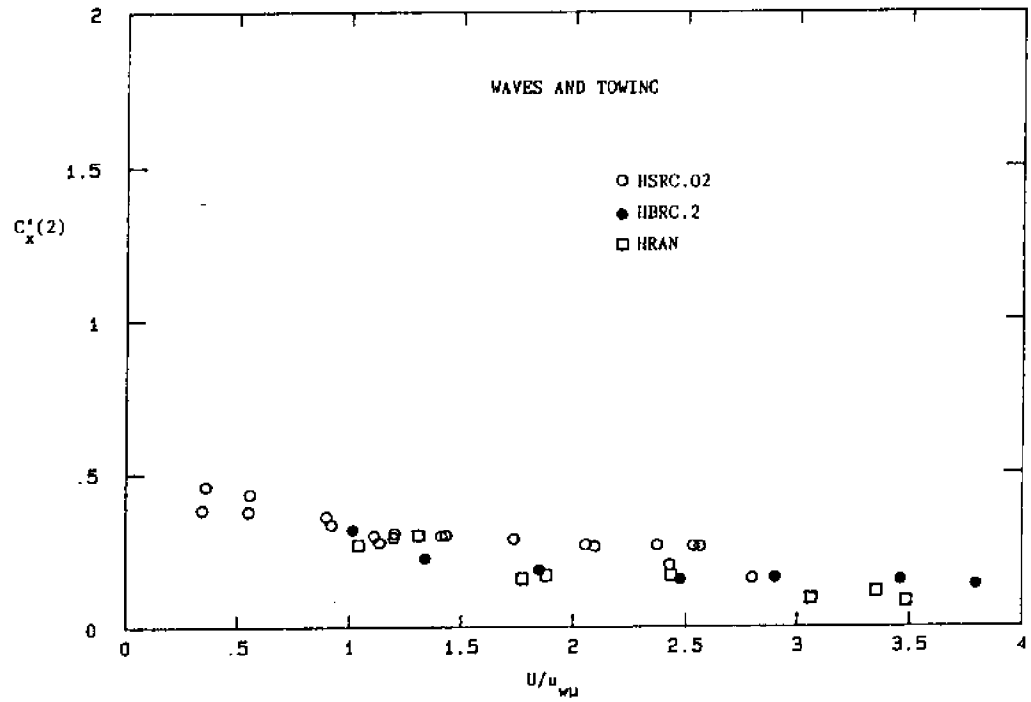

Fig. 6.3-11 $C'_x(2)$ versus $U/u_{w\mu}$ for horizontal cylinders under waves and towing (all values based on the smooth cylinder diameter).

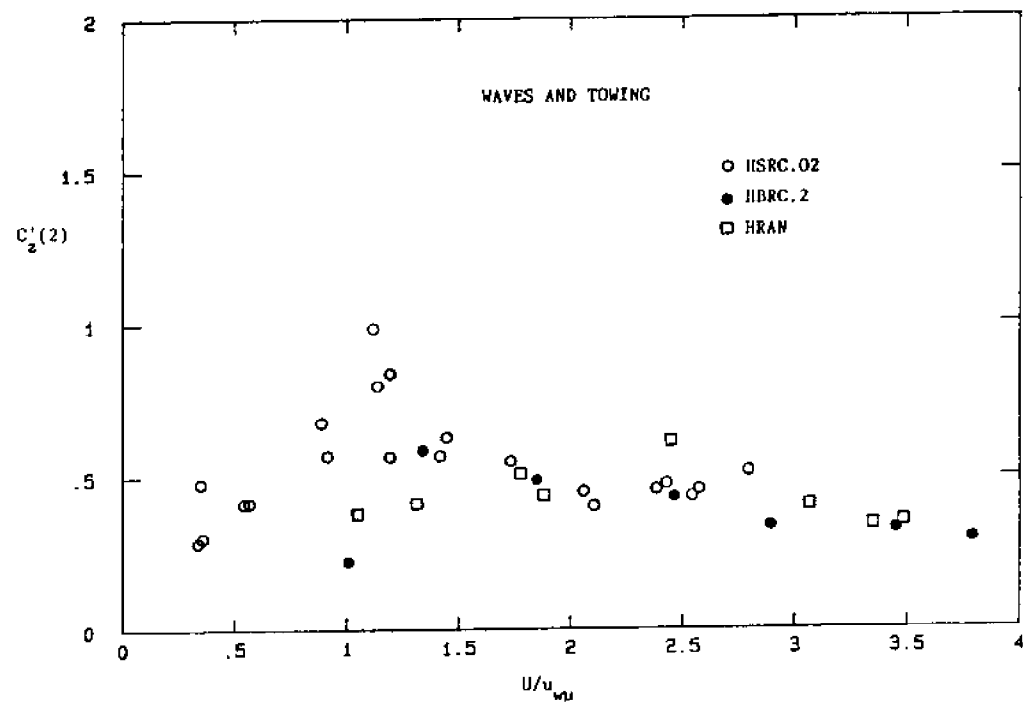

Fig. 6.3-12 $C'_z(2)$ versus $U/u_{w\mu}$ for horizontal cylinders under waves and towing (all values based on the smooth cylinder diameter).

Due to the small portion of the second harmonic force, compared to the total force (mainly the steady force), the data are not well-conditioned for determining phase angle. Thus, the phase angles for the second harmonic forces are not reliable and not presented here.

7. CONCLUSIONS

The following major conclusions from this study can be drawn.

(1) The flow patterns around a horizontal cylinder in waves are not symmetric between the forward and the reverse half wave cycles due to the nonlinearity of waves, velocity gradient between upper and lower surface of the cylinder, and the interaction effect between vortices. In general, the vortices in the forward half cycle (under the wave crest) are stronger than those in the second half cycle. In the forward half cycle, the first vortex formed from the top half of the cylinder is the largest and dominant one. The patterns of formation and movement of wake and vortices are dominated by the dimensionless parameters K and Ω.

(2) The vortex shedding phenomena have great contributions to the wave-to-wave variations of forces. Thus, variations of the vertical forces, that contain more vortex-induced forces, are more severe than those of the horizontal forces. For smaller Ω, variations of horizontal forces are smaller and variations of vertical forces are greater. It seems that variations are smaller for the rougher cylinders.

(3) The flow visualization experiments indicated that the wake and vortices do not always rotate synchronously with the velocity vector around a horizontal cylinder, especially for small Ω. This fact makes the force predictions through the use of the Morison equation (or other techniques based on the instantaneous velocity vector) less accurate.

(4) For horizontal cylinders in periodic waves, the vector form of the Morison equation under-predicts the maximum forces up to 20% and generates rms errors of from 15% to 40%. Based on the maximum force prediction and the rms error, the Morison equation force predictions for a rough cylinder are better than those for a smooth cylinder and predictions for the waves and towing case, by assuming the linear superposition principle, are better than those for the waves only case. Predictions using the vector form of the Morison equation have the following inherent weaknesses: (i) lack of a term taking the vortex-induced force (mainly higher harmonic forces) into account, and (ii) wake direction may not be colinear with the velocity vector. However, the vector form of the Morison equation is still an acceptable first approximation for predicting forces on horizontal cylinders. It is more useful if a factor of safety is applied to the maximum force determination.

(5) The rms (horizontal, vertical, and total) force coefficients correlate well with K and some degree of dependence of these coefficients on Ω is observed. The maximum total force coefficients, which include the drag, the inertia, and the vortex-induced forces, correlate with K and no trend on Ω is observed.

(6) Both the force coefficients (amplitudes) and phases of the fundamental harmonic forces, which are mainly from the drag and inertia forces, correlate well with K. Some degree of correlation with Ω is also shown. Thus, it is thought that the scatter of C_d and C_m as observed in Section 5.2 is largely from the higher harmonic forces which are mostly due to the vortex shedding phenomenon.

(7) Both the force coefficients and phases of the higher harmonic forces (which contain the vortex-induced forces and the nonlinear Morison forces) have greater scatter than those of the fundamental harmonic forces. The higher harmonic forces become important as K increases or Ω decreases. None of the higher harmonic forces exceed the fundamental harmonic force in the horizontal direction. The second and third harmonic vertical forces exceed the fundamental harmonic vertical force for small Ω.

(8) In this study, the horizontal steady force is mainly due to the return current in a closed wave flume. For the smooth cylinder, both the horizontal and vertical steady forces decrease as Ω decreases (or T increases). For roughened cylinders, the vertical steady force becomes positive.

(9) For small Ω and small K, the vertical velocity is too small to make the wake move in the vertical direction. Thus, the vertical force is much smaller than the horizontal force. For larger Ω (laboratory values herein are between 0.67 and 0.81), the vertical velocity is large enough to make the wake rotate around the cylinder and the vertical (fundamental or rms) forces have almost the same magnitude as the horizontal forces.

(10) For a vertical cylinder, the maximum and rms force coefficients in line with the wave propagation are greater than those for a horizontal cylinder, due to (i) the reduction of the wake encounter effect, and (ii) the confinement of the formation and movement of wake and vortices. However, the rms vertical force coefficient of horizontal cylinders is greater than the rms transverse force coefficient of vertical cylinders. (Note that both are normal to the axis and to the wave direction.)

(11) As a cylinder is towed in a wave field, the force coefficients increase. However, when the tow velocity is greater than the maximum of the wave-induced velocity, the flow becomes unidirectional and oscillatory and the force coefficients decrease rapidly because the wake and vortices are not swept back on to the cylinder to enhance the relative velocity. When a cylinder is towed in waves, the amplitude of the fundamental harmonic of the horizontal forces strongly increase due to the presence of towing. The steady component of horizontal forces is mainly from the tow velocity and its coefficient approaches the steady flow drag coefficient for large tow velocity.

(12) When the waves and towing case is considered as an extension of the waves only case, the use of K (which includes the wave-induced velocity and tow velocity) and the use of the linear superposition principle for the kinematics are acceptable for estimating C_d and C_μ. The relative velocity $(U/u_{w\mu})$, which is a measure of flow bias, is an important parameter.

(13) Generally, force coefficients for rougher cylinders have less scatter and are more stable than for smooth cylinders. When the relative roughness increases, the vertical forces on horizontal cylinders

in waves do not increase as significantly as the horizontal forces, especially for those with small Ω. The dependences of force coefficients on Ω are clearer for rougher cylinders.

(14) In this study, the data cover a limited range of parameters, especially for the waves and towing case. Thus, it is risky to use the present results for a wider range of conditions.

BIBLIOGRAPHY

Bearman, P.W., Graham, J.M.R. and Singh, S., (1978), "Forces on Cylinders in Harmonically Oscillating Flow," Symposium on Mechanics of Wave-Induced Forces on Cylinders, University of Bristol, Sep.

Bearman, P.W., Graham, J.M.R., and Naylor, P., and Obasaju, E.D., (1981), "The role of Vortices in Oscillatory Flow about Bluff Cylinders," International Symposium on Hydrodynamics in Ocean Engineering, pp. 621-643.

Bearman, P.W., Chaplin, J.R., Graham, J.M.R., Kostense, J.K., Hall, P.R., and Kolpman, G., (1985a), "The Loading on a Cylinder in Post-Critical Flow Beneath Periodic and random Waves," Proceedings of the 4th BOSS Conference, Delft, pp. 213-225.

Bearman, P.W., Downie, M.J.G., Graham, J.M.R., and Obasaju, E.D., (1985b), "Forces on Cylinders in Viscous Oscillatory Flow at Low Keulegan-Carpenter Numbers," J. Fluid Mech. Vol. 154, pp. 337-356.

Bryndum, M.B., Jacobsen, V., and Brand, L.P., (1983), "Hydrodynamic Forces from Wave and Current Loads on Marine Pipelines," Proceedings of Offshore Technology Conference, OTC No. 4454, pp. 95-102.

Chakrabarti, S.K., Wolbert, A.L. and Tam, W.A., (1976) "Wave Forces on Vertical Circular Cylinder," Journal of Waterways, Harbors, and Coastal Engineering, ASCE, Vol. 102, No. WW2, May, pp. 203-221.

Chakrabarti, S.K., (1980), "Inline Forces on Fixed Vertical Cylinder," Journal of Waterway, Port, Coastal and Ocean, ASCE, Vol. 106, No. WW2, may, pp.145-155.

Chaplin, J.R., (1981), "Boundary Layer Separation from a Cylinder in Waves," International Symposium on Hydrodynamics in Ocean Engineering, Norwegian Institute of Technology, pp. 645-666.

Chaplin, J.R., (1984), "Nonlinear Forces on a Horizontal Cylinder beneath Waves," J. Fluid Mech., Vol. 147, pp. 449-464.

Chaplin, J.R., (1985a), "Morison Inertia Coefficients in Orbital Flow," Journal of the Waterway, Port, Coastal and Ocean Engineering Division, ASCE, Vol. 111, No. 2, pp. 201-215.

Chaplin, J.R., (1985b), "Loading on a Cylinder in Uniform Elliptical Orbital Flow," Report MCE/JUL/85, Dept. of Civil Engineering, University of Liverpool, England.

Dean, R.G., (1976), "Methodology for Evaluating Suitability of Wave and Wave Force Data for Determining Drag and Inertia Coefficients," Proceeding of Conference on Behavior of Offshore Structures, pp. 40-64.

Fallon, J.W. (1984), "An Experimental Study of Some of the Fundamental Aspects of Wave Induced Forces on Cylindrical Objects," Doctoral Dissertation, University of California, Berkeley.

Garrison, C.J. (1980), "A Review of Drag and Inertia Forces on Circular Cylinders," OTC 3760, pp. 205-218.

Grass, A.J., Kemp, P.H. and Stuart R.J., (1981), "Vortex Induced Velocity Magnification and Loading Effects for Cylinders in Oscillatory Flow," London Centre for Marine Technology, Report No. FL 28, January.

Grass, A.J., Simons, R.R. and Cavanagh, N.J., (1984), "Fluid Loading on Horizontal Cylinders in Wave Type Orbital Flow," Proceedings of the 4th International Symposium on Offshore Mechanics and Arctic Engineering, Dallas, Paper No. OMAE 262.

Heaf, N.J., (1979), "The Effect of Marine Growth on the Performance of Fixed Offshore Platforms in the North Sea," OTC 3386, pp. 255-268.

Heideman, J.C., Olsen, O.A., and Johansson, P.I., (1979), "Local Wave Force Coefficients," Civil Engineering in the Oceans IV, pp. 684-699.

Hogben, N., Miller, B.L., Searle, J.W., and Ward, G. (1977), "Estimation of Fluid Loading on Offshore Structures," Proc. Instn. Civ. Engrs, Part 2, 63, Sept., pp. 515-562.

Holmes, P.and Chaplin, J.R., (1978), "Wave Loads on Horizontal Cylinders," Proceedings of the 16th International Conference on Coastal Engineering, Hamburg, pp. 2449-2460.

Ikeda, S., and Yamamoto, Y. (1981), "Lift Force on Cylinders in Oscillatory Flows," Report of Dept. Found. Eng. & Const. Eng., Saitama Univ., 10.

Isaacson, M. and Maull, D.J., (1976), "Transverse Forces on Vertical Cylinders," Journal of The Waterways Harbors and Coastal Engineering Division, ASCE, Vol. 102, No. WW1, Feb., pp. 49-60.

Ismail, N.M., (1983), "Effects of Wave-Current Interaction on the Design of Marine Structure," Proceedings of Offshore Technology Conference, OTC No. 4615, pp. 307-316.

Kato, M., Abe, T., Tamiya, M., and Kumakiri, T., (1983) "Drag Forces on Oscillating Cylinders in a Uniform Flow," Offshore Technology Conference, Paper OTC 4591, pp. 95-102.

Kim, T.I., (1985), "Mass Transport in Laboratory Water Wave Flumes," Ph.D. Thesis, Dept. of Civil Engineering, Oregon State University, Corvallis, Oregon.

Knoll, D.A. and Herbich, J.B., (1980), "Wave and Current Forces on a Submerged Offshore Pipeline," Proceedings of Offshore Technology Conference, OTC No. 3762, pp. 227-234.

Koterayama, W., (1984), "Wave Forces Acting on a Vertical Circular Cylinder with a Constant Forward Velocity," Ocean Engr., Vol. 11, No. 4, pp. 363-379.

Lin, C.W., and Nath, J.H.,(1980),"Fluid Forces on Smooth and Rough Circular Cylinders," Wave Research Facility, T.R. 11, Department of Civil Engineering, Oregon State University, Corvallis, Oregon.

Longuet-Higgins, M.S., and Stewart, R.W. (1961), "Changes in The Amplitude of Short Gravity Waves on Steady Non-Uniform Currents," J. of Fluid Mechanics, Vol. 10, pp. 529-549.

Matten, R.B., (1976),"Calculation of Drag forces on a Circular Cylinder in a Combined Plane Oscillatory and Uniform Flow Field Using Morison' Equation," (Unpublished Communication to the National Maritime Institute, England).

Maull, D.J. and Milliner, M.G., (1978), "Sinusoidal Flow Past a Circular Cylinder," Coastal Engineering, 2, pp. 149-168.

Maull, D.J. and Norman, S.G., (1979), "A Horizontal Cylinder Beneath waves," Mechanics of Wave-Induced Forces on Structures, T.L. Shaw (ed.), Pitman, pp. 359-378.

Mercier, J.A., (1973), "Large Amplitude Oscillations of a Circular Cylinder in Low-Speed Stream," Thesis presented to Stevens Institute of Technology, Castle Point, Hoboken, N.J., in partial fulfillment of the requirements for the degree of Doctor of Philosophy.

Morison, J.R., O'Brien, M.P., Johnson, J.W., and Schaaf, S.A. (1950), "The Force Exerted by Surface Wave on Piles," Petroleum Transactions, AIME, Vol. 189, pp. 149-157.

Nath, J.H., (1981a), "Hydrodynamic Coefficients for Cylinders with Pronounced Marine Growths -- API PRAC Project 80-31," Final Report to American Petroleum Institute, Dept. of Civil Engineering, Oregon State University, Corvallis, Oregon.

Nath, J.H., (1981b), "Hydrodynamic Coefficients for Macro-Roughnesses," Proceedings of the 13th Annual Offshore Technology Conference, May 4-7.

Nath, J.H., (1982), "Heavily Roughened Horizontal Cylinders in Waves," Proceeding, Conference on Behavior of Offshore Structure.

Nath, J.H., (1983a), "Vertical vs. Horizontal Cylinders in Waves," Proceedings of the Conference on Pipelines in Adverse Environments, ASCE pp. 704-721.

Nath, J.H., (1983b), "Hydrodynamic Coefficients for Cylinders with Pronounced Marine Growths -- API PRAC Project 80-31B - Vertical Cylinder," Final Report to American Petroleum Institute, Dept. of Civil Engineering, Oregon State University, Corvallis, Oregon.

Nath, J.H., (1983c), "Hydrodynamic Coefficients for Cylinders Roughened by Marine Growths from the Gulf of Mexico -- API PRAC Project 82-31," Final Report to American Petroleum Institue, Dept. of Civil Engineering, Oregon State University, Corvallis, Oregon.

Nath, J.H., (1984a), "Hydrodynamic Coefficients for Cylinders Covered with Soft Organisms, Particularly Sea Anemones," Final Report to the American Petroleum Institute, Dept. of Civil Engineering, Oregon State University, Corvallis, Oregon.

Nath, J.H., Hsu, M.K. Hudspeth, R.T. and Dummer, J., (1984b), "Laboratory Wave Forces on Vertical Cylinders," Proceedings of Specialty Conference on Ocean Structural Dynamics Symposium, Oregon State University, pp. 312-330.

Nath, J.H., (1985a), "Wave Force-Phase Method for Vertical Cylinders," Final Report to Minerals Management Service, Department of Interior and Naval Civil Engineering Laboratory, Civil Engineering Department, Oregon State University.

Nath, J.H., (1985b), "Hydrodynamic Coefficients for Marine Roughened Cylinders," Final Report to the American Petroleum Institute.

Nath, J.H., (1986), "Wave Force Coefficient Variability for Cylinders," Prodeeding of Conference on Ocean Structural Dynamics Symposium, Oregon State University.

Ralph, R. and Troake, R.P., (1980), "Marine Growth on North Sea Oil and Gas Platforms," OTC 3860, pp.49-51.

Ramberg, S.E. and Niedzwecki, J.M., (1979), "Some Uncertainties and Errors in wave Force Computations," Proceedings of the 11th OTC, Houston, paper No. OTC 3597, pp. 2091-2102.

Ramberg, S.E. and Niedzwecki, J.M., (1983), "Cycle-to-Cycle Variations in the Wave Forces on Horizontal Cylinders," Proceedings of the 2th International Symposium on Offshore Mechanics and Artic Engineering ASME OMAE 262, pp. 165-170.

Rodenbusch, G. and Gutierrez, C.A., (1983), "Forces on Cylinders in Two-Dimensional Flows," Technical Progress Report BRC 13-83, Shell Development Company, Houston.

Sarpkaya, T., (1976), "In-line and Transverse Forces on Smooth and Sand-Roughened Cylinders in Oscillatory Flow at High Reynolds Numbers," Naval Post-Graduate School, T.R. No. NPS-69SL76062, Monterey, CA.

Sarpkaya, T., and Isaacson, M., (1981), "Mechanics of Wave Forces on Offshore Structures," Van Nostrand.

Sarpkaya, T., (1982), "Hydrodynamic Resistance in Harmonic Flow-Current Field," Naval Post-graduate School, T.R. No. NSP-69-82-004, Monterey, CA.

Sarpkaya, T., Bakmis, C. and Storm, M.A. (1984), "Hydrodynamic Forces from Combined Wave and Current Flow on smooth and Rough Circular Cylinders at High Reynolds Numbers," Proceedings of Offshore Technology Conference OTC No. 4830, pp. 455-462.

Sarpkaya, T., and Wilson, J.R., (1984), "Pressure Distribution on smooth and Rough Cylinders in Harmonic Flow," Proceedings of Specialty Conference on Ocean Structural Dynamics Symposium, Oregon State University, pp. 341-355.

Sarpkaya, T., (1984), Discussion of "Quasi-2-D forces on a Vertical Cylinder in waves," Stansby, P.K., Bullock, G.N. and Short, I., Journal of the Waterways, Port, Coastal and Ocean Division, ASCE, Vol. 110, pp. 120-123.

Sarpkaya, T., (1986), "In-line and Transverse Forces on Smooth and Rough Cylinders in Oscillatory Flow at High Reynolds Numbers," Naval Post-Graduate School, Technical Report No. NPS69-86-003, Monterey, CA.

Sawaragi ,T., Nakamura, T., and Kita, H., (1976), "Characteristics of Lift Forces on a Circular Pile in Waves," Coastal Engineering in Japan, Vol. 19, pp. 59-71.

Sawaragi, T., and Nakamura, T., (1979), "Analytical Study of wave Force on a Cylinder in Oscillaroty Flow," Costal Structures, pp. 155-173.

Sharma, J.N., (1983), "Marine Growth on the Hondo Platform in the Santa Barbara Channel," OTC 4569, pp. 469-474.

Teng, C.C. and Nath, J.H., (1983), "Hydrodynamic Forces on a Horizontal Cylinder under Waves and Current," Interim Report for National Science Foundation and Oregon State University Sea Grant Program, Dept. of Civil Engineering, Oregon State University, Corvallis.

Teng, C.C., and Nath, J.H., (1984),"Wave and Current Forces on Horizontal Cylinders," Ocean Structural Dynamics Symposium '84, Oregon State University, Corvallis, pp. 369-398.

Teng, C.C., and Nath, J.H., (1985), "Forces on Horizontal Cylinder Towed in Waves," Journal of Waterway, Port, Coastal and Ocean Engineering, ASCE Vol. 111, No. 6, November.

Verley, R.L.P., and Moe, G., (1979), "The Forces on a Cylinder Oscillating in a Current," VHL Report STF60 A79061, Norwegian Institute of Technology.

Williamson, C.H.K., (1985), "Sinusoidal Flow Relative to Circular Cylinders," J. Fluid Mech., Vol. 155, pp. 141-174.

Yamamoto, T. and Nath, J.H., (1976), "High Reynolds Number Oscillating Flow by Cylinders," Proceedings of the 15th International Conference of Coastal Engineering, Hawaii, pp. 2321-2340.

Zdravkovich, M.M. and Namork, J.E., (1977), "Formation and Reversal of Vortices around Circular Cylinders Subjected to Water Waves," Technical Notes, Journal of Waterway, Port, Coastal and Ocean Engineering, ASCE Vol. 103, No. WW3, August, pp. 378-383.

APPENDICES

APPENDIX A - Similarity of Average C_d and C_m

When data (wave profile, force measurements, etc.) from n consecutive waves under the same wave condition are recorded, there are three ways to obtain a representative C_d and C_m for this flow and cylinder condition if the least square method is applied (see Section 2.3):

(a) Get C_d and C_m for each wave cycle, and then average these n pairs of coefficients to get an average pair. [They are designated as $(C_d)_a$ and $(C_m)_a$.]

(b) Average these n cycles of wave data to obtain an average wave record, and then obtain C_d and C_m for this representative wave. [$(C_d)_b$ and $(C_m)_b$.]

(c) Get one pair of C_d and C_m by using the continuous n wave record as a whole. [$(C_d)_c$ and $(C_m)_c$.]

If the n cycles of waves are perfectly repeatable, i.e, the undisturbed velocity and acceleration used in the Morison equation are perfectly repeatable from wave to wave, but force measurements are not necessarily repeatable, the representative pairs of C_d and C_m from the above three methods are theoretically identical as proven in the following. The equations for C_d, C_m and associated abbreviations [AA, BB, etc.] presented in Section 2.3, i.e., Eqs. (2-8) to (2-14) are used here.

(1) $(C_d)_a=(C_d)_b$

The number subscripts (from 1 to n) represent the number of waves. From Eq. (2-8),

$$C_{d1} = \frac{(AA)_1(BB)_1 - (DD)_1(EE)_1}{\frac{1}{2}\rho DL[(CC)_1(BB)_1 - (DD)_1^2]}$$

$$(C_d)_a = \frac{C_{d1} + C_{d2} + \ldots + C_{dn}}{n}$$

$$= \frac{\dfrac{(AA)_1(BB)_1 - (DD)_1(EE)_1}{\frac{1}{2}\rho DL[(CC)_1(BB)_1 - (DD)_1^2]} + \ldots + \dfrac{(AA)_n(BB)_n - (DD)_n(EE)_n}{\frac{1}{2}\rho DL[(CC)_n(BB)_n - (DD)_n^2]}}{n}$$

Since the undisturbed velocity and acceleration are identical from cycle to cycle, from Eqs. (2-11) to (2-13), we have

$$(CC)_1 = (CC)_2 = \ldots = (CC)_n = (CC)$$

$$(BB)_1 = (BB)_2 = \ldots = (BB)_n = (BB)$$

and

$$(DD)_1 = (DD)_2 = \ldots = (DD)_n = (DD).$$

Thus,

$$(C_d)_a = \frac{(AA)_1(BB)_1 - (DD)_1(EE)_1 + \ldots + (AA)_n(BB)_n - (DD)_n(EE)_n}{n \cdot \frac{1}{2}\rho DL \cdot [(CC)(BB) - (DD)^2]}$$

$$= \frac{(BB)\dfrac{[(AA)_1 + \ldots + (AA)_n]}{n} - (DD)\dfrac{[(EE)_1 + \ldots + (EE)_n]}{n}}{\frac{1}{2}\rho DL[(CC)(BB) - (DD)^2]}$$

From Eq. (2-10), it is known that

$$\frac{[(AA)_1+\ldots+(AA)_n]}{n} = \frac{\int_o^{2\pi}[F_{xm1}u_1+F_{2m1}w_1]\left|\vec{q}\right|_1 d\theta+\ldots+\int_o^{2\pi}[F_{xmn}u_n+F_{zmn}w_n]\left|\vec{q}\right|_n d\theta}{n}$$

$$= \frac{\int_o^{2\pi}\{[F_{xm1}u_1+F_{zm1}w_q]\left|\vec{q}\right|_1 d\theta+\ldots+[F_{xmn}u_n+F_{zmn}w_n]\left|\vec{q}\right|_n\}d\theta}{n}$$

(Note: $u_1 = \ldots = u_n = u$, $w_1 = \ldots = w_n = w$)

$$= \int_o^{2\pi}\left\{\frac{[F_{xm1}+\ldots+F_{xmn}]}{n}u + \frac{[F_{zm1}+\ldots+F_{zmn}]}{n}w\right\}\left|\vec{q}\right|d\theta$$

$$= (AA)$$

Similarly,

$$\frac{[(EE)_1+\ldots+(EE)_n]}{n} = (EE)$$

Thus,

$$(C_d)_a = \frac{(BB)(AA)-(DD)(EE)}{\frac{1}{2}\rho DL[(CC)(BB)-(DD)^2]} = (C_d)_b$$

(2) $(C_d)_b = (C_d)_c$

$$(C_d)_b = \frac{(BB)(AA)-(DD)(EE)}{\frac{1}{2}\rho DL[(CC)(BB)-(DD)^2]}$$

Set $AA = \int A$, $BB = \int B$, $CC = \int C$, $DD = \int D$, and $EE = \int E$

$$(C_d)_b = \frac{\int B \int A - \int D \int E}{\frac{1}{2}\rho DL[\int C \cdot \int B - (\int D)^2]}$$

$$= \frac{\int (\frac{B_1+\ldots+B_n}{n}) \int (\frac{A_1+\ldots+A_n}{n}) - \int (\frac{D_1+\ldots+D_n}{n}) \int (\frac{E_1+\ldots+E_n}{n})}{\frac{1}{2}\rho DL[\int (\frac{C_1+\ldots+C_n}{n}) \cdot \int (\frac{B_1+\ldots+B_n}{n}) - (\int (\frac{D_1+\ldots+D_n}{n}))^2]}$$

$$= \frac{[\int(B_1+\ldots+B_n) \cdot \int(A_1+\ldots+A_n) - \int(D_1+\ldots+D_n)\int(E_1+\ldots+E_n)}{\frac{1}{2}\rho DL[\int(C_1+\ldots+C_n) \int(B_1+\ldots+B_n) - (\int(D_1+\ldots+D_n))^2]}$$

$$= (C_d)_c$$

In the laboratory, it is very difficult, if not impossible, to generate a series of waves with exactly the same wave height and shape. Thus, the undisturbed kinematics are not exactly the same from wave to wave. However, even with slight variations of wave heights from wave to wave in this study, it is found that the C_d and C_m from method (a) and (b) are almost the same. Figure A-1 shows this result for the HSRC.02 in periodic waves.

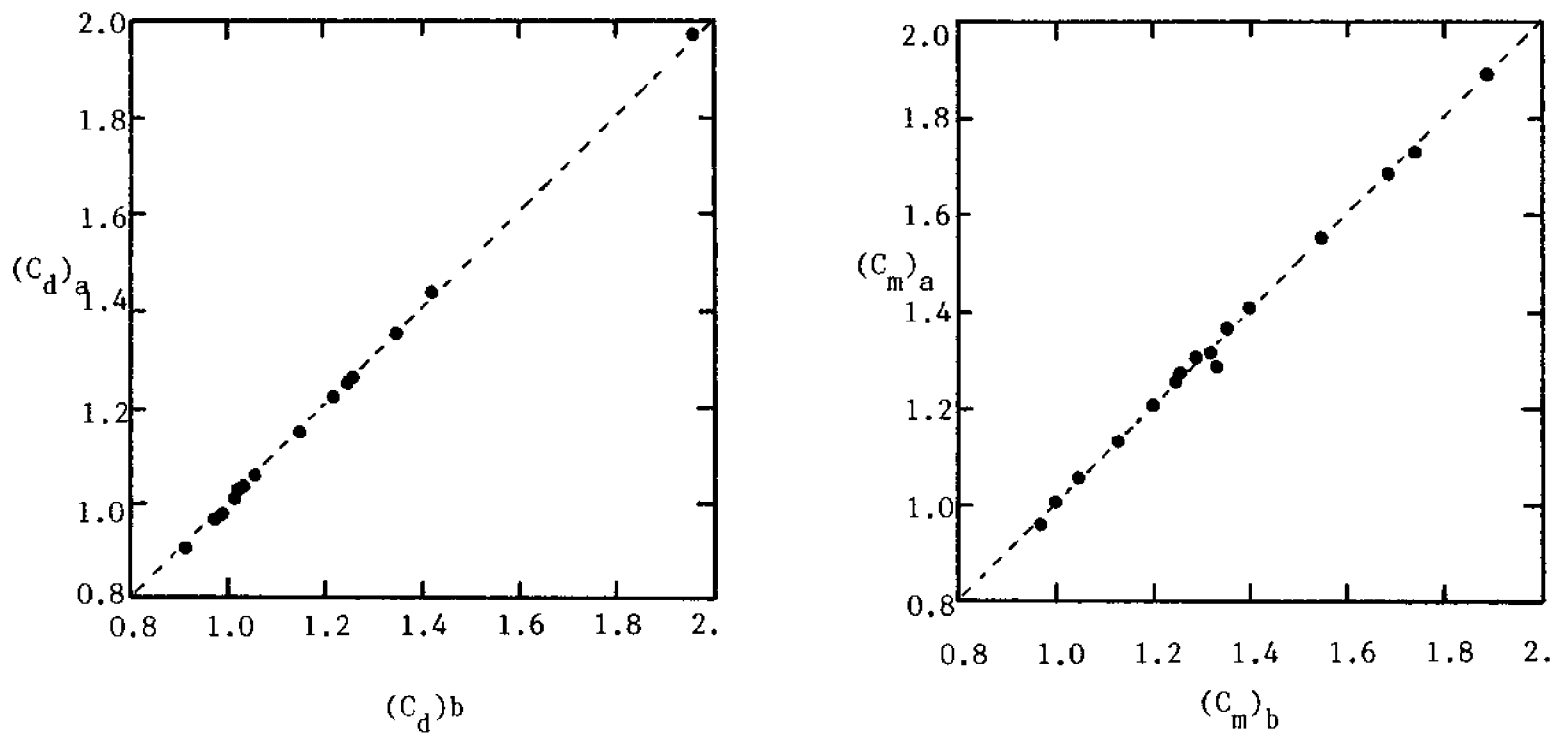

Fig. A-1 Comparisons of C_d and C_m for HSRC.02 from different average methods.

Table B-1. Data of HSMC8 in waves.

RUN	T	H	K	R	C_d	C_m	C_{xr}	C_{zr}	C_{tr}	C_μ	$C_x(1)$	$C_z(1)$	$C_x(2)$
278	2.50	1.20	2.75	0.40	0.33	0.93	5.333	4.383	6.903	4.17	3.793	3.711	0.199
280	2.50	1.80	4.16	0.61	1.11	1.58	5.180	4.864	7.106	5.51	4.819	4.249	0.620
281	2.50	2.87	6.69	0.98	0.93	1.03	2.753	2.677	3.840	2.66	2.300	2.070	0.605
283	2.50	3.80	8.53	1.25	0.62	1.19	2.319	2.103	3.130	2.11	2.119	1.674	0.417
284	3.70	1.00	3.87	0.38	0.37	0.91	4.106	1.784	4.477	3.09	2.817	1.195	0.067
285	3.70	2.20	8.45	0.84	0.64	1.09	2.010	1.534	2.529	1.85	1.497	1.059	0.277
286	3.70	3.39	12.64	1.25	0.53	0.84	1.136	1.030	1.533	1.07	0.851	0.638	0.145
287	3.70	4.71	16.64	1.65	0.26	1.13	0.978	0.812	1.271	0.95	0.714	0.540	0.221
288	3.70	4.80	16.89	1.67	0.37	1.10	0.998	0.789	1.272	0.83	0.744	0.533	0.211
289	4.61	1.03	5.17	0.41	0.64	0.84	2.590	1.008	2.780	2.15	1.909	0.733	0.221
290	4.61	1.91	9.63	0.77	0.77	0.94	1.767	1.165	2.117	1.53	1.144	0.729	0.178
291	4.61	3.60	17.74	1.41	0.66	0.64	1.037	0.771	1.293	0.83	0.685	0.456	0.075
292	4.61	4.50	22.03	1.75	0.39	0.93	0.879	0.743	1.151	0.61	0.496	0.338	0.114
293	5.29	0.90	5.38	0.37	0.99	0.82	2.930	1.240	3.182	2.22	1.838	0.647	0.280
294	5.29	1.65	9.99	0.69	0.51	0.77	1.598	0.943	1.855	1.33	0.926	0.329	0.270
295	5.29	2.90	17.63	1.22	0.45	0.96	1.043	0.786	1.306	0.72	0.591	0.297	0.266
296	5.29	4.00	24.07	1.67	0.43	0.88	0.756	0.684	1.019	0.71	0.335	0.300	0.177
297	6.00	1.25	8.87	0.54	0.96	1.08	2.362	1.195	2.647	2.04	1.431	0.318	0.505
298	6.00	2.08	15.06	0.92	0.62	1.07	1.549	1.092	1.896	1.20	0.777	0.284	0.290
299	6.00	2.75	19.82	1.21	0.60	0.97	1.104	0.937	1.448	1.05	0.536	0.335	0.184
300	6.00	3.16	22.83	1.39	0.59	1.03	1.050	0.751	1.291	0.81	0.490	0.304	0.199
313	2.50	1.20	2.75	0.40	1.05	0.92	5.524	4.728	7.271	4.15	3.948	3.741	0.224
315	2.50	1.75	4.05	0.59	0.71	1.30	5.316	4.931	7.251	4.94	3.881	3.607	0.574
316	2.50	2.65	6.13	0.90	0.81	1.25	3.138	3.071	4.390	2.86	2.567	2.639	0.651
318	2.50	3.82	8.56	1.25	0.21	1.24	2.182	1.947	2.925	2.58	1.891	1.805	0.612
319	3.70	1.00	3.87	0.38	0.21	0.80	3.980	1.539	4.268	3.72	2.659	0.920	0.018
320	3.70	2.11	8.00	0.80	0.60	1.00	2.251	1.671	2.803	2.37	1.510	1.019	0.360
321	3.70	2.90	10.99	1.09	0.69	1.18	1.681	1.343	2.152	1.59	1.287	1.014	0.105
322	3.70	3.91	14.13	1.40	0.85	1.43	1.385	1.169	1.812	1.17	0.999	0.835	0.314
323	3.70	4.15	15.20	1.51	0.40	1.34	1.295	1.015	1.645	1.06	0.987	0.757	0.240
324	4.61	0.88	4.44	0.35	0.82	0.95	3.743	1.415	4.001	3.13	2.604	0.835	0.145
325	4.61	1.78	9.01	0.72	0.79	0.77	2.041	1.349	2.446	1.49	1.202	0.599	0.085
326	4.61	3.62	17.83	1.42	0.53	0.92	1.026	0.755	1.274	0.93	0.684	0.412	0.054
327	4.61	4.37	21.35	1.70	0.54	0.88	0.941	0.770	1.216	0.61	0.513	0.385	0.160
328	5.29	0.94	5.63	0.39	0.87	0.65	2.408	0.691	2.505	1.87	1.550	0.343	0.225
329	5.29	1.72	10.40	0.72	0.70	0.80	1.498	0.850	1.723	1.21	0.945	0.403	0.245
331	5.29	3.95	23.75	1.64	0.47	0.86	0.831	0.738	1.112	0.55	0.364	0.290	0.187
332	6.00	1.30	9.22	0.56	0.67	0.98	2.349	1.562	2.821	1.52	1.249	0.196	0.342
334	6.00	2.70	19.54	1.19	0.73	0.97	1.293	0.897	1.568	0.93	0.626	0.265	0.238
335	6.00	3.15	22.74	1.39	0.56	1.03	1.035	0.724	1.263	0.86	0.498	0.267	0.205
340	2.50	1.23	2.82	0.41	-1.34	0.99	5.855	5.404	7.967	5.90	4.066	4.388	0.846
341	3.70	0.95	3.66	0.36	0.31	0.86	4.301	1.721	4.633	3.42	2.955	1.059	0.056
342	4.61	0.88	4.44	0.35	0.79	0.93	3.506	1.288	3.735	2.97	2.514	0.882	0.110
343	5.29	0.97	5.81	0.40	0.79	0.66	2.219	0.751	2.343	1.63	1.445	0.472	0.230
344	6.00	1.31	9.28	0.57	1.07	1.08	2.378	1.311	2.715	1.65	1.422	0.586	0.514
345	3.70	3.00	11.37	1.13	0.52	0.92	1.478	1.275	1.952	1.28	1.096	0.647	0.189
346	4.61	3.42	16.88	1.34	0.75	0.34	1.077	0.924	1.419	0.77	0.612	0.466	0.063
347	6.00	2.66	19.24	1.17	0.77	0.99	1.352	0.947	1.651	0.89	0.646	0.323	0.268
349	5.29	3.90	23.46	1.62	0.37	0.93	0.785	0.627	1.004	0.59	0.362	0.217	0.224
350	4.61	4.37	21.35	1.70	0.23	1.20	0.906	0.725	1.160	0.64	0.507	0.387	0.150

Table B-1. Data of HSMC8 in waves (continued).

RUN	$C_z(2)$	$C_x(3)$	$C_z(3)$	$\phi_x(1)$	$\phi_z(1)$	$\phi_x(2)$	$\phi_z(2)$	$\phi_x(3)$	$\phi_z(3)$	$F_x(0)$	$F_z(0)$
278	0.082	0.066	0.019	86.659	170.813	280.420	354.154	285.970	5.126	0.434	0.000
280	0.892	0.094	0.070	81.654	156.457	331.711	74.856	269.499	275.097	-0.620	0.704
281	0.840	0.080	0.093	63.599	153.292	33.023	122.228	258.065	302.186	-2.374	0.161
283	0.616	0.026	0.046	72.396	156.686	35.284	119.199	269.298	321.536	-2.181	0.222
284	0.098	0.201	0.132	86.862	149.115	347.482	278.502	274.992	318.630	0.034	0.190
285	0.526	0.098	0.062	75.102	136.886	58.041	157.637	308.699	36.225	-0.858	-0.498
286	0.289	0.056	0.081	66.861	121.898	55.736	159.997	338.494	95.469	-1.733	-1.371
287	0.364	0.106	0.122	79.754	144.333	46.195	179.362	78.884	141.740	-1.823	-1.835
288	0.345	0.112	0.134	72.475	127.849	81.614	172.713	38.560	144.844	-1.249	-1.158
289	0.489	0.095	0.113	78.179	122.285	333.550	53.563	249.715	49.518	-0.060	0.219
290	0.400	0.037	0.068	66.026	116.618	11.638	113.542	358.343	88.654	-0.729	-0.412
291	0.177	0.035	0.103	50.071	67.824	92.095	150.544	341.896	53.220	-2.072	-1.799
292	0.123	0.055	0.138	60.694	107.871	57.185	104.394	14.912	143.797	-1.454	-0.893
293	0.384	0.109	0.140	66.925	110.365	38.346	78.120	194.168	334.597	0.124	0.118
294	0.305	0.052	0.092	69.663	91.165	47.005	103.683	226.647	6.369	-0.062	-0.056
295	0.312	0.058	0.130	66.255	66.255	58.669	58.669	283.891	283.891	-0.130	0.027
296	0.187	0.140	0.196	53.379	115.870	68.518	162.487	21.943	121.560	-0.504	-0.501
297	0.513	0.166	0.417	62.781	116.623	41.593	68.835	294.491	15.223	0.095	0.145
298	0.324	0.093	0.265	64.766	97.318	63.919	118.112	336.985	56.589	0.026	-0.140
299	0.185	0.125	0.280	55.956	105.800	78.999	115.367	18.702	121.260	-0.022	-0.280
300	0.126	0.139	0.255	52.542	105.489	68.432	142.386	10.846	113.538	-0.148	-0.023
313	0.186	0.087	0.057	74.761	160.909	257.832	312.781	286.724	322.265	0.376	0.090
315	0.643	0.084	0.057	82.995	161.374	320.457	44.598	257.573	226.968	0.876	1.481
316	0.853	0.091	0.111	74.037	159.451	40.719	139.346	256.968	318.212	-2.290	0.289
318	0.802	0.104	0.070	80.152	171.602	92.302	178.787	282.633	345.326	-2.662	-0.200
319	0.124	0.182	0.131	91.314	134.251	124.512	188.642	282.676	24.799	0.263	0.060
320	0.614	0.037	0.072	76.800	138.670	37.909	148.617	322.784	299.321	-1.128	-0.463
321	0.491	0.145	0.088	72.493	125.969	49.030	165.813	334.480	71.020	-1.280	-0.713
322	0.267	0.102	0.275	98.946	151.845	75.272	222.494	138.448	194.615	-1.293	-1.385
323	0.425	0.141	0.120	76.515	137.269	80.522	180.376	53.515	151.907	-0.991	-0.723
324	0.185	0.025	0.168	78.126	109.754	162.574	350.115	48.624	337.466	0.255	0.247
325	0.338	0.092	0.072	63.691	91.382	21.083	82.221	226.466	348.265	-0.418	-0.102
326	0.205	0.045	0.076	63.835	103.480	27.842	111.586	348.583	109.876	-1.613	-1.008
327	0.179	0.074	0.146	54.591	113.627	35.366	180.475	17.638	136.350	-1.566	-0.876
328	0.842	0.085	0.103	62.605	70.517	67.389	72.104	108.596	302.260	0.030	0.137
329	0.341	0.074	0.071	58.461	94.297	66.314	151.845	168.770	292.572	-0.087	0.018
331	0.202	0.087	0.167	48.571	112.039	65.019	152.998	12.859	117.138	-0.288	-0.259
332	0.533	0.107	0.373	68.769	83.580	66.368	85.899	296.751	7.763	0.047	0.154
334	0.131	0.076	0.258	46.356	104.453	63.459	118.028	355.377	128.819	0.112	0.059
335	0.158	0.119	0.217	53.500	99.175	81.753	122.969	21.224	127.482	-0.287	0.042
340	0.494	0.411	0.160	113.503	194.018	290.955	35.655	298.756	38.054	0.179	-0.161
341	0.122	0.181	0.140	89.424	136.924	240.950	246.949	284.527	34.815	0.247	0.146
342	0.219	0.049	0.157	78.484	116.475	105.364	351.912	227.916	353.787	0.232	0.149
343	0.139	0.097	0.116	65.978	91.521	26.838	114.843	163.243	284.679	0.073	0.115
344	0.596	0.023	0.173	57.854	79.859	81.824	225.274	270.507	16.950	-0.030	0.045
345	0.337	0.132	0.102	71.895	118.090	56.063	166.337	311.865	57.985	-0.830	-1.020
346	0.151	0.036	0.081	33.009	74.723	353.316	102.916	23.426	106.782	-1.538	-0.939
347	0.192	0.078	0.216	46.584	92.808	63.078	137.506	13.145	116.784	-0.176	-0.049
349	0.191	0.096	0.122	60.344	106.874	66.199	156.445	27.024	129.294	-0.577	0.012
350	0.125	0.110	0.144	51.203	139.385	63.221	145.489	89.401	180.085	-1.024	0.018

Table B-2. Data of HSRC.02 in waves.

RUN	T	H	K	R	C_d	C_m	C_{xr}	C_{zr}	C_{tr}
39	4.61	4.24	20.80	1.66	0.97	1.32	1.567	0.998	1.441
40	3.70	2.01	7.70	0.76	1.25	1.09	2.827	1.932	2.355
41	3.70	3.22	12.10	1.20	1.35	0.97	2.203	1.618	1.901
42	3.70	4.17	15.00	1.48	1.02	1.13	1.745	1.322	1.536
43	4.61	4.08	20.00	1.59	1.06	1.36	1.683	1.146	1.579
44	4.61	2.08	10.50	0.84	1.22	1.00	2.255	1.400	2.041
45	4.61	3.29	16.50	1.31	1.15	1.05	1.768	1.096	1.606
46	4.61	4.09	20.00	1.59	1.01	1.24	1.605	0.982	1.459
47	5.29	2.15	13.10	0.90	0.91	1.20	1.843	1.047	1.720
48	5.29	3.12	18.90	1.31	0.97	1.55	1.733	1.253	1.738
49	5.29	3.48	21.00	1.46	1.03	1.40	1.701	1.091	1.642
50	4.61	4.21	20.70	1.64	0.99	1.26	1.565	0.975	1.430
51	6.00	2.11	15.20	0.93	1.42	1.89	2.692	1.659	2.671
52	6.00	2.66	19.30	1.18	1.26	1.74	2.207	1.440	2.223
53	6.00	2.88	20.70	1.26	1.22	1.68	2.085	1.215	2.037
54	4.61	4.08	19.80	1.57	1.06	1.32	1.714	1.078	1.570

RUN	C_μ	$C_x(1)$	$C_z(1)$	$C_x(2)$	$C_z(2)$	$C_x(3)$	$C_z(3)$	$\phi_x(1)$
39	1.05	3.065	4.298	0.755	3.231	0.156	0.186	44.02
40	2.43	2.001	1.121	0.226	0.288	0.208	0.256	59.73
41	1.74	1.552	1.037	0.311	0.373	0.256	0.334	44.19
42	1.43	1.207	0.825	0.236	0.172	0.240	0.270	47.17
43	1.22	1.010	0.583	0.229	0.161	0.190	0.234	42.89
44	1.72	1.434	0.664	0.041	0.271	0.250	0.308	47.90
45	1.27	1.091	0.552	0.168	0.286	0.120	0.160	39.82
46	1.10	0.987	0.538	0.154	0.105	0.122	0.152	42.21
47	1.38	1.095	0.443	0.260	0.252	0.128	0.226	49.62
48	1.44	0.896	0.451	0.423	0.446	0.192	0.218	46.46
49	1.41	0.870	0.355	0.361	0.324	0.218	0.174	40.43
50	1.12	0.934	0.479	0.137	0.103	0.172	0.224	43.02
51	2.16	1.445	0.546	0.367	0.327	0.194	0.438	45.72
52	1.70	1.101	0.367	0.404	0.435	0.198	0.234	42.96
53	1.74	1.040	0.341	0.408	0.347	0.180	0.230	41.19
54	1.23	1.032	0.571	0.203	0.138	0.174	0.178	40.96

RUN	$\phi_z(1)$	$\phi_x(2)$	$\phi_z(2)$	$\phi_x(3)$	$\phi_z(3)$	$F_x(0)$	$F_z(0)$
39	114.90	20.46	131.25	47.44	142.42	-0.915	0.275
40	116.55	89.39	181.24	283.47	21.92	0.067	0.580
41	103.13	4.89	119.73	313.90	51.38	-1.856	-0.414
42	113.81	21.11	127.08	32.05	139.42	-1.158	0.390
43	116.32	26.54	134.04	7.42	113.69	-2.440	1.051
44	111.58	350.32	76.69	96.61	337.39	-0.627	0.538
45	111.46	341.06	100.40	343.58	107.60	-1.430	0.345
46	110.01	24.57	151.19	38.80	162.82	-1.081	0.131
47	130.98	70.19	181.66	228.22	311.85	0.269	1.195
48	140.48	44.44	133.96	336.65	98.38	0.047	0.716
49	120.62	44.41	127.22	351.92	106.93	0.389	1.395
50	114.11	23.95	128.17	28.98	150.47	-1.980	0.154
51	154.38	47.41	145.87	349.76	168.54	0.195	0.855
52	142.10	38.99	128.78	336.86	123.87	0.132	0.618
53	127.81	44.07	131.63	342.20	152.16	0.539	0.958
54	120.19	5.37	136.90	50.52	159.31	-1.161	0.078

Table B-3. Data of HBRC.02 in waves.

RUN	T	H	K	R	C_d	C_m	C_{xr}	C_{zr}	C_{tr}
51	3.70	2.12	8.0	0.79	1.36	1.72	3.785	2.356	3.067
52	3.70	3.42	12.4	1.23	1.73	1.49	2.765	1.958	2.353
53	3.70	4.44	15.7	1.56	1.12	1.64	2.185	1.297	1.789
54	3.70	4.54	16.2	1.60	1.12	1.71	2.197	1.255	1.787
55	4.61	2.16	11.2	0.89	1.64	1.31	2.837	1.757	2.563
56	4.61	3.37	16.8	1.34	1.39	1.53	2.342	1.134	2.010
57	4.61	4.21	20.1	1.63	1.19	1.88	2.167	0.976	1.844
58	5.29	2.25	13.7	0.95	1.09	1.58	2.340	1.211	2.138
59	5.29	3.22	20.1	1.42	1.13	1.96	2.252	1.051	2.018
60	5.29	3.68	22.3	1.55	1.20	1.72	2.058	0.847	1.808
61	6.00	2.14	15.5	0.41	1.56	2.40	3.330	1.419	3.058
62	6.00	2.76	20.1	1.22	1.49	2.00	2.641	0.933	2.361
63	6.00	2.97	21.2	1.30	1.43	2.27	2.579	1.001	2.333

RUN	C_μ	$C_x(1)$	$C_z(1)$	$C_x(2)$	$C_z(2)$	$C_x(3)$	$C_z(3)$	$\phi_x(1)$
51	2.45	2.694	1.503	0.557	0.728	0.208	0.246	67.87
52	1.93	1.887	1.297	0.266	0.283	0.260	0.340	41.29
53	1.48	1.536	0.845	0.392	0.349	0.210	0.230	49.14
54	1.63	1.596	0.866	0.395	0.304	0.270	0.240	47.50
55	1.74	1.727	0.936	0.321	0.518	0.144	0.176	43.28
56	1.42	1.463	0.631	0.194	0.216	0.162	0.238	41.39
57	1.33	1.335	0.559	0.222	0.113	0.174	0.170	46.47
58	1.32	1.362	0.424	0.483	0.596	0.170	0.240	53.05
59	1.33	1.179	0.378	0.496	0.428	0.160	0.124	47.37
60	1.42	1.042	0.335	0.445	0.279	0.140	0.096	39.80
61	1.76	1.826	0.464	0.468	0.529	0.172	0.332	51.39
62	1.56	1.301	0.331	0.438	0.234	0.144	0.172	41.20
63	1.53	1.279	0.333	0.473	0.320	0.138	0.158	42.79

RUN	$\phi_z(1)$	$\phi_x(2)$	$\phi_z(2)$	$\phi_x(3)$	$\phi_z(3)$	$F_x(0)$	$F_z(0)$
51	135.34	348.15	89.97	346.79	104.05	-0.635	0.988
52	122.54	27.76	147.34	34.98	135.65	-1.607	1.286
53	129.51	40.87	129.33	35.86	128.77	-1.442	0.756
54	132.54	42.56	140.08	68.16	169.62	0.841	1.238
55	130.08	337.24	58.19	290.21	24.08	-0.959	1.051
56	122.38	11.15	78.78	353.63	57.10	-1.539	1.137
57	125.11	41.23	86.76	54.51	166.38	-1.770	1.925
58	151.56	42.35	111.12	309.19	355.96	-0.176	0.618
59	139.76	44.44	123.49	355.02	96.28	0.565	1.411
60	125.50	43.43	124.11	23.80	185.69	-1.013	1.635
61	161.78	42.65	130.71	341.08	11.64	-0.408	1.091
62	117.65	48.14	119.01	19.34	188.75	0.539	1.405
63	123.37	47.90	126.33	1.87	185.39	0.666	1.506

Table B-4. Data of HRAN in waves.

RUN	T	H	K	R	C_d	C_m	C_{xr}	C_{zr}	C_{tr}
14	2.50	3.28	7.80	1.14	1.94	1.46	4.30	3.231	3.062
15	3.70	2.06	7.90	0.78	2.63	1.87	5.08	2.805	3.993
16	3.70	3.39	12.40	1.23	2.10	1.57	3.48	2.013	2.791
17	3.70	4.27	15.20	1.50	1.64	2.19	3.15	1.637	2.492
18	3.70	4.36	16.60	1.60	1.69	2.09	3.11	1.593	2.451
19	4.61	2.13	10.80	0.86	2.59	1.68	4.10	2.236	3.589
20	4.61	3.30	16.60	1.32	2.12	1.85	3.31	1.520	2.815
21	5.29	4.11	24.90	1.72	1.70	2.40	2.87	1.308	2.562
22	5.29	2.24	13.70	0.95	1.68	1.87	3.26	1.248	2.838
23	5.29	3.18	19.50	1.35	1.73	2.26	3.06	1.222	2.672
24	5.29	3.70	22.40	1.55	1.64	2.07	2.66	1.101	2.343
25	6.00	2.18	15.60	0.95	2.14	2.72	4.19	1.492	3.755
26	6.00	2.69	19.70	1.20	1.92	2.78	3.68	1.246	3.276
27	6.00	2.95	22.40		1.90	2.49	3.44	1.218	3.080

RUN	C_μ	$C_x(1)$	$C_z(1)$	$C_x(2)$	$C_z(2)$	$C_x(3)$	$C_z(3)$	$\phi_x(1)$
14	3.52	4.177	3.065	0.556	0.755	0.172	0.160	54.83
15	2.97	3.685	1.998	0.514	0.658	0.214	0.226	51.37
16	2.09	2.418	1.307	0.302	0.365	0.178	0.238	40.95
17	1.95	2.201	1.053	0.452	0.396	0.270	0.334	50.41
18	1.76	2.152	1.015	0.398	0.346	0.292	0.374	46.87
19	2.46	2.682	1.334	0.424	0.607	0.160	0.160	40.04
20	1.91	2.056	0.871	0.291	0.269	0.170	0.234	40.66
21	1.44	1.535	0.638	0.236	0.135	0.172	0.238	42.98
22	1.81	1.959	0.401	0.559	0.639	0.086	0.158	47.48
23	1.69	1.634	0.452	0.619	0.492	0.100	0.126	45.43
24	1.59	1.384	0.461	0.566	0.308	0.160	0.184	41.29
25	2.06	2.237	0.364	0.607	0.643	0.186	0.330	47.51
26	1.89	1.834	0.444	0.691	0.382	0.152	0.170	47.18
27	1.60	1.643	0.445	0.637	0.328	0.174	0.194	40.36

RUN	$\phi_z(1)$	$\phi_x(2)$	$\phi_z(2)$	$\phi_x(3)$	$\phi_z(3)$	$F_x(0)$	$F_z(0)$
14	127.16	30.12	128.43	347.36	139.28	-2.02	1.04
15	119.14	358.42	86.03	19.55	111.91	-0.52	1.91
16	105.19	8.77	104.86	359.67	86.20	-2.93	1.46
17	117.88	20.34	117.13	67.63	156.58	-2.00	2.09
18	115.49	29.62	128.51	62.46	154.18	-1.57	2.50
19	116.84	316.30	46.53	354.03	102.40	-1.45	1.77
20	104.61	329.92	58.96	35.92	148.80	-3.06	1.36
21	106.94	20.81	65.36	59.58	172.18	-3.54	1.22
22	120.31	26.47	108.56	141.54	339.15	-0.34	0.87
23	102.22	31.53	112.96	8.44	123.53	0.19	1.67
24	97.19	44.54	116.26	43.21	168.55	0.48	1.81
25	134.13	22.83	107.28	290.57	8.46	-0.61	1.01
26	106.35	43.86	119.10	13.21	148.92	0.22	1.41
27	94.88	44.79	107.79	17.27	160.43	0.44	1.68

Table B-5. Data of HSRC.02 under waves and towing.

RUN	T	H	K	R	U	VM	U/u_{wp}	C_d	C_m	C_{xr}	C_{zr}	C_{rr}	C_μ	$C_x(1)$	$C_z(1)$
1	4.6	4.06	20.84	1.59	0.00	0.00	0.00	1.12	1.14	1.659	1.040	1.517	0.79	0.984	0.503
2	4.6	4.17	26.55	2.24	1.22	7.30	0.34	1.31	0.91	2.215	1.140	1.998	1.16	0.692	0.306
3	4.6	4.08	26.33	2.23	1.27	7.58	0.36	1.05	1.73	2.226	1.047	1.982	0.96	0.704	0.227
4	4.6	3.82	24.53	2.08	1.16	6.96	0.36	1.07	0.95	1.976	1.039	1.790	1.16	0.651	0.256
5	4.6	3.77	29.10	2.39	1.80	10.44	0.56	1.22	1.49	1.894	1.190	1.873	1.32	0.526	0.319
6	4.6	3.81	27.36	2.41	1.80	10.44	0.55	1.16	1.84	2.119	1.060	2.000	1.36	0.626	0.311
7	4.6	3.86	32.35	3.02	2.96	16.18	0.90	1.21	1.33	1.882	0.923	1.898	1.27	0.555	0.217
8	4.6	3.82	32.28	3.02	2.99	16.32	0.92	1.19	1.60	1.900	0.788	1.867	1.31	0.572	0.188
9	4.6	3.79	34.76	3.36	3.69	19.46	1.14	1.21	1.77	1.762	0.657	1.753	1.18	0.545	0.153
10	4.6	3.90	35.38	3.43	3.73	19.63	1.12	1.17	1.17	1.696	0.678	1.701	1.35	0.524	0.135
11	4.6	4.24	39.03	3.89	4.37	22.32	1.20	0.97	0.92	1.380	0.368	1.342	1.10	0.427	0.105
12	4.6	4.19	38.68	3.86	4.33	22.15	1.20	1.02	0.84	1.437	0.459	1.418	1.13	0.433	0.111
13	4.6	4.08	39.84	4.08	4.93	24.53	1.44	1.05	1.53	1.388	0.386	1.376	1.14	0.440	0.110
14	4.6	4.05	39.86	4.11	4.94	24.44	1.42	0.98	1.66	1.302	0.279	1.270	1.12	0.409	0.113
15	4.6	3.85	41.71	4.43	5.74	27.55	1.74	1.03	1.66	1.281	0.277	1.267	1.20	0.410	0.108
16	4.6	3.94	45.48	5.09	6.95	31.69	2.06	0.96	2.46	1.154	0.203	1.143	0.88	0.348	0.102
17	4.6	3.83	44.95	5.02	6.91	31.55	2.11	1.00	2.03	1.176	0.203	1.166	0.97	0.362	0.103
18	4.6	3.92	48.09	5.61	8.00	34.95	2.38	1.02	3.51	1.165	0.183	1.157	1.13	0.355	0.095
19	4.6	3.87	48.96	5.81	8.44	36.23	2.55	0.91	3.74	1.040	0.136	1.032	0.97	0.302	0.081
20	4.6	4.09	49.94	5.95	8.52	36.46	2.43	1.01	1.76	1.151	0.211	1.150	1.05	0.308	0.092
21	4.6	4.10	51.18	6.31	9.05	37.94	2.57	0.89	4.98	1.026	0.137	1.019	0.84	0.270	0.084
22	4.6	4.00	52.02	6.47	9.59	39.39	2.80	0.90	4.02	1.001	0.147	0.999	0.84	0.239	0.084

RUN	$C_x(2)$	$C_z(2)$	$C_x(3)$	$C_z(3)$	$\phi_x(1)$	$\phi_z(1)$	$\phi_x(2)$	$\phi_z(2)$	$\phi_x(3)$	$\phi_z(3)$	$F_x(0)$	$F_z(0)$	$C_x(0)$	$C_z(0)$
1	0.221	0.150	0.130	0.186	37.31	102.78	49.51	132.76	8.35	130.22	-1.636	0.421	-	-
2	0.263	0.089	0.156	0.326	20.70	101.27	353.61	67.86	298.30	285.14	4.154	0.513	4.003	0.494
3	0.323	0.068	0.164	0.440	36.38	131.05	18.40	178.82	266.37	323.69	6.047	1.526	5.378	1.357
4	0.298	0.122	0.118	0.346	21.23	119.03	349.78	155.23	333.84	248.78	4.227	1.122	4.506	1.196
5	0.228	0.132	0.244	0.360	26.66	109.16	10.63	95.70	36.71	22.14	10.119	2.227	4.480	0.986
6	0.232	0.129	0.262	0.234	32.85	117.81	10.66	103.92	57.58	23.26	10.214	2.035	4.522	0.901
7	0.198	0.147	0.238	0.542	13.32	97.69	8.19	134.78	29.15	166.98	20.470	2.963	3.351	0.485
8	0.196	0.105	0.196	0.314	16.04	112.64	14.71	127.60	18.54	101.21	20.740	1.629	3.327	0.261
9	0.151	0.122	0.286	0.488	13.87	119.13	24.31	106.30	350.23	56.58	28.800	1.755	3.034	0.185
10	0.154	0.133	0.362	0.392	11.94	110.25	25.76	82.09	346.57	44.52	28.207	2.201	2.988	0.227
11	0.124	0.058	0.280	0.236	11.93	99.26	11.30	86.56	309.92	134.56	24.452	1.463	2.383	0.110
12	0.132	0.094	0.260	0.262	7.07	99.75	7.80	82.29	329.28	92.68	28.265	1.462	2.515	0.112
13	0.132	0.074	0.394	0.334	10.50	98.59	356.60	102.92	309.44	152.72	32.099	1.480	2.377	0.087
14	0.122	0.063	0.320	0.222	12.86	97.39	1.80	107.20	321.54	56.49	30.100	1.383	2.247	0.081
15	0.117	0.059	0.344	0.294	10.24	93.01	350.78	108.51	312.51	54.56	39.432	1.956	2.218	0.085
16	0.092	0.045	0.340	0.170	12.79	93.50	4.60	121.26	296.97	66.56	55.142	1.607	2.058	0.050
17	0.095	0.041	0.204	0.252	10.09	92.13	7.95	108.81	318.77	91.55	69.652	1.504	2.092	0.045
18	0.093	0.043	0.252	0.262	4.92	92.89	7.12	101.45	356.28	103.44	94.664	1.054	2.122	0.024
19	0.078	0.035	0.236	0.204	14.71	90.97	28.79	110.45	69.60	139.49	93.867	1.557	1.890	0.031
20	0.060	0.043	0.634	0.306	5.54	91.60	321.42	98.13	285.89	67.83	86.216	1.355	2.131	0.027
21	0.070	0.030	0.216	0.242	-18.13	95.56	45.49	125.65	281.58	133.22	108.706	1.236	1.904	0.022
22	0.036	0.043	0.422	0.346	14.56	90.33	32.88	116.63	240.76	126.37	120.721	0.909	1.883	0.014

Table B-6. Data of HBRC.2 under waves and towing.

RUN	T	H	K	R	U	VN	U/u_{wp}	C_d	C_m	C_{xr}	C_{zr}	C_{rr}	C_μ	$C_x(1)$	$C_z(1)$	$C_x(2)$
78	3.7	3.38	23.39	2.45	-2.41	10.8	1.01	1.51	2.55	2.527	1.139	2.378	1.27	0.827	0.476	0.261
79	3.7	3.78	26.49	3.22	-3.61	15.2	1.34	1.34	1.57	1.916	0.631	1.829	1.11	0.588	0.239	0.130
80	3.7	3.47	28.18	3.59	-4.57	18.3	1.85	1.38	2.32	1.766	0.445	1.717	1.15	0.626	0.220	0.114
81	3.7	3.39	31.33	4.25	-5.94	22.3	2.47	1.30	3.44	1.539	0.305	1.514	1.08	0.531	0.194	0.082
82	3.7	3.44	33.86	4.85	-7.07	25.5	2.90	1.25	3.97	1.421	0.239	1.404	0.84	0.464	0.170	0.073
83	3.7	3.38	36.23	5.44	-8.28	28.1	3.46	1.20	9.37	1.346	0.201	1.335	1.02	0.434	0.152	0.064
84	3.7	2.79	36.23	5.65	-9.14	29.9	3.80	1.30	12.80	1.403	0.204	1.402	1.14	0.451	0.169	0.059

RUN	$C_z(2)$	$C_x(3)$	$C_z(3)$	$\phi_x(1)$	$\phi_z(1)$	$\phi_x(2)$	$\phi_z(2)$	$\phi_x(3)$	$\phi_z(3)$	$F_x(0)$	$F_z(0)$	$C_x(0)$	$C_z(0)$
78	0.104	0.264	0.596	36.30	120.92	342.43	26.62	300.05	275.39	18.750	2.821	4.630	0.496
79	0.139	0.240	0.712	15.12	118.60	27.96	58.62	359.43	51.81	32.268	2.043	3.551	0.225
80	0.107	0.230	0.674	18.15	104.25	11.41	83.52	281.13	138.14	44.709	1.924	3.071	0.132
81	0.084	0.242	0.412	19.39	101.96	27.93	113.19	318.20	194.63	67.470	2.436	2.743	0.099
82	0.057	0.124	0.250	18.51	96.89	23.54	111.70	321.21	203.54	90.186	3.124	2.588	0.090
83	0.049	0.288	0.240	34.61	102.98	55.60	130.72	256.56	105.20	118.020	5.587	2.469	0.117
84	0.049	0.538	0.714	32.27	98.62	63.49	134.63	225.74	313.02	150.416	4.431	2.583	0.076

Table B-7. Data of HRAN under waves and towing.

RUN	T	H	K	R	U	VM	U/u_{wu}	C_d	C_m	C_{xr}	C_{zr}	C_{tr}	C_μ	$C_x(1)$	$C_z(1)$	$C_x(2)$
42	3.7	3.36	21.95	2.48	-2.49	11.22	1.05	1.68	2.81	2.733	1.028	2.523	1.30	0.996	0.437	0.260
43	3.7	3.81	26.68	3.21	-3.57	15.14	1.31	1.39	2.75	2.018	0.779	1.957	1.07	0.669	0.352	0.198
44	3.7	3.43	28.37	3.59	-4.60	18.55	1.89	1.50	3.32	1.954	0.473	1.898	1.16	0.728	0.265	0.121
45	3.7	3.43	31.36	4.28	-5.95	22.26	2.45	1.42	4.60	1.702	0.414	1.689	1.08	0.584	0.247	0.094
46	3.7	3.45	33.39	4.72	-6.82	24.57	2.78	1.39	6.62	1.647	0.395	1.647	1.06	0.533	0.248	0.082
47	3.7	3.66	36.29	5.41	-8.00	27.37	3.07	1.33	4.65	1.487	0.328	1.489	0.88	0.489	0.232	0.035
48	3.7	3.45	36.87	5.61	-8.55	28.66	3.49	1.35	8.63	1.492	0.302	1.495	0.90	0.406	0.226	0.032
49	3.7	3.57	37.07	5.64	-8.52	28.56	3.36	1.42	7.78	1.582	0.306	1.581	1.06	0.458	0.221	0.049

RUN	$C_z(2)$	$C_x(3)$	$C_z(3)$	$\phi_x(1)$	$\phi_z(1)$	$\phi_x(2)$	$\phi_z(2)$	$\phi_x(3)$	$\phi_z(3)$	$F_x(0)$	$F_z(0)$	$C_x(0)$	$C_z(0)$
42	0.165	0.220	0.278	30.19	122.97	23.43	95.04	162.96	37.43	19.223	3.267	4.449	0.756
43	0.143	0.188	0.542	23.68	126.05	30.88	55.39	349.57	48.58	31.964	4.864	3.597	0.547
44	0.114	0.450	0.476	23.22	103.21	25.29	82.39	268.18	75.18	40.688	2.541	3.300	0.172
45	0.149	0.782	0.442	25.44	111.69	24.15	96.19	288.65	273.96	74.579	1.759	3.022	0.071
46	0.126	0.348	0.922	33.02	98.81	45.83	111.99	45.90	36.47	95.279	0.899	2.938	0.028
47	0.093	0.566	0.954	25.66	262.12	5.33	106.06	260.74	78.60	124.988	-0.758	2.801	-0.170
48	0.078	0.870	0.984	35.32	93.53	7.86	119.77	284.45	327.74	143.166	-2.317	2.809	-0.045
49	0.075	0.320	0.634	26.73	262.63	39.73	113.44	332.91	71.20	149.701	-2.857	2.958	-0.056